Cryogenic Electron Microscopy Studies: Structure and Formation of Self-assembled Nanostructures in Solution

A DISSERTATION
SUBMITTED TO THE FACULTY OF THE GRADUATE SCHOOL
OF THE UNIVERSITY OF MINNESOTA
BY

Han Seung Lee

IN PARTIAL FULFILLMENT OF THE REQUIREMENTS
FOR THE DEGREE OF
DOCTOR OF PHILOSOPHY

Alon V. McCormick, Advisor

May, 2015

Acknowledgements

I am very grateful to have Professor Alon V. McCormick as my adviser and Professor. H. Ted Davis (Deceased May in 2009), as my first adviser who allowed me join his research. I would like thank to his longtime support, patience, guidance, and inspiration. I am also thankful to Dr. Eric D. Morrison who has been directed me through the most of my research as an IPRIME industrial fellow. I thanks, professors Christopher W. Macosko, Joseph A. N. Zasadzinski, Efie Kokkoli, Frank S. Bates, and Jan Sefcik in the University of Strathclyde who allowed me participate to their research and also guide me during my graduate school. I would like to thank Dr. Jayesh Bellare in India Institute of Technology, Bombay, and Dr. Yeshayahu Talmon in Technion, Israel Institute of

Technology for their helpful discussion on their insights in cryogenic transmission electron microscopy of soft materials and their teaching from cryogenic electron microscopy short course. I am also grateful to have received support for this work and my education from the Industrial Partnership for Research in Interfacial and Materials Engineering at the University of Minnesota.

I have benefited greatly from assistances and interactions with Mr. Chris D. Frethem, Ms. Linda Sauer, Ms. Fang Zhou, Drs. Ozan Ugurlu, Robert S. Hafner, Wei Zhang, Bing Luo, and Jason Myers have been patiently taught me how to operate instruments in the characterization facility. There are many colleagues that I should thank for their warmest help and friendship: Drs. Tobias Foster, Apostolos Nikolaou Vagias, and Sangwoo Lee helped me start the experiment in the lab. Dr. Manickam Adhimoolam Arunagirinathan guided me how to operate electron microscope and gave me advice on sample preparation. I am also thankful for working with Dr. Benjamin Wong during my visit to the University of California, Santa Barbara for experiments with freeze-fracture electron microscopy. I would like to express thanks to the Hackel group members and polymer group members for sharing the office and creating a friendly environment. I also would like to express thanks to my group member, David Riehm, who shared valuable discussions in the lab and Julie Prince as a program associate in graduate studies. I also thank Qiao Zhang who helped me as an undergraduate researcher until he graduates.

Lastly, my deepest thanks and gratitude must go to my family. They have been given endless encouragement and have supported me in my every endeavor.

To God and my dearest family: Dad, Mom, and Sister

Abstract

Cryogenic electron microscopy (Cryo-EM) techniques are among the most powerful to characterize self-assembling soft materials (colloids, polymers, and microemulsions, etc.) at the nanometer scale, without any need for implicit models or assumptions about the structure. We can even visualize structure under dynamic conditions, capturing each stage of development. In this thesis, cryo-EM has been used to investigate the formation and structure of a variety of self-assembling soft materials. Visualization is complemented by small angle X-ray scattering (SAXS), dynamic light scattering, and conductivity measurements. In each case, cryo-EM provides new insights, not otherwise available, into the nanostructure development.

Self-assembly phenomena at the molecular level are critical to the performance of tremendous number of applied systems ranging from personal care products to industrial

products. To evaluate these self-assembled materials, multiple characterization techniques are required.

We investigated aggregation behavior of cesium dodecyl sulfate (CsDS) ionic surfactant in aqueous solution. Coupled with the real space data from cryogenic transmission electron microscopy (Cryo-TEM) and the inverse space data from SAXS, the experimental result of CsDS in aqueous solution gave a new insight in CsDS micellar structures and their development as a function of concentration. Cryo-TEM showed the presence of the liquid-like hydrocarbon core in the CsDS micelles and relatively thick shell structures at a low CsDS concentration. The core-shell sphere structure micelle shifted to core-shell cylindrical micelle structure at high concentration.

The morphology and structure of paclitaxel silicate (PTX) prodrug, encapsulated with amphiphilic poly(ethylene glycol)-*b*-poly(lactic-co-glycolic acid) diblock copolymers were studied. The six different silicate PTX prodrug candidates were characterized with cryo-TEM. Direct imaging with cryo-TEM illustrated structure of prodrug morphology prepared with flash nanoprecipitation method. Cryo-TEM also visualized drug release kinetics of the silicate PTX prodrugs, suggesting diffusion or degradation release mechanisms.

Lastly, formulation of nanoemulsion through phase change emulsification of water/alkane/alkylphenolethoxylate non-ionic surfactant microemulsions is investigated. The amount of cosurfactant determined phase behavior characteristics of microemulsions. The initial structure of the microemulsions determined resulting nanoemulsions. The oil-in-water microemulsions became an exfoliating lamellar intermediate structure during quenching and dilution. The process produced small, simple, and uniform nanoemulsions. Complimentary electron microscopy techniques such as cryo-TEM, cryogenic scanning electron microscopy, and freeze-fracture electron microscopy elucidated microstructural development at each stage. This result enables to control both intra- and inter-molecular forces that govern structure and properties relationship, therefore, to correlate the optimization and the performance of engineered liquid systems within the specified constraints.

Table of Contents

List of Tables

List of Figures

Chapter 1.
Introduction

The idiom "Seeing is believing" simply represents how humans have heavily depended on their eyesight to recognize the world. Whereas astronomers endeavored to discover the farthest objects in the universe using telescopes, a group of physicists attempted to elucidate the smallest structures in matter by inventing microscopes at the opposite end of the research scale. The discovery of electron microscopy, conceived by de Broglie's hypothesis on "wave-particle duality" of electrons, allowed to surpass the image resolution which was limited by wavelength of light.[1] These phenomenal inventions of transmission electron microscopy by Knoll and Ruska in 1931 and scanning electron microscopy by Zworykin in 1942 enabled researchers to observe morphology of materials ultimately at the molecular level.[2, 3]

Based on the understanding of fundamental properties of materials with advanced imaging techniques, scientists analyze the microstructure of materials and develop their processing.[4, 5] As a result, the application of these electron microscopies toward modern material research challenges sheds light on invention of sophistically engineered products, ranging from commodities in our modern daily life to industrial materials for application of advanced technologies.[6, 7, 8, 9]

Electron microscopy (EM) imaging is the single technique that provides the most intuitive and direct interpretation in materials characterizations with high resolution. However, the high vacuum environment in the electron microscope has limited the selection of materials. Although a relatively limited number of chemically fixed (dehydrated and substituted with fixatives) biological samples have been allowed in the electron microscope, for some time only hard materials have been suitable candidates for high resolution imaging for structural characterization.[10] However, high resolution EM imaging of soft materials such as complex liquids, colloids, polymers, and liquid crystals is also essential for fundamental understandings of soft materials and their applications.[11, 12, 13, 14]

To understand the characteristics of self-assembled materials or supramolecular aggregates, the surfactant, colloids, and polymer groups in University of Minnesota have pioneered the development of specimen preparation technique, investigation of sample and electron beam interactions, and methodology of cryogenic electron microscopy through Characterization Facility, a member of National Science Foundation funded Materials Research Facilities Network via Materials Research Science and Engineering Center program.[15, 16, 17, 18, 19, 20, 21, 22, 23, 24, 25, 26] The research performed here is a continuation of University of Minnesota's three decades devoted research with Nanostructural Materials and Processes Program in Industrial Partnership for Research in Interfacial Materials & Engineering and its precursor program, pioneered by Dr. H. Ted Davis. Following this expertise in soft matter EM imaging, we attempted to understand new materials and develop principles for the engineering of systems that grow nanostructures using amphiphilic materials.

In this thesis, the structure and formation of surfactant related self-assemblies are mainly covered. The word "Surfactant" is a blend name of surface-active agent. It adsorbs at interfaces between two immiscible fluids and lowers interfacial tension. The surfactant consists of water-like (hydrophilic) polar headgroup and oil-like (lipophilic) hydrocarbon chain tail-group. Because of their amphiphilic duality, surfactant can increase the solubility and miscibility between the two phases, resulting in characteristic features of ternary phase diagram of surfactant, water, and oil, as shown in Figure 1.1.

We employed cryogenic electron microscopy (Cryo-EM) to elucidate the microstructure of these structured complex fluids. The technique includes cryogenic transmission electron microscopy (Cryo-TEM), cryogenic scanning electron microscopy (Cryo-SEM), and freeze-fracture electron microscopy (FF-TEM). Combined with scattering methods, these complementary microscopy methods provides highly reliable experimental results.

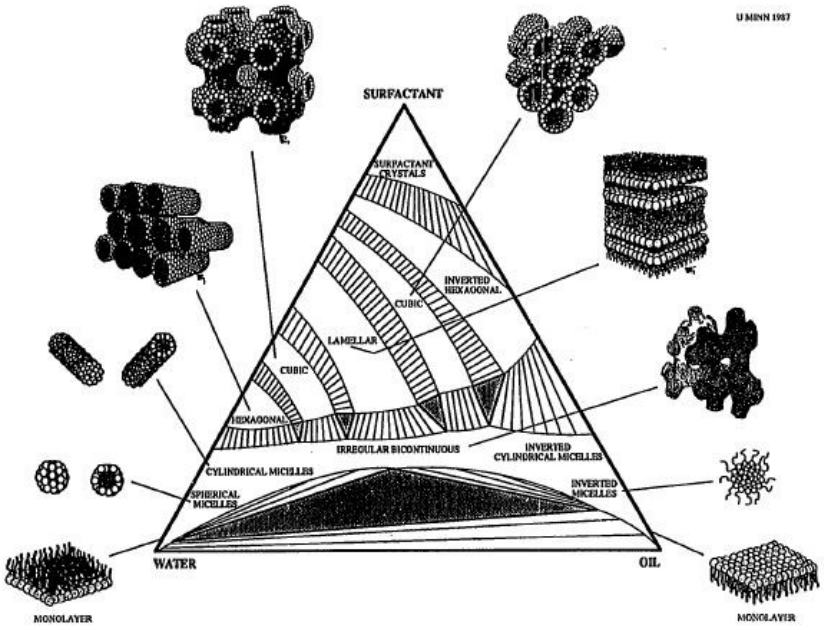

Figure 1.1. Schematic surfactant/water/oil phase diagram with representative models of microstructure at their phase. Adapted from Bellare, J. R., "Cryo-electron and optical microscopy of surfactant microstructure.[27]

1.1 Thesis Overview

This thesis provides a fundamental understanding of the structure of labile materials or their processing through cryogenic electron microscopy or small angle X-ray scattering (SAXS) methods, primarily focusing on (i) re-interpretation of unusual ionic surfactant micelles, (ii) structural investigation of polymer-encapsulated nanoparticles, (iii) examination of preparation of oil-in-water nanoemulsions, and (iv) the exploration of

nanoemulsion formulation in different systems. The order of the chapters is presented according to dimensional increases of the soft matter characterization.

In Chapter 2, the self-assembly of cesium dodecyl sulfate (CsDS) micelle in aqueous solution is discussed and the overall dimension of here reaches up to 10 nm. Much of this chapter has been published as:

> Han Seung Lee, Manickam Adhimoolam Arunagirinathan, Apostolos Vagias, Sangwoo Lee, Jayesh R. Bellare, H. Ted Davis, Eric W. Kaler, Alon V. McCormick, and Frank S. Bates, "Almost fooled again: New insights into cesium dodecyl sulfate micelle structures", *Langmuir* **2014**, *30* (43), 12743 (DOI: 10.1021/la502809y).

In this work, we examined the microstructure of CsDS micelle at different concentrations using two complementary characterization methods. By combining SAXS and cryo-TEM, the structural transition of the CsDS micelle from sphere form at 2.0 wt % to wormlike structure 5.0 and 8.1 wt % is observed. Cryo-TEM revealed a core-shell structure suggesting presence of liquid-like hydrocarbon chains in the core of CsDS micelle, strong binding between sulfate headgroup, and its complexing hydrated cesium counterions in the shell. The charge shielding in the shell of micelle allows cesium cations deeply penetrate into the micelles, resulting in larger micelles. The shell thickness decreases as the micelle becomes a two dimensional cylinder structure.

In Chapter 3, the morphology of therapeutic nanoparticles and the structural changes during drug release are discussed. The dimension of drug nanoparticles are about 150 nm in size scale. This chapter has been worked in collaboration with the Hoye, Macosko, and Panyam research groups in University of Minnesota and the Magdassi research group in the Hebrew University of Jerusalem. Portions of this chapter have been published as:

> 1. Kevin M. Pustulka, Adam R. Wohl, Han Seung Lee, Andrew R. Michel, Jing Han, Thomas R. Hoye, Alon V. McCormick, Jayanth Panyam, and Christopher W. Macosko, "Flash nanoprecipitation: Particle structure and stability", *Molecular Pharmaceutics*, **2013**, *10* (4), 4367 (DOI: 10.1021/mp400337f) and
>
> 2. Katherine Margulis, Shlomo Magdassi, Han Seung Lee, and Christopher W. Macosko, "Formation of curcumin nanoparticles by flash nanoprecipitation from

emulsions", *Journal of Colloid Interface Science*, **2014**, *65*, 434 (DOI: 10.1016/j.jcis.2014.07.040).

A portion of this chapter is also being prepared for submission as:

Jing Han, Andrew R. Michel, Han Seung Lee, Stephen Kalscheuer, Adam R. Wohl, Thomas R. Hoye, Alon V. McCormick, Jayanth Panyam, and Christopher W. Macosko, "Nanoparticles containing high loads of paclitaxel silicate prodrugs: Formulation, drug release, and anitcancer efficacy", *In preparation.*

In these works, therapeutic paclitaxel (PTX) silicate nanoparticles are encapsulated with amphiphilic poly(ethylene glycol)-*b*-poly(lactic-co-glycolic acid) (PEG-*b*-PLGA) diblock copolymers using a flash nanoprecipitation technique through a confined impingement jets with dilution mixer. According to the selection of silicate derivatives, the physical characteristics of prodrug nanoparticles are varied (hydrophobicity, morphology, drug loading, drug release). *In-vitro* drug release mechanism could be explained by microscopy. Cryo-TEM investigation of nanoparticles after *in-vitro* release experiments may suggest either diffusion of PTX silicate from the prodrugs, or release by degradation of the PEG-*b*-PLGA block copolymer, or drug release by osmotic pressure difference between the buffer solution and nanoparticles.

In Chapter 4, preparation of long-lived nanoscale oil-in-water dispersions by phase change emulsification is discussed. The dimension of nanoemulsions in this chapter ranges from 50 nm to 5 μm. Portions of this chapter have been published as:

1. Han Seung Lee, Eric D. Morrison, Chris D. Frethem, Joseph A. Zasadzinski, and Alon V. McCormick, "Cryogenic electron microscopy study of nanoemulsion formation from microemulsions", *Langmuir* **2014**, *30* (36), 10826 (DOI: 10.1021/la502207f) and

2. Han Seung Lee, Eric D. Morrison, and Alon V. McCormick, "Cryo-electron microscopy: Attempts to watch the formation of dilute emulsion via microemulsion", *Microscopy and Microanalysis* **2013** *19* (S2), 260 (DOI: 10.1017/S1431927613003292).

In these works, the initial microstructure of precursor water/*n*-hexadecane/alkylphenolethoxylate surfactant microemulsion determined the final characteristics of nanoemulsions. Water-continuous or bicontinuous microemulsions gave

a simple and uniformly dispersed nano-dispersions whereas lamellar microemulsions gave larger, more complex structures. Intermediate microstructure by cryo-EM may explain the formation of unilamellar or multilamellar nanoemulsions. Examination of nanoemulsion formation through complementary cryo-EM techniques may explain the formation mechanism of nanoemulsion.

In Chapter 5, formation of oil-in-water dispersions in various oil systems is discussed. The size scale of the oil-in-water dispersions in this chapter is similar to the nanoemulsions appeared in the previous chapter. This chapter has been prepared for submission as:

> Han Seung Lee, Eric D. Morrison, Qiao Zhang, and Alon V. McCormick, "Preparation of nanoemulsions by quenching microemulsions–effect of alkane chain length", *Submitted.*

In this work, our modified phase change emulsification technique is explored using different microemulsion systems. A small amount of cosurfactant or a longer alkane oil in the system gave simple nanoemulsions, but excess cosurfactant or shorter alkanes produced complex nanoemulsions. The structure of kinetically stable nanoemulsions are observed with cryo-TEM and dynamic light scattering.

In Chapter 6, lessons from cryogenic electron microscopy are discussed. As I started my research on liquid based soft materials and complex fluids using cryo-EM technique, I had to get trial and error experiment on cryogenic method until I acquired meaningful results. Therefore, I briefly describe lessons from my attempt on cryo-EM characterization and discuss how I distinguish my sample from artifacts in this chapter. Artifacts frequently arise during sample preparation and characterization. The artifact is deteriorative because it generates from the sample itself resulting in phase separation and modify the original status of the sample. In this chapter, some collaborative work with the Zasadzinski research group in University of California, Santa Barbara and the Epand research group at McMaster University.

In addition to these studies, I contributed to collaborative research with the Sefcik research group in University of Strathclyde to understand microstructure of evolution of mesocrystals in amino acid solutions. I also contributed to collaborative research with the

Kokkoli and Bates research groups to understand morphology of biodegradable block copolymer micelle and the structural development of the block copolymer micelle.

1. Anna Jawor-Baczynska, Barry D. Moore, Han Seung Lee, Alon V. McCormick, and Jan Sefcik, "Population and size distribution of solute-rich mesospecies within mesostructured aqueous amino acid solutions", *Faraday Discussions* **2013,** *167* (0), 425 (DOI: 10.1039/C3FD00066D) and
2. Ajay Vidyasagar, Kamlesh Shroff, Han Seung Lee, Timothy R. Pearce, Alon V. McCormick, Frank S. Bates, and Efie Kokkoli, "Biodegardable and thermosensitive PVLA-b-PEG block copolymer", *In preparation.*

1.2 References

1. Atkins, P. W.; De Paula, J. *Atkins' Physical Chemistry*; Oxford University Press 2002.

2. Bogner, A.; Jouneau, P. H.; Thollet, G.; Basset, D.; Gauthier, C. A history of scanning electron microscopy developments: Towards "wet-STEM" imaging. *Micron* **2007,** *38* (4), 390-401.

3. Williams, D. B.; Carter, C. B. The Transmission electron microscope. In *Transmission Electron Microscopy*; Springer, 1996, pp 3-17.

4. Talmon, Y. Transmission electron microscopy of complex fluids: The state of the art. *Berichte der Bunsengesellschaft für physikalische Chemie* **1996,** *100* (3), 364-372.

5. Cao, G. *Nanostructures and Nanomaterials - Synthesis, Properties and Applications*; Imperial College Press: London, 2004.

6. Jacobs, D. S.; Boissy, Y. L.; Lindberg, S. E. Low temperature SEM as a tool for understanding dynamic events in consumer products research manufacture and use. *Microscopy and Microanalysis* **2002,** *8* (SupplementS02), 786-787.

7. Shen, H.; Jacobs, D.; Burns, J.; Boissy, Y.; Domaschko, D. Modern electron microscopy applications in the consumer products industry. *Microscopy and Microanalysis* **2003,** *9* (SupplementS02), 156-157.

8. Bollmann, W.; Spreadborough, J. Action of graphite as a lubricant. *Nature* **1960,** *186* (4718), 29-30.

9. Frank, S.; Poncharal, P.; Wang, Z. L.; Heer, W. A. d. Carbon nanotube quantum resistors. *Science* **1998,** *280* (5370), 1744-1746.

10. Wang, Z. L. Transmission electron microscopy of shape-controlled nanocrystals and their assemblies. *The Journal of Physical Chemistry B* **2000,** *104* (6), 1153-1175.

11. *Microemulsions : properties and applications*; Boca Raton : CRC Press: Boca Raton, Florida, 2009.

12. McClements, D. J. Encapsulation, protection, and release of hydrophilic active components: Potential and limitations of colloidal delivery systems. *Adv. Colloid Interface Sci.* **2015,** *219*, 27-53.

13. Lodge, T. P. A Unique platform for materials design. *Science* **2008,** *321* (5885), 50-51.

14. Gennes, P.-G. d. *The physics of liquid crystals*; Oxford : Clarendon Press
New York : Oxford University Press: Oxford : New York, 1979.

15. Hatfield, J. C. Freeze-fracture electron microscopy and electrical conductivity of microemulsions. Ph.D., University of Minnesota 1978.

16. Talmon, Y. Fluid microstructure: Cold stage electron microscopy and theoretical modeling. Ph.D., University of Minnesota 1979.

17. Falls, A. H. Electron microscopy and molecular theory of microstructured fluids (ice, frozen). Ph.D., University of Minnesota 1982.

18. Zasadzinski, J. A. N. Liquid crystal structure by electron microscopy (liposomes, vesicles, surfctants). Ph.D., University of Minnesota 1985.

19. Bellare, J. R.; Kaneko, T.; Evans, D. F. Seeing micelles. *Langmuir* **1988,** *4* (4), 1066-1067.

20. Vinson , P. K. Cryo-electron microscopy of microstructures in complex liquids. Ph. D., University of Minnesota 1990.

21. Lin, Z. Microstructure and phase behavior of surfactants in solution. Ph.D., University of Minnesota 1993.

22. Li, X. Phase behavior, microstructure and transitions in self-assembled colloidal systems. Ph.D., University of Minnesota 1996.

23. Zheng, Y. Cryo-electron microscopy of microstructures in self-assembled colloidal systems. Ph.D., University of Minnesota 2000.

24. Won, Y.-Y. Block copolymer micelles in water. Ph.D., University of Minnesota 2000.

25. Davis, K. P. Role of molecular architecture in amphiphilic dispersions. Ph.D., University of Minnesota 2009.

26. Lee, S. Structure and dynamics of block copolymer based soft materials. Ph.D., University of Minnesota 2011.

27. Bellare, J. R. Cryo-electron and optical microscopy of surfactant microstructures. Ph. D., University of Minnesota 1988.

Chapter 2.
Almost Fooled Again – New Insights into Cesium Dodecyl Sulfate Micelle Structures*

2.1 Overview

Replacing sodium with cesium as the counterion for dodecylsulfate in aqueous solution results in stronger complexation and charge shielding, which should lead to larger micelles and ultimately to a cylindrical structure (cf. spheres for sodium dodecyl sulfate). But small angle X-ray scattering (SAXS) and small angle neutron scattering patterns previously have been interpreted with ellipsoidal micelle models. We directly image cesium dodecyl sulfate micelles with cryogenic transmission electron microscopy and report large core-shell spherical micelles at low concentrations ($\leq$ 2 wt %) and cylindrical micelles at higher concentrations (5.0 and 8.1 wt %). These structures are shown to be consistent with SAXS patterns modeled using established form factors. These findings highlight the importance of combining real and reciprocal space imaging techniques in the characterization of self-assembled soft materials.

2.2 Introduction

Now more than a century after the concept of a surfactant micelle was introduced by McBain[1] there remain surprises about how micelle morphology evolves in response to changes in conditions or concentrations of surfactant or additive. Micelles of an ionic

* Parts of this chapter are reproduced with permission from Han Seung Lee, Manickam Adhimoolam Arunagirinathan, Apostolos Vagias, Sangwoo Lee, Jayesh R. Bellare, H. Ted Davis, Eric W. Kaler, Alon V. McCormick, and Frank S. Bates, "Almost Fooled Again: New Insights into Cesium Dodecyl Sulfate Micelle Structures", *Langmuir* **2014**, 30 (43), 12743 (DOI: 10.1021/la502809y).

surfactant are typically considered to be spherical, elliptical or cylindrical (rod-like or worm-like), and that progression of shape changes is often observed with increasing surfactant or salt concentration. For example, sodium dodecyl sulfate (SDS) micelles at low concentration are roughly spherical, but grow into rods as sodium chloride is added.[2, 3] The progression toward shapes with lower curvature is thought to reflect the closer packing of surfactant head groups as their electrostatic repulsions are shielded, but the details of shape changes and micelle sizes depend strongly on the kind of counterion. Counterion specific interactions with surfactant ions have been explored using a variety of computational and experimental tools,[4, 5, 6, 7] and in particular the tight binding of cesium ions with sulfate and carboxylate surfactants has been documented.[8, 9, 10, 11] This suggests that the properties of cesium dodecyl sulfate (CsDS) micelles could be qualitatively different from those formed with sodium.[12, 13, 14]

Small angle X-ray scattering (SAXS) and small angle neutron scattering patterns of CsDS micelles in low concentration aqueous solution (ca. 3 wt %) have been interpreted using a core-shell ellipsoid model, with the core occupied by hydrocarbon chain ends and the shell comprising a monolayer of sulfate headgroups strongly bound to cesium counterions.[15, 16, 17] At higher concentration (ca. 12 wt %) scattering patterns have again been interpreted with a core-shell prolate ellipsoid model, similar in minor axis width, but considerably longer.[18, 19] It is possible that the CsDS surfactants are at the cusp of a transition, leading to ellipsoids.

What we expect, though, in such a system, with increased charge-shielding, is that the interfacial curvature should decrease, leading to a transition from spheres (with SDS) to cylinders (with CsDS). It is puzzling why the scattering interpretation would suggest no transition to cylinders, and it is a pressing question whether the models arrived at, different length prolate ellipsoids, might actually be abstractions of more straightforward structures, spheres and cylinders is a pressing one.

Cryogenic transmission electron microscopy (cryo-TEM) allows direct observation of the micelle structure to answer this question, and the CsDS system affords enhanced contrast benefiting from the electron-rich cesium. The combined use of cryo-TEM and

SAXS has allowed us to conclusively show a transition from spherical to cylindrical micelles with increasing CsDS concentration in water.

2.3 Experimental Methods

Cesium dodecyl sulfate (CsDS) preparation

Sodium dodecyl sulfate (SDS, L4509, Sigma-Aldrich, Reagentplus 98.5%) and cesium chloride (Sigma-Aldrich, Grade I, 99%) were used as received. The cesium dodecylsulfate (CsDS) samples were prepared by recrystallizing aqueous SDS with cesium chloride. The dried CsDS powder was dissolved in water (Milli-Q system; resistivity >18.2 MΩ·cm) to provide samples at concentrations and temperatures. The purity of the CsDS powder is characterized with transmission electron microscopy energy dispersive X-ray spectroscopy shown in Figure 2.1.

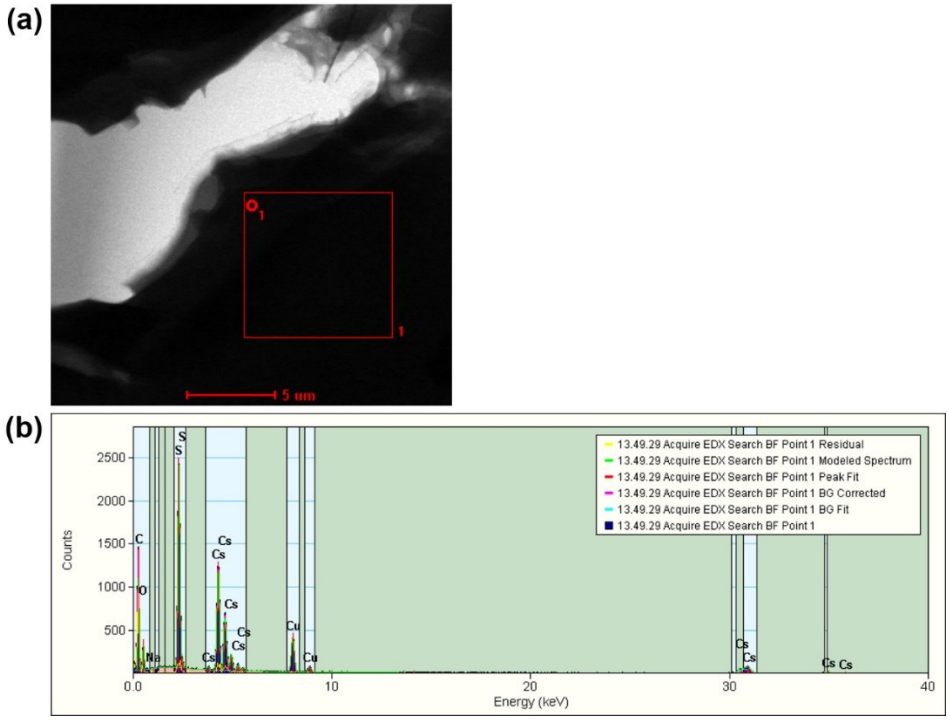

Figure 2.1. Demonstration of the purity of the cesium dodecyl sulfate solid prepared in this paper using transmission electron microscopy-energy dispersive X-ray spectroscopy (TEM-EDX).

(a) TEM of cesium dodecyl sulfate powder, showing the selection of a thick region for EDX.

(b) At area 1 in the micrograph, the EDX pattern shows no residual Na.

In addition to TEM-EDX, Inductively Coupled Argon Plasma Optical Emission Spectrometry gave only The concentration of your sample is 269,961 mg/kg Cs and 2,339 mg/kg Na.

We prepared aqueous CsDS solutions at 2.0, 5.0, and 8.1 wt % (well above the CMC[9]) for observation at 35–40 °C (well above the Krafft temperature[9]). The reported is CsDS/H_2O) at various concentrations are shown in Table 2.1. Our sample concentrations are reported in wt %; conversions from molarity reported in other papers use the assumption that the solution density is about the same as of water.

Table 2.1. Demonstration that our sample temperatures provide neat solutions. These are reported Krafft temperatures of CsDS/H_2O at various concentrations.[9] Liquid crystal appears only above 32.6 wt % CsDS.[20]

Concentration (M)	Temperature (°C)
0.0516 (~2.03 wt %)	28
0.100 (~3.94 wt %)	29.3
0.235 (~9.25 wt %)	31

Cryogenic-transmission electron microscopy (Cryo-TEM)

Taking advantage of the high electron density of Cs, the CsDS micelles were characterized with cryo-TEM. A lacey carbon-coated grid (01881, 200-mesh, Ted Pella, Ltd., Redding, CA) was glow discharged in a vacuum evaporator at 70 mTorr (DV-502A, Denton Vacuum Moorestown, NJ) for 1 minute to create a hydrophilic surface on the carbon coated side of the grid. A 2 μL drop of sample was pipetted onto the carbon side at a desired temperature (40 °C for 2.0 and 5.0 wt % and 35 °C for 8.1 wt %) in a Mark III Vitrobot chamber (FEI Company, Hillsboro, OR) with a relative humidity of ~100%, and the specimen was allowed to relax 25–90 seconds. Excess sample was blotted with 595 filter papers (Ted Pella, Ltd., Redding, CA) 1–2 times with a -2 to -1 mm offset parameter for 5 seconds to form a thin liquid film. After the blotting, the sample was relaxed for 3 seconds and plunged into liquid ethane cooled by liquid nitrogen. The sample was transferred to a Gatan 626 cryo-transfer unit and examined with a FEI Tecnai G^2 Spirit BioTWIN operated at 120 kV with the sample stage maintained at -178 °C. To avoid beam damage, each micrograph was recorded with only 10–20 $e^-/Å^2$ using a low-dose program in TEM Imaging and Analysis software using an Eagle 2048 × 2048 pixels CCD camera. The nominal underfocus during imaging was 2–4 μm and the Cs (spherical aberration)

value of the FEI Tecnai G^2 Spirit BioTWIN instrument was 6.3 mm. Typical electron beam radiation damage of the sample is shown in Figure 2.2.

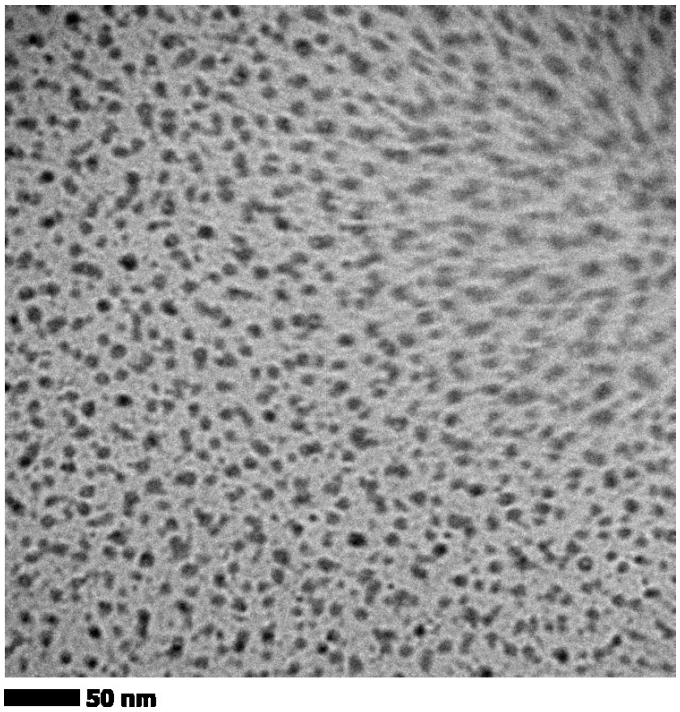

Figure 2.2. Demonstration of typical beam damage in a cryo-TEM micrograph obtained from 2.0 wt % of cesium dodecyl sulfate aqueous solution at 40 °C. The vitrified film here is so thin it does not show typical damage (e.g. bubble formation), but rather tends to blur and disappear in regions, as on the right hand side of this micrograph.

Small angle X-ray scattering (SAXS)

Small angle X-ray scattering (SAXS) experiments were conducted at the Advanced Photon Source at Argonne National Laboratory at the Sector DND-CAT (5-ID-D) beamline. Liquid specimens were held in quartz capillary tubes during the SAXS measurements and mounted on the L-HFS91 temperature controlled stage, after having been pre-heated to the specified temperature about 2 hours prior to the characterization. The wavelength (λ) was 0.729 Å, corresponding to radiation of 17 keV, and the sample-to-detector distance was 3.97 m. Data were recorded using a MAR 165 mm diameter CCD area detector with 2048 × 2048 pixels. The two-dimensional scattering patterns were azimuthally averaged to the one dimensional form of intensity (I) as a function of the magnitude of scattering vector $[\vec{q}]= (4\pi/\lambda) \sin(\theta/2)$, where θ is a scattering angle. The

background contributions from solvent and optics were eliminated by subtracting the data taken for a pure water sample. Scattering curves were calculated using IGOR Pro software from WaveMetrics Inc.

The scattering intensity, $I(q)$ can be described generally by the combination of two interacting interferences. The form factor $P(q)$ accounts for the size and shape of a single micelle, and the structure factor $S(q)$ accounts for the spatial arrangement of the micelles.

$$I(q) \sim S(q) \cdot P(q) \tag{2.1}$$

The IGOR Pro software allows selection of specific models for each, and entry of the parameters, to calculate scattering intensities.

In the 2.0 wt % CsDS aqueous solution, a core-shell sphere model[21] was used for the form factor $P(q)$:

$$P(q)=\left[\begin{array}{c} 3(\rho_{core}-\rho_{shell})v_{core}\frac{j_1(q\,r_{core})}{q\,r_{core}}+ \\ 3(\rho_{shell}-\rho_{solvent})v_{shell}\frac{j_1\{q\,(r_{core}+r_{shell})\}}{q\,(r_{core}+r_{shell})} \end{array}\right] \tag{2.2}$$

where q is the scattering vector and ρ is the electron contrast, and

$$v_{core}=\frac{4\pi}{3}{r_{core}}^3 \tag{2.3}$$

$$v_{shell}=\frac{4\pi}{3}[(r_{core}+r_{shell})^3-{r_{core}}^3] \tag{2.4}$$

$$j_1(x)=\left[\frac{sinx-xcosx}{x^2}\right] \tag{2.5}$$

where $j_1(x)$ is the first-order spherical Bessel function.

In the 8.1wt % aqueous solution, the core-shell cylinder model[22] was used for the form factor $P(q)$.

$$\mathrm{P(q)} = 2j_0\left(q\frac{L}{2}\cos\alpha\right)\left[\frac{j_1(qr\sin\alpha)}{qr\sin\alpha}\right]v_{core}(\rho_{core}-\rho_{shell}) + 2j_0\left\{q\left(\frac{L}{2}+t\right)\cos\alpha\right\}\left[\frac{j_1\{q(r+t)\}\sin\alpha}{q(r+t)\sin\alpha}\right]v_{shell}(\rho_{shell}-\rho_{solvent}) \quad (2.6)$$

where ρ is electron contrast, r is the core-radius of the cylinder, L is the length of the cylinder, t is the shell thickness, and α is the angle between the cylinder axis and the scattering vector q,

$$v_{core}=\pi r^2 L \quad (2.7)$$

$$v_{shell}=\pi(r+t)^2 L \quad (2.8)$$

$$j_o(x)=\left[\frac{sinx}{x}\right] \quad (2.9)$$

$$j_1(x)=\left[\frac{sinx-xcosx}{x^2}\right] \quad (2.10)$$

where $j_0(x)$ is the zeroth-order spherical Bessel function and $j_1(x)$ is the first-order spherical Bessel function. L is taken to be 100 nm, but the scattering pattern is insensitive to L in that range.

The structure factor, *S(q)* was calculated with the mean spherical approximation with a screened Coulomb interaction between charged micelles as described by Hayter and Penfold.[23, 24]

$$S(q)= 1 + 4\pi n \int (g(r)-1)\frac{sinqr}{qr}r^2 dr \quad (2.11)$$

where n is particle number density, and *g(r)* is the Fourier transform of the pair distribution function, which describes local order of the each scattering particle and depends on the interparticle interaction potential.

This pair correlation function is calculated by the Ornstein-Zernicke equation with the closure relations:

$$h(r) = g(r) - 1 = c(r) + n \int c|r - r'|h(r')dr' \quad (2.12)$$

where *r* is interionic center-to-center distance and *n* is particle number density. The total correlation, *h(r)* comes from the summation of *c(r)*, the direct correlations between neighboring scattering particles.

To solve the Ornstein-Zernicke equation, with a mean spherical approximation closure, the closure relations of *h(r)* and *c(r)* are:

$$c(r) = -\frac{u(r)}{k_B T}, \quad r > \sigma \quad (2.13)$$

$$h(r) = -1, \quad r < \sigma \quad (2.14)$$

where *u(r)* is the repulsive potential between two micelles and σ is the diameter of the micelle. With this closure, a rescaled mean spherical approximation (RMSA).[25] is implemented by the IGOR Pro software as appropriate for our volume fraction. The parameters input go toward the calculation of *u(r)* using the Yukawa hard core potential.

2.4 Results and Discussion

Cryo-TEM

Cryo-TEM images of the CsDS micelles at low concentration (Figure 2.3) on average show core-shell spheres rather than uniform ellipsoids. (Here we note that the micelles shown in Figure 2.3 appear to fluctuate somewhat from perfectly spherical shapes. The influence of such shape fluctuations on the predicted scattering profile, discussed below, is essentially indistinguishable from the effects of dispersity in micelle diameter as shown from Table 2.2 to Table 2.4). The hydrocarbon core shows up clearly as a bright center owing to phase contrast, and the Cs-rich shell shows up clearly as a dark ring at the sides of the sphere owing to scattering contrast. (A lighter core is evident in many but not all the micelles. We attribute this to variations in the location of the micelles within the imaged aqueous film compounded by the finite depth of focus.) Acquiring these images is facilitated by ensuring that the cryofixed specimen is made thin enough and by using low-dose imaging. The overall diameter (ca. 57 Å) of the spheres is comparable to the average of the model ellipsoids previously inferred from scattering at this concentration. The core diameter (ca. 32 Å) of the spheres is slightly smaller than the minor axis core diameter of the previously inferred ellipsoids, and the shell of the spheres is thicker. The dimension of CsDS micelle is measure by cryo-TEM is shown in Figure 2.4.

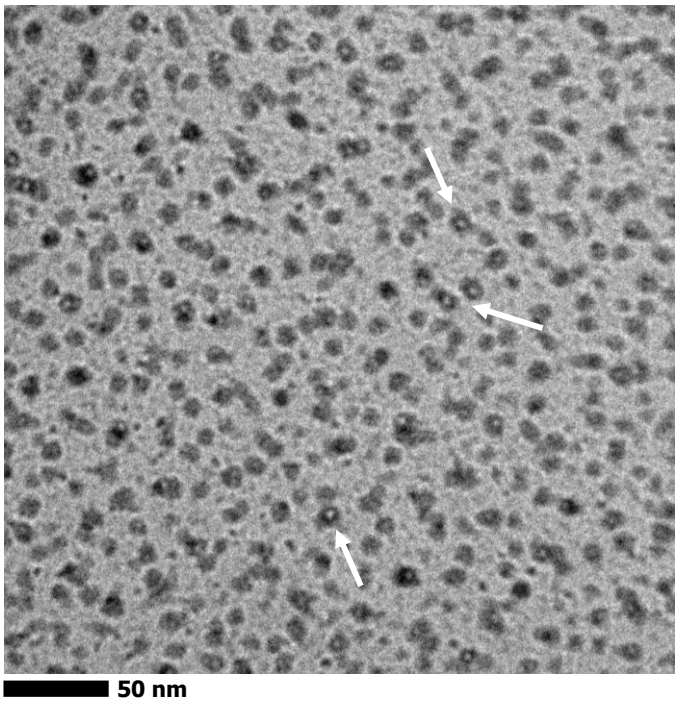

Figure 2.3. Typical cryo-TEM micrograph obtained from a 2.0 wt % cesium dodecyl sulfate aqueous solution at 40 °C. The micelles show a core-shell sphere structure. We interpret the bright regions at the core of the micelles as resulting from densely packed hydrocarbon chains, while the dark shells are attributed to electron-rich (partially) hydrated cesium counterions and the associated sulfate head groups at the end of the chains. Structural variations are attributed to the effects of depth of focus and projection through the relatively thick film (ca. 50 nm), and dynamic shape fluctuation (as predicted by molecular dynamic simulations[26]), which are arrested by cryofixation.

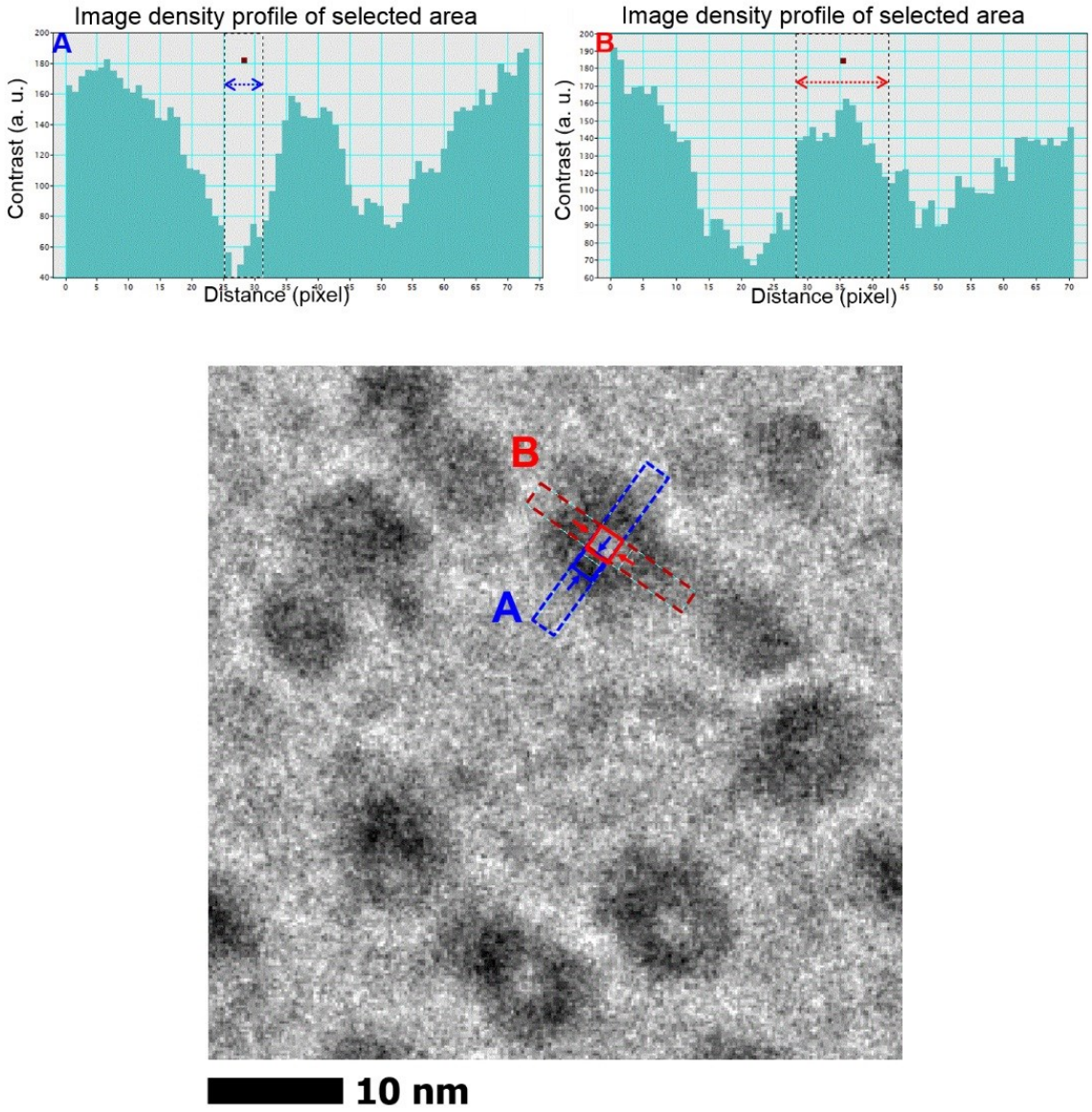

Figure 2.4. Typical image density profile and dimensions they illustrate, from a cryo-TEM micrograph of 2.0 wt % of cesium dodecyl sulfate aqueous solution at 40 °C. The segment density profiles of one core-shell micelle is shown in inset. One pixel is 0.23 nm. The bars in inset A indicate the shell thickness and the bars in inset B indicate the core diameter shown in the schematic on Figure 2.11b.

At higher concentration, our cryo-TEM images clearly show rearrangement to cylindrical micelles (5.0 wt % CsDS is shown in Figure 2.5; 8.1 wt % CsDS is shown in Figure 2.6). At 5.0 wt % we see transitional structures. The cylinders range in length, all the way down to spheres, and intersections and occasional branches are evident in the micrograph. Some micelles show contrast exchange along the length of the cylinder and it is attributed to the arrangement of the micelles. When the cylindrical micelles is vertically or diagonally placed, two-dimensional projected image of the micelle in the cryo-TEM shows some variance in contrast along the line. Some short cylinders with swollen endcaps are observed, but no ellipsoidal structures are evident. However, we were not able to convincingly resolve a core-shell morphology for the cylinders based on the cryo-TEM images. Figure 2.7 shows image analysis of 8.1 wt % CsDS micelle by cryo-TEM.

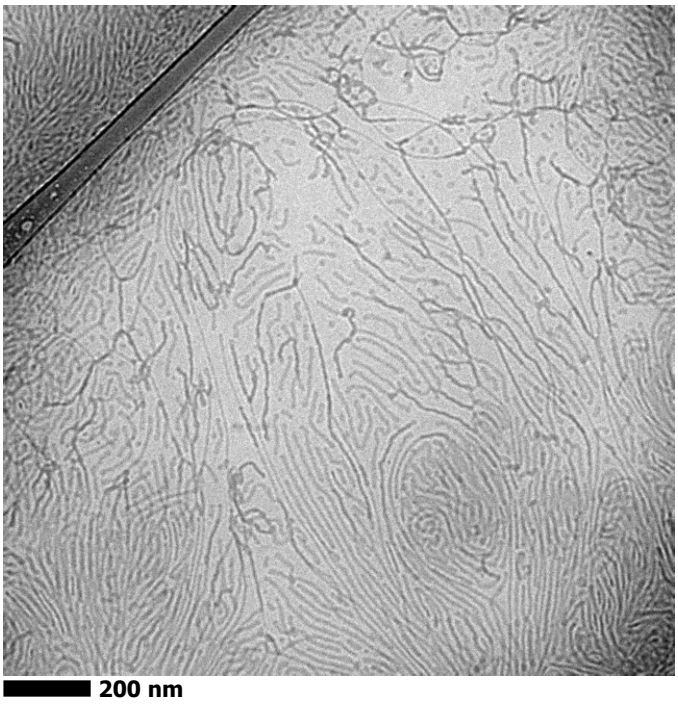

Figure 2.5. Representative cryo-TEM micrograph obtained from a 5.0 wt % of cesium dodecyl sulfate (CsDS) aqueous solution at 40 °C. The CsDS micelles are a mixture of long and short cylinders and a small percentage of spheres. Variations in the apparent micelle density are a result of specimen preparation.

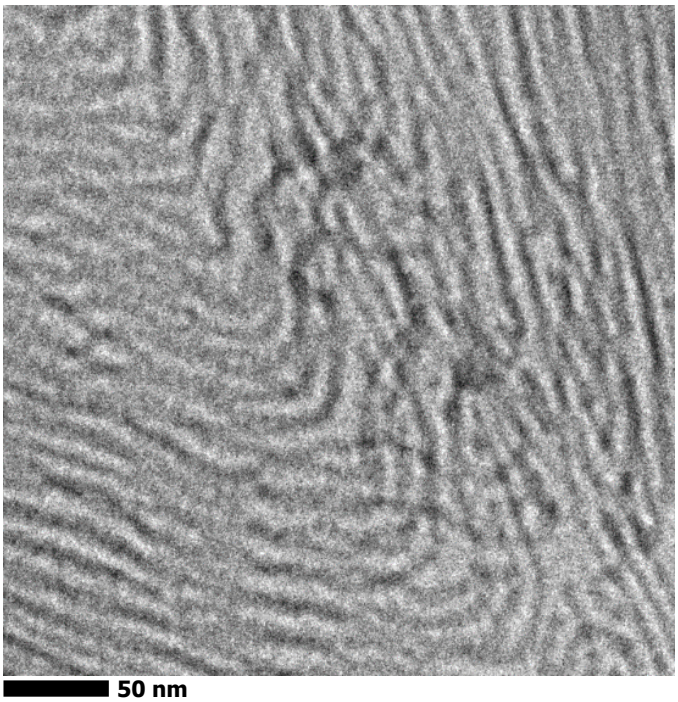

Figure 2.6. Typical cryo-TEM micrograph obtained from 8.1 wt % of cesium dodecyl sulfate aqueous solution at 35 °C.

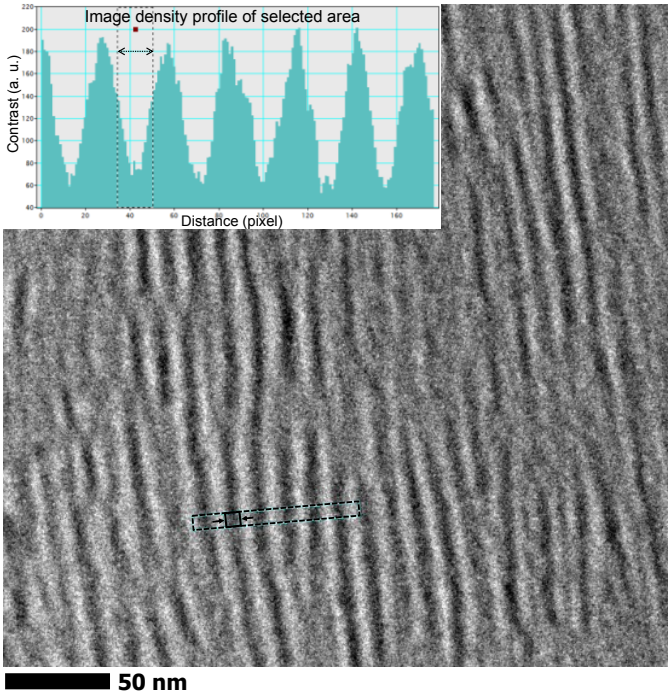

Figure 2.7. Representative image density profile and the dimension from a cryo-TEM micrograph of 8.1 wt % of cesium dodecyl sulfate aqueous solution at 35 °C. The segment density profile of several cylindrical micelles is shown by the bars in inset. The bar in the inset indicates a cylinder diameter consistent with Figure 2.11c. One pixel is 0.45 nm.

SAXS

To test that these solutions are in fact the same as those examined by previous researchers, SAXS patterns were collected at the Advanced Photon Source are Argonne National Laboratory. Figure 2.8 shows the series of SAXS patterns we obtained from CsDS solutions with concentration ranging from 0.2 to 8.1 wt % at 35–40 °C. (Figure 2.9 plotted on different scales.) Near the CMC (6.4 mM ≈ 2.5 wt % at 40 °C), the 0.2 wt % SAXS pattern shows a broad background peak consistent with a disordered, pre-micellar state, but well above the CMC, the SAXS patterns contain characteristic peaks produced by the micelles. Table 2.2 summarizes the SAXS analysis of dimensions and electron contrast of 2 wt % CsDS micelle.

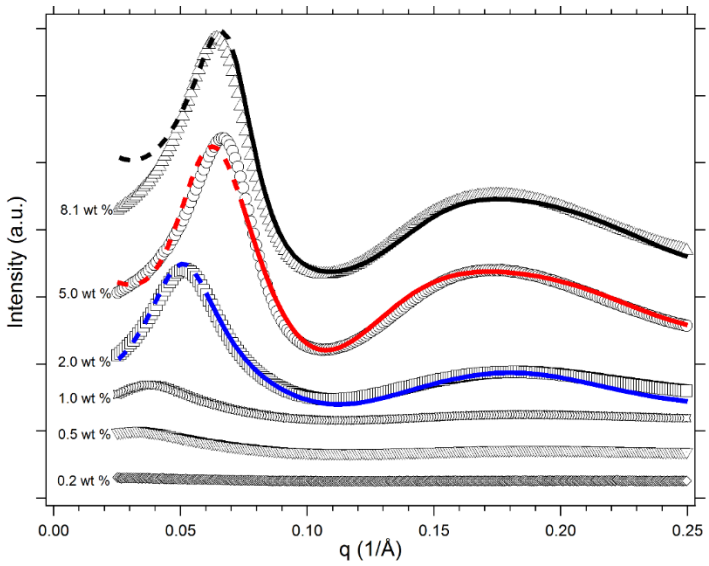

Figure 2.8. Synchrotron SAXS patterns obtained from cesium dodecyl sulfate (CsDS) in aqueous solution from 0.2 to 5.0 wt % at 40 °C and 8.1 wt % at 35 °C. The high *q* peak reflects the micelle form (form factor), and the low *q* peak is dominated by intermiceller interactions (structure factor). The CMC of CsDS in water is about 0.25 wt %.[9] The solid curves show optimal fit models using core-shell spherical (2.0 wt %) and cylindrical (5.0 and 8.1 wt %) form factors. Figure 2.11 illustrates the structural features derived from cryo-TEM and these calculations. The dashed curves show optimal fit models using both the form factor (fit to high *q* data) and also the structure factor. Figures 2.13 to 2.22 show the sensitivity of these calculations to the fitting parameters. Results are shifted vertically for clarity.

Table 2.2. Micelle dimensions and electron contrasts at ~2 wt % cesium dodecyl sulfate aqueous solution used in our work and in earlier studies for the form factor. Sensitivity studies are shown in Figures 2.13–2.15.

Parameter	Our work (2.0 wt % at 40 °C)	Chen et al.[15] (3% in D_2O at 40 °C)	Vass et al.[16] (0.0729 M D_2O at 40 °C) (~3 wt %)	Kanungo et al.[17] (0.075 M at 30 °C) (~3 wt %)
Overall diameter (Å)	57	52.6 (avg. diameter) 44.7* (minor-axis diameter*)	52.2** (axial ratio 1.287)	51.6*** (minor-axis diameter) 63**** (major-axis diameter)
Shell thickness (Å)	12.5	5.65 (hydrophilic layer)	10.01	9.1
Core contrast	0.270 $e^-/Å^3$	0.269 $e^-/Å^3$	-1.7 x 10^{10} cm^{-2}†	0.266 $e^-/Å^3$ (7.554 x 10^{10} cm^{-2})
Shell contrast	0.383 $e^-/Å^3$	0.460 $e^-/Å^3$	2.2 x 10^{10} cm^{-2}†	11.7 x 10^{10} cm^{-2} (0.412 $e^-/Å^3$)
Solvent contrast	0.333 $e^-/Å^3$	0.327 $e^-/Å^3$	-	0.33 $e^-/Å^3$ (9.37 x 10^{10} cm^{-2})

* 2 x (16.7 Å) + 2 x (5.65 Å) = 44.7 Å†
** 2 x (16.1 Å) + 2 x (10.01 Å) = 52.2 Å†
*** 2 x (16.7 Å) + 2 x (9.1 Å) = 51.6 Å†
**** 2 x (22.4 Å) + 2 x (9.1 Å) = 63 Å†
† Estimated using figures or data in the reference.
- Not available from the reference.

Our data at 2.0 wt % CsDS is similar to SAXS patterns (Figure 2.9) of Chen and coworkers[15] and of Bellare, Goyal, and coworkers.[17]

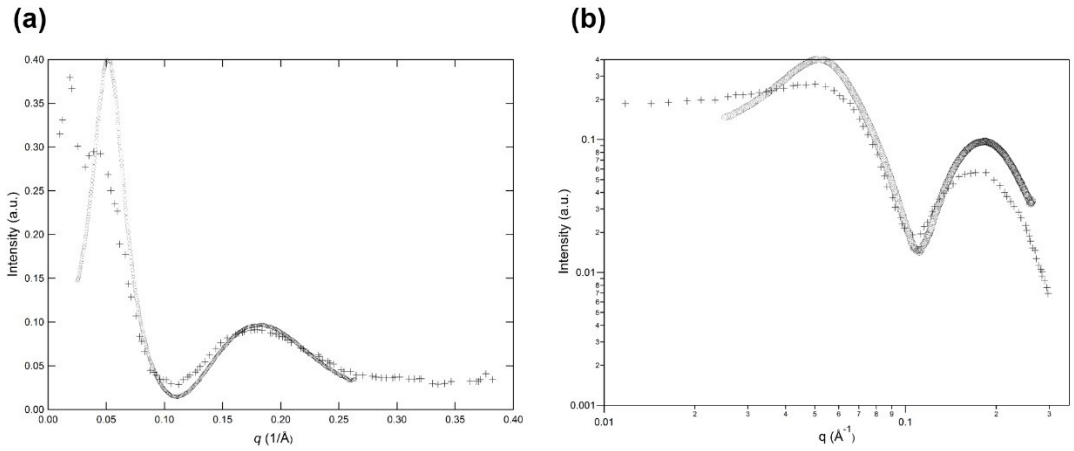

Figure 2.9. A comparison of the SAXS intensity profiles of cesium dodecyl sulfate aqueous solution solutions at 2–3 wt %. This work: open circles, 2.0 wt % in H_2O at 40 °C. Scales used are those used in the references.
(a) 3% in D_2O at 40 °C by Chen and coworkers[15] (cross marks)
(b) 0.075 M (~ 3 wt %) in D_2O at 30 °C by Goyal and coworkers[17] (cross marks)

Increasing the concentration to 5.0 wt % shifts the peaks to higher q value and results in a noticeable change in the relative peak height. Finally, the 8.1 wt % CsDS slightly moves toward higher scattering vector. Table 2.3 summarizes the SAXS analysis of dimensions and electron contrast of 5 wt % and 8.1 wt % CsDS micelle.

Table 2.3. Micelle dimensions and electron contrasts at higher cesium dodecyl sulfate aqueous solution concentrations used in our work and in earlier studies for the form factor. Sensitivity studies are shown in Figures 2.16–2.18.

Parameter	Our work (5.0 wt % at 40 °C)	Our work (8.1 wt % at 35 °C)	Joshi et al.[19] (0.3 M at 30 °C) (~12 wt %)
Overall diameter (Å)	48 (cylinder)	48 (cylinder)	52.2* (minor-axis diameter) 165.8** (major-axis diameter) (ellipsoid)
Shell thickness (Å)	11 (cylinder)	11 (cylinder)	9.4 5.3 (headgroup thickness) 4.1 (counterions thickness) (ellipsoid)
Core contrast	0.270 $e^-/Å^3$	0.270 $e^-/Å^3$	7.89 x 10^{10} cm^{-2}†
Shell contrast	0.431 $e^-/Å^3$	0.435 $e^-/Å^3$	11.32 x 10^{10} cm^{-2}† (counterions) 9.82 x 10^{10} cm^{-2}† (headgroup)
Solvent contrast	0.333 $e^-/Å^3$	0.333 $e^-/Å^3$	9.39 x 10^{10} cm^{-2}†

* 2 x (16.7 Å) + 2 x (5.3 Å) + 2 x (4.1 Å) = 52.2 Å†
** 2 x (73.5 Å) + 2 x (5.3 Å) + 2 x (4.1 Å) = 52.2 Å†
† Estimated using figures or data in the reference

Our data for 8.1 wt % is similar (above q~0.1 Å^{-1}) to SAXS patterns at somewhat higher concentration reported by Goyal and coworkers (Figure 2.10).[19]

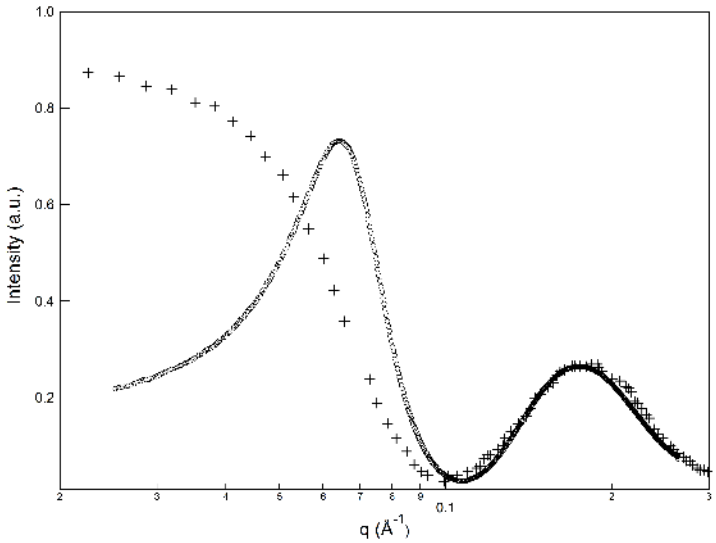

Figure 2.10. A comparison of the SAXS intensity profiles of cesium dodecyl sulfate aqueous solution solutions at higher concentration. This work: open circles, 8.1 wt % in H_2O at 35 °C. From Josh et al.[19]: cross marks, 0.3 M (~12 wt %) in D_2O at 30 °C. The scale used is that used in the reference. Note that 30 °C is close to the reported Krafft temperature.[9, 20]

Table 2.4 summarizes the SAXS analysis of structure factor of 2 wt %, 5 wt %, and 8.1 wt % CsDS micelle.

Table 2.4. Structure factor parameters used for 2 wt % and 8.1 wt % cesium dodecyl sulfate aqueous solution, respectively. Micelle diameter was adopted from form factor. Charge and volume fraction were fit to our low q data. Sensitivity studies are shown in Figures 2.19–2.22.

Parameter	Our work (2.0 wt % at 40 °C)	Chen et al.[15] (3% in D_2O at 40 °C)	Kanungo et al.[17] (0.075 M at 30 °C) (~3 wt %)	Our work (5.0 wt % at 40 °C)	Our work (8.1 wt % at 35 °C)	Joshi et al.[19] (0.3 M at 30 °C) (~12 wt %)
Charge (C)	25	25	Fractional charge: 0.156	40	45	Fractional charge: 0.04 Counterion condensation: 96%
Volume fraction	0.04	0.0307	-	0.06	0.062	-
Temperature (K)	313	313	303	313	308	303
Salt conc. (M)*	0.005	-	-	0.005	0.005	-
Dielectric constant of solvent	80	-	-	80	80	-

- Not available from the reference.
* Chose critical micelle concentration value.

It may seem puzzling how these SAXS patterns can be consistent with the structures we observe with cryo-TEM, structures which differ strikingly from the ellipsoidal models inferred by previous workers. Nevertheless, numerical simulations of the scattering data, shown as solid curves (for 2.0, 5.0, and 8.1 wt %), indeed show that the structures documented by cryo-TEM can be accounted for based on standard scattering models.

For the 2.0 wt % data, we used a core-shell sphere form factor. A reasonable fit is consistent with a core 32 Å in diameter and a shell thickness of 12.5 Å. These are consistent with the dimensions evident in the cryo-TEM images. This structure is depicted schematically in Figure 2.11b (and contrasted with the SDS spherical micelle of Figure 2.11a).

The SAXS pattern at 8.1 wt % CsDS in Figure 2.8 is consistent with a core-shell cylinder about 26 Å in core diameter and 11 Å in shell thickness, as shown schematically in Figure 2.11c. From Table 2.2 to Table 2.4 we show the method and parameters used to in the key parameters used in the calculations.

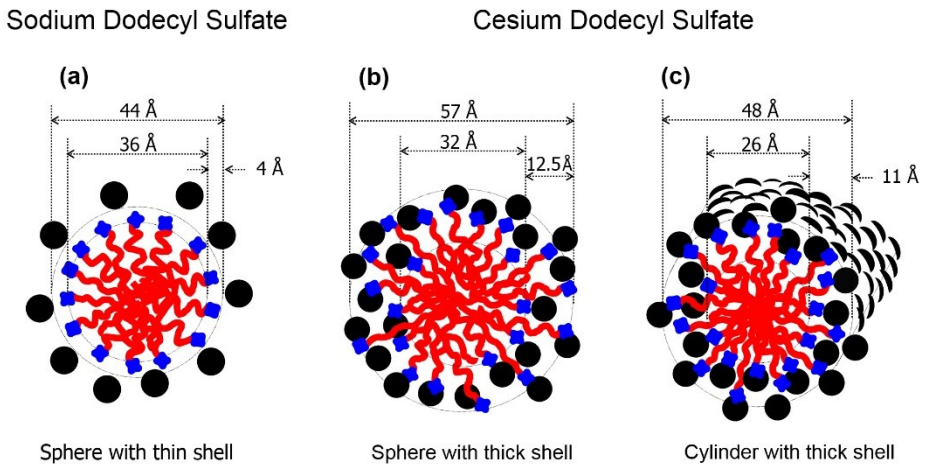

Figure 2.11. Schematic cross sections of (a) Spherical sodium dodecyl sulfate micelles based on literature report.[2] (b) Spherical cesium dodecyl sulfate (CsDS) micelles (2.0 wt %), and (c) cylindrical CsDS micelles (5.0 and 8.1 wt %), each in aqueous solution. The hydrocarbon tails are depicted in red, while the sulfate head groups and hydrated cations are represented in blue and black, respectively. To help depict the shell accurately, hydrated cations are shown to scale.[27] The CsDS micelle geometries were established by cryo-TEM (Figures 2.3. and 2.5) and the indicated core and shell dimensions were determined based on the calculated form factors (Figure 2.8).

Like previous studies, we postulate that the core is occupied exclusively by liquid-like hydrocarbon chain ends and the shell comprises sulfate headgroups strongly bound to complexing hydrated Cs^+ cations. But contrasting with earlier models, our shell is thicker, and we envision it having significant staggering of headgroups to allow deeper penetration of the Cs^+ into the shell. Of course, this also requires that some of the hydrocarbon chains stretch to bring some headgroups close to the surface of the shell.

Indeed, a key reason that the CsDS micelle can be so large at 2 wt %, while remaining practically spherical, is that the Cs^+ ions are not constrained to sit only at a smooth monolayer of sulfate headgroups. Cs^+ penetration to create a thick shell is favored by two factors. First, the counterions and headgroups shield each other's charge very effectively, so there is less energy cost than one might expect for the complexed ion pair to penetrate into the micelle, especially if this affords extra ion-pair interactions. Figure 2.11b shows that a Cs^+–sulfate pair buried deep in the shell can enjoy more charge shielding with neighboring pairs that are staggered at different penetration depths. This allows the Cs^+ to coordinate with more sulfates, and vice versa. The enthalpic benefit of more Coulombic attraction can pay for the penalty of extending hydrocarbon chains into the shell. The second reason is suggested by the change of structure we observe when the concentration increases; the effective size of the charge-shielded, ion-paired headgroup is small enough that, when the aggregation number grows large, the micelle prefers less curvature and adopts a cylindrical structure. The sphere that was adopted at low concentration may represent a transitional structure, resembling in many ways fused swollen end-caps of the cylinder. Also, that the spherical micelles appear to fluctuate in shape (perhaps on average slightly ellipsoidal with an estimated average aspect ratio of less than 1.2 (see Figure 2.3) is consistent with the notion that these swollen objects are at the cusp of transitioning to cylinders, i.e., they are highly susceptible to changes in shape.

Why did earlier scattering studies suggest ellipsoidal micelles at low concentration? The models inferred by Chen and coworkers[15] and Goyal and coworkers[18] have a much thinner shell, a smooth monolayer of headgroups and associated counterions at the surface. Moreover, in those models the smallest diameter is limited by the fully stretched hydrocarbon chain. Thus, a large aggregation number has to be accommodated by an

ellipsoid shape. In contrast to those constraints, our spherical micelle model shows a thicker shell, but a slightly smaller core (since some hydrocarbon chains extend somewhat into the shell).

With the transition from spheres to cylinders at higher concentration, our interpretation of the scattering data suggests that the shell becomes thinner. This can be attributed to the fact that the two dimensional cylinder-shell structure helps provide the smaller curvature more appropriate for the Cs^+–sulfate ion pair headgroup. This transition to cylinders resembles the transition behavior of amphiphilic block copolymers as smaller headgroups are used.[28] Perhaps in CsDS the effective headgroup size is further decreased as concentration increases by the additional charge shielding afforded by interactions between adjacent micelles.

2.5 Conclusions

The main point is that the structures clearly shown by cryo-TEM are consistent with the scattering data. This work shows the importance of using cryo-TEM to assign structures, shedding the need for strict assumptions about the structure (e.g., assuming minor core axis diameter, ellipsoidal structure, or smooth monolayer shell). More generally, real space data (cryo-TEM) is needed to inform how best to interpret inverse space data (scattering). In this case, cryo-TEM allowed us to directly image the core-shell spheres and cylinder structures that happen to be expected from previous studies of surfactants with charge-shielded ionic headgroups.

2.6 Supporting Information

SAXS patterns of CsDS using different scales

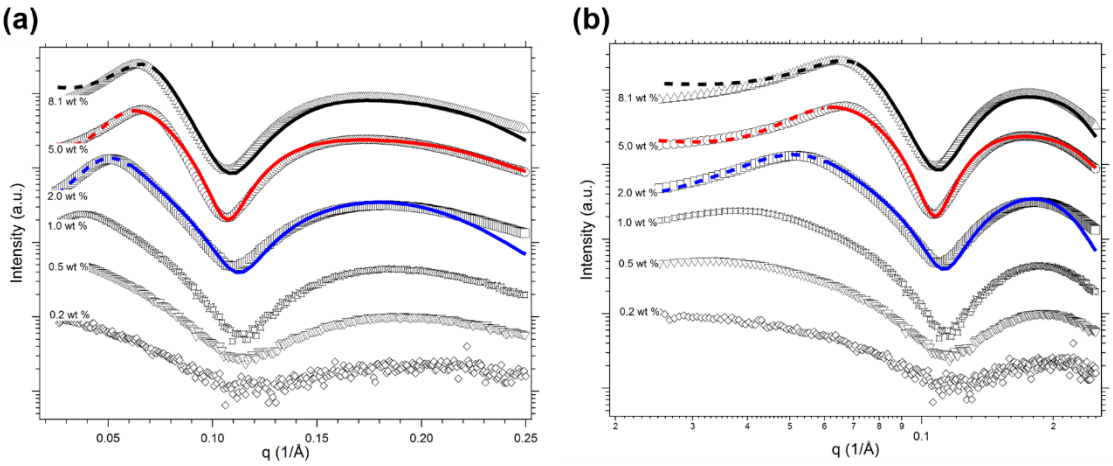

Figure 2.12. Synchrotron SAXS patterns of Figure 2.8 plotted on different scales. (a) Log-linear plot, (b) log-log plot. The core shell sphere form factor fit to the 2 wt % data noticeably drops below the data at q >0.2; this might reflect the need for a more detailed micelle model to account for density gradients near the surface of the micelle, as suggested schematically in Figure 2.11b. We note that Vass et al. have reported such an approach.[16]

Sensitivity tests on form factor parameters, 2.0 wt % of CsDS solution at 40 °C

Figures 2.13 to 2.15 show sensitivity tests on form factor parameters, 2.0 wt % of CsDS solution at 40 °C.

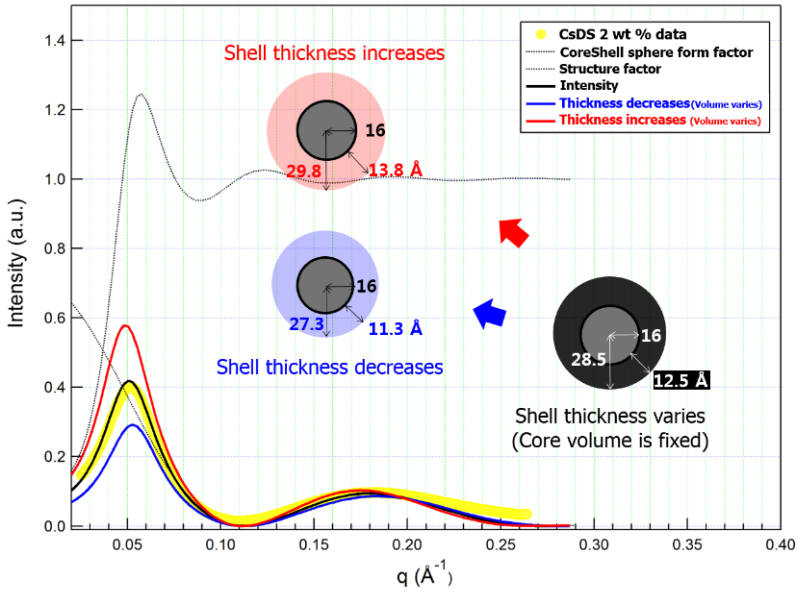

Figure 2.13. Sensitivity test on 2.0 wt % of cesium dodecyl sulfate aqueous solution at 40 °C. Core volume is fixed and shell thickness varies. Other parameters are shown in Table 2.2.

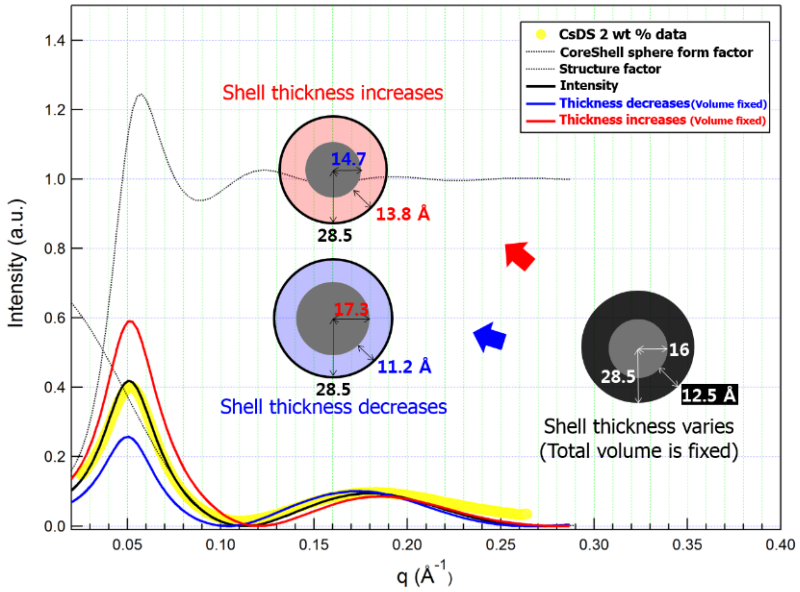

Figure 2.14. Sensitivity test on 2.0 wt % of cesium dodecyl sulfate aqueous solution at 40 °C. Total volume is fixed and shell thickness varies. Other parameters are shown in Table 2.2.

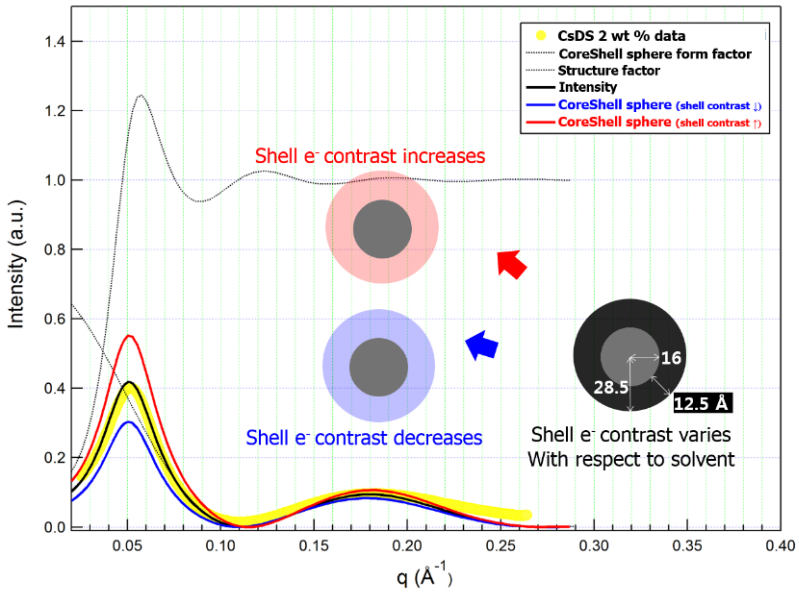

Figure 2.15. Sensitivity test on 2.0 wt % of cesium dodecyl sulfate aqueous solution at 40 °C. The difference between shell and solvent electron contrast varies by ± 10%. Other parameters are shown in Table 2.2.

Sensitivity tests on form factor parameters, 8.1 wt % of CsDS solution at 35 °C

Figures 2.16 to 2.18 show sensitivity tests on form factor parameters, 8.1 wt % of CsDS solution at 35 °C.

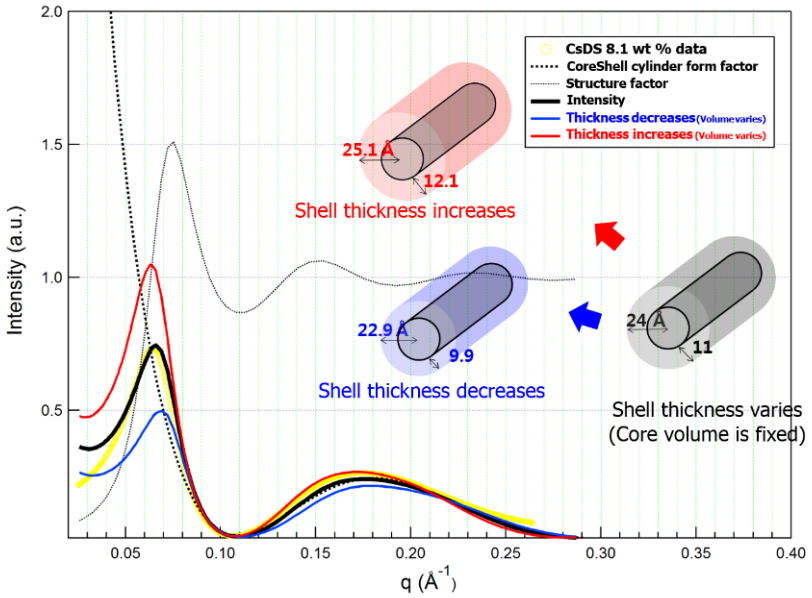

Figure 2.16. Sensitivity test on 8.1 wt % of cesium dodecyl sulfate aqueous solution at 35 °C. Core volume is fixed and shell thickness varies. Other parameters are shown in Table 2.3.

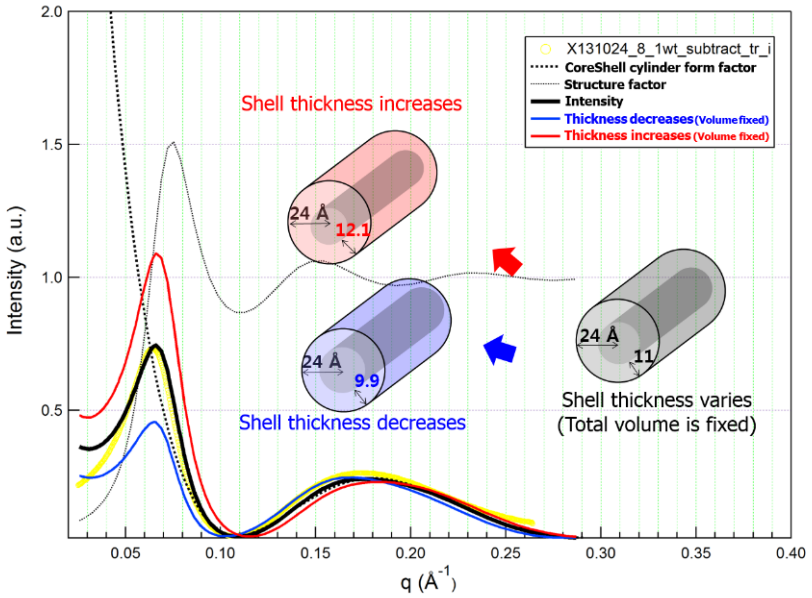

Figure 2.17. Sensitivity test on 8.1 wt % of cesium dodecyl sulfate aqueous solution at 35 °C. Total volume is fixed and shell thickness varies. Other parameters are shown in Table 2.3.

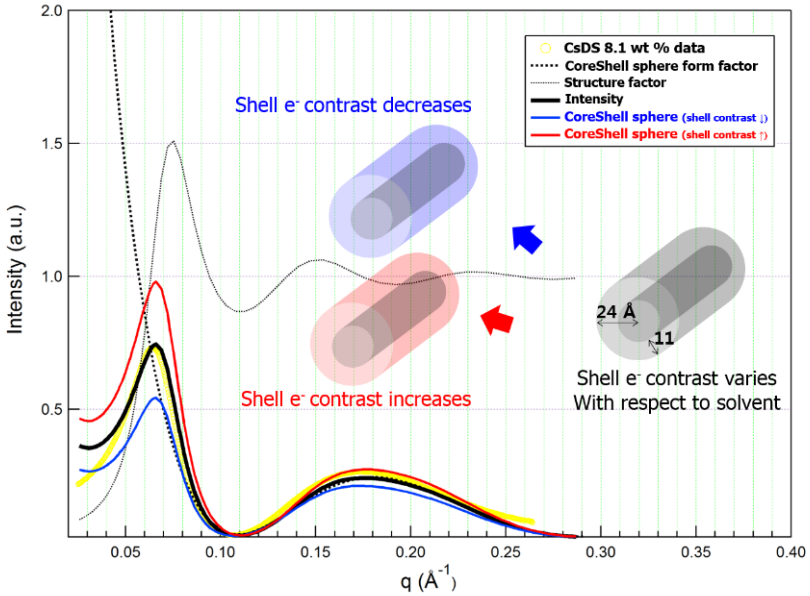

Figure 2.18. Sensitivity test on 8.1 wt % of cesium dodecyl sulfate aqueous solution at 35 °C. The difference between shell and solvent electron contrast varies by ± 10%. Other parameters are shown in Table 2.3.

Sensitivity tests on structure factor parameters, 2.0 wt % of CsDS solution at 40 °C

Figures 2.19 to 2.20 show sensitivity tests on structure factor parameters, 2.0 wt % of CsDS solution at 40 °C.

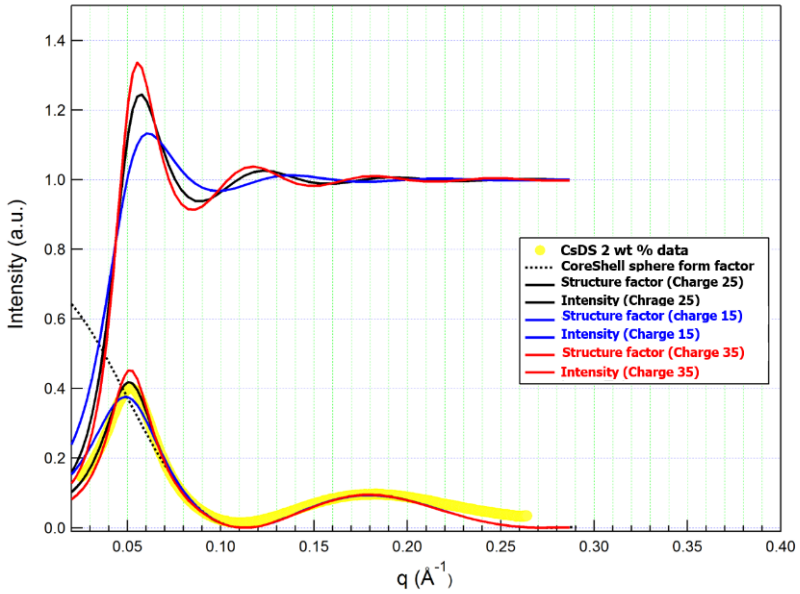

Figure 2.19. Sensitivity test on 2 wt % of cesium dodecyl sulfate aqueous solution at 40 °C. Charge varies at constant volume fraction. Other parameters are shown in Table 2.4.

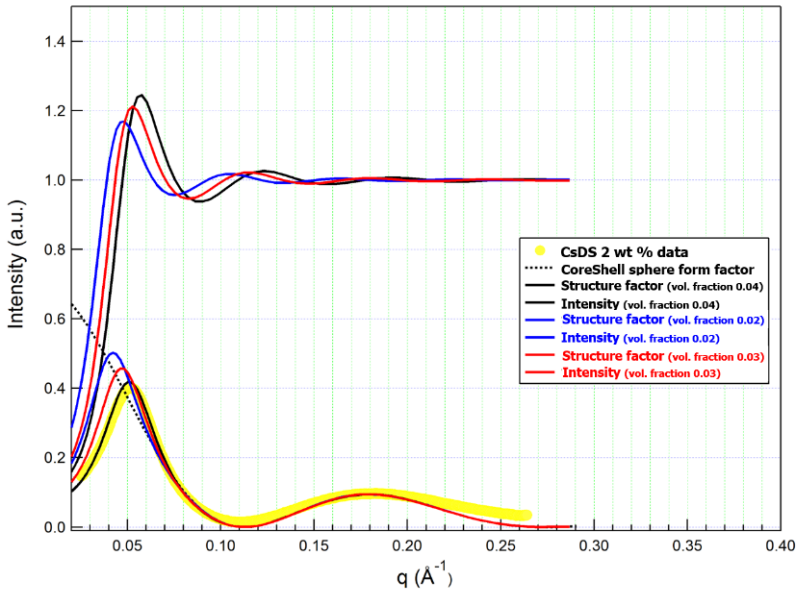

Figure 2.20. Sensitivity test on 2 wt % of cesium dodecyl sulfate aqueous solution at 40 °C. Volume fraction varies at constant charge. Other parameters are shown in Table 2.4.

Sensitivity tests on structure factor parameters, 8.1 wt % of CsDS solution at 35 °C

Figures 2.21 to 2.22 show sensitivity tests on structure factor parameters, 8.1 wt % of CsDS solution at 35 °C.

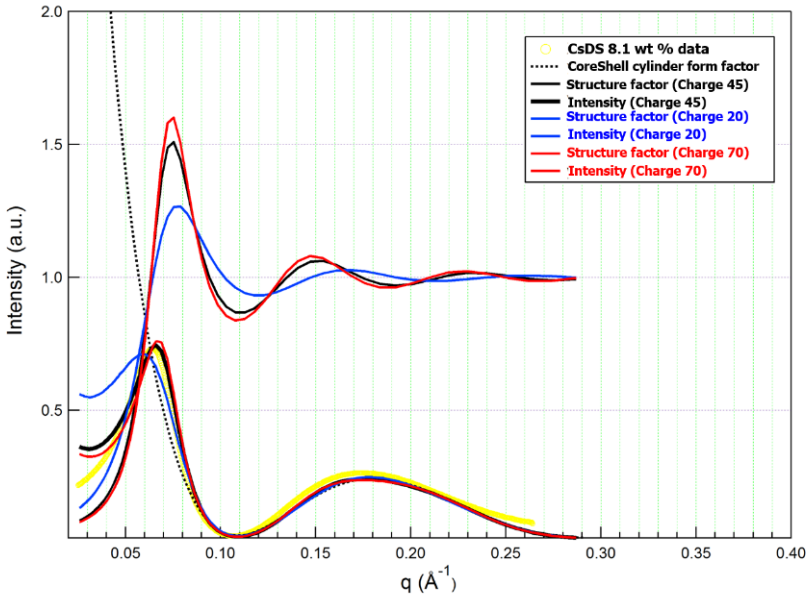

Figure 2.21. Sensitivity test on 8.1 wt % of cesium dodecyl sulfate aqueous solution at 35 °C. Charge varies at constant volume fraction. Other parameters are shown in Table 2.4.

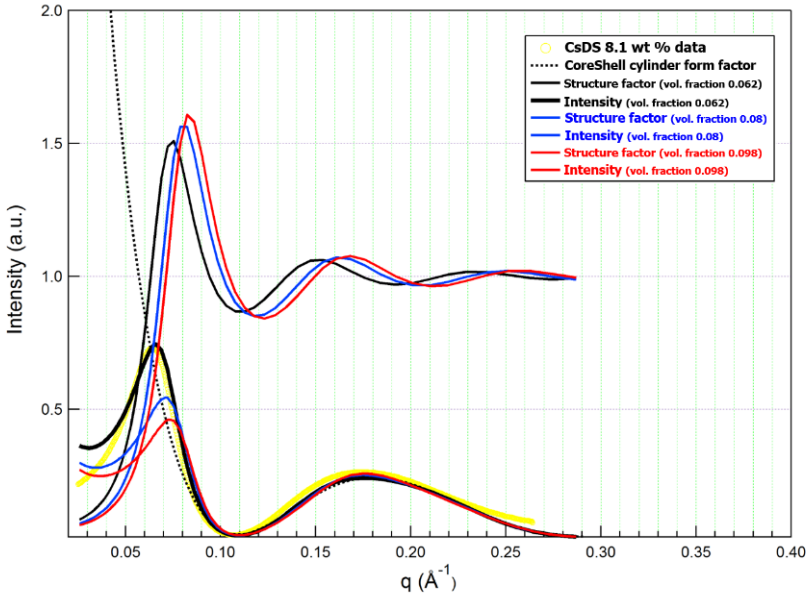

Figure 2.22. Sensitivity test on 8.1 wt % of cesium dodecyl sulfate aqueous solution at 35 °C. Volume fraction varies at constant charge. Other parameters are shown in Table 2.4.

2.7 References

1. Schryver, S. B.; Ramsden, W.; Cross, C. F.; Schidrowitz, P.; Dreaper, W. P.; McBain, J. W.; Turner, T.; Worley, F. P.; Martin, C. J.; Bousfield, W. R.; Morse, H. N.; Henri, V.; Freundlich, H.; The, C.; Ostwald, W.; Chapman, C.; Senter, G. Discussion. *Trans. Faraday Soc.* **1913,** *9*, 93-107.

2. Zemb, T.; Charpin, P. Micellar structure from comparison of X-ray and neutron small-angle scattering. *J. Phys. France* **1985,** *46* (2), 249-256.

3. Almgren, M.; Gimel, J. C.; Wang, K.; Karlsson, G.; Edwards, K.; Brown, W.; Mortensen, K. SDS micelles at igh ionic strength. A light scattering, neutron scattering, fluorescence quenching, and cryoTEM investigation. *J. Colloid Interface Sci.* **1998,** *202* (2), 222-231.

4. Lin, Z.; Cai, J. J.; Scriven, L. E.; Davis, H. T. Spherical-to-wormlike micelle transition in CTAB solutions. *J. Phys. Chem.* **1994,** *98* (23), 5984-5993.

5. Raghavan, S. R.; Kaler, E. W. Highly Viscoelastic wormlike micellar solutions formed by cationic surfactants with long unsaturated tails. *Langmuir* **2000,** *17* (2), 300-306.

6. Hassan, P. A.; Fritz, G.; Kaler, E. W. Small angle neutron scattering study of sodium dodecyl sulfate micellar growth driven by addition of a hydrotropic salt. *J. Colloid Interface Sci.* **2003,** *257* (1), 154-162.

7. Wang, Z.; Larson, R. G. Molecular dynamics simulations of threadlike cetyltrimethylammonium chloride micelles: Effects of sodium chloride and sodium salicylate salts. *J. Phys. Chem. B* **2009,** *113* (42), 13697-13710.

8. Blackburn, J. C.; Kilpatrick, P. K. Transitional liquid crystalline phases between the hexagonal and lamellar phases in ternary cesium *n*-tetradecanoate-water-additive Mixtures. *J. Colloid Interface Sci.* **1993,** *157* (1), 88-99.

9. Bales, B. L.; Benrraou, M.; Zana, R. Krafft temperature and micelle ionization of aqueous solutions of cesium dodecyl sulfate. *J. Phys. Chem. B* **2002,** *106* (35), 9033-9035.

10. Vlachy, N.; Jagoda-Cwiklik, B.; Vácha, R.; Touraud, D.; Jungwirth, P.; Kunz, W. Hofmeister series and specific interactions of charged headgroups with aqueous ions. *Adv. Colloid Interface Sci* **2009,** *146* (1–2), 42-47.

11. Akpinar, E.; Reis, D.; Figueiredo Neto, A. M. In *Investigation of the interaction of alkali ions with surfactant head groups for the formation of lyotropic biaxial nematic phase via optical birefringence measurements*, Society of Photo-Optical Instrumentation Engineers, San Francisco, California, USA, February 2, 2013; 2013; SPIE, pp 864203-864208.

12. Sheu, E. Y.; Wu, C. F.; Chen, S. H. Effects of ion sizes on the aggregation and surface charge of ionic micelles in 1:1 electrolyte solutions. *J. Phys. Chem.* **1986,** *90* (17), 4179-4187.

13. Missel, P. J.; Mazer, N. A.; Carey, M. C.; Benedek, G. B. Influence of alkali-metal counterion identity on the sphere-to-rod transition in alkyl sulfate micelles. *J. Phys. Chem.* **1989,** *93* (26), 8354-8366.

14. Benrraou, M.; Bales, B. L.; Zana, R. Effect of the nature of the counterion on the properties of anionic surfactants. 1. Cmc, ionization degree at the cmc and aggregation number of micelles of sodium, cesium, tetramethylammonium, tetraethylammonium,

tetrapropylammonium, and tetrabutylammonium dodecyl sulfates. *J. Phys. Chem. B* **2003,** *107* (48), 13432-13440.

15. Liu, Y. C.; Ku, C. Y.; LoNostro, P.; Chen, S. H. Ion correlations in a micellar solution studied by small-angle neutron and X-ray scattering. *Phys. Rev. E* **1995,** *51* (5), 4598-4607.

16. Vass, S.; Pleštil, J.; Laggner, P.; Gilányi, T.; Borbély, S.; Kriechbaum, M.; Jákli, G.; Décsy, Z.; Abuja, P. M. Models of micellar structure tested by SANS and SAXS (from a Kratky camera) in cesium dodecyl sulfate solution. *J. Phys. Chem. B* **2003,** *107* (46), 12752-12761.

17. Kanungo, S.; Narayanan, J.; Aswal, V. K.; Bellare, J. R.; Goyal, P. S. Study of core–shell structure of cesium dodecylsulfate micelles using small-angle X-ray and neutron scattering. *J. Mol. Liq.* **2012,** *175*, 38-43.

18. Joshi, J. V.; Aswal, V. K.; Bahadur, P.; Goyal, P. S. Role of counterion of the surfactant molecule on the micellar structure in aqueous solution. *Curr. Sci.* **2002,** *83* (1), 47-49.

19. Joshi, J. V.; Aswal, V. K.; Goyal, P. S. Combined SANS and SAXS studies on alkali metal dodecyl sulphate micelles. *J. Phys.: Condens. Matter* **2007,** *19* (19), 196219.

20. Vagias, A. N. Cesium dodecyl sulphate phase behavior in aqueous solutions and comparision with the sodium dodecyl sulphate/water phase diagram. M.S. Thesis, University of Minnesota 2010.

21. Guinier, A.; Fournet, G. *Small-angle scattering of X-rays*; Wiley 1955.

22. Livsey, I. Neutron scattering from concentric cylinders. Intraparticle interference function and radius of gyration. *J. Chem. Soc., Faraday Trans. 2* **1987,** *83* (8), 1445-1452.

23. Grillo, I. Small-angle neutron scattering and applications in soft condensed matter. In *Soft Matter Characterization*, Borsali, R.; Pecora, R., Eds.; Springer Netherlands, 2008, pp 723-782.

24. Hayter, J. B.; Penfold, J. An analytic structure factor for macroion solutions. *Mol. Phys.* **1981,** *42* (1), 109-118.

25. Hansen, J.-P.; Hayter, J. B. A rescaled MSA structure factor for dilute charged colloidal dispersions. *Mol. Phys.* **1982,** *46* (3), 651-656.

26. Watanabe, K.; Klein, M. L. Shape fluctuations in ionic micelles. *J. Phys. Chem.* **1989,** *93* (19), 6897-6901.

27. Israelachvili, J. N. *Intermolecular and surface forces*; Burlington, MA : Academic Press: Burlington, MA, 2011.

28. Jain, S.; Bates, F. S. On the origins of morphological complexity in block copolymer surfactants. *Science* **2003,** *300* (5618), 460-464.

Chapter 3.

Structural Investigation of Therapeutic Nanoparticles[*,†,‡]

3.1 Overview

We report an investigation of morphology, interior structure, particle size, distribution, and structural changes during drug release kinetics of paclitaxel (PTX) silicate prodrugs, encapsulated with amphiphilic poly(ethylene glycol)-*b*-poly(lactic-co-glycolic acid) (PEG-*b*-PLGA) diblock copolymers using a novel strategy that uses labile silicate esters [tetra-alkoxysilanes, $Si(OR)_4$] as the prodrug construct. Thus, a hydroxyl group in the drug molecule, PTX can be readily derivatized with a trialkoxychlorosilane. Nanoparticles were formulated by flash nanoprecipitation using the confined impingement jets with dilution mixer. The prodrug incorporates about 45–60% of PTX, ranging from 80–150 nm. Careful selection of the aliphatic character and the steric nature of the alkoxy moieties allows control of both the hydrophobicity and the rate of hydrolysis of the resulting prodrug nanoparticles. A suite of PTX silicate (Si) prodrugs has been used to

[*] A portion of this chapter presents results from a collaboration with members in Hoye research group and Macosko research group at the University of Minnesota. Adam R. Wohl synthesized silicate derivatives of paclitaxel. Kevin M. Pustulka prepared particles. The chapter is partly reprinted from Kevin M. Pustulka, Adam R. Wohl, Han Seung Lee, Andrew R. Michel, Jing Han, Thomas R. Hoye, Alon V. McCormick, Jayanth Panyam, and Christopher W. Macosko, "Flash nanoprecipitation: Particle Structure and Stability", *Mol. Pharmaceutics*, **2013**, 10 (11), 4367 (DOI: 10.1021/mp400337f). Copyright 2013 American Chemical Society.

[†] A portion of this chapter presents results from a collaboration with members in Hoye research group, Macosko research group, and Panyam research group at the University of Minnesota. Andrew R. Michel synthesized silicate derivatives of paclitaxel. Jing Han prepared particles. Stephen Kalscheuer performed *in-vivo* tests. "Nanoparticles containing high loads of paclitaxel silicate prodrugs: Formulation, drug release, and anitcancer efficacy". *Manuscript in preparation*.

[‡] A portion of this chapter was done in collaboration with member in Magdassi research group at the Hebrew University of Jerusalem. Katherine Margulis prepared the nanoparticles. This chapter is partly reprinted from *J. Colloid Interface Sci.*, 434, Katherine Margulis, Shlomo Magdassi, Han Seung Lee, and Christopher W. Macosko, "Formation of curcumin nanoparticles by flash nanoprecipitation from emulsions", 65 (DOI: 10.1016/j.jcis.2014.07.040), Copyright (2014), with permission from Elsevier.

demonstrate the effectiveness of this design. Increasing hydrophobicity of the PTX Si prodrugs allowed a preparation of stable nanoparticles but, decreased hydrolysis rate. Additionally the controlled co-precipitation process was applied to prepare curcumin based nanoparticles by co-mixing of emulsion and water with food grade surfactants.

3.2 Introduction

† The following paragraphs are adapted from Han et al.[1], and Pustulka et al.[2] Jing Han and Kevin Pustulka are lead authors on these papers. This part represents an adaptation of excerpts from these papers to show my contribution to the team project.

Cancer has been one of the most prevalent human disease.[3] There has been numerous types of medication methods to enhance human healthcare such as radiation therapy, surgery, and chemotherapy. Among these conventional types of treatments, drug administration method using therapeutic nanoparticles has been significantly improved last few decades.[4, 5, 6, 7, 8, 9, 10] To enhance efficacy and minimize toxicity of drugs, it is imperative that there should be an invention of new molecular entities, guided delivery of drugs, precise targeting to the sites, understanding of drug release mechanism and maintenance of drugs at a therapeutic concentration over specific periods of time.[11] Of these topics, the entrapment in pharmaceuticals with high dosage and its targeted delivery via phospholipid and polymeric materials has received great attention in recent years for its potential applications.[12, 13] Although nanocarriers using liposomes may need incorporation of pharmaceuticals process and a multiple manufacturing steps (e.g. liposome preparation including purification), biocompatible polymer-drug conjugates that enables encapsulation of therapeutic agents.[14] Furthermore recent advances in molecular cellular biology has allowed scientists to minimize anti-immunological response in the human body by mimicking nanoparticles as red blood cell membranes: functionalizing with biodegradable polymeric nanoparticles with natural membranes and the corresponding surface proteins.[15]

Among these candidates prodrugs, paclitaxel (PTX) has been widely used for a medication for the types of ovarian, breast, lung and pancreatic cancers where it inhibits mitosis or cell division, resulting in arrest of cell cycle and cell death.[16] The first PTX prodrug Taxol®, developed by Bristol Myers Squibb where it is solubilized by the emulsifier Cremophor EL® [CrEL®, a 1:1 (v/v) mixture of polyethoxylated castor oil and absolute ethanol]. This formulation comprises a significant advance in chemotherapeutics, but the drug loading is merely ca. 1 wt % of PTX in the drug. Therefore this intravenous administration limits the amount of dosage that can be injected to patients and causes a sets of side effects such as hypersensitivity, nephrotoxicity, and neurotoxicity.[17] Recently a new form of protein-bound PTX, Abraxane® was developed by Abraxis Bioscience. Abraxane® is complexed with human serum albumin and carries ca. 10 wt % of PTX. Both anticancer drugs are highly effective antitumor agent however, it is only minimally water-soluble and also harm normal tissue due to non-specific delivery.

Therefore it is important that a new nano-scale formulations should demonstrate higher drug loading level and enhanced permeation and retention (EPR) effect. In addition, the particle size of potential prodrug matters. A growing tumor cells promotes a growth of new vascularization as a result new blood vessels become irregular and defective in shape. Consequently the endothelial cells are misaligned and disorganized with some fenestrations.[18] Thus these leaky vessels may allow sub 200 nm drug-loaded nanoparticles pass through the vessel walls shown in Figure 3.1.[19]

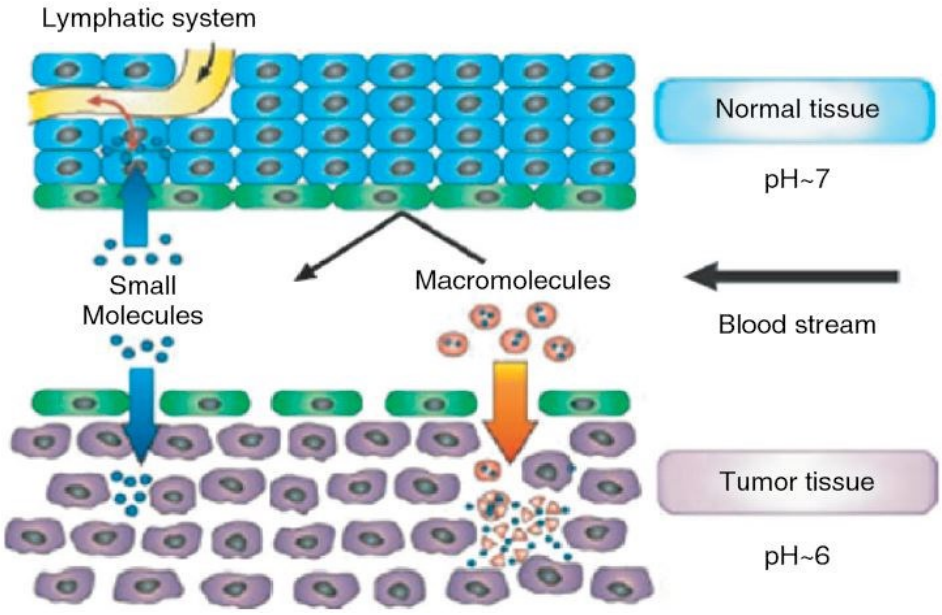

Figure 3.1. Schematic representation of anatomical differences between normal and tumor tissues. The open tumor vasculature allows preferential extravasation of the circulating macromolecular drug carriers due to enhanced permeability and retention effect. Adapted from Bisht et al.,[19] [Bisht, S.; Maitra, A. Dextran–doxorubicin/chitosan nanoparticles for solid tumor therapy. *Wiley Interdisciplinary Reviews: Nanomedicine and Nanobiotechnology* **2009,** *1* (4), 415-425]. © 2009 WILEY

To precisely control the particle size of the prodrug and improve its loading efficiency, flash nanoprecipitation (FNP) method was established by Prud'homme and coworkers.[20, 21] They proposed formation of prodrug incorporated nanoparticles through attraction and aggregation between hydrophobic block of diblock copolymer (BCP) and drug.[22] The FNP method incorporates inlets of two or four stream multi stream and micro confined chamber. The confined space in the chamber allows a rapid turbulent mixing of impinging jet-like streams from the inlets resulting a supersaturation environment in the mixer. In either two or multiple stream cases, organic solutes and amphiphilic BCPs are dissolved in a water miscible solvent such as tetrahydrofuran, acetone with antisolvent water leading flash nano co-precipitation. A schematic of FNP process uses multi inlet vortex mixer or confined impingement jets (CIJ) mixer are shown in Figure 3.2. A simple but straightforward version of CIJ mixer with dilution (CIJ-D) was developed by Macosko and coworkers.[23]

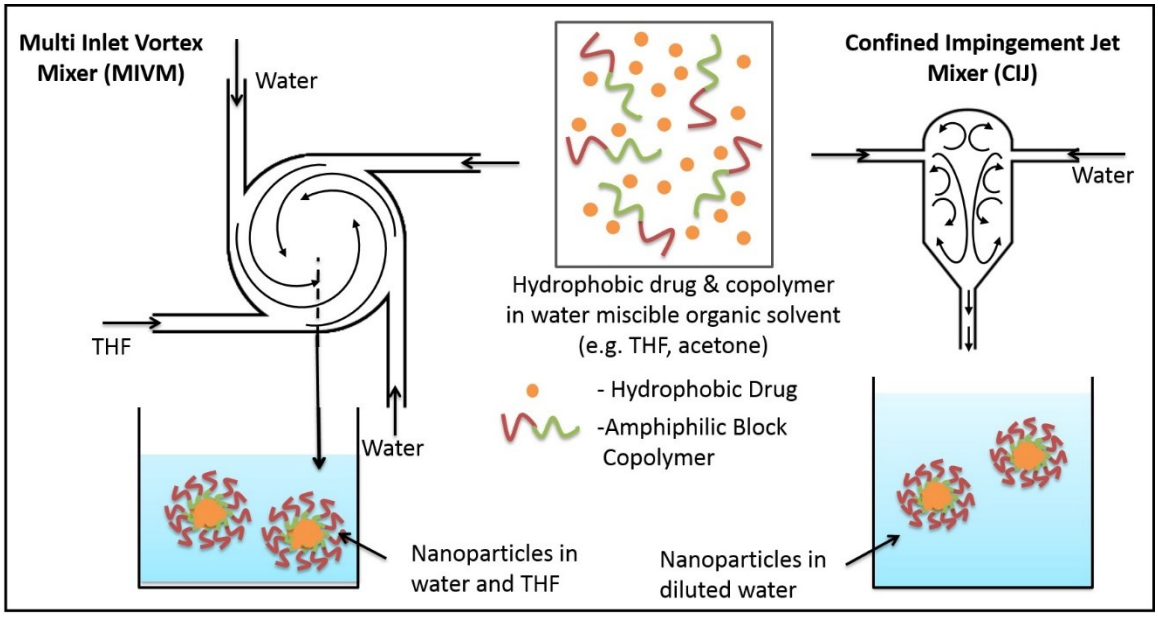

Figure 3.2. Schematic representation of flash nanoprecipitation process of multi inlet vortex mixer and confined impingement jet mixer. Adapted from Pustulka et al.,[2] [Pustulka, K. M.; Wohl, A. R.; Lee, H. S.; Michel, A. R.; Han, J.; Hoye, T. R.; McCormick, A. V.; Panyam, J.; Macosko, C. W. Flash Nanoprecipitation: Particle Structure and Stability. Mol. Pharmaceutics 2013, 10 (11), 4367-4377]. © 2013 American Chemical Society

In this work, we prepare high load of drug (silicate derivatives of PTX) nanoparticle but small enough to permeate into tumor tissue. The morphology and size were characterized by cryogenic transmission electron microscopy (Cryo-TEM) and dynamic light scattering (DLS).

3.3 Experimental Section

Materials and methods

† *The paragraph below is adapted from Wohl et al.[24], and Han et al.[1] Adam Wohl and Jing Han are lead authors on these paper. This part represents an adaptation of excerpts from these papers to highlight my contribution to the team project.*

A suite of silicate derivatives PTX prodrugs and PEG-*b*-PLGA copolymer (MW. 5K-10K) was synthesized by Hoye and coworkers.[24, 25] Figure 3.3 shows a reaction scheme for the formulation of the PTX Si prodrugs. Figure 3.4 shows molecular structure of PEG-*b*-PLGA block copolymer. Figure 3.5 shows typical

microstructure of PEG-*b*-PLGA and the PTX Si prodrugs suspended in water imaged by cryo-TEM.

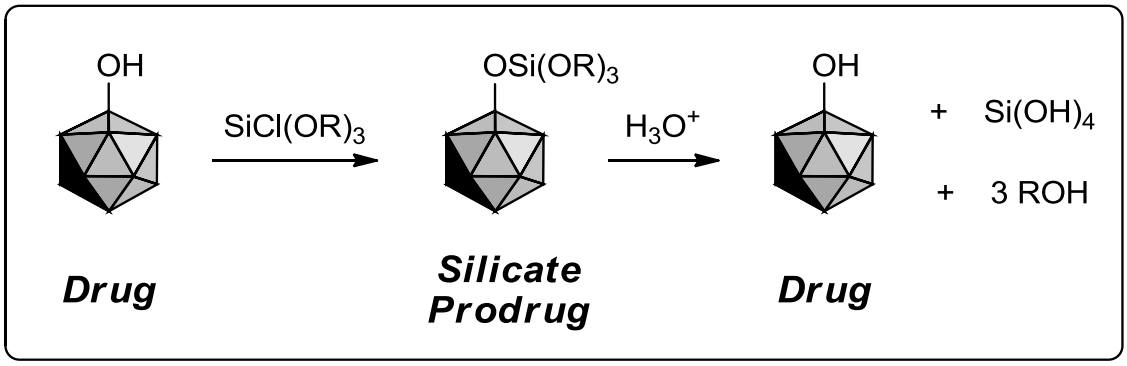

Figure 3.3. The strategy of the reaction scheme for the formation of silicate derivatives. Modification of a hydroxyl group in the drug with a trialkoxychlorosilane generates the (labile) silicate prodrug. Adapted from Wohl et al.[24], [Wohl, A. R.; Michel, A. R.; Kalscheuer, S.; Macosko, C. W.; Panyam, J.; Hoye, T. R. Silicate Esters of Paclitaxel and Docetaxel: Synthesis, Hydrophobicity, Hydrolytic Stability, Cytotoxicity, and Prodrug Potential. Journal of Medicinal Chemistry 2014, 57 (6), 2368-2379]. © 2014 American Chemical Society

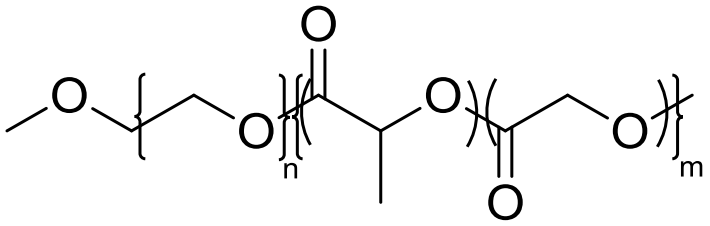

Figure 3.4. Chemical structures of amphiphilic poly(ethylene glycol)-*b*-poly(lactic-co-glycolic acid) (PEG-*b*-PLGA) diblock copolymer

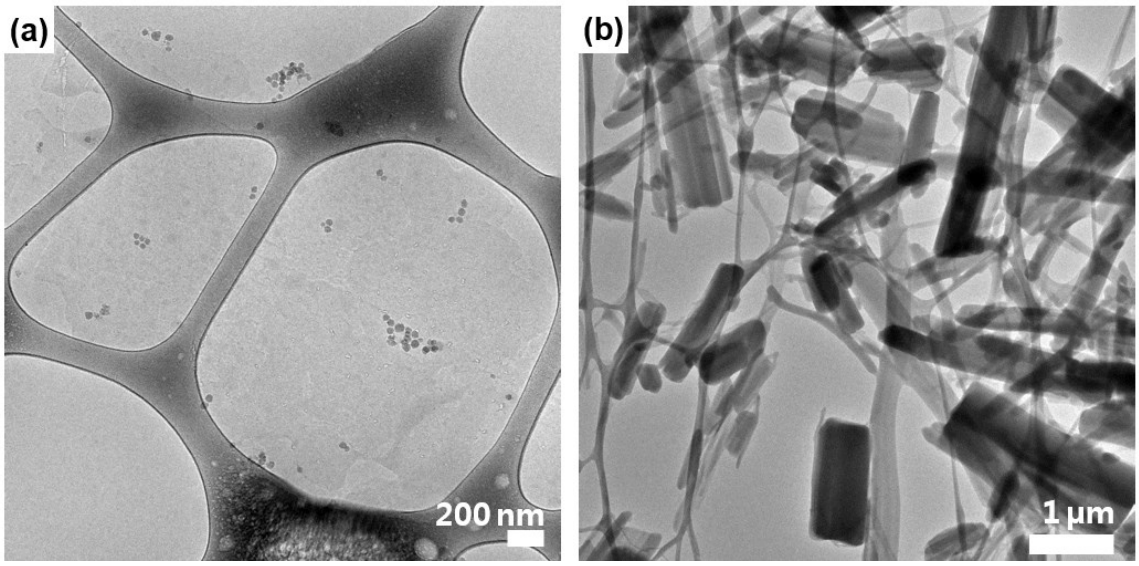

Figure 3.5. Representative cryo-TEM micrographs of (a) PEG-*b*-PLGA (MW: 5k-10k Da.) block copolymer, (b) DI-water suspended paclitaxel.

† *The paragraph below is adapted from Han et al.*[1] *Jing Han is a lead author on this paper. This part represents an adaptation of excerpts from this paper to highlight my contribution to the team project.*

The PTX Si prodrugs including BCPs were formulated by FNP using CIJ-D mixer by Macokso and coworkers.[23] Fresh particles were ultracentrifuged to separate unencapsulated prodrug and blank polymer nanoparticles. Supernatants were removed and the remaining pellets were resuspended in water. The collected nanoparticles were freeze-dried using lyophilizer. Six silicate derivatives PTX prodrugs (Figure 3.6a. 2′-tri-ethoxy PTX Si, Figure 3.6b. 2′-tri- isopropoxy PTX Si, Figure 3.6c. 2′-tri-menthoxy PTX Si, and Figure 3.6d. 2′,7-tri-ethoxy PTX Si, Figure 3.6e. 2′-di-tert-butoxy/ethoxy PTX Si, Figure 3.6f. 2′-tri-octoxy PTX Si) were synthesized with varying hydrophobicity and hydrolytic sensitivity. The molecular structures of PTX Si prodrugs are shown in Figure 3.6

.

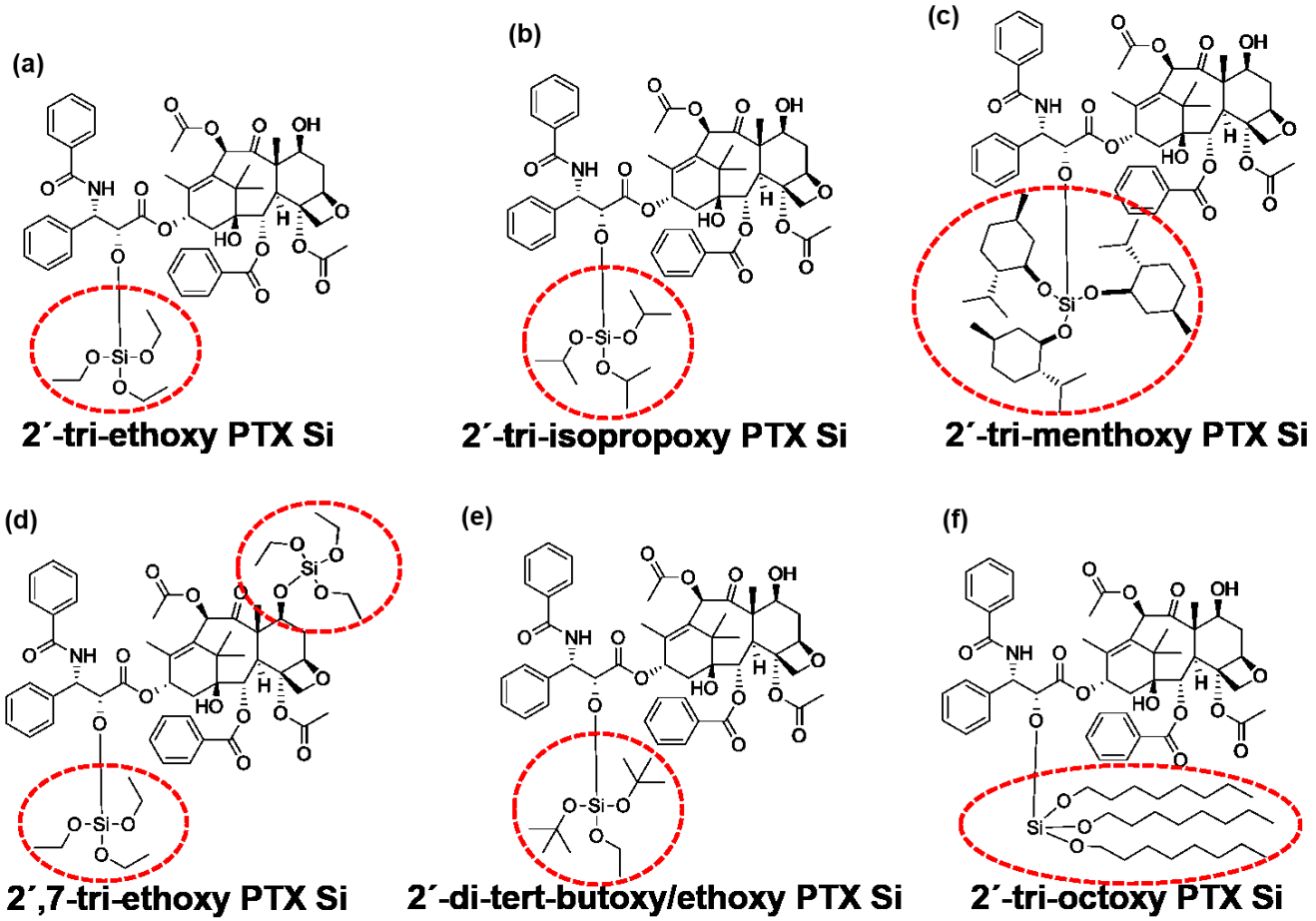

Figure 3.6. Chemical structures of (a) 2´-tri-ethoxy paclitaxel (PTX) silicate (Si), (b) 2´-tri-isopropoxy PTX Si, (c) 2´-tri-menthoxy PTX Si, (d) 2´,7-tri-ethoxy PTX Si, (e) 2´-di-tert butoxy/ethoxy PTX Si, and (f) 2´-tri-octoxy PTX Si prodrugs. Adapted from Han et al.[1], [Han, J.; Michel, A. R.; Lee, H. S.; Kalscheuer, S.; Wohl, A. R.; Hoye, T. R; McCormick, A. V.; Panyam, J.; Macosko, C. W. Nanoparticles containing high loads of paclitaxel silicate prodrugs: Formulation, drug release, and anitcancer efficacy. *Manuscript in preparation*.].

The morphology of the nanoparticle was observed by cryo-TEM. Samples were prepared from either nanoparticle suspension or dried nanoparticle powder. A lacey carbon Cu grid (01881, 200-mesh, Ted Pella, Ltd., Redding, CA) was glow discharged in a vacuum evaporator at 70 mTorr (DV-502A, Denton Vacuum Moorestown, NJ) for 30 seconds to create hydrophilic surface on the carbon coated side of the grid. A 2−7 μL volume of fresh sample was pipetted onto the carbon side at 22 °C in a Mark III Vitrobot chamber (FEI Company, Hillsboro, OR) with a relative humidity of ~100 %. The excess sample was blotted with 595 filter papers (Ted Pella, Ltd., Redding, CA) 1−2 times with a ~1.5 mm offset parameter for 5 seconds to create a thin liquid film. After the blotting, the sample was relaxed for ~3 seconds and immediately plunged into liquid ethane cooled by liquid nitrogen. The vitrified sample was transferred to a Gatan 626 cryo-transfer unit (Gatan, Pleasanton, CA) at -194 °C and characterized at -178 °C in the microscope. A 120 kV FEI Tecnai Spirit BioTWIN was used and images were taken digitally with Eagle™ 2k CCD camera (FEI Company, Hillsboro, OR) in low-dose mode. The images were processed with TEM Imaging and Analysis software package. (Version 4.2 SP1 build 816, FEI Company, Hillsboro, OR). To enhance phase contrast, the images were observed with objective lens in an underfocused mode. (2−4 μm). The underfocused mode was controlled intentionally so that Fresnel fringe (white rings on the boundary of nanoparticle structure) can appear and that elucidates core and shell regions in the nanoparticles. Beam damage was only used to differentiate the microstructures between prodrug in the core and polymer in the shell. In this case, PEG-*b*-PLGA BCP was susceptible to selective damage to the incoming electron beam and the sample showed evidence of radiation damage, producing white bubbles.

3.4 Results and Discussion

The physical characteristics (e.g. hydrophobicity, particle size, and level of drug loading) of silicate derivatives PTX prodrugs are tabulated in Table 3.1.

Table 3.1. Characteristics of silicate derivatives paclitaxel (PTX) prodrugs.

Prodrug (Particle count)	Before ultracentrifuge						After ultracentrifuge	
	aLogP*	Diameter** (DLS)‡	Drug loading (HPLC)†,‡	Measurements by Cryo-TEM			Diameter (DLS)‡	Drug loading (HPLC)†,‡
				Diameter *(NPs w/visible core, % of NPs show cores)*	Core diameter	Drug loading		
2′-tri-ethoxy PTX Si (196)	4.96	145 ± 9 nm	49.1%	110 ± 110 nm (245 ± 80 nm, 20%)	175 ± 65 nm	35 ± 15%	423 ± 56 nm	63.0%
2′-tri-isopropoxy PTX Si (464)	5.60	136 ± 1 nm	53.3%	100 ± 125 nm (310 ± 90 nm, 15%)	250 ± 75 nm	55 ± 15%	201 ± 32 nm	58.0%
2′-tri-menthoxy PTX Si (914)	7.37	95 ± 2 nm	56.8%	55 ± 40 nm (100± 45 nm, 5%)	70 ± 25 nm	40 ± 10%	197 ± 25 nm	73.5%
2′,7-tri-ethoxy PTX Si (453)	6.31	118 ± 13 nm	51.2%	60 ± 40 nm (100 ± 30 nm, 15%)	70 ± 30 nm	35 ± 30%	312 ± 18 nm	60.4%
2′-di-tert-butoxy/ethoxy PTX Si (147)	5.81	86 ± 2 nm	60.7%	40 nm ± 25 nm (85 ± 30 nm, 10%)	60 ± 20 nm	35 ± 10%	245 ± 27 nm	73.5%
2′-tri-octoxy PTX Si (282)	7.74	83 ± 6 nm	55.3%	35 ± 15 nm (60 ± 40 nm, 5%)	55 ± 35 nm	65 ± 15%	214 ± 23 nm	65.0%
PEG-*b*-PLGA	-	30 ± 10 nm	-	15 - 25 nm	-	-	-	-

* aLogP is calculated by using ALOPS 2.1

** DLS diameter is intensity particle diameter by DLS + standard deviation of averaged particle size within three batches of particles prepared in same condition and formula.

† Drug loading (%) is total of encapsulated prodrug/drug in nanoparticles (after ultracentrifugation) determined by HPLC

‡ Adapted from Han et al.[1], [Han, J.; Michel, A. R.; Lee, H. S.; Kalscheuer, S.; Wohl, A. R.; Hoye, T. R; McCormick, A. V.; Panyam, J.; Macosko, C. W. Nanoparticles containing high loads of paclitaxel silicate prodrugs: Formulation, drug release, and anitcancer efficacy. *Manuscript in preparation*.]

† *The following paragraph is adapted from Han et al.[1] Jing Han is a lead author on this paper. This part represents an adaptation of excerpts from this paper to show my contribution to the team project.*

As seen on Table 3.1, hydrophobicity (aLogP) affinity of the prodrug is enhanced as the size of side group in the PTX Si prodrugs increases. The steric hindrance from –R group also contribute the hydrophobicity of the prodrug. The particle size was ranging from 80 to 150 nm after CIJ-D mixing and the dimension of prodrugs was suitable for passive targeting via EPR effect. The PTX Si prodrugs were remained homogeneous and kinetically stable as a function of time therefore no significant aggregation was observed. For example, the 2′-tri-ethoxy PTX Si prodrug was stable for 24 hours. The 2′-tri-octoxy PTX Si prodrug was stable for 3 days. The 2′-tri- isopropoxy PTX Si, 2′-tri-menthoxy PTX Si, and 2′-di-tert-butoxy/ethoxy PTX Si prodrugs were stable over 2 weeks. We suggest that slow aggregation occurs because the hydrophilic PEG layer might surround the prodrug as an outmost corona layer and sterically stabilize the particles by preventing further aggregation.

The 2′,7-tri-ethoxy PTX Si prodrug does not follow aLogP tendency because number of silicate derivative and their position may be affected the characteristics of prodrug. Figure 3.7 is a representative cryo-TEM images of six candidates with no ultracentrifugation. The images show distinct core-shell structures that suggest encapsulation of PTX Si prodrug. The inlet of Figure 3.7f supports that even the smallest PTX Si prodrug was successfully formulated as a core-shell prodrugs. The overall size of nanoparticles decrease as their hydrophobicity is increased. The white bubbles on the lacey carbon struts in Figure 3.7d and 7e are results of beam radiation. The hydrophilic PEG corona was not observed because they are likely swollen status and has low electron contrast.

Figure 3.8 shows size distribution histogram of six PTX Si prodrugs. All prodrug particles show high intensities in sub 50 nm because of presence of unencapsulated PEG-*b*-PLGA BCPs.

† *The following paragraph is adapted from Pustulka et al.[2] Kevin Pustulka is a lead author on this paper. This part represents an adaptation of excerpts from this paper to show my contribution to the team project.*

We further attempted to characterize PEG-*b*-PLGA and 2′,7-tri-ethoxy PTX Si prodrug formulation, guided by its mosaic of prodrug characteristics (ease of synthesis and handling, hydrophobic character, rate of hydrolysis, cytotoxicity, and nature of the byproducts). The average loading level of the 2′,7-tri-ethoxy PTX Si prodrug was determined by high performance liquid chromatography (HPLC) to be about to be 47 ± 5 wt %. The DLS measurement of 2′,7-tri-ethoxy PTX Si prodrug was 120 nm in diameter with intensity average hydrodynamic diameter.

Figure 3.9 shows that the nanoparticles are predominately spherical in nature. The higher resolution micrographs in Figure 3.7b and 3.7c confirm the core-shell microstructure suggested by the nuclear magnetic resonance and differential scanning calorimetry experiments described elsewhere.[24] A white ring in Figure 3.9c indicates a Fresnel fringe, suggesting an underfocused condition. Similar structures have been observed in Pluronics-based PTX nanoparticle system.[26] A subset of substantially smaller nanoparticles can be also seen in Figure 3.9a. These smaller particles are maybe indication of unloaded block copolymer only particles in Figure 3.9d. Below part of Figure 3.9d shows an electron beam-damaged unloaded block copolymer particles. They are of similar size to particles prepared with only PEG-*b*-PLGA shown in Figure 3.5a.

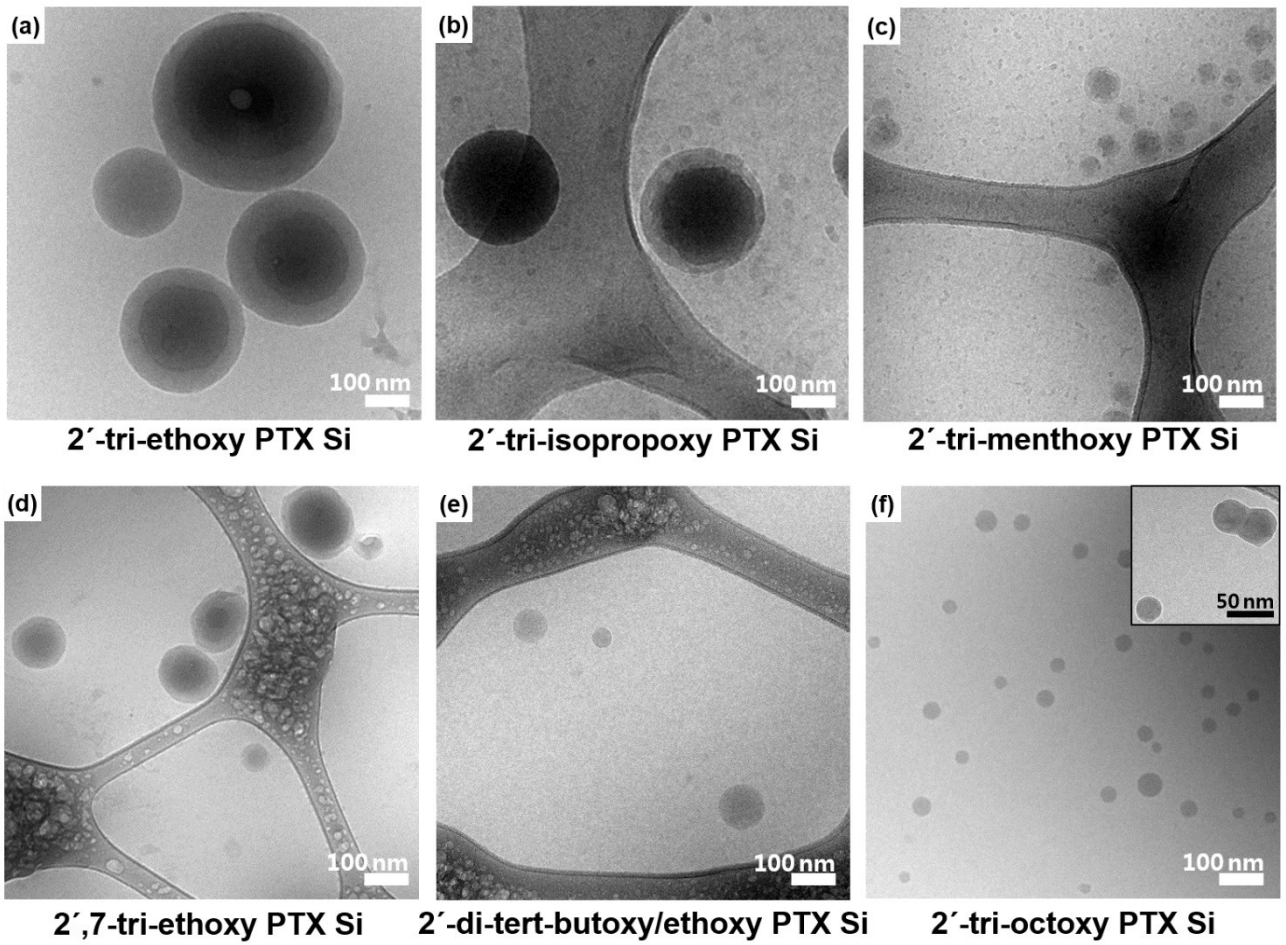

Figure 3.7. Representative cryo-TEM micrographs of fresh paclitaxel (PTX) silicate (Si) loaded PEG-*b*-PLGA protected nanoparticles. All images are taken before ultracentrifugation. Adapted from Han et al.,[1] [Han, J.; Michel, A. R.; Lee, H. S.; Kalscheuer, S.; Wohl, A. R.; Hoye, T. R; McCormick, A. V.; Panyam, J.; Macosko, C. W. Nanoparticles containing high loads of paclitaxel silicate prodrugs: Formulation, drug release, and anitcancer efficacy. *Manuscript in preparation*.]

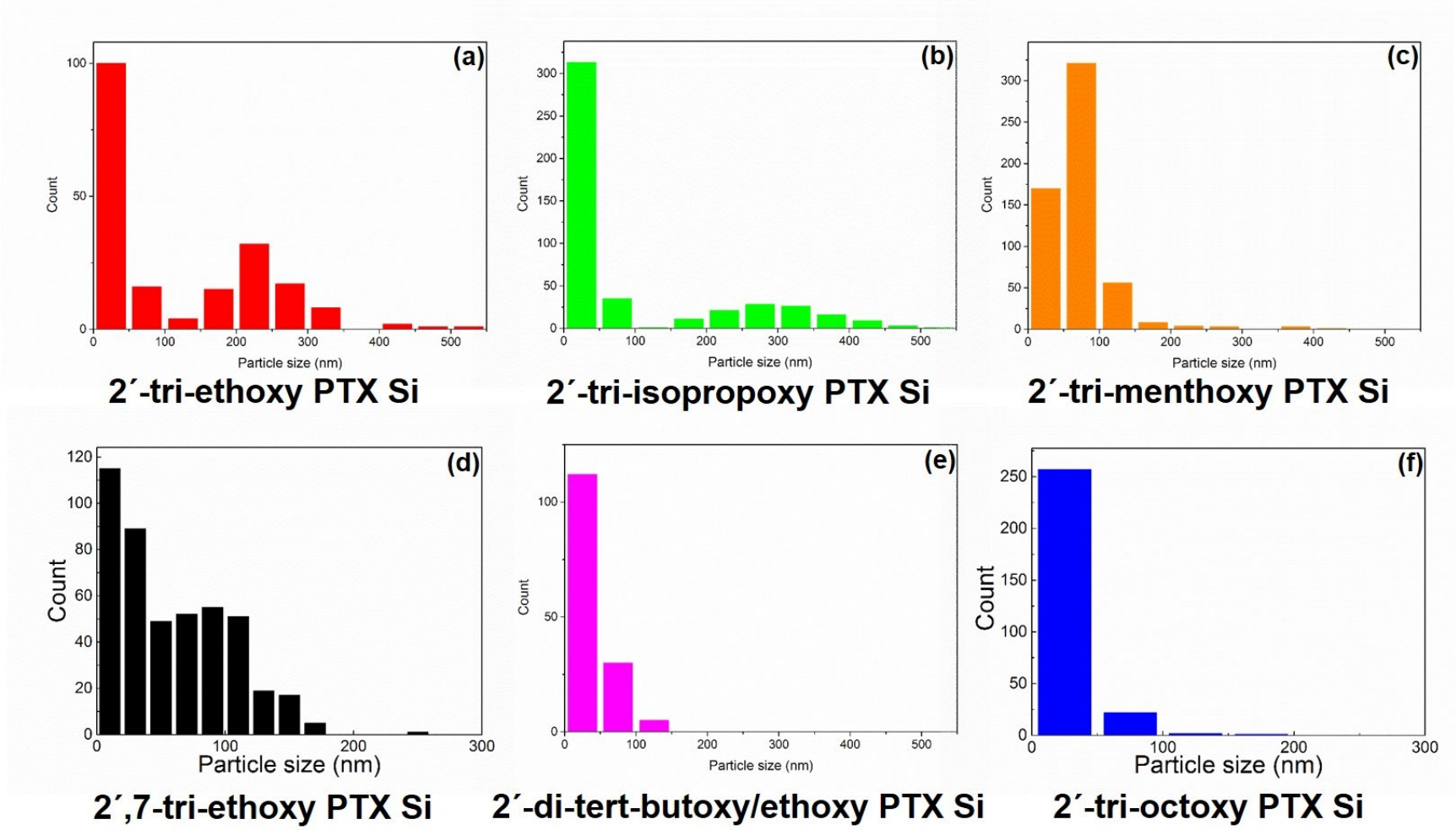

Figure 3.8. Size distribution of freshly prepared paclitaxel (PTX) silicate (Si) loaded PEG-*b*-PLGA protected nanoparticles. The histograms are counted from cryo-TEM micrographs. The particles are counted before ultracentrifugation.

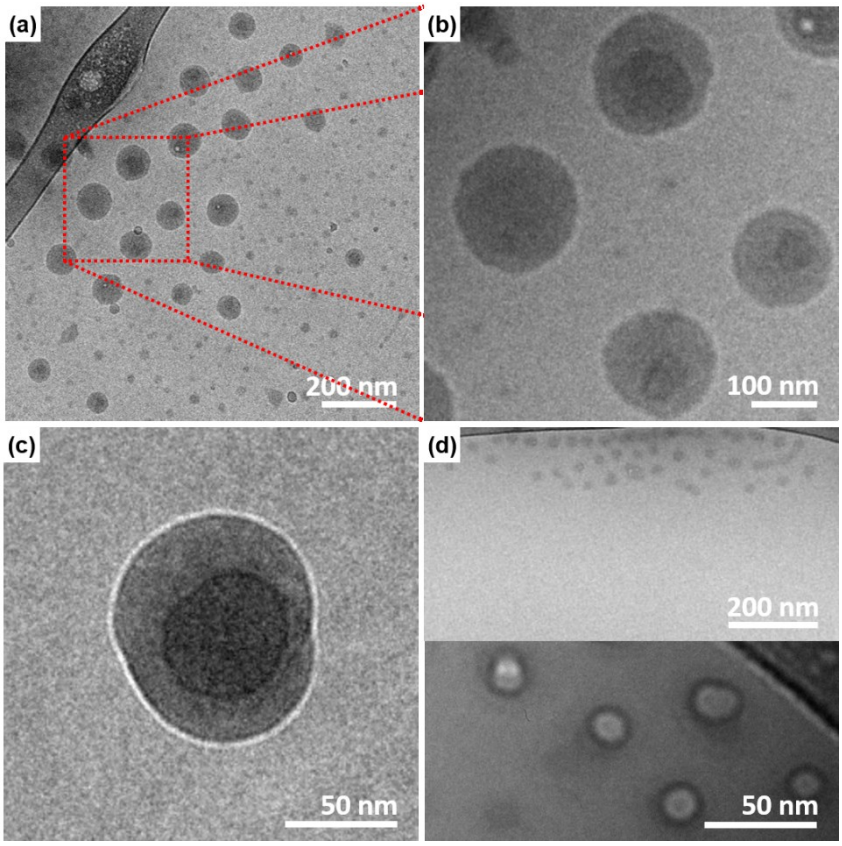

Figure 3.9. Representative cryo-TEM micrographs of nanoparticles loaded with 2′,7-tri-ethoxy paclitaxel (PTX) silicate (Si) prodrug. (a) A low magnification image showing spherical nanoparticles and their size distribution. (b) A higher magnification image of a portion of that field showing core-shell features. (c) An underfocused image that emphasizes the core-shell nature of one particle. The prodrug is encapsulated with the solid-like PLGA block of the copolymer which is in turn surrounded by the soluble corona of the hydrophilic PEG blocks of the copolymer. The PEG corona is not visible because of its low electron density. (d) Upper: Polymer only particles prepared the same way but without the PTX Si prodrug. Lower: Electron beam radiated block copolymers. DLS gave similar size, 30−40 nm. All images are taken before ultracentrifugation. Adapted from Pustulka et al.,[2] [Pustulka, K. M.; Wohl, A. R.; Lee, H. S.; Michel, A. R.; Han, J.; Hoye, T. R.; McCormick, A. V.; Panyam, J.; Macosko, C. W. Flash Nanoprecipitation: Particle Structure and Stability. Mol. Pharmaceutics 2013, 10 (11), 4367-4377]. © 2013 American Chemical Society

† *The following paragraph is adapted from Han et al.*[1] *Jing Han is a lead author on this paper. This part represents an adaptation of excerpts from this paper to show my contribution to the team project.*

After ultracentrifugation and lyophilization, nanoparticle powders were redispersed in water and put in a dialysis capsule for *in-vitro* release study. The release studies for six PTX Si prodrugs were performed in phosphate buffered saline (PBS) at pH=7.4 and 37 °C. Hydrolysis of prodrugs and diffusion by concentration difference may contribute the diffusion of prodrug nanoparticles. The rate of change of drug loading level with respect to time was proportional to

the difference between the concentration of outer environment of dialysis capsule and the inside of prodrug. Most of drug release linearly up to 24 hours and the diffusions slow down once the nanoparticles were dispersed in buffer solution. In 48 hours release study, most prodrug particles with single side group released about 60% of drugs and 2′,7-tri-ethoxy PTX Si prodrug released 90% of its original loading from *in-vitro* experiments.

Figure 3.10 shows representative micrographs of selected 0 hour PTX Si prodrugs after ultracentrifugation and lyophilization. The overall particle sizes are increased after they are centrifuged. The unencapsulated small PEG-*b*-PLGA particles was not observed.

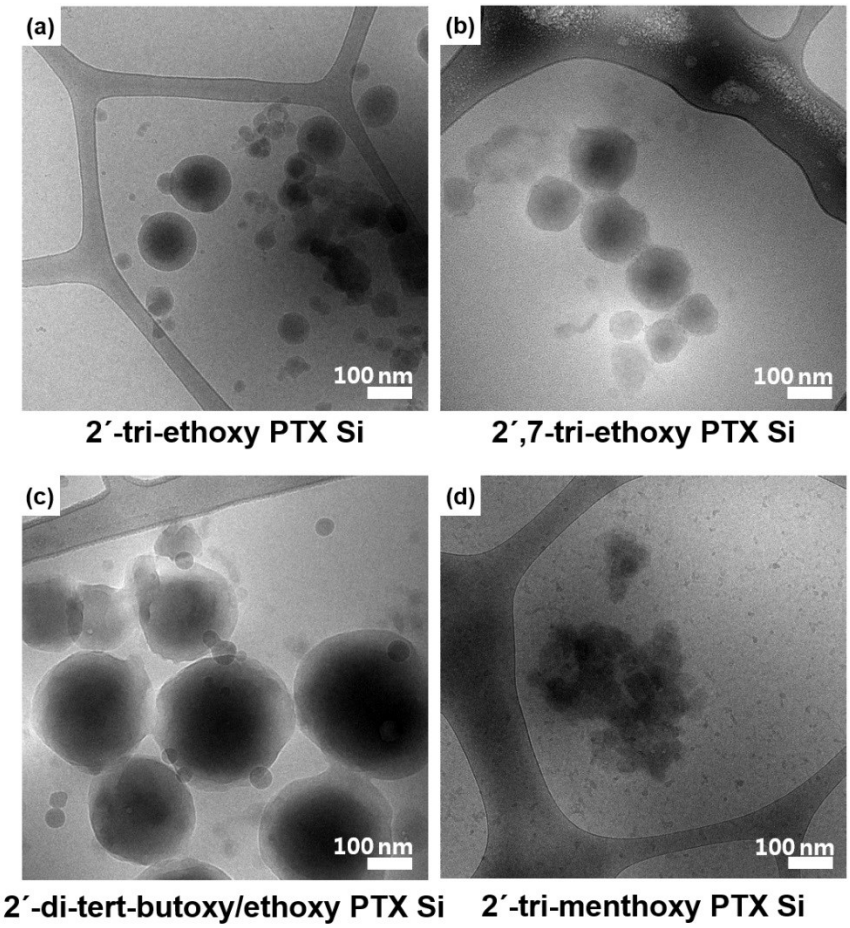

Figure 3.10. Representative cryo-TEM micrographs of paclitaxel (PTX) silicate (Si) prodrugs after ultracentrifugation and lyophilization. Adapted from Han et al.,[1] [Han, J.; Michel, A. R.; Lee, H. S.; Kalscheuer, S.; Wohl, A. R.; Hoye, T. R; McCormick, A. V.; Panyam, J.; Macosko, C. W. Nanoparticles containing high loads of paclitaxel silicate prodrugs: Formulation, drug release, and anitcancer efficacy. Manuscript in preparation.]

Figure 3.11 shows selected PTX Si prodrugs after 24 hours *in-vitro* release experiments. The overall size of nanoparticles are decreased as the drug releases from the core of the particle. The spherical drug particles became rugged during the release. The images in Figure 3.11 indicate some possible polymer release mechanisms as Langer suggested.[11] The most common release mechanism shown in our images are diffusion where the drug migrates from its core to the outside of the polymer carrier. However, the PTX Si prodrugs are also released by degradation of the PEG-*b*-PLGA block copolymer shown in bottom of Figure 3.11c. The other possible release mechanism is that Phosphate PBS or acetic acid buffer solution may permeate into a prodrugs because of osmotic pressure difference. Therefore, it makes pores inside the prodrug nanoparticles and brings the drug release.

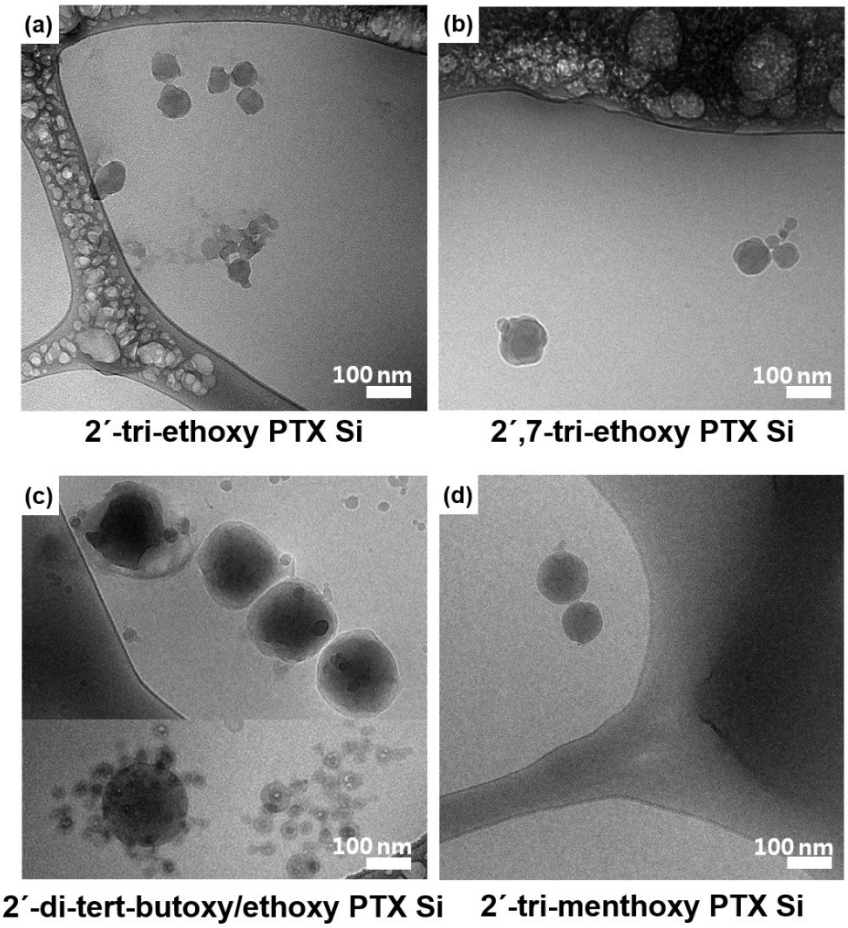

Figure 3.11. Representative cryo-TEM micrographs of paclitaxel (PTX) silicate (Si) nanoparticles after 24 hours release. Adapted from Han et al.,[1] [Han, J.; Michel, A. R.; Lee, H. S.; Kalscheuer, S.; Wohl, A. R.; Hoye, T. R; McCormick, A. V.; Panyam, J.; Macosko, C. W. Nanoparticles containing high loads of paclitaxel silicate prodrugs: Formulation, drug release, and anitcancer efficacy. Manuscript in preparation.]

† *The following paragraph is adapted from Margulis et al.*[27] *Katherine Margulis is a lead author on this paper. This part represents an adaptation of excerpts from this paper to show my contribution to the team project.*

The CIJ-D mixer technique is also applied to test curcumin-loaded nanoparticles potentially known as preventive and therapeutic agent in neurological, cardiovascular, pulmonary, autoimmune and neoplastic disorders.[28] The nanoparticle is composed of curcumin, cyclopentanone (The oil is used to dissolve curcumin and surfactants.), non-polymeric, food grade surfactants, soybean phosphatidylcholine, ammonium glycyrrhizinate dipotassium glycyrrhizinate salts. Cyclopentanone is later spray dried after curcumin is

encapsulated. Figure 3.12 shows a curcumin-loaded nanoparticles images with cryo-TEM.

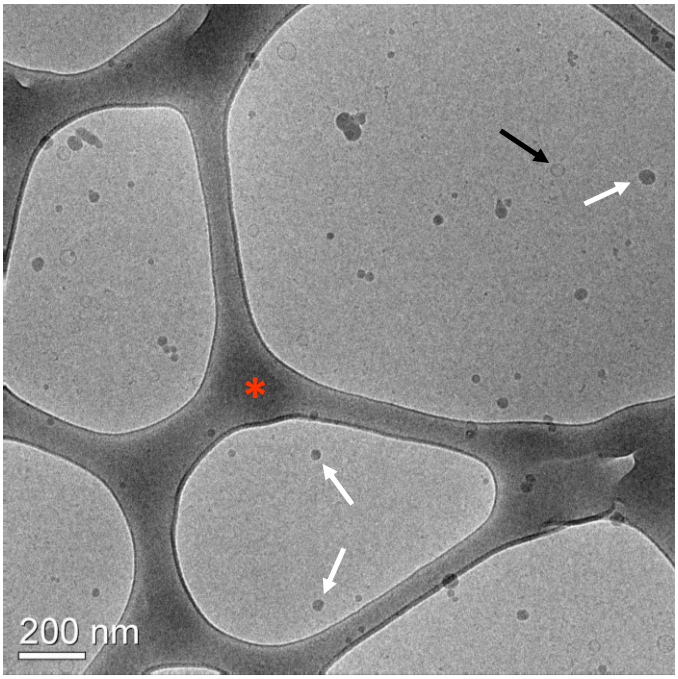

Figure 3.12. Representative cryo-TEM micrograph of curcumin-loaded nanoparticles as an aqueous solution. The size of spherical particles from 20 to 50 nm. Adapted Margulis et al.,[27] [Margulis, K.; Magdassi, S.; Lee, H. S.; Macosko, C. W. Formation of curcumin nanoparticles by flash nanoprecipitation from emulsions. J. Colloid Interface Sci. 2014, 434 (0), 65-70]. © 2014 Elsevier

3.5 Conclusions

We formulated a suite of silicate derivative paclitaxel prodrug nanoparticles using the active chemotherapeutic agent with biocompatible PEG-*b*-PLGA block copolymers. Excipients used in our formulations ameliorate undesirable side effects. To prepare nanoparticles, CIJ-D mixer via FNP techniques was applied. The size of the side group in the silicate PTX prodrugs influenced the physical characteristics of PTX Si prodrugs. Cryo-TEM was effective characterization technique for distinguishing the core-shell nanostructures of fresh prodrugs and the structure of nanoparticles after *in-vitro* release test, helping to give insight on the drug release mechanism.

3.6 References

1. Han, J.; Michel, A. R.; Lee, H. S.; Kalscheuer, S.; Wohl, A. R.; McCormick, A. V.; Panyam, J; Hoye, T. R.; Macosko, C. W. Nanoparticles containing high loads of paclitaxel silicate prodrugs: Formulation, drug release, and anitcancer efficacy. *manuscript in preparation*.

2. Pustulka, K. M.; Wohl, A. R.; Lee, H. S.; Michel, A. R.; Han, J.; Hoye, T. R.; McCormick, A. V.; Panyam, J.; Macosko, C. W. Flash nanoprecipitation: Particle structure and stability. *Mol. Pharmaceutics* **2013,** *10* (11), 4367-4377.

3. Stewart, B. W.; Wild, C. P. *World cancer report 2014*; World Health Organization Press: Geneva, 2014. p 630.

4. Gref, R.; Minamitake, Y.; Peracchia, M.; Trubetskoy, V.; Torchilin, V.; Langer, R. Biodegradable long-circulating polymeric nanospheres. *Science* **1994,** *263* (5153), 1600-1603.

5. Langer, R. Drug delivery and targeting. *Nature* **1998,** *392* (6679), 5-10.

6. Kataoka, K.; Harada, A.; Nagasaki, Y. Block copolymer micelles for drug delivery: design, characterization and biological significance. *Adv. Drug Deliv. Rev.* **2001,** *47* (1), 113-131.

7. Allen, T. M.; Cullis, P. R. Drug delivery systems: Entering the mainstream. *Science* **2004,** *303* (5665), 1818-1822.

8. Peer, D.; Karp, J. M.; Hong, S.; Farokhzad, O. C.; Margalit, R.; Langer, R. Nanocarriers as an emerging platform for cancer therapy. *Nat. Nano.* **2007,** *2* (12), 751-760.

9. Zhang, L.; Gu, F. X.; Chan, J. M.; Wang, A. Z.; Langer, R. S.; Farokhzad, O. C. Nanoparticles in medicine: Therapeutic applications and developments. *Clin. Pharmacol. Ther.* **2008,** *83* (5), 761-769.

10. Ferrari, M. Cancer nanotechnology: Opportunities and challenges. *Nat. Rev. Cancer* **2005,** *5* (3), 161-171.

11. Langer, R. New methods of drug delivery. *Science* **1990,** *249* (4976), 1527-1533.

12. Torchilin, V. P. Recent advances with liposomes as pharmaceutical carriers. *Nat. Rev. Drug Discov.* **2005,** *4* (2), 145-160.

13. Duncan, R. Polymer conjugates as anticancer nanomedicines. *Nat. Rev. Cancer* **2006,** *6* (9), 688-701.

14. Chan, J. M.; Zhang, L.; Yuet, K. P.; Liao, G.; Rhee, J.-W.; Langer, R.; Farokhzad, O. C. PLGA–lecithin–PEG core–shell nanoparticles for controlled drug delivery. *Biomaterials* **2009,** *30* (8), 1627-1634.

15. Hu, C.-M. J.; Zhang, L.; Aryal, S.; Cheung, C.; Fang, R. H.; Zhang, L. Erythrocyte membrane-camouflaged polymeric nanoparticles as a biomimetic delivery platform. *Proc. Natl. Acad. Sci.* **2011,** *108* (27), 10980-10985.

16. Wani, M. C.; Taylor, H. L.; Wall, M. E.; Coggon, P.; McPhail, A. T. Plant antitumor agents. VI. Isolation and structure of taxol, a novel antileukemic and antitumor agent from Taxus brevifolia. *J. Am. Chem. Soc.* **1971,** *93* (9), 2325-2327.

17. Weiss, R. B.; Donehower, R. C.; Wiernik, P. H.; Ohnuma, T.; Gralla, R. J.; Trump, D. L.; Baker, J. R.; Van Echo, D. A.; Von Hoff, D. D.; Leyland-Jones, B. Hypersensitivity reactions from taxol. *J. Clin. Oncol.* **1990,** *8* (7), 1263-1268.

18. Maeda, H.; Wu, J.; Sawa, T.; Matsumura, Y.; Hori, K. Tumor vascular permeability and the EPR effect in macromolecular therapeutics: a review. *J. Control. Release* **2000,** *65* (1–2), 271-284.

19. Bisht, S.; Maitra, A. Dextran–doxorubicin/chitosan nanoparticles for solid tumor therapy. *Wiley Interdiscip. Rev. Nanomed. Nanobiotechnol.:* **2009,** *1* (4), 415-425.

20. Johnson, B. K.; Prud'homme, R. K. Flash nanoprecipitation of organic actives and block copolymers using a confined impinging jets mixer. *Aust. J. Chem.* **2003,** *56* (10), 1021-1024.

21. Johnson, B. K.; Prud'homme, R. K. Chemical processing and micromixing in confined impinging jets. *AIChE Journal* **2003,** *49* (9), 2264-2282.

22. Gindy, M. E.; Panagiotopoulos, A. Z.; Prud'homme, R. K. Composite block copolymer stabilized nanoparticles: Simultaneous encapsulation of organic actives and inorganic nanostructures. *Langmuir* **2008,** *24* (1), 83-90.

23. Han, J.; Zhu, Z.; Qian, H.; Wohl, A. R.; Beaman, C. J.; Hoye, T. R.; Macosko, C. W. A simple confined impingement jets mixer for flash nanoprecipitation. *J. Pharm. Sci.* **2012,** *101* (10), 4018-4023.

24. Wohl, A. R.; Michel, A. R.; Kalscheuer, S.; Macosko, C. W.; Panyam, J.; Hoye, T. R. Silicate esters of paclitaxel and docetaxel: Synthesis, hydrophobicity, hydrolytic stability, cytotoxicity, and prodrug potential. *J. Med. Chem.* **2014,** *57* (6), 2368-2379.

25. Qian, H.; Wohl, A. R.; Crow, J. T.; Macosko, C. W.; Hoye, T. R. A Strategy for control of "Random" copolymerization of lactide and glycolide: Application to synthesis of PEG-*b*-PLGA block polymers having narrow dispersity. *Macromolecules* **2011,** *44* (18), 7132-7140.

26. Oh, K. S.; Song, J. Y.; Cho, S. H.; Lee, B. S.; Kim, S. Y.; Kim, K.; Jeon, H.; Kwon, I. C.; Yuk, S. H. Paclitaxel-loaded pluronic nanoparticles formed by a temperature-induced phase transition for cancer therapy. *J. Control. Release* **2010,** *148* (3), 344-350.

27. Margulis, K.; Magdassi, S.; Lee, H. S.; Macosko, C. W. Formation of curcumin nanoparticles by flash nanoprecipitation from emulsions. *J. Colloid Interface Sci.* **2014,** *434*, 65-70.

28. Aggarwal, B. B.; Harikumar, K. B. Potential therapeutic effects of curcumin, the anti-inflammatory agent, against neurodegenerative, cardiovascular, pulmonary, metabolic, autoimmune and neoplastic diseases. *Int. J. Biochem. Cell Biol.* **2009,** *41* (1), 40-59.

Chapter 4.
Cryogenic Electron Microscopy study of Nanoemulsion Formation from Microemulsions[*,†]

4.1 Overview

We examine a process of preparing oil-in-water nanoemulsions by quenching (diluting and cooling) precursor microemulsions made with nonionic surfactants and a cosurfactant. The precursor microemulsion structure is varied by changing the concentration of the cosurfactant. Water-continuous microemulsions produce initial nanoemulsion structures that are small and simple, mostly unilamellar vesicles, but microemulsions that are not water-continuous produce initial nanoemulsion structures that are larger and multi-lamellar. Examination of these structures by cryo-electron microscopy supports the hypothesis that they are initially vesicular structures formed via lamellar intermediate structures, and they fail to produce small simple structures, if the lamellar structures are too well ordered.

4.2 Introduction

Finely dispersed oil-in-water emulsions have drawn considerable interest for use in personal care products, food products, and pharmaceuticals.[1, 2, 3, 4, 5, 6, 7, 8, 9] The term

[*] This chapter is reproduced with Han Seung Lee, Eric D. Morrison, Chris D. Frethem, Joseph A. Zasadzinski, and Alon V. McCormick, "Cryogenic electron microscopy study of nanoemulsion formation from microemulsions", *Langmuir* **2014**, 30 (36), 10826 (DOI: 10.1021/la502207f). Copyright 2014 American Chemical Society.

[†] Portions of this chapter is reproduced with permission from Han Seung Lee, Eric D. Morrison, and Alon V. McCormick, "Cryo-Electron Microscopy: Attempts to watch the formation of dilute emulsion via microemulsion", *Microscopy and Microanalysis* **2013** 19 (S2), 260 (DOI: 10.1017/S1431927613003292). Copyright 2013 Cambridge University Press.

nanoemulsion[10] is usually used to imply that the oil droplets are in the range of 20–500 nm[11] and kinetically stable in a low viscosity aqueous dispersion.

To prepare nanoemulsions mechanically it is necessary to provide a great deal of power, overcoming increasing Laplace pressure to create droplets small enough to achieve kinetic stability.[12, 13, 14] Alternatively, there is increasing interest in low-energy chemical methods that create nanodroplets using paths in the phase diagram that induce high interfacial curvature.[15] When the path is created by temperature change, these methods are usually termed phase inversion temperature methods,;[16, 17, 18] when the path is created by a composition change, they are variously termed spontaneous emulsification,[8, 11, 19, 20] phase inversion concentration,[11, 21, 22] emulsion inversion point,[23, 24, 25] catastrophic phase inversion,[26] or self-emulsification methods.[8, 27] Wadle et al. showed with such methods that the structure of the precursor emulsion can affect the stability of nanoemulsion,[28] and Kühnle and coworkers suggested that the smallest nanodroplets may form if the composition path traverses regions of lamellar or microemulsion-like structures.[23] Solans and coworkers[16] and Dong and coworkers[29] noted the merit of simply beginning with a deliberately prepared, stable microemulsion as precursor, then diluting that microemulsion to make a kinetically-stable nanoemulsion. Pons et al.[30] showed that, with such an approach, larger amounts of water in the microemulsion can result in smaller nanoemulsion structures.

A modification of this last approach is what we undertake in this work; we examine the preparation of nanoemulsions by quenching microemulsion precursors, adding cooled water to warm microemulsions both to quickly dilute and to cool to room temperature. The microemulsions are made with *n*-hexadecane, water, and nonionic alkylphenolethoxylate surfactants.[31] Varying amounts of alkylphenol cosurfactant were used to afford the opportunity to examine the use of differently structured precursor microemulsions (cf. Salager and coworkers[32, 33]).

Like previous works,[22, 34, 35, 36, 37] in this paper conductivity and visual transparency are used to detect the microemulsion temperatures, and light scattering is used to determine the average size of the structures in the quenched nanoemulsion (well before any ripening or separation). We also directly image the structures with cryo-electron microscopy (cryo-

EM), seeking to rationalize their structure and formation mechanism. Previously Saupe and coworkers[38] showed the usefulness of cryogenic scanning electron microscopy (cryo-SEM) to investigate the effect of compositional variables in a nanoemulsion preparation, and Heunemann et al.[39] used cryogenic transmission electron microscopy (cryo-TEM) images to support a hypothesis of a bicontinuous intermediate structure.

In this work, we show that using enough cosurfactant to produce water-continuous or bicontinuous microemulsions favors the creation of nanoemulsions with small, simple initial structure (lending kinetic stability). The microemulsions that are not water-continuous lead to large, complex structures in the quenching process (degrading kinetic stability). Cryo-EM helps to reveal reasons that these lamellar structures develop from and depend on the precursor microemulsion structure.

4.3 Experimental Methods

Materials

The nonionic surfactants isononylphenol-4-ethoxylate and isononylphenol-20-ethoxylate (commercial names Marlophen NPE-4 and NPE-20) were obtained from Sasol GmbH (Marl, Germany) and were used as received. Both products were found to be essentially free from unethoxylated isononylphenol using gas chromatography-mass spectrometry (detection limit approximately 1000 ppm).

The cosurfactant isononylphenol (commercial name NP, the same isononylphenol feedstock that is ethoxylated to produce both NPE-4 and NPE-20) was also obtained from Sasol GmbH (Marl, Germany) and used as received. The structures of these molecules are shown in Figure 4.1. For each of these materials, only one lot number of material was used.

The oil *n*-hexadecane (Reagentplus, 99%) was purchased from Sigma-Aldrich Co. (Milwaukee, WI) and used as received. Distilled water (Premium Water Inc., Chippewa Falls, WI, conductivity<1.8 μS/cm) was also used.

Alkylphenol ethoxylates were of interest because these surfactants are widely used in industry;[31] the particular surfactants used were chosen because microemulsions could be

easily prepared at a convenient temperature, and the structure of the microemulsion could be controlled simply by adjusting the concentration of a cosurfactant that is simply the corresponding unethoxylated alkylphenol. *n*-hexadecane was chosen as the oil phase so that it could be conveniently heated safely (i.e., relatively high autoignition temperature) while maintaining low room-temperature viscosity.

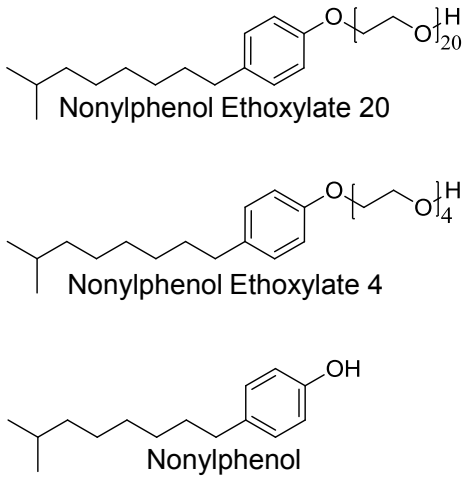

Figure 4.1. Molecular structure of the two nonionic alkylphenolethoxylate surfactants and the alkylphenol cosurfactant used.

Conductivity

Phase behavior was monitored with conductivity measurements using a portable conductivity meter (Orion 3-Star Plus, Thermo Electron Corp., MA) with an epoxy/graphite electrode (cell constant 0.475 cm^{-1} at 25 °C). The conductivity and temperature of the sample was measured every 10 seconds while stirring in a sealed vessel, as it was gradually cooled from about 90 °C (about 1.3 °C/min).

Dynamic light scattering (DLS)

The apparent droplet size was measured by dynamic light scattering (DLS), diluting the sample immediately (<10 minutes) before measurement with surfactant-free de-ionized water. Ordinarily a 5 μL volume of sample was diluted to 3 ml total volume; a series of further dilutions was also performed to check that this did not affect the scattering results. Distilled water was used for the reference viscosity and refractive index. A particle size

analyzer (ZetaPALS 90Plus/BI-MAS, Brookhaven Instruments Corporation, NY) with 670 nm wavelength light was used at 22 °C with a 90° scattering angle. The size distribution, derived from the autocorrelation function, was obtained using the vendor-provided software.

In dynamic light scattering, the Brownian motion of diffusing particles cause intensity fluctuations that are recorded in a correlator (or comparator). The intensity autocorrelation function, $g_2(q,\tau)$ describes the experimentally measured random fluctuation from time *t* to a later time $t+\tau$.[40]

The electric field correlation function, $g_1(q,\tau)$ correlates the motion of the particles relative to each other. The Siegert relationship relates these two autocorrelation functions.

$$g_2(q,\tau) = B[1 + \beta\{g_1(q,\tau)\}^2] \tag{4.1}$$

where q is the scattering vector, B is the baseline constant, and β is an instrumental constant.

The cumulant method[41] is used to analyze $g_1(q,\tau)$ when one assumes a unimodal (typically Gaussian) distribution):

$$g_1(q,\tau) = \exp(-\bar{\Gamma}\tau)(1 + \tfrac{1}{2!}\mu_2\tau^2 + \cdots) \tag{4.2}$$

where $\bar{\Gamma}$ is the average decay rate, μ_2 is the second momentum, and $\mu_2/\bar{\Gamma}^2$ characterizes the width of the decay (used to calculate polydispersity).

The hydrodynamic diameter is estimated with Stokes-Einstein equation (here shown for radius).[42]

$$R_h = \frac{k_B T}{6\pi\eta D} \tag{4.3}$$

where k_B is Boltzmann's constant, T is the temperature (K), η is the viscosity of the liquid, and D is the diffusion coefficient. The relationship between diffusion coefficient and the average decay rate:[41]

$$\bar{\Gamma} = Dq^2 \tag{4.4}$$

For distribution that were not unimodal, the Laplace inversion routine REPES was also used to find the particle size distribution.[43]

Cryogenic-scanning electron microscopy (Cryo-SEM)

A small amount (~1 μL) of the sample was applied to a brass planchet (Type A, Ted Pella Inc., Redding, CA) designed for use with a high-pressure-freezer. The planchet has a diameter of 2 mm (cylindrical cavity) and a well depth of 200 μm. The floor of well is scored with a nail to increase adhesion of the sample when frozen. Then, the sample was covered with another planchet with a 100 μm deep well to make a sandwich. The entire assembly, including the holder, was pre-equilibrated at the desired specimen temperature.

The sandwich assembly and holder were loaded into a Bal-Tec HPM 010 high-pressure freezing machine (Bal-Tec AG, Balzers, Liechtenstein), which can cool the specimen to -182 °C with liquid nitrogen jets within 5–8 milliseconds at 2100 bar. The high pressure was maintained for 0.5 seconds, and the cold temperature (-182 °C) was maintained for at least 5 seconds thereafter. During this period the sample was transferred to a liquid nitrogen bath.

The cooled planchet sandwich was cleaved with a pre-cooled scalpel in the liquid nitrogen bath. One of the planchets, with frozen fractured specimen, was mounted in a Gatan 626 DH cryo-transfer specimen holder modified for Hitachi S-900 In-Lens SEM (Gatan, Pleasanton, CA). The cryo-transfer holder was transferred to Balzers MED 010 sputter coater (Bal-Tec AG, Balzers, Liechtenstein) equipped with a Meissner condensation trap, and the specimen could be sublimed at -96 °C and 3 x 10^{-4} Pa for up to 3 minutes to increase topographic imaging contrast. After sublimation, the sample was coated with 10 nm of platinum by sputter-deposition at -130 °C. The thickness of the Pt coating was monitored with a QSZ 301 quartz crystal thickness monitor (Bal-Tec AG, Balzers, Liechtenstein).

Finally, the Pt-coated sample was transferred via an airlock to a Hitachi S-900 scanning electron microscope with an in-lens stage and cold field emission gun. The sample was imaged at -174 °C with 2 kV accelerating voltage. Figure 4.2 shows a schematic illustrations of cryo-SEM specimen preparation method.

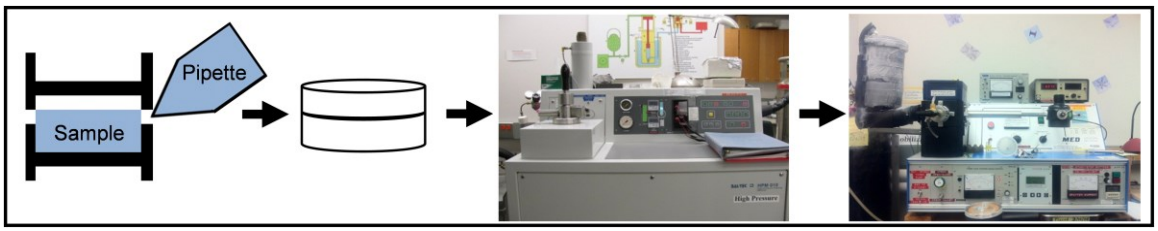

Figure 4.2. Schematic illustrations of cryogenic scanning electron microscopy specimen preparation method.

Cryogenic-transmission electron microscopy (Cryo-TEM)

A small amount (~3 μL) of the sample was placed on a copper TEM grid covered by a lacey carbon film (200–300 mesh, Ted Pella, Ltd., Redding, CA). Beforehand, the grid had been cleaned by plasma glow discharge for 1 minute in a DV-502A vacuum system (Denton Vacuum, Moorestown, NJ) at 60–70 millitorr. The cryo-TEM specimen was prepared with a Mark III Vitrobot (FEI Company, Hillsboro, OR) at 22 °C and relative humidity of 95–100% to avoid loss of water. The grid was blotted to remove excess sample to produce a thin film (<300 nm) of the solution.[44] The grid was plunged into liquid ethane (cooled by liquid nitrogen) to vitrify the sample. The sample was transferred to a Gatan 626 cryo-transfer unit (Gatan, Pleasanton, CA) and imaged at -178 °C in low-dose mode. TEM imaging was performed on a FEI Tecnai^{TM} Spirit BioTWIN at 120 kV with the Eagle 2048 x 2048 CCD camera (FEI Company, Hillsboro, OR) and using the TEM Imaging and Analysis 4.2 software (FEI Company, Hillsboro, OR). Additional TEM imaging was carried out with a FEI Tecnai^{TM} G^2 F30 S-TWIN at 300 kV with the Gatan UltraScan 4000 4096 x 4096 CCD camera (Gatan, Pleasanton, CA) and using Gatan Digital Micrograph 3.11.1 software (Gatan, Pleasanton, CA). Under-focus was used (3–6 μm) to improve the phase contrast, and the measured average electron dose was <10 $e^-/Å^2$. Figure 4.3 shows a schematic illustrations of cryo-TEM specimen preparation method.

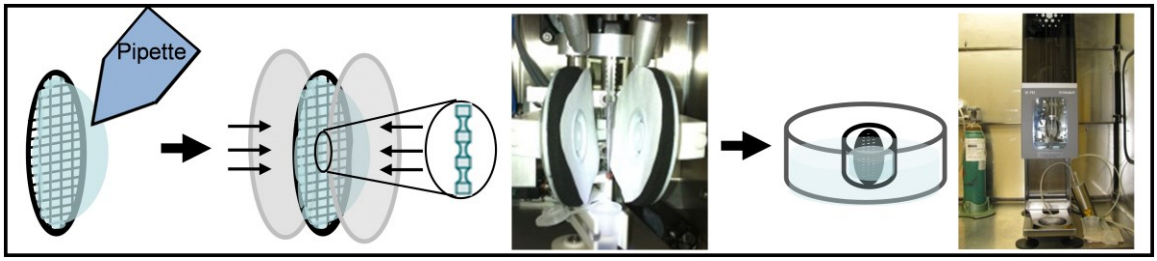

Figure 4.3. Schematic illustrations of Cryogenic transmission electron microscopy specimen preparation method.

Freeze-fracture transmission electron microscopy (FF-TEM)

A small amount (~1.5 µL) of the sample was deposited on the flat copper specimen carrier (LZ 02131 VN, Bal-Tec AG, Balzers, Liechtenstein). Then, another specimen carrier was placed onto the sample, and the edges of the specimen carrier were blotted with filter paper. The specimen carriers were then manually plunged into propane/ethane mixture. The assembly was fractured in the RFD-9010 (RMC products, Boeckeler Instruments, Inc., Tucson, AZ) and the surfaces were replicated with platinum/carbon and carbon. The replicas were collected on lacey Carbon/Formvar stabilized 200 mesh TEM grids (Electron Microscopy Sciences, Hatfield, PA), and TEM imaging was performed on a FEI TecnaiTM Spirit BioTWIN at 120 kV. This methodology is described in detail by Zasadzinski and Bailey.[45] Figure 4.4 shows a schematic illustrations of FF-TEM specimen preparation method.

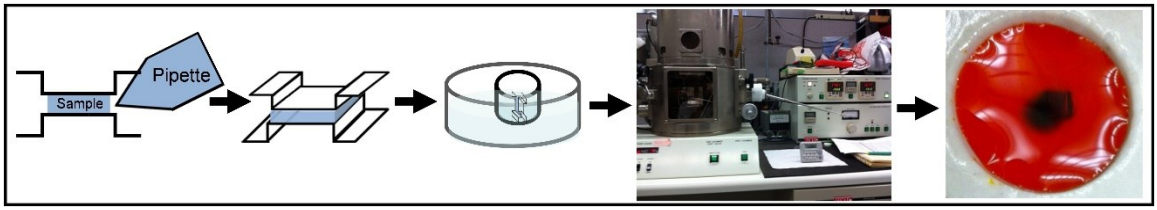

Figure 4.4. Schematic illustrations of freeze-fracture electron microscopy specimen preparation method.

Preparing and characterizing the microemulsions using conductivity

Mixtures of 8.7 g of NPE-4, 11.3 g of NPE-20, 40.0 g of *n*-hexadecane and variable amounts of cosurfactant NP (0–4.0 g) were warmed to about 40 °C. Then 40.0 g of distilled

water was added with stirring, and the samples were then heated to 85–90 °C to make a cloudy emulsion. The sample was allowed to cool with constant stirring (about 1.3 °C/min). The temperature range was recorded where the sample became transparent (microemulsion temperature, typically 60–70 °C, vide infra). When the sample was transparent, stirring could be stopped and the sample remained stable indefinitely if the temperature was maintained. Conductivity was also measured as the sample was cooled from 90 °C to as low as 45 °C (below which viscosity typically grew too high to easily ensure mixing). Within this temperature range and with gentle stirring, the conductivity and transparency patterns were reversible and reproducible.

Quenching microemulsions to make nanoemulsions

To prepare a nanoemulsion, the prepared microemulsion was rapidly poured into about 320 g of ~20 °C distilled water with gentle stirring to give nanoemulsions with 85 wt % water at 25 °C; the process is shown schematically in Figure 4.5. The resulting nanoemulsion was stable for various periods of time, depending on how much cosurfactant was used (vide infra).

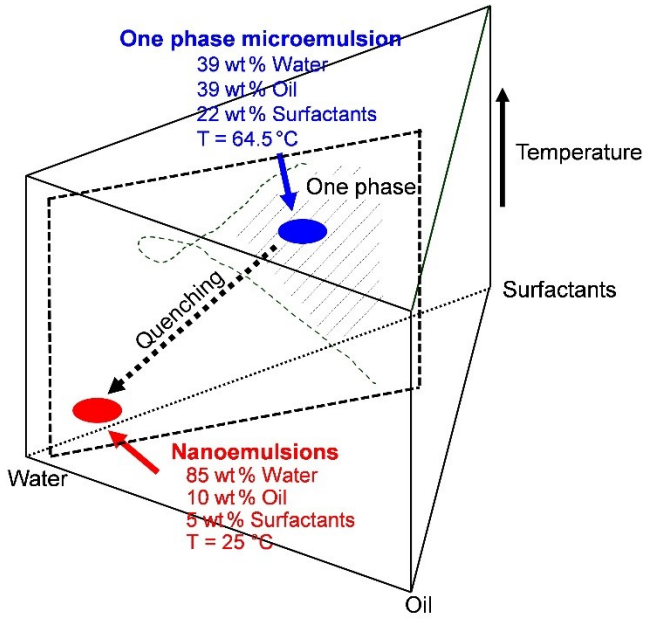

Figure 4.5. Schematic path on the phase diagram showing nanoemulsion preparation by quenching from a precursor microemulsion by adding precooled water.

4.4 Results and Discussion

A. Microemulsion temperature and conductivity patterns

The nanoemulsion preparation method we are investigating involves preparing a microemulsion as the first step. One way to characterize the microemulsion is to monitor conductivity and transparency through a temperature scan[16, 34, 46] as shown in Figure 4.6, as the stirred emulsions are slowly cooled from a high temperature. Cosurfactant concentrations are expressed as parts per hundred (pph) by mass of the sample used to prepare the precursor microemulsion.

At the initial temperature (85–90 °C) the cloudy emulsions are plainly water-in-oil (W/O) with a low conductivity for all cosurfactant concentrations. As the emulsions are cooled with stirring, conductivity starts to rise at about 87 °C.

With enough cosurfactant (greater than 2.0 pph cosurfactant, Figure 4.7 shows conductivity plots as a function of temperature with below 2.2 pph cosurfactant), the emulsion becomes transparent, suggesting a microemulsion. When the sample is transparent, if stirring is ceased and the temperature is maintained, no separation occurs. Moreover, the conductivity curve is reproducible as the temperature is increased or decreased (with gentle stirring). These observations lend further confidence that stable microemulsion regions have been found at the specific temperature.

The sample with 2.2 pph cosurfactant shows the highest conductivity in the transparent microemulsion region. The high conductivity can be attributed to a water-continuous microemulsion structure. With 2.4 pph cosurfactant, the conductivity starts high, but it drops dramatically as the sample is cooled through the transparent microemulsion region; this has been suggested to correspond to the behavior of a bicontinuous microemulsion.[46] With further cooling this sample changes abruptly from transparent to translucent and pearlescent, suggesting that the poorly conducting structure has become lamellar.

With higher cosurfactant concentration (3.1 or 4.0 pph), the conductivity is low in the transparent microemulsion region. The low conductivity suggests the microemulsion structure is not water-continuous, but rather is either lamellar or oil-continuous (W/O).

These results strongly suggest that increasing the cosurfactant amount affects the structure of the microemulsion, tending to convert from structures that are water-continuous to structures that are bicontinuous or oil-continuous. Table 4.1 shows microemulsion temperature range as a function of added cosurfactant.

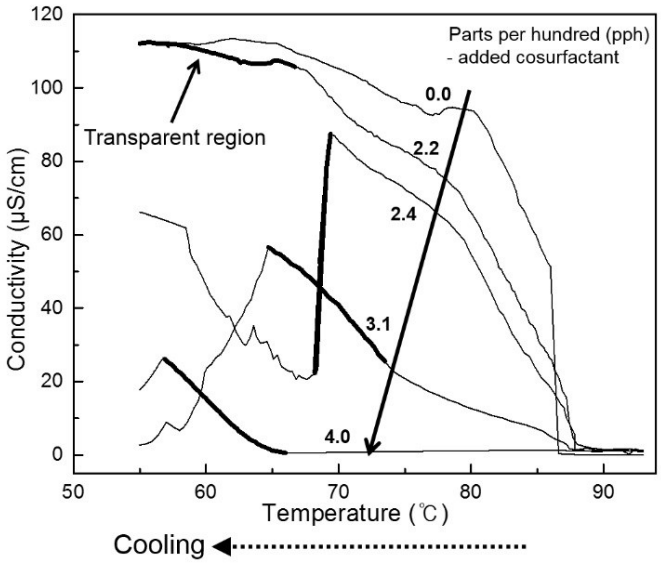

Figure 4.6. Temperature scans of conductivity and transparency (shown with bold segments) for the emulsions studied, using varying amounts of cosurfactant. Numbers indicate parts per hundred of cosurfactant.

Table 4.1. The microemulsion temperature range as a function of added cosurfactant.

Cosurfactant concentration (pph)	Microemulsion temperature (°C)
2.2	49.1 – 66.7
2.4	68.2 – 70.1
3.1	64.7 – 73.5
4.0	56.9 – 66.0

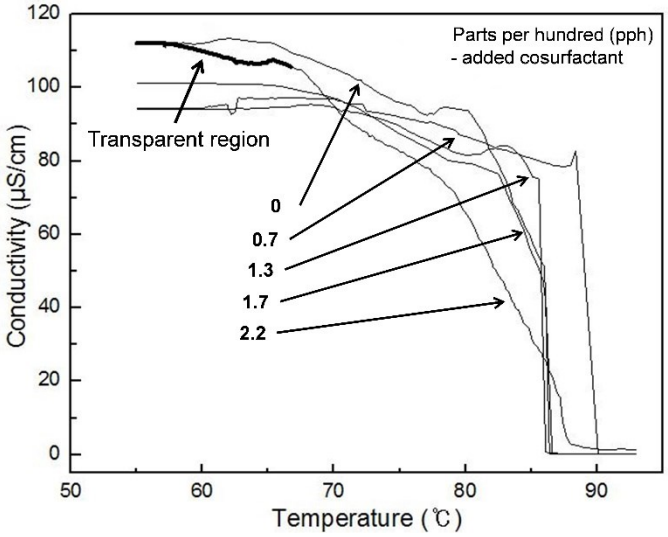

Figure 4.7. Temperature dependence of conductivity for the emulsions studied using varying amounts of cosurfactant. Bold segments represent transparent microemulsion regions. Each number on the curve is parts per hundred of cosurfactant (basis: total sample mass). Conductivity and temperature were measured at 10 second intervals while the temperature slowly decreased at a rate of about 1.3 °C/min.

B. Characterizing Initial Nanoemulsion Structures

DLS

Nanoemulsions were prepared by quenching microemulsions, adding pre-cooled water to bring the water concentration to 85 wt % and the temperature to about 25 °C. Freshly prepared nanoemulsions were characterized with dynamic light scattering; the apparent diameter of structures formed is shown in Table 4.2. Figure 4.8 illustrates bimodal plots of 3.1 pph and 4.0 pph cosurfactant. These results suggest a relationship between the structure of the precursor microemulsions and the size and structure of the quenched nanoemulsion structures. The smallest structures are made using a cosurfactant concentration that is the minimum needed to establish a microemulsion (about 2 pph cosurfactant). These nanoemulsions remain stable, with no cream separation, for over a month. Using more cosurfactant (3.1 or 4 pph) gives nanoemulsions with some kinetic stability, but with larger structures varying in size from 100 nm to almost micrometer diameter. These size of the structures in these nanoemulsions grow significantly over the course of days, separating macroscopically to make an oil (cream) layer in a manner similar to that described by Delmas et al.[47] Representative aging results are shown in Figure 4.9.

Table 4.2. Hydrodynamic diameter and polydispersity of nanoemulsion structures prepared by quenching microemulsions with cosurfactant concentrations indicated. Higher cosurfactant concentration (3.1 parts per hundred (pph) and 4.0 pph) gave bimodal distributions; in these cases, we list the intensity fraction corresponding to the two sizes. Parameters and bimodal distributions are further described more in Supporting Information. For comparison, a sample that was quenched from stirred, cloudy emulsion using no cosurfactant gave diameter >500 nm.

The amount of added nonylphenol cosurfactant (pph, parts per hundred cosurfactant)	Hydrodynamic diameter at the peak (nm)	Polydispersity
2.2	85.7	0.036
2.4	70.5	0.075
3.1	65.1 (9%), 238 (91%)	Bimodal
4.0	111 (12.5%), 455 (87.5%)	Bimodal

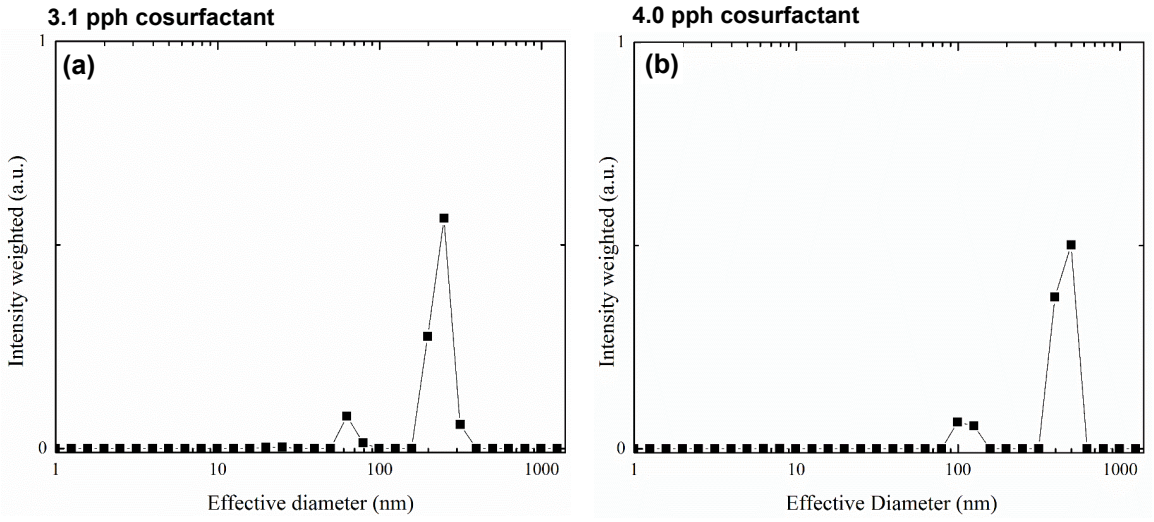

Figure 4.8. Effective diameter distribution of (a) 3.1 parts per hundred (pph) and (b) 4.0 pph cosurfactant.

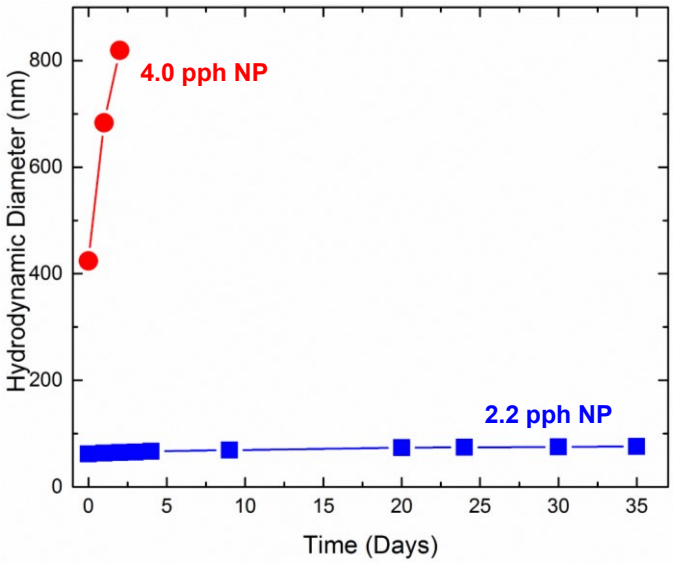

Figure 4.9. Representative scattering data showing destabilization of nanoemulsions quenched from microemulsions with 2.2 parts per hundred (pph) and 4.0 pph cosurfactant.

Cryo-EM

Selected freshly-made nanoemulsions were also characterized by cryo-EM. Cryo-SEM[38] and cryo-TEM[39] offer complementary methods. Cryo-SEM permits us to view large structures, avoiding the size segregation and shearing associated with the film-thinning needed for cryo-TEM specimens. Also, SEM using secondary electrons allows better observation of 3D morphologies revealed by the cryofracture.

Figure 4.10 shows the size of the nanoemulsion structures revealed by cryo-SEM of a cryo-fractured surface. Consistent with DLS analysis, cryo-SEM shows that using the optimal amount of cosurfactant (about 2 pph) produced simple small structures with uniform size distribution. Typical micrographs (Figure 4.10a and 4.10b) show only intact, small structures. However, using too much cosurfactant (4 pph) results in much larger structures with a much broader size distribution. Cryo-SEM shows that these are much more complex structures, and some structures are much larger than the average suggested by DLS. Typical micrographs show that the cryofracture has broken open some of the larger structures, revealing internal details; they are giant multi-lamellar structures, some with concentric lamellae (in Figure 4. 10c) and hierarchical 'peas-in-a-pod' structures

(Figure 4. 10d). Figure 4. 11 also shows additional cryo-SEM micrographs of fresh nanoemulsions.

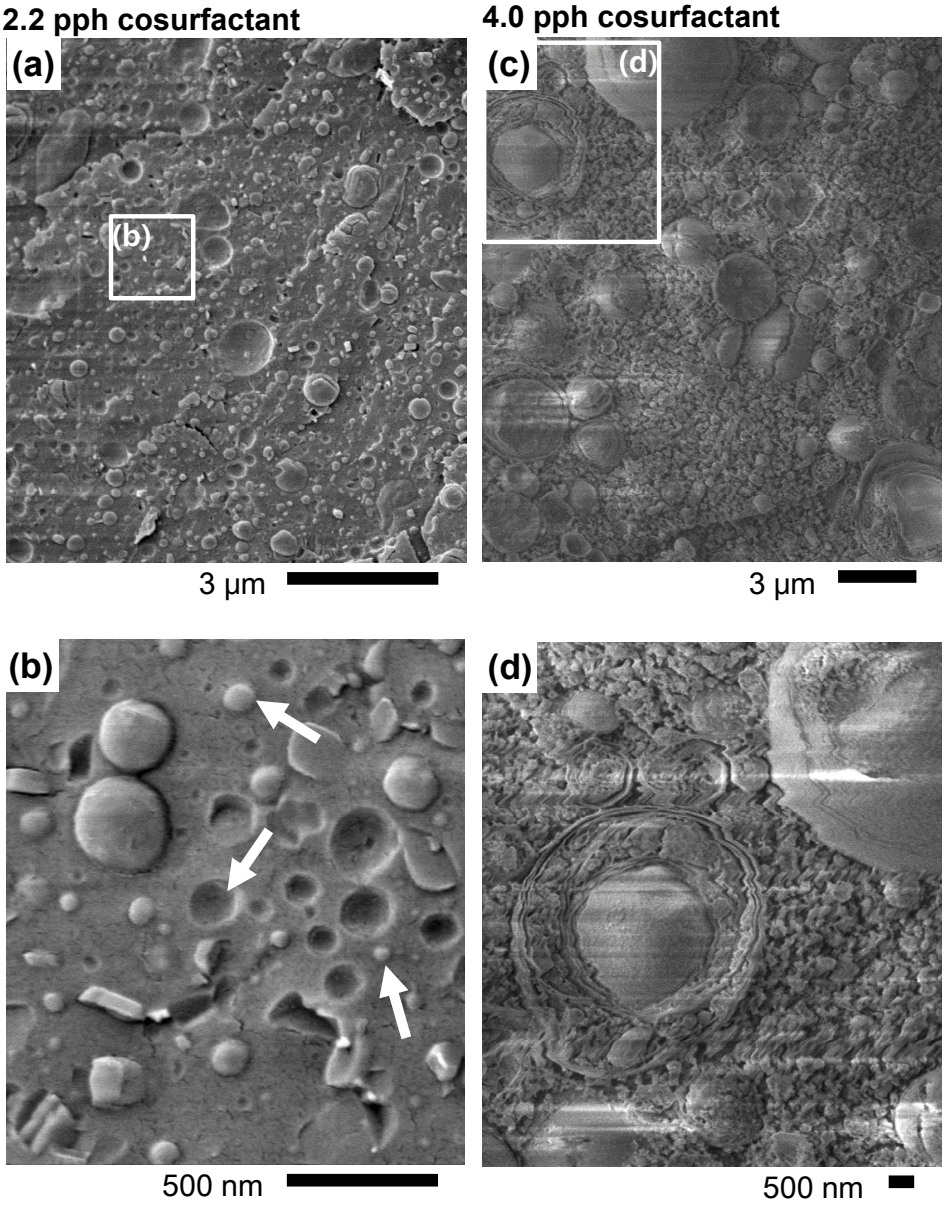

Figure 4.10. Representative cryo-SEM micrographs of fresh nanoemulsions. Using 2.2 parts per hundred (pph) cosurfactant (a, b) in the precursor microemulsion give many sub-100 nm simple structures. The fractured surface shows both unbroken structures and divots from structures plucked out (white arrows). Using 4.0 pph cosurfactant gives (c) evidence of very large multi-lamellar nanoemulsion structures and (d) multiply-nested compartments in structures of micrometer scale. The largest structures are typically broken open by the cryofracture, revealing internal structure. Charging artifacts (bright lateral smears) are typically observed. Images with 2.2 pph cosurfactant are similar to those with 2.4 pph cosurfactant. No sublimation was used in preparing the cryo-SEM specimens.

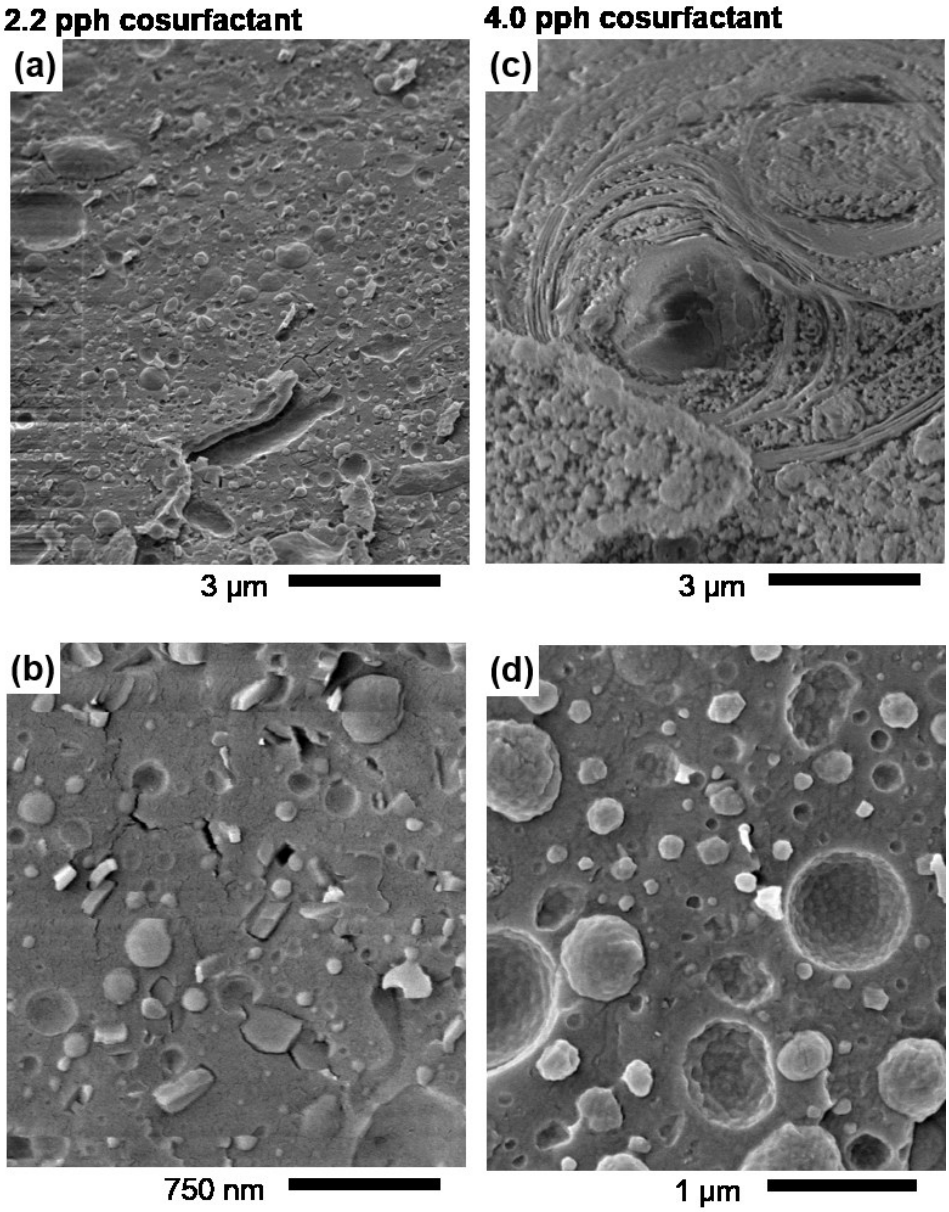

Figure 4.11. Representative cryo-SEM micrographs of fresh nanoemulsions quenched from microemulsions with (a, b) 2.2 parts per hundred (pph) and (c, d) 4.0 pph cosurfactant. Note that the 2.2 pph and 2.4 pph cosurfactant show similar size and distributions.

In contrast to cryo-SEM, cryo-TEM gathers images using transmitted (or diffracted) electrons from the sample, helping to reveal internal morphology; but the preparation to make the specimen thin enough by blotting excess sample off grid probably removes large structures, so we caution that these images reveal only the smallest structures. Moreover, the meniscus-shape of the thinned specimen film causes size segregation, so most of the surviving structures are typically observed at the edge of the film near struts, where the remaining film is the thickest. Finally, note that even these small structures can appear distorted if they are compressed by the film free surface.[48]

Typical cryo-TEM images of the small structures that survive the specimen preparation are shown in Figure 4.12. Even the smallest structures with minimal cosurfactant, when freshly prepared, are revealed to be small vesicles with oil inside swollen bilayers rather than simple oil droplets. Figure 4.12a shows little contrast difference between the background and the area inside the vesicle; this suggests the smallest structures are simple vesicles rather than multilamellar structures. Only a few of the larger structures seem multilayered, showing darker TEM contrast increased in the center due to mass-thickness contrast. The surfactant bilayers are about 5 nm thick (indicated with arrows).

With the 4.0 pph cosurfactant sample, though, even the smallest structures captured in the specimen commonly show multilamellar structures, with 'peas-in-the-pod' structures such as that shown in Figure 4.12b (white arrow). In addition, selective beam-radiation damage generates white bubbles in Figure 4.12b (white arrowhead). We speculate that these beam-damaged structures are small oil droplets.

In summary, cryo-TEM supports the indication from cryo-SEM that the optimal cosurfactant concentration allows the formation of smaller and simpler structures in the quenched nanoemulsion. Figure 4. 13 also shows additional cryo-TEM micrographs of fresh nanoemulsions.

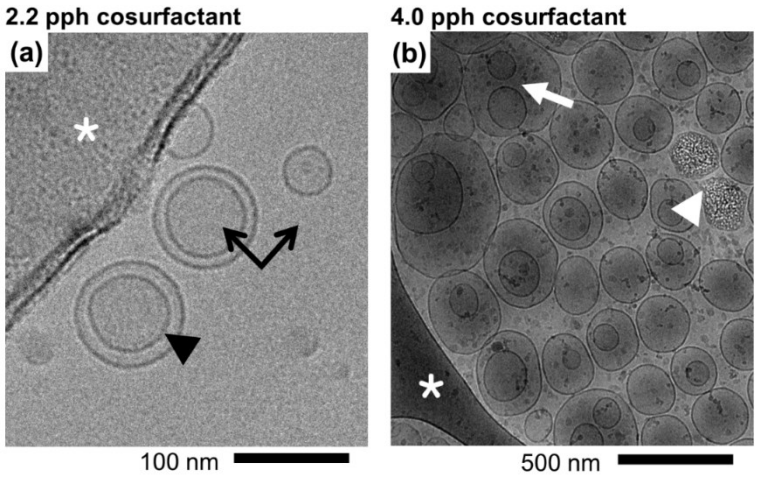

Figure 4.12. Representative cryo-TEM micrographs of nanoemulsions; structures observed are comparable to the smaller structures seen in corresponding cryo-SEM micrographs in Figure 4.10 and 4.11. (a) Nanoemulsion from 2.2 parts per hundred (pph) cosurfactant microemulsion. The black arrowhead shows surfactant layers. Black arrows show contrast similarities inside the vesicles and the surrounding fluid, suggesting a simple vesicle structure. (b) Nanoemulsions from 4.0 pph cosurfactant microemulsion. The white arrow shows multi-compartment structures with darker contrast of interior vesicles, and the white arrowhead shows beam-damaged oil droplets. The asterisk marks show the lacey carbon struts of the cryo-TEM grid, where structures tend collect. The 2.2 pph cosurfactant images are similar to the 2.4 pph cosurfactant.

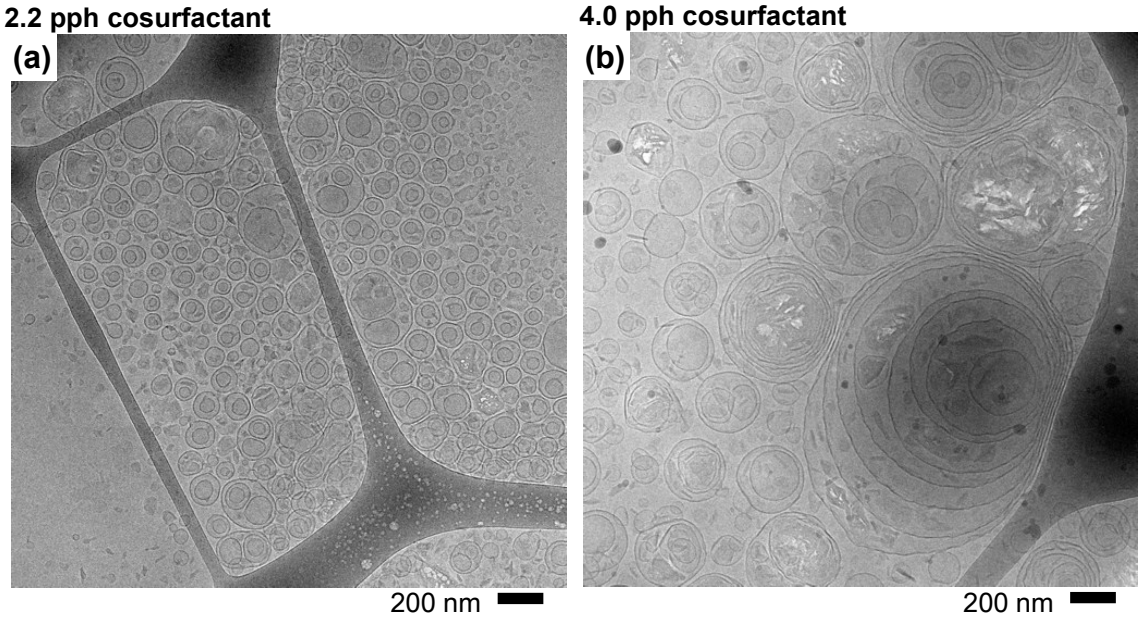

Figure 4.13. Representative cryo-TEM micrographs of fresh nanoemulsions quenched from microemulsions with (a) 2.4 parts per hundred (pph) and (b) 4.0 pph cosurfactant. Note that the 2.2 pph and 2.4 pph cosurfactant show similar size and distributions.

The fresh nanoemulsions are also characterized with FF-TEM to observe a fractured surface of the sample. Figure 4.14a shows 2.2 pph cosurfactant, displaying small-sized unilamellar vesicles. On the contrary, 4.0 pph cosurfactant in Figure 4.14b illustrates more complex decoration on the surface of Pt-C thin layer. Cosurfactant contributed to form a concentric or multi-layered structures in the sample, exhibiting divots, bumps, and cross-fractured traits.

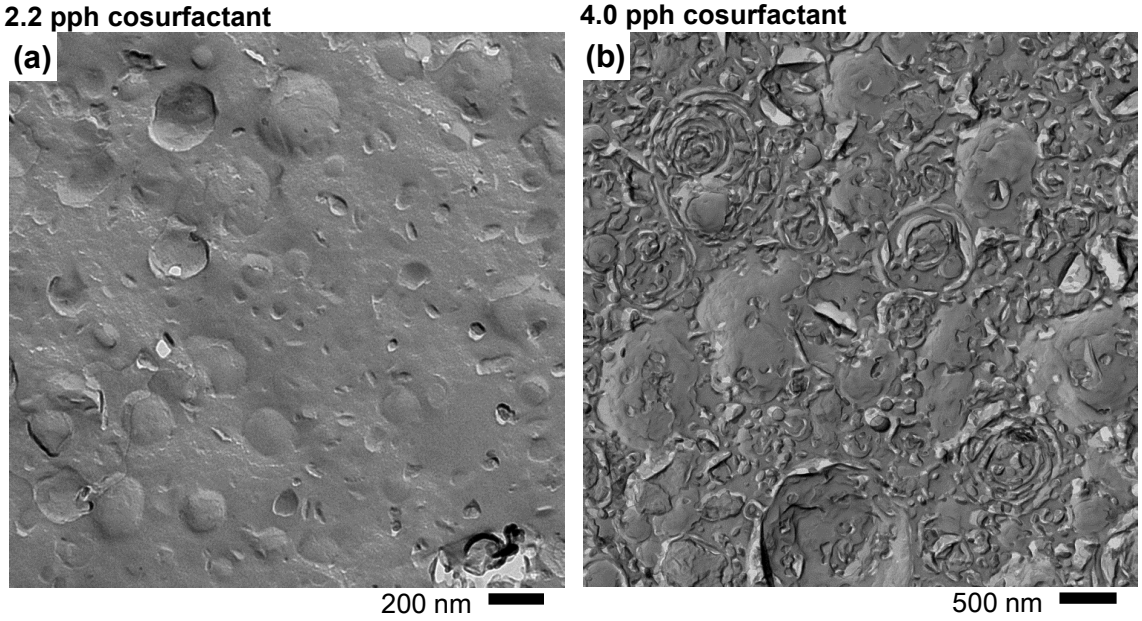

Figure 4.14. Representative FF-TEM micrographs of fresh nanoemulsions quenched from microemulsions with: (a) 2.2 parts per hundred (pph) and (b) 4.0 pph cosurfactant. Note that the 2.2 pph and 2.4 pph cosurfactant show similar size and distributions.

C. Characterizing Precursor Microemulsions and Possible Intermediates

Precursor microemulsions

The smallest structure nanoemulsions (with minimal cosurfactant) are associated with a precursor microemulsion structure that has high conductivity, suggesting a structure that is O/W or bicontinuous. The less stable, larger structure nanoemulsions result from precursor microemulsion structure that has low conductivity, suggesting a structure that is W/O or strongly lamellar. To better understand why these nanoemulsion structures might have formed, it is important to confirm the precursor microemulsion structures. Figure 4.15 shows representative cryo-SEM and FF-TEM images that supports the microemulsion structures suggested by the conductivity.

Figure 4.15a shows a typical cryo-SEM of the microemulsion with 2.2 pph cosurfactant; it displays ca. 50 nm diameter spherical oil domains in a continuous water domain, consistent with high conductivity. Figure 4.15c shows a typical cryo-SEM of the microemulsion with 4.0 pph cosurfactant. It confirms the suggestion that the low conductivity of this microemulsion arises from a lamellar structure, even though the sample was clear with no obvious pearlescence or anisotropy. While it is possible of course that our cryo-SEM does not capture the original structure perfectly, it is clear that this microemulsion is not aqueous-continuous.

Neither cryo-SEM nor cryo-TEM characterization were successful in imaging the structure of the microemulsion with 2.4 pph cosurfactant, where conductivity suggests a bicontinuous structure. Our attempts with cryo-TEM were fruitless because the sample was too viscous, and our attempts with cryo-SEM were unsuccessful because of excess charging; both may be characteristic of bicontinuous microemulsions. Better success with cryo-SEM might become possible with deceleration techniques and a charge compensation system, as recently demonstrated by Talmon and coworkers.[49] However, replica FF-TEM has been used successfully to image bicontinuous microemulsions; this is explained well by Burauer et al.[50] The replica TEM image in Figure 4.15b indeed shows two coexisting continuous phases in the structures that are similar to those shown by previous workers such for bicontinuous microemulsions.

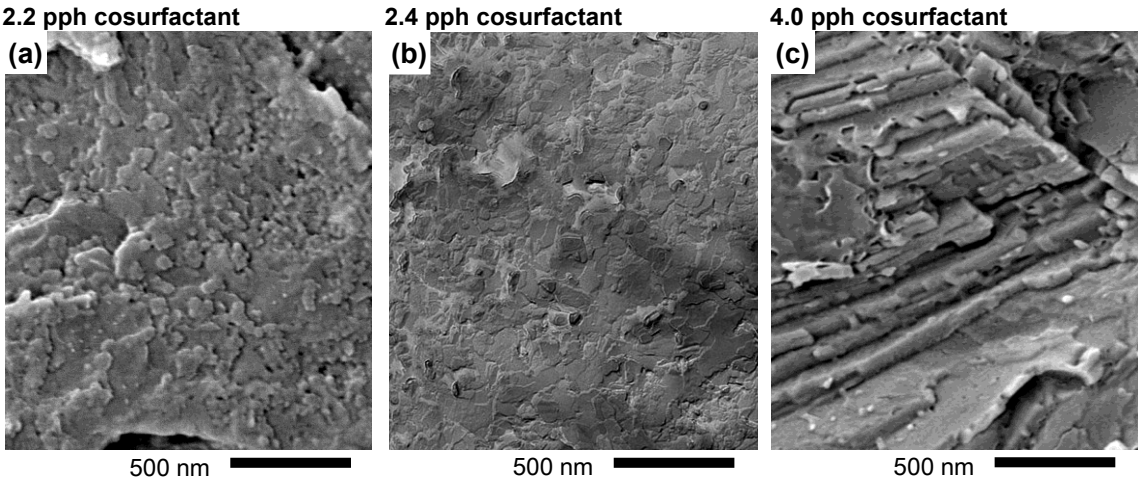

Figure 4.15. Representative (a, c) cryo-SEM micrographs and (b) FF-TEM of microemulsions used as precursors to nanoemulsions. (a) Oil-in-water microemulsion structure (high conductivity) with 2.2 parts per hundred (pph) cosurfactant at 64 °C. (b) Bicontinuous microemulsions with 2.4 pph cosurfactant at 69 °C. (c) Lamellar structure (low conductivity) in 4.0 pph cosurfactant at 64 °C. Cryo-SEM samples were sublimed for 3 minutes at -96 °C.

Possible intermediate structures

Kühnle and coworkers have suggested that nanoemulsions form through a lamellar intermediate, which permits the formation of droplets (or vesicles) by exfoliation from the lamellar surface.[23] To explore whether this seems reasonable, and to see whether too much cosurfactant seems to impede this process, the samples were quenched only to the midpoint on the phase emulsification path. Using only 40 g of the pre-cooled quenching water brought the system to 45–50 °C and 51 wt % water. Then these samples were quickly cryofixed within 10 seconds for imaging. The fractured intermediate structure was successfully imaged by cryo-SEM, and representative micrographs are shown in Figure 4.16.

The intermediate-quenched samples do seem to show the formation of the liquid lamellar structures, supporting Kühnle's suggestion.[23] When quenched from high-conductivity microemulsions with minimal cosurfactant, the thickness of plate-like assemblies of lamellae (Figure 4.16a and 4.16c) reaches only several hundred nanometers. The assembly (Figure 4.16a and 4.16c) seems to consist of many layers of thin sheets, each a few nanometers thick (comparable to the characteristic dimensions of nanoemulsions). These thin sheets seem to be exfoliating at the surface. White arrows (Figure 4.16b and 4.16d) indicate thin exfoliating sheets in the liquid lamellae that may produce the sub-100 nm structures. The formation of small and monodisperse nanoemulsions might be associated with the development of these exfoliating sheets in the intermediate phase.

We observe strikingly different features, though, as the cosurfactant is increased. With excess cosurfactant (Figure 4.16e and 4.16f), only rigid, thick, well-ordered ledges are apparent (Figure 4.16f, white arrow), and there is no suggestion of thin sheets exfoliating. The rigidity of the lamellar structure at 4.0 pph cosurfactant may help explain the generation of multi-lamellar, large structures. Figure 4. 17 and Figure 4.18 also show additional cryo-SEM and FF-TEM micrographs of possible intermediate structures.

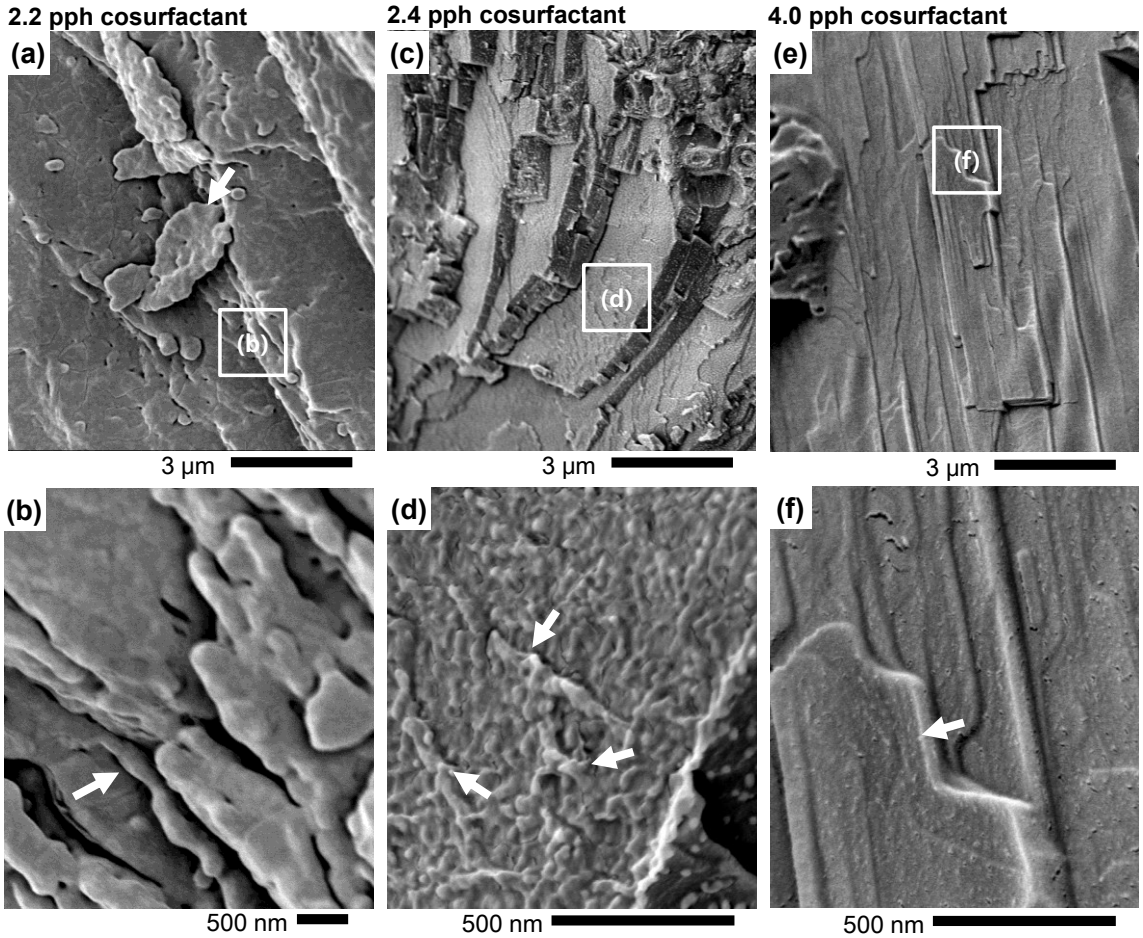

Figure 4.16. Representative cryo-SEM micrographs of intermediate quenched samples from microemulsions with the indicated cosurfactant concentration. With each cosurfactant concentration, lamellar structures are observed. Thin exfoliated flakes on the lamellar surface are observed with 2.2 parts per hundred (pph) cosurfactant (a, b) and with 2.4 pph cosurfactant (c, d), suggesting a possible mechanism of formation of very small vesicles in nanoemulsions. However, only unperturbed and smooth surfaces are observed with 4.0 pph cosurfactant (e, f). Cryo-SEM samples were sublimed for 3–6 minutes at -96 °C.

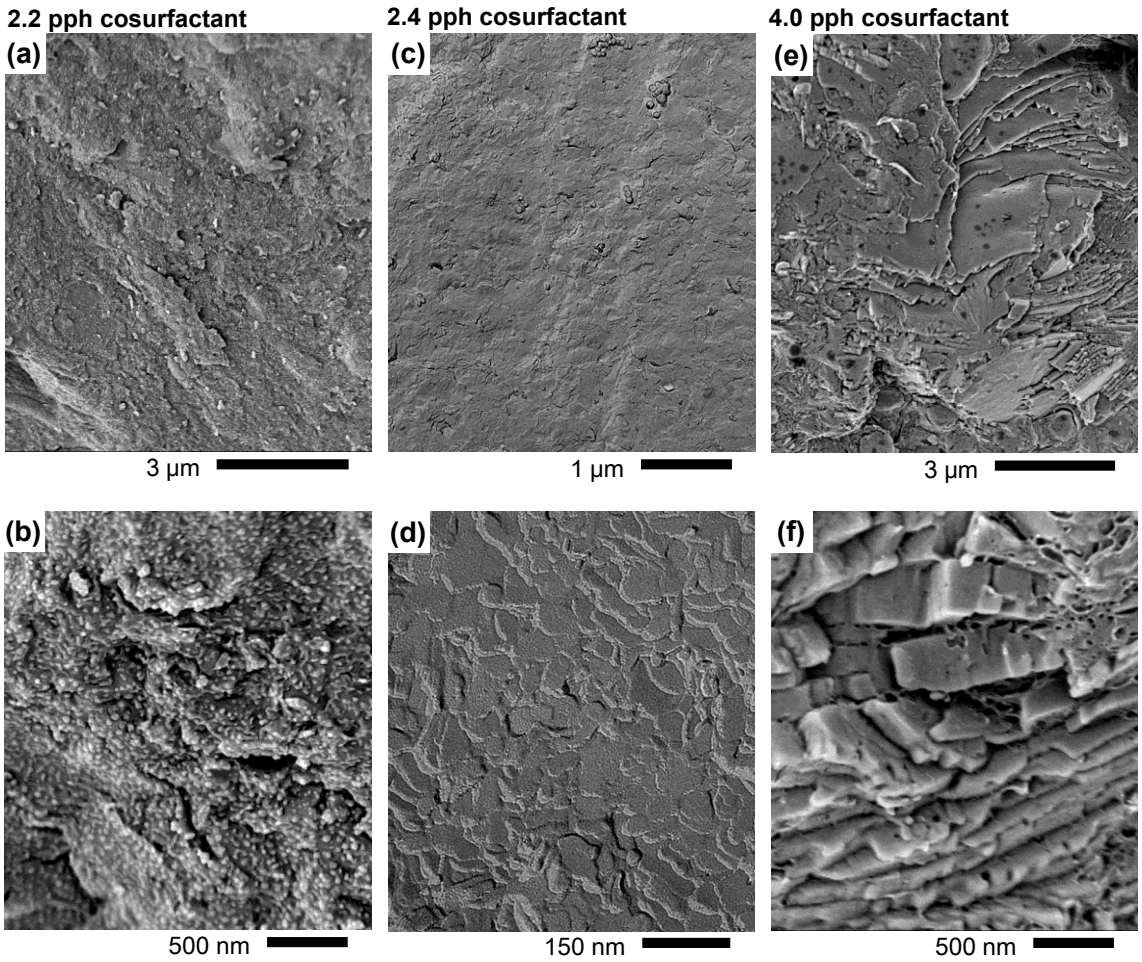

Figure 4.17. Representative images of precursor microemulsions. Cryo-SEM (2.2 parts per hundred (pph) and 4.0 pph cosurfactant at 64 °C) and FF-TEM (2.4 pph cosurfactant at 69 °C) micrographs of microemulsions used as precursors to nanoemulsions.

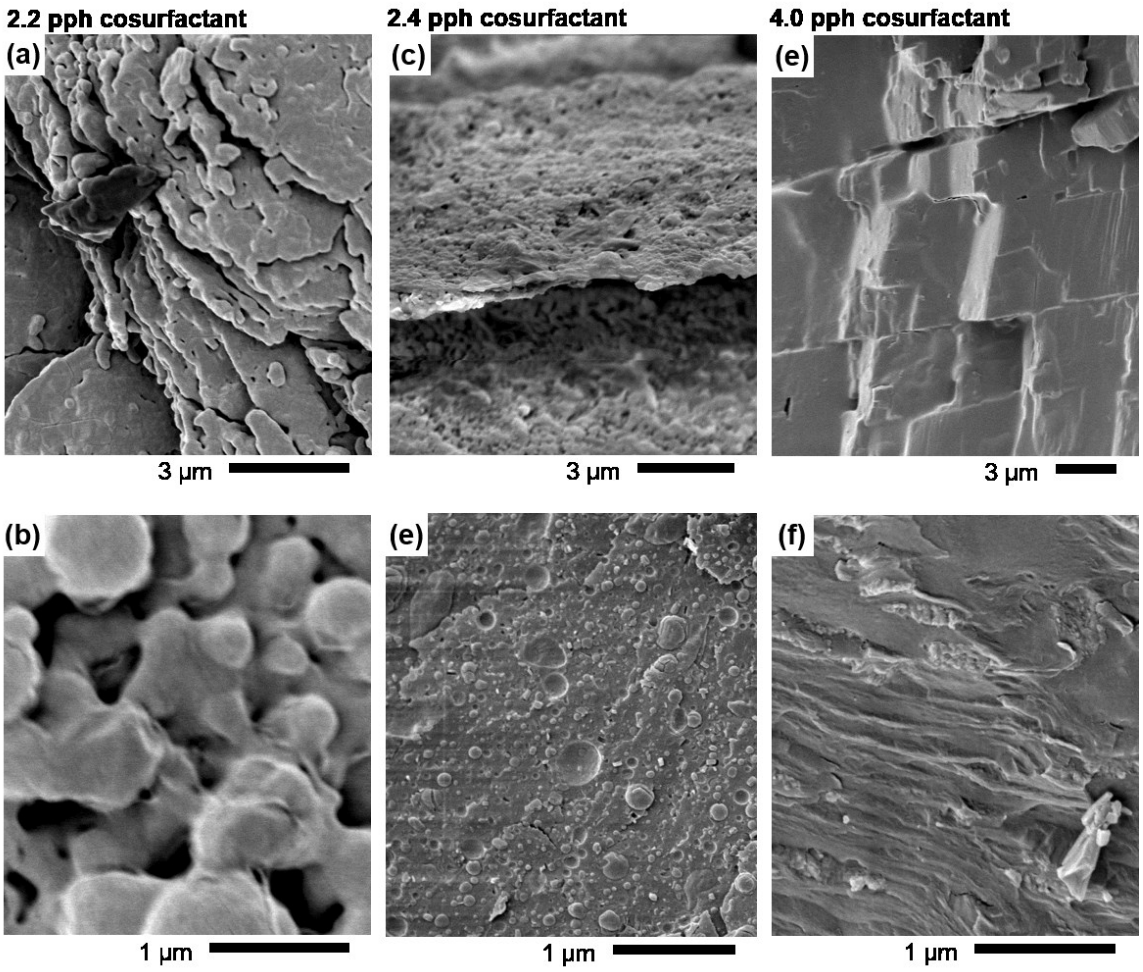

Figure 4.18. Representative cryo-SEM micrographs of intermediate quenched samples made from microemulsions with the indicated cosurfactant concentrations.

Discussion

In our system, the addition of the lipophilic linker cosurfactant should increase the compatibility between surfactants and linear alkanes.[32, 33] More specifically, substituted phenols both to water and the nonionic surfactants, which may increase the rigidity and decrease the curvature of the interface.[51] Therefore, increasing the amount of cosurfactant should alter the microemulsion structure. In the chosen system of this paper, we confirm that low cosurfactant concentration creates a high conductivity O/W or bicontinuous microemulsion which can make a successful nanoemulsion when quenched to dilute and cool. When quenching is initiated from high conductivity microemulsions, the abrupt introduction of water to the microemulsion may create an unstable lamellar structure with increased hydration of the surfactant headgroups. Simultaneously, expansion of the aqueous domain may drive vesicle formation from the lamellae as described very early by Israelachivili et al.[52] This facile exfoliation from the lamellar structure may lead to uniformly sized, small simple vesicle structures. It has been suggested that the unilamellar structure may originate from lamellar microstructure in the intermediates.[53] A schematic diagram is drawn in Figure 4.19a. This process is consistent with the description offered by Kühnle and coworkers[23] and the trend described by Pons et al.[30]

However, with excess cosurfactant, a lamellar structure may already be present in the precursor microemulsion (consistent with low conductivity). When quenching is initiated, the uptake of water is not facile enough to rearrange the initial microstructure and easily make small simple vesicles. The increased hydration of the head group upon quenching might instead lead to the growth of a well-organized intermediate lamellar structure, as shown in from Figure 4.16 to 4.18. As a result, while the additional infusion of water may mechanically break the lamellar structure, this seems to forms only large, multilamellar structures. The proposed process for excess amount of cosurfactant is shown in Figure 4.19b. These initial nanoemulsion structures are kinetically unstable because they are large enough (and polydispersed) to allow fast aggregation and Ostwald ripening.[12]

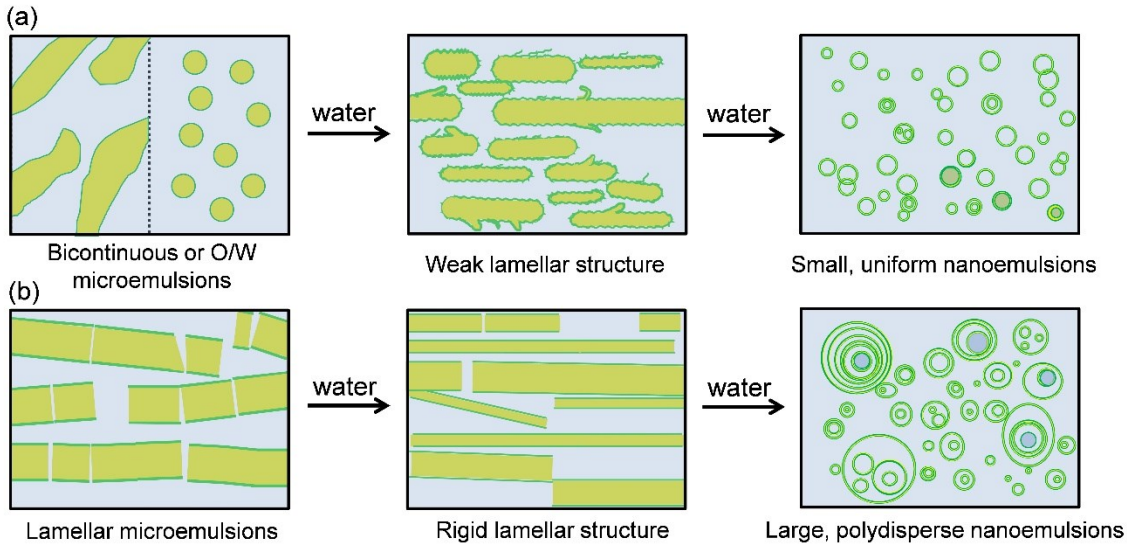

Figure 4.19. Schematic of proposed nanoemulsion structure changes when diluting from microemulsions to nanoemulsions. (a) Small amounts of cosurfactant promote weakly organized lamellar intermediates that exfoliate to small uniform vesicles. (b) Excess cosurfactant promotes well-organized lamellar structures, and dilution results in large polydisperse multilayered structures. Green is surfactant, blue is water, and greenish yellow is oil.

4.5 Conclusions

We have demonstrated how the initial structures in the product of phase change nanoemulsification can vary with the structure of precursor microemulsions used to produce the nanoemulsion. When the precursor microemulsion shows high conductivity and is either water-continuous or bicontinuous, the quenched nanoemulsion has small simple structures. Examination of a possible intermediate stage suggests this may occur because of the creation of a weak lamellar intermediate that easily exfoliates to small vesicles as suggested by Kühnle and coworkers.[23] However, when the precursor microemulsion is oil-continuous or lamellar, the nanoemulsion made from it has large complex multilamellar structures, perhaps because the lamellar intermediate becomes well organized and exfoliates with difficulty to make larger, more multilamellar structures. Cryo-EM has helped to reveal these trends; further study with scattering may further elucidate these relationships in similar nanoemulsification processes.

4.6 Supporting Information

Comparisons between parts per hundred (pph) and other composition conventions

The following shows the conversion of our "pph"(parts per hundred of cosurfactant in the precursor nanoemulsion) to the total surfactant mass fraction (γ) and to the fraction of surfactant which is the cosurfactant (δ) (which would both need to be shown to reflect our change in composition):

$$\gamma = \frac{m_{surfactants}}{m_{water}+m_{n-hexadecane}+m_{surfactants}} \tag{4.5}$$

For 2.2 pph NP, γ=0.217

For 2.4 pph NP, γ=0.219

For 4.0 pph NP, γ=0.231

$$\delta = \frac{m_{NP}}{m_{NP4}+m_{NP20}+m_{NP}} \tag{4.6}$$

For 2.2 pph NP, δ =0.099

For 2.4 pph NP, δ =0.107

For 4.0 pph NP, δ =0.167

The image of microemulsions, fresh and aged nanoemulsions of 2.2 parts per hundred (pph) and 4.0 pph cosurfactant

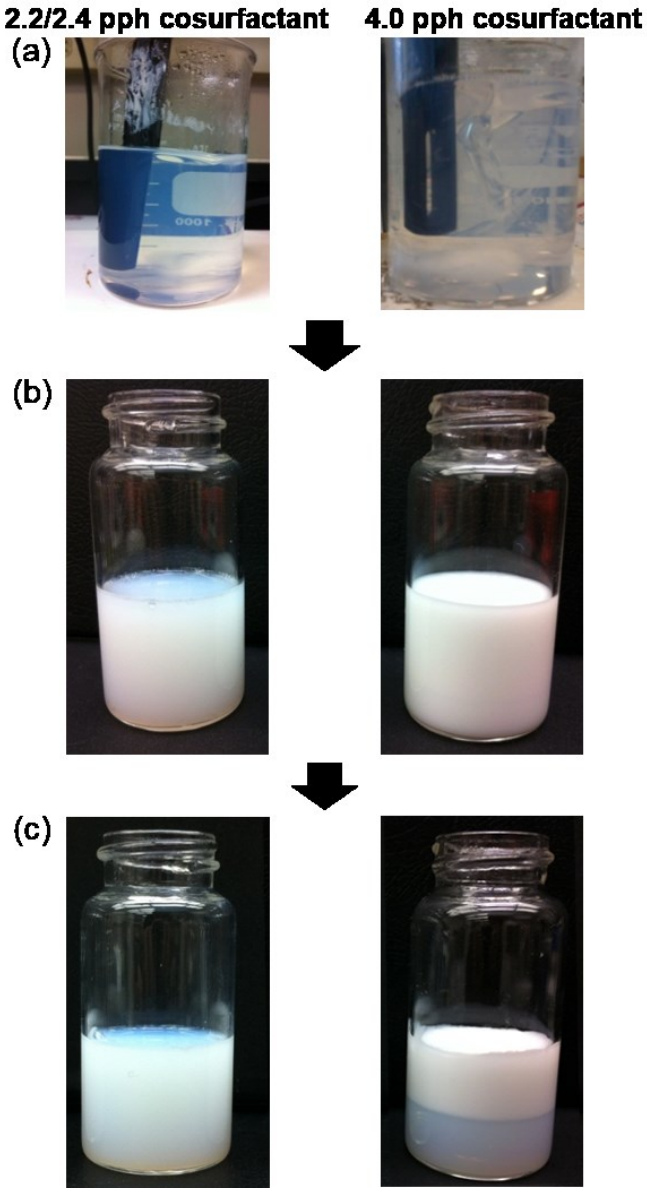

Figure 4.20. Image take from (a) transparent microemulsions, (b) fresh nanoemulsions, and (c) aged nanoemulsion of 2.2 parts per hundred (pph) and 4.0 pph cosurfactant, respectively. Note that the 2.2 pph and 2.4 pph cosurfactant shows similar size and distributions.

Characterization of matured nanoemulsions

The matured nanoemulsion showed inclusion of oil phase in the nanoparticles.

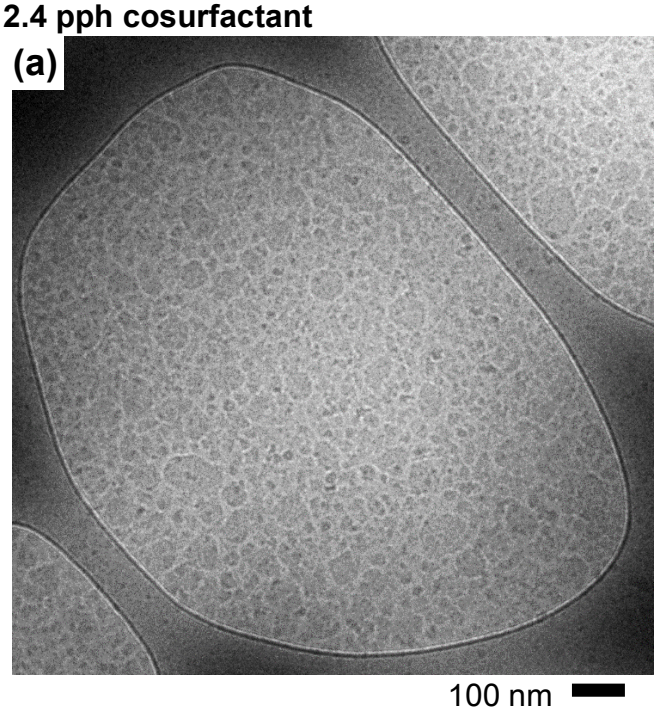

Figure 4.21. Representative cryo-TEM micrograph of matured nanoemulsions (7 days old) quenched from microemulsions with 2.4 parts per hundred (pph) cosurfactant; the angular edges are attributed to crystallization of the oil. Note that the 2.2 pph and 2.4 cosurfactant show similar size and distributions.

4.7 References

1. Cao, G. *Nanostructures and nanomaterials - Synthesis, properties and applications*; Imperial College Press: London, 2004.

2. Mason, T. G.; Wilking, J. N.; Meleson, K.; Chang, C. B.; Graves, S. M. Nanoemulsions: Formation, structure, and physical properties. *J. Phys.: Condens. Matter* **2006,** *18* (41), R635-R666.

3. Tadros, T. F. Surfactants in nano-emulsions. Wiley-VCH: Weinheim, 2005, pp 285-308.

4. Binks, B. P. *Modern aspects of emulsion science*; Royal Society of Chemistry: Cambridge, 1998.

5. Sonneville-Aubrun, O.; Simonnet, J. T.; L'Alloret, F. Nanoemulsions: A new vehicle for skincare products. *Adv. Colloid and Interface Sci.* **2004,** *108-109*, 145-149.

6. Rao, J.; McClements, D. J. Formation of flavor oil microemulsions, nanoemulsions and emulsions: Influence of composition and preparation method. *J. Agric. Food. Chem.* **2011,** *59* (9), 5026-5035.

7. Lawrence, M. J.; Rees, G. D. Microemulsion-based media as novel drug delivery systems. *Adv. Drug Deliv. Rev.* **2000,** *45* (1), 89-121.

8. Wang, L.; Li, X.; Zhang, G.; Dong, J.; Eastoe, J. Oil-in-water nanoemulsions for pesticide formulations. *J. Colloid Interface Sci.* **2007,** *314* (1), 230-235.

9. Schwarz, J. C.; Kählig, H.; Matsko, N. B.; Kratzel, M.; Husa, M.; Valenta, C. Decrease of liposomal size and retarding effect on fluconazole skin permeation by lysine derivatives. *J. Pharm. Sci.* **2011,** *100* (7), 2911-2919.

10. Nakajima, H.; Tomomasa, S.; Okabe, M. Preparation of nano-emulsions. In *Proceedings of First Emulsion Conference*; EDS: Paris, 1993; Vol. 1, pp 1-11.

11. Usón, N.; Garcia, M. J.; Solans, C. Formation of water-in-oil (W/O) nano-emulsions in a water/mixed non-ionic surfactant/oil systems prepared by a low-energy emulsification method. *Colloids Surf., A* **2004,** *250* (1-3), 415-421.

12. Mason, T. G.; Graves, S. M.; Wilking, J. N.; Lin, M. Y. Extreme emulsification: formation and structure of nanoemulsions. *Condens. Matter Phys.* **2006,** *9* (1), 193-199.

13. Helgeson, M. E.; Moran, S. E.; An, H. Z.; Doyle, P. S. Mesoporous organohydrogels from thermogelling photocrosslinkable nanoemulsions. *Nat. Mater.* **2012,** *11* (4), 344-352.

14. Kim, J.; Gao, Y.; Hebebrand, C.; Peirtsegaele, E.; Helgeson, M. E. Polymer-surfactant complexation as a generic route to responsive viscoelastic nanoemulsions. *Soft Matter* **2013,** *9* (29), 6897-6910.

15. Anton, N.; Vandamme, T. F. The universality of low-energy nano-emulsification. *Int. J. Pharm.* **2009,** *377* (1-2), 142-147.

16. Izquierdo, P.; Esquena, J.; Tadros, T. F.; Dederen, C.; Garcia, M. J.; Azemar, N.; Solans, C. Formations and stability of nano-emulsions prepared using the phase inversion temperature method. *Langmuir* **2002,** *18* (1), 26-30.

17. Morales, D.; Gutiérrez, J. M.; García-Celma, M. J.; Solans, Y. C. A Study of the relation between bicontinuous microemulsions and oil/water nano-emulsion formation. *Langmuir* **2003,** *19* (18), 7196-7200.

18. Izquierdo, P.; Esquena, J.; Tadros, T. F.; Dederen, J. C.; Feng, J.; Garcia-Celma, M. J.; Azemar, N.; Solans, C. Phase behavior and nano-emulsion formation by the phase inversion temperature method. *Langmuir* **2004,** *20* (16), 6594-6598.

19. Miller, C. A. Spontaneous emulsification produced by diffusion - A review. *Colloids Surf.* **1988,** *29* (1), 89-102.

20. López-Montilla, J. C.; Herrera-Morales, P. E.; Pandey, S.; Shah, D. O. Spontaneous emulsification: Mechanisms, physicochemical aspects, modeling, and applications. *J. Dispersion Sci. Technol.* **2002,** *23* (1-3), 219-268.

21. Meyer, J.; Polak, G.; Scheuermann, R. Preparing PIC emulsions with a very fine particle size. *Cosmetics & Toiletries* **2007,** *122* (1), 61-70.

22. Pey, C. M.; Maestro, A.; Solé, I.; González, C.; Solans, C.; Gutiérrez, J. M. Optimization of nano-emulsions prepared by low-energy emulsification methods at constant temperature using a factorial design study. *Colloids Surf., A* **2006,** *288* (1-3), 144-150.

23. Fernandez, P.; André, V.; Rieger, J.; Kühnle, A. Nano-emulsion formation by emulsion phase inversion. *Colloids Surf., A* **2004,** *251* (1-3), 53-58.

24. Sajjadi, S. Nanoemulsion formation by phase inversion emulsification: On the nature of inversion. *Langmuir* **2006,** *22* (13), 5597-5603.

25. Solè , I.; Maestro, A.; González, C.; Solans, C.; Gutiérrez, J. M. Optimization of nano-emulsion preparation by low-energy methods in an ionic surfactant system. *Langmuir* **2006,** *22* (20), 8326-8332.

26. Bilbao-Sáinz, C.; Avvena-Bustillos, R. J.; Wood, D. F.; Williams, T. G.; McHugh, T. H. Nanoemulsions prepared by a low-energy emulsification method applied to edible films. *J. Agric. Food Chem.* **2010,** *58* (22), 11932-11938.

27. Date, A. A.; Nagarsenker, M. S. Design and evaluation of self-nanoemulsifying drug delivery systems (SNEDDS) for cefpodoxime proxetil. *Int. J. Pharm.* **2007,** *329* (1–2), 166-172.

28. Wadle, A.; Förster, T.; von Rybinski, W. Influence of the microemulsion phase structure on the phase inversion temperature emulsification of polar oils. *Colloids Surf., A* **1993,** *76*, 51-57.

29. Wang, L.; Tabor, R.; Eastoe, J.; Li, X.; Heenan, R. K.; Dong, J. Formation and stability of nanoemulsions with mixed ionic-nonionic surfactants. *Phys. Chem. Chem. Phys.* **2009,** *11*, 9772-9778.

30. Pons, R.; Carrera, I.; Caelles, J.; Rouch, J.; Panizza, P. Formation and properties of miniemulsions formed by microemulsions dilution. *Adv. Colloid and Interface Sci.* **2003,** *106* (1-3), 129-146.

31. Ying, G.-G.; Williams, B.; Kookana, R. Environmental fate of alkylphenols and alkylphenol ethoxylates—a review. *Envirom. Int.* **2002,** *28* (3), 215-226.

32. Graciaa, A.; Lachaise, J.; Cucuphat, C.; Bourrel, M.; Salager, J. L. Improving solubilization in microemulsions with additives. 1. The lipophilic linker role. *Langmuir* **1993,** *9* (3), 669-672.

33. Graciaa, A.; Lachaise, J.; Cucuphat, C.; Bourrel, M.; Salager, J. L. Improving solubilization in microemulsions with additives. 2. Long chain alcohols as lipophilic linkers. *Langmuir* **1993,** *9* (12), 3371-3374.

34. Forgiarini, A.; Esquena, J.; González, C.; Solans, C. Formation of Nano-emulsions by low-energy emulsification methods at constant temperature. *Langmuir* **2001,** *17* (7), 2076-2083.

35. Wang, L.; Mutch, K. J.; Eastoe, J.; Heenan, R. K.; Dong, J. Nanoemulsions prepared by a two-step low-energy process. *Langmuir* **2008,** *24* (12), 6092-6099.

36. Zhao, Y.; Zhang, J.; Wang, Q.; Li, J.; Han, B. Water-in-oil-in-water double nanoemulsion induced by CO_2. *Phys. Chem. Chem. Phys.* **2011,** *13* (2), 684-689.

37. López-Montilla, J. C.; Herrera-Morales, P. E.; Shah, D. O. New method to quantitatively determine the spontaneity of the emulsification process. *Langmuir* **2002,** *18* (11), 4258-4262.

38. Saupe, A.; Gordon, K. C.; Rades, T. Structural investigations on nanoemulsions, solid lipid nanoparticles and nanostructured lipid carriers by cryo-field emission scanning electron microscopy and Raman spectroscopy. *Int. J. Pharm.* **2006,** *314* (1), 56-62.

39. Heunemann, P.; Prevost, S.; Grillo, I.; Marino, C. M.; Meyer, J.; Gradzielski, M. Formation and structure of slightly anionically charged nanoemulsions obtained by the phase inversion concentration (PIC) method. *Soft Matter* **2011,** *7*, 5697-5710.

40. Hiemenz, P. C.; Lodge, T. P. *Polymer Chemistry*; CRC Press, Boca Raton, FL, 2007; pp 354- 355.

41. Koppel, D. E. Analysis of macromolecular polydispersity in intensity correlation spectroscopy: The method of cumulants. *J. Chem. Phys.* **1972,** *57* (11), 4814-4820.

42. Hiemenz, P. C.; Paul, C. H. Principles of colloid and surface chemistry; 3rd ed.; CRC Press, Boca Raton, FL, 2007; pp 237-240

43. Jaromír, J. Regularized positive exponential sum (REPES) program - A way of inverting laplace transform data obtained by dynamic light scattering. *Collect. Czech. Chem. Commun.* **1995,** *60*, 1781-1797.

44. Zheng, Y.; Lin, Z.; Zakin, J. L.; Talmon, Y.; Davis, H. T.; Scriven, L. E. Cryo-TEM imaging the flow-induced transition from vesicles to threadlike micelles. *J. Phys. Chem. B* **2000,** *104* (22), 5263-5271.

45. Zasadzinski, J. A. N.; Bailey, S. M. Applications of freeze-fracture replication to problems in materials and colloid science. *J. Electron Micr. Tech.* **1989,** *13* (4), 309-334.

46. Di Biasio, A.; Cametti, C.; Codastefano, P.; Tartaglis, P.; Rouch, J.; Chen, S. H. Phase behavior of dense three-component ionic microemulsions and electrical conductivity in the lamellar phase. *Phys. Rev. E* **1993,** *47* (6), 4258-4264.

47. Delmas, T.; Piraux, H.; Couffin, A. C.; Texier, I.; Vinet, F.; Poulin, P.; Cates, M. E.; Bibette, J. How to prepare and stabilize very small nanoemulsions. *Langmuir* **2011,** *27* (5), 1683-1692.

48. Cui, H.; Hodgdon, T. K.; Kaler, E. W.; Abezgauz, L.; Danino, D.; Lubovsky, M.; Talmon, Y.; Pochan, D. J. Elucidating the assembled structure of amphiphiles in solution via cryogenic transmission electron microscopy. *Soft Matter* **2007,** *3*, 945-955.

49. Issman, L.; Talmon, Y. Cryo-SEM specimen preparation under controlled temperature and concentration conditions. *J. Microsc.* **2012,** *246* (1), 60-99.

50. Burauer, S.; Belkoura, L.; Stubenrauch, C.; Strey, R. Bicontinuous microemulsions revisited: A new approach to freeze fracture electron microscopy (FFEM). *Colloids Surf., A* **2003,** *228* (1-3), 159-170.

51. Tan, G.; Ford, C.; John, V. T.; He, J.; McPherson, G. L.; Bose, A. surfactant solubilization and the direct encapsulation of interfacially active phenols in mesoporous silicas. *Langmuir* **2008,** *24* (3), 1031-1036.

52. Israelachvili, J. N.; Mitchell, D. J.; Ninham, B. W. Theory of self-assembly of hydrocarbon amphiphiles into micelles and bilayers *J. Chem. Soc., Faraday Trans. 2* **1975,** *72*, 1525-1568.

53. Miller, C. A. Spontaneous Emulsification: Recent developments with emphasis on self-emulsification. In *Emulsions and emulsion stability*, Johan, S., Ed.; CRC Press: Boca Raton, 2006, pp 107-126.

Chapter 5.
Preparation of Nanoemulsions by Quenching Microemulsions-Effect of the Alkane Chain Length*

5.1 Overview

We previously showed that long-lived nanoemulsions might be prepared easily by diluting and cooling (quenching) warm microemulsions with precooled water, but one condition for this to work was that the microemulsion needed to have a water-continuous structure. In this paper we show that this requirement is true for alkanes with a range of chain lengths, from *n*-octane to *n*-hexadecane. Nanoemulsions are prepared from alkane/alkylphenolethoxylate/water microemulsions (weight ratio about 2:1:2) with up to 4 parts per hundred cosurfactant. The nanostructures of fresh nanoemulsions using *n*-decane and *n*-dodecane, imaged with cryogenic transmission electron microscopy (cryo-TEM), followed the same pattern shown previously with *n*-hexadecane, high conductivity, water-continuous microemulsions gave simple vesicle structures in the fresh nanoemulsions, typically less than 100 nm in diameter, and these nanoemulsions avoided separation for over 2 months, but a low conductivity microemulsion gave large, complex nanostructures in the fresh nanoemulsion, and these allowed fast coalescence and separation. Selected samples were also prepared using halogenated alkanes to create additional contrast in the cryo-TEM, allowing us to confirm that the oil is located in the observed nanostructures.

* Portions of this chapter have been prepared for submission as Han Seung Lee, Eric D. Morrison, Qiao Zhang, and Alon V. McCormick, "Preparation of nanoemulsions by quenching microemulsions-effect of the alkane chain length".

5.2 Introduction

Production of nanoemulsions has received growing interest in the recent years,[1, 2, 3] with promising applications in materials science, pharmaceutics, food sciences and personal care products,[4, 5, 6, 7, 8, 9, 10, 11] as well as potential role in drug delivery systems with control of size, stability,[12, 13] bio-availability,[14] and active agents.[10, 15] Nanoemulsion preparation methods include those relying on mechanical and fast-mixing routes (e.g., high pressure homogenization,[16, 17, 18] flash nanoprecipitation through rapid mixing,[14] ultrasonication[19]) and those using chemical routes (e.g., emulsion polymerization[20] and self-emulsification[21, 22, 23]).

Chemical methods avoid the need for intensive agitation or shear, so they may be especially promising for scale-up.[24] Moreover, they can be tuned by adjusting the temperature or composition parameters used to accomplish the rapid phase change,[25, 26, 27, 28] and they can be used with biocompatible surfactants which might find application in drug delivery and food systems.[29, 30, 31, 32, 33, 34, 35]

We recently examined a self-emulsification process to make oil-in-water nanoemulsions by quenching a warm microemulsion with cooled water to room temperature.[36] In that study, *n*-hexadecane/alkylphenolethoxylate/water precursor microemulsions (using a 2/1/2 mass ratio) were systematically varied in the cosurfactant concentration (0–4 parts per hundred (pph) alkylphenol) to change their structure; this allowed us to investigate the effect of the precursor microemulsion structure on the nanoemulsion, particularly, on the fresh nanostructures formed and the stability of the nanoemulsion. We concluded that a water-continuous (oil-in-water or bicontinuous) microemulsion structure was needed in order to form the small, simple vesicles nanostructures that resulted in a long-lived, finely dispersed nanoemulsion. This concept may also be relevant to other self-emulsification chemistries.[37, 38, 39, 40, 41]

To begin to explore how broadly this concept might apply, in this paper we systemically varied the length of the alkane chain of the oil. To characterize the nanostructures in the freshly-prepared nanoemulsions, we again used cryogenic transmission electron microscopy (cryo-TEM) and dynamic light scattering (DLS). In

addition, in this paper we also introduced halogenated oil in certain samples to provide extra contrast in the image so as to confirm that the oil is in the observed nanostructures.

5.3 Experimental Methods

Materials

Isononylphenol (NP), isononylphenol-4-ethoxylate (NPE4), and isononylphenol-20-ethoxylate (NPE20) were received from Sasol GmbH (Marl, Germany). The structures of these molecules are shown in Figure 5.1. For each of these materials, only one lot number of material was used. *n*-octane (Reagent grade, 98%), *n*-decane (ReagentPlus, ≥99%), *n*-dodecane (ReagentPlus, ≥99%), and *n*-hexadecane (ReagentPlus, 99%) were purchased from Sigma-Aldrich Co. (Milwaukee, WI). *n*-tetradecane (≥99%), *n*-octadecane (99%), 1-bromodecane (98%), 1-bromohexadecane (97%), and 1-chlorohexadecane (95%) were purchased from Aldrich (Milwaukee, WI). 1-bromotetradecnae (97%) and 1-iodohexadecnae (98%) were purchased from Alfa Aesar (Ward Hill, MA). All chemicals were used as received. Water purified from a Millipore Direct-Q 3 water (Billerica, MA, resistivity>18.2 MΩ cm) was used in all experiments.

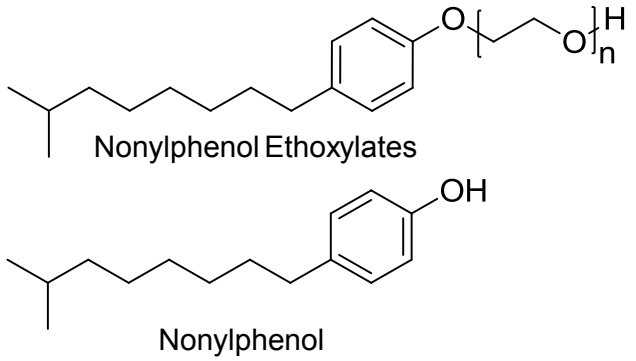

Figure 5.1. Molecular structure of nonylphenol ethoxylates and nonylphenol.

Methods

A. Preparing microemulsions

Microemulsions with an oil/surfactant/water mass ratio of about 2/1/2 were prepared as follows. First, oil (40.0 g) and surfactants (8.7 g of NPE4, 11.3 g of NPE20)

and cosurfactant (between 0–4.0 g of NP) were mixed at room temperature. Gentle stirring was used throughout the procedure. DI-water (40.0 g) was then added at 40−45 °C to yield an emulsion. Then the emulsion was heated to 90 °C. The composition and the surfactants were chosen to yield easily-obtained microemulsions somewhere in the temperature range 50–80 °C. This range is convenient because it is warm enough to allow appreciable cooling to room temperature when the dilution with water is performed, but not so warm as to introduce much risk of evaporation or boiling.

The emulsion at 90 °C was allowed to cool slowly with gentle stirring to as low as 50 °C (below this temperature the viscosity was too high to mix with gentle stirring). In all systems except *n*-octadecane, a transparent isotropic stable microemulsion was observed somewhere in the temperature range between 50 and 75 °C.

B. Quenching the microemulsions to make nanoemulsions

To prepare a nanoemulsion, the precursor microemulsion (brought to its transparent temperature range) is quickly diluted and cooled, with gentle stirring, by sudden addition of 320 g of precooled DI-water to bring the system to 20 °C and 85 wt % water, this result is the nanoemulsion.

Many samples in this paper were prepared with a cosurfactant concentration of 2.2 pph by weight in the precursor microemulsion, since this was the concentration that gave the most long-lived nanoemulsions with *n*-hexadecane (at the composition oil/surfactant/water of about 2/1/2). In this paper we will explore the two types of variation. First, we will vary the alkane oil used (keeping the cosurfactant concentration constant) to see whether the microemulsion still produces long-lived nanoemulsions. Second, for certain alkanes we will increase the amount of cosurfactant to see if there is the same tendency (as seen for *n*-hexadecane) for too much cosurfactant to cause low conductivity, water-discontinuous microemulsions and, from them, large complex nanostructures in the nanoemulsion (which cause fast separation).

C. Characterization

Conductivity

The electrical conductivity of the precursor emulsions was measure with an Orion 3-Star Plus (ThermoFisher Scientific, Tewksbury, MA) with an epoxy/graphite electrode cell (cell constant 0.475 cm^{-1} at 25 °C). Measurements were recorded every 10 seconds at the emulsion was cooled slowly on a Pc-520 hot plate magnetic stirrer (Corning, Corning, NY).

Dynamic Light Scattering (DLS)

Approximate particle size and distribution of the nanostructures in freshly prepared nanoemulsions (within one hour of preparation) was obtained by dynamic light scattering (DLS) using the ZetaPALS 90PLUS/BI-MAS (Brookhaven Instruments, Holtsville, NY) at room temperature. A 3–5 μL portion of sample was diluted with 3 mL of DI-water. Light scattering was detected at 90 º with a 670 nm laser at 22 °C using BI-SCP 100 plastic rectangular cuvette (Brookhaven Instruments, Holtsville, NY). DLS data was analyzed using regularized positive exponential sum method, which is based on the method of cumulants and described in cited references.[36, 42, 43] For certain nanoemulsion samples, the conductivity was also monitored with aging time (Figure 5.13).

Cryogenic transmission electron microscopy (Cryo-TEM)

The morphology of the nanostructures in freshly-prepared nanoemulsions was imaged by cryogenic-transmission electron microscopy (cryo-TEM). A freshly made 1–3 μL amount of sample was applied to a 200 mesh lacey carbon TEM grid (Ted Pella, Redding, CA). To increase its wettability, the TEM grid had been subjected to plasma glow discharge with DV-502A vacuum system (Denton Vacuum, Moorestown, NJ) for 1 minute. The grid was held by a tweezers inside Mark III Vitrobot (FEI, Hillsboro, OR) chamber at 22 °C with a relative humidity of 95−100%, and the grid was blotted to produce an electron-transmissible specimen thickness. The specimen was relaxed for 3−5 seconds and then plunged into liquid ethane cooled by liquid nitrogen to vitrify the sample. The grid was transferred to a 626 cryo-transfer unit (Gatan, Pleasanton, CA) using a cryo-grid

box and a cryo-handling tool (Ted Pella, Redding, CA). The vitrified specimen was imaging using a FEI Tecnai Spirit BioTWIN at 120 kV with Eagle 2048 x 2048 CCD camera (FEI Company, Hillsboro, OR). The specimen was kept below -178 °C in the microscope and was imaged in an underfocused (1−6 μm) and low−dose mode (<20 $e^{-}/Å^{2}$). The images were processed with the TEM Imaging and Analysis 4.2 software (FEI Company, Hillsboro, OR).

5.4 Results and Discussion

A. The effect of alkane chain length on nanoemulsion formation at fixed composition

To determine the microemulsion temperature range, we monitor the transparency as we cool slowly with gentle stirring from the 90 °C starting temperature; at 90 °C all of the stirred emulsions are opaque. We also monitor the conductivity to characterize the microemulsion; at the 90 °C starting temperature, all emulsions have low conductivity, indicating they are oil-continuous emulsions.[44, 45] The amount of cosurfactant in each emulsion is fixed as a 2.2 pph (weight basis).

Figure 5.2 shows the conductivity and the transparency of emulsions using various oils as function of temperature. All conductivity plots were reproducible and reversible.

With only two exceptions at the extremes of the size range used, all of these systems produced long-lived nanoemulsions, avoiding separation over many weeks. The first exception, at the long chain-length extreme, is the *n*-octadecane system, which is failed to produce a transparent isotropic microemulsion at this composition. Second, at the short chain length extreme, the *n*-octane microemulsion produced a nanoemulsion that is not long-lived; it separated fairly rapidly (over a period of days).

These results reinforce the pattern found in our previous study, where we reported a stable isotropic microemulsion phase in the *n*-hexadecane system at this cosurfactant concentration (2.2 pph). The conductivity patterns of the alkane systems ranging from *n*-hexadecane to *n*-decane show microemulsion regions that resemble those in our previous paper (with *n*-hexadecane and varying cosurfactant concentration) that produced long-

lived nanoemulsions. Here, we find that the oil size affect the microemulsion temperature range, and the conductivity data indicates that microemulsions are water-continuous for alkanes ranging from an *n*-hexadecane to *n*-decane. Also, shorter alkane microemulsions produced somewhat lower conductivity at low temperatures, consistent with the suggestion by Shah and coworker of better molecular packing in the oil.[46] With the shorter alkanes, we see abrupt swings in conductivity and intermediate nonisotropic appearances, which may suggest interconversion between lamellar and bicontinuous structures. An important and consistent observation is that water-continuous conductive microemulsions produce long-lived nanoemulsions.

In contrast, the *n*-octane emulsion showed a microemulsion with very low conductivity, suggesting a more strongly lamellar, water-discontinuous structure similar to what we observed in our previous work with the hexadecane using 4.0 pph cosurfactant. The nanoemulsion produced by diluting this microemulsion was more opaque, had larger particle size, and was short-lived, phase separating in only days.

It is interesting to note that the patterns shown with decreasing alkane chain length, patterns both of microemulsion appearance, and of microemulsion conductivity, are similar to the patterns shown previously with just one oil (*n*-hexadecane) when increasing the cosurfactant concentration from 0 to 4 pph (w/w). It is believed that decreasing alkane chain length, like increasing the cosurfactant concentration, tends increase the degree of lamellar character in microemulsion phases.

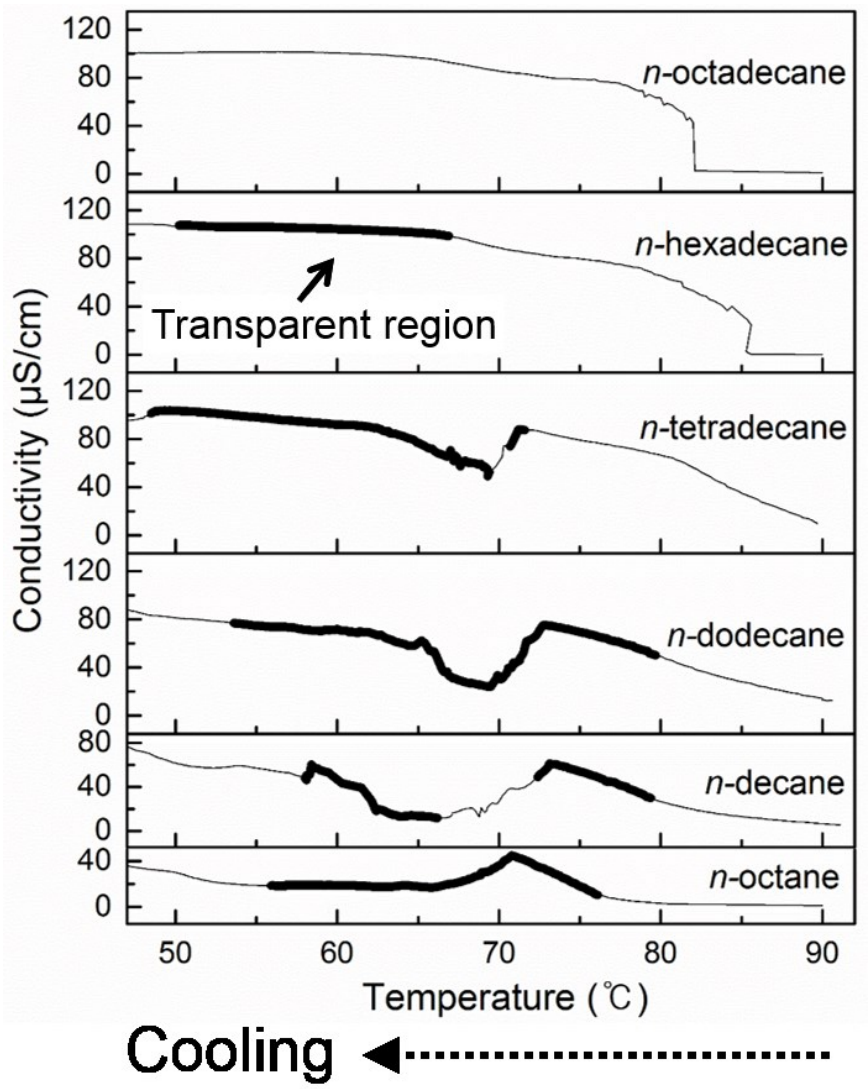

Figure 5.2. Temperature dependence of conductivity for H_2O/oil/alkylphenol nonionic surfactants with a fixed amount of 2.2 parts per hundred cosurfactant. Conductivities are measured as the emulsions are gradually cooled from high temperature with gentle mixing (about 1.3 °C/min). Bold segments represent transparent microemulsion regions.

B. Conductivity of *n*-decane microemulsions and characterization of nanoemulsion structure, varying the cosurfactant concentration

To establish whether the pattern of nanoemulsion structure, with a change in cosurfactant concentration, is similar for other oils as found earlier for *n*-hexadecane, we varied the cosurfactant concentration using *n*-decane and *n*-dodecane (Figure 5.8). We seek to confirm whether for these shorter alkanes it remains true that the nanostructures in the freshly made nanoemulsions are simplest and smallest when using high-conductivity microemulsions, and that such nanoemulsions are long-lived.

Figure 5.3 shows the transparency and conductivity scans with temperature of the *n*-decane emulsion with varying cosurfactant concentrations. At both 2.2 and 2.4 pph cosurfactant, there are two distinct isotropic microemulsion temperature ranges. The abrupt changes of both conductivity and appearance of 2.2 pph cosurfactant from 75 to 60 °C suggests the inverconversion of lamellar and bicontinuous structures.[47] The low conductivity of the microemulsions in 2.4 and 4.0 pph cosurfactant could suggest a development of lamellar structure.[48] Indeed, the 4.0 pph cosurfactant showed a near-zero conductivity of its microemulsion, suggesting a strong lamellar structure.

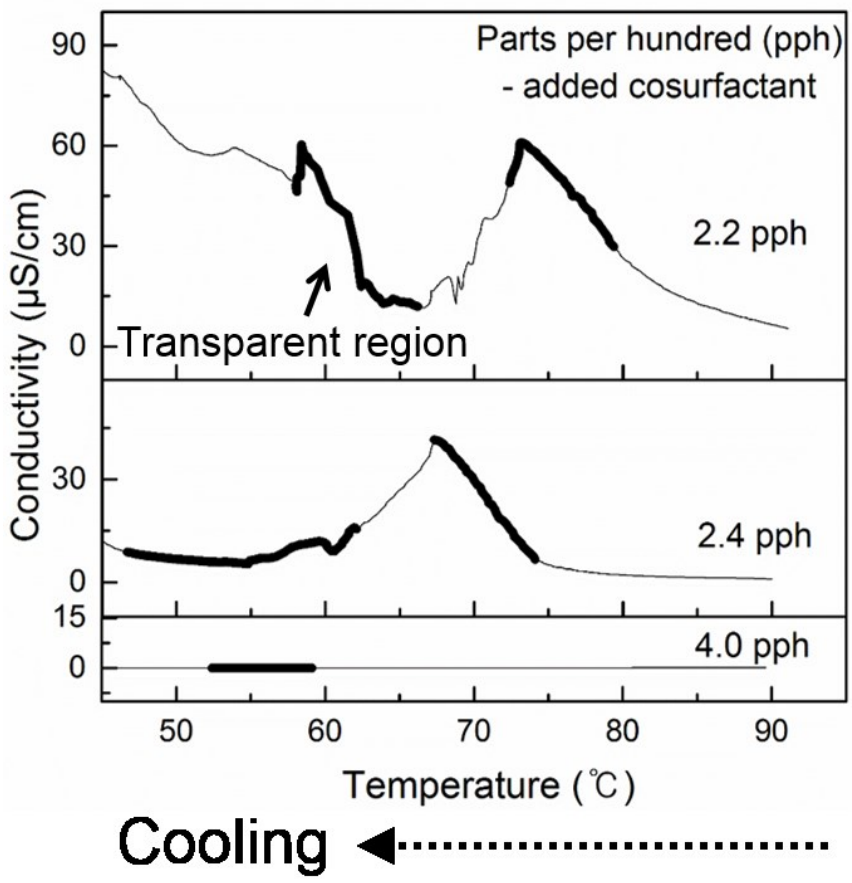

Figure 5.3. Temperature dependence of conductivity for H_2O/*n*-decane/alkylphenol nonionic surfactants. The concentration of add nonylphenol cosurfactant varied from 2.2 parts per hundred (pph) to 4.0 pph. Bold segments represent transparent microemulsion regions.

After the isotropic microemulsions were found, the 2.2, 2.4, and 4.0 pph cosurfactant microemulsions are diluted and quenched to make the nanoemulsions. Diluting and cooling from any temperature in the microemulsion range gives similar behavior. Freshly prepared nanoemulsions made from the transparent microemulsions were analyzed with DLS (Figure 5.4). DLS showed that the fresh nanostructures in the nanoemulsions with 2.2 pph and 2.4 pph cosurfactant systems were about 100 nm in diameter. These nanoemulsions showed no phase separation for over a month. However, DLS showed the nanostructures in the 4.0 pph cosurfactant nanoemulsions were about 300nm in diameter, and the separated to form a cream layer in only a few days.

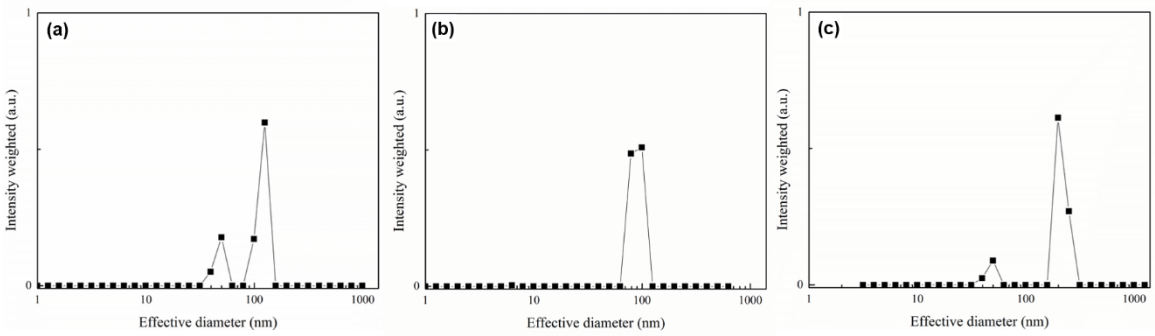

Figure 5.4. Intensity weighted dynamic light scattering result of (a) 2.2 parts per hundred (pph), (b) 2.4 pph, and (c) 4.0 pph cosurfactant. The sample are fresh nanoemulsions of H_2O/*n*-decane/alkylphenol nonionic surfactants.

The nanostructures in the fresh nanoemulsions were imaged with cryo-TEM, and representative micrographs are shown in Figure 5.5. The nanostructures show a similar pattern with changing cosurfactant as the pattern seen in our previous work with *n*-hexadecane. At low cosurfactant concentration, which gave high conductivity microemulsions, the nanoemulsion has simpler and smaller nanostructures. In Figure 5.5a, using 2.2 pph cosurfactant, vesicles of about 100 nm diameter are observed; this is comparable to the DLS size. Most vesicles are unilamellar but some are double-walled (white arrowhead). Some threadlike micelles are also observed, which may suggest that some excess surfactant fails to remain associated with the oil (black arrow in Figure 5.5a). Some rough-featured structures also appear, perhaps suggesting some crystallization of the oil during the cryo-fixation process.

With a slight increase in cosurfactant concentration from 2.2 pph to 2.4 pph cosurfactant, the nanostructure changes abruptly, though it remains small. As can be seen in Figure 5.5b, multilamellar and concentric vesicular structures are common. The development of these complex structures with more cosurfactant is similar to our earlier observations in the *n*-hexadecane system.

Figure 5.5c shows that too much cosurfactant leads to the formation of larger and complex structures, just as it did for the *n*-hexadecane system. Multi-compartment particles with a broad size distribution are observed for nanoemulsions with 4.0 pph cosurfactant.

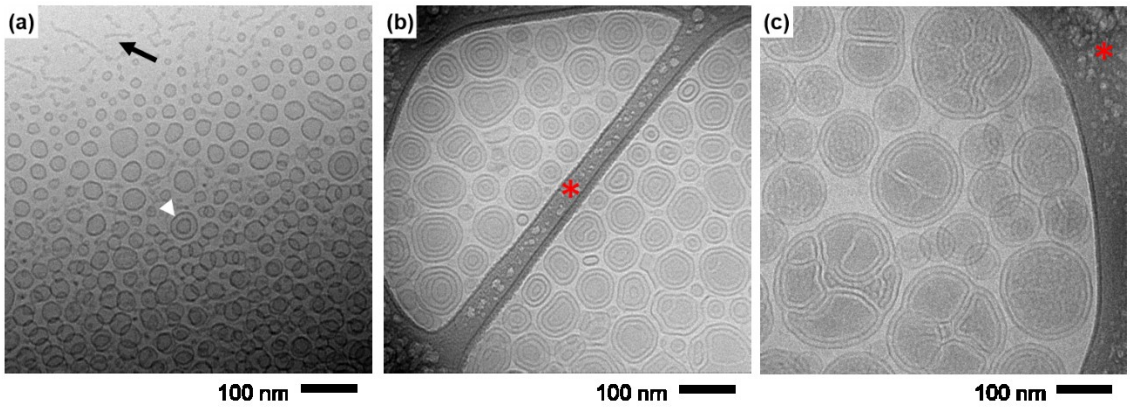

Figure 5.5. Representative cryo-TEM micrographs of fresh nanoemulsions of H_2O/*n*-decane/alkylphenol nonionic surfactants with (a) 2.2 parts per hundred (pph), (b) 2.4 pph, and (c) 4.0 pph cosurfactant. Size and structural complexity of the nanoemulsions increase as cosurfactant concentration increases. In 2.2 pph cosurfactant, some segregated surfactants are shown as a threadlike micelles (black arrow) and double layered nanoemulsions are also observed (white arrowhead). Red asterisk marks indicate beam-damaged lacey carbon struts on the TEM grid.

Oil may be present inside the bilayer, swelling the inter-leaf gallery, but it was difficult to image this directly because *n*-decane has very low electron contrast. To confirm the presence of the oil in the nanostructures, we also used halogen-substituted alkanes to provide increased scattering contrast in cryo-TEM characterization. Information in the supporting material supports that the halogenated oils behaved in a qualitatively similar manner as the non-substituted oils. A representative cryo-TEM image with 1-bromodecane is shown in Figure 5.6. The micrograph shows strong scattering contrast inside of the freshly prepared nanoemulsions, confirming that the oil is present in the nanostructures observed in the previous figure. However, the rough structure suggests that the halogenated oil crystallizes in the cryogenic fixation process; this damages the nanostructure, so it is still not proven precisely where in the vesicle the oil resides. It is reasonable, though, to presume that in the freshly made nanoemulsion the oil remains in close association with the hydrophobic tail of the surfactant (presumably assisted by the hydrophobic linker cosurfactant), so it would reside within the gallery of the vesicle bilayer wall structure. As the nanoemulsion ages, thought, it is certainly possible that these vesicular structures might ripen to nanodroplets.

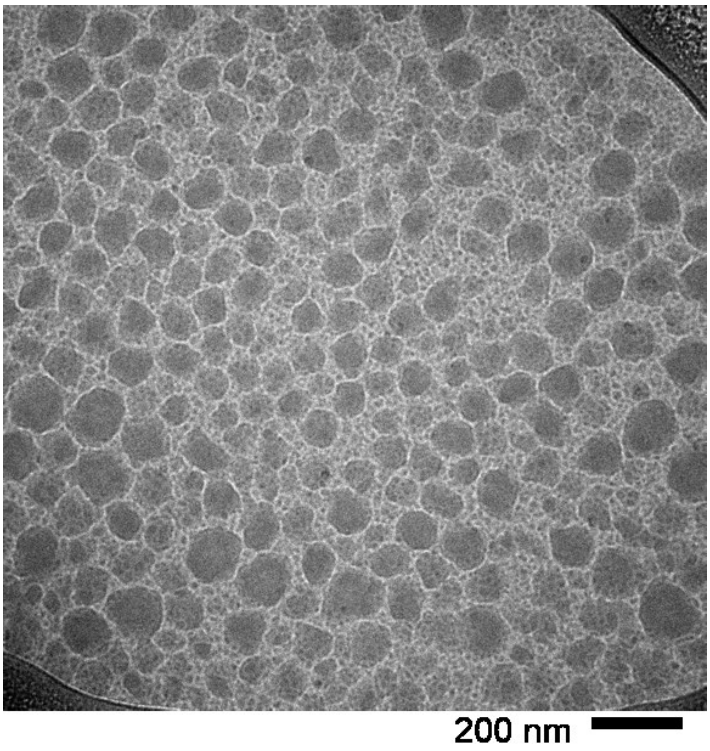

Figure 5.6. Representative cryo-TEM micrograph of fresh nanoemulsions of H_2O/1-bromodecane/alkylphenol nonionic surfactants in 2.2 parts per hundred cosurfactant.

To check the location of oil component during phase change emulsification, we also performed confocal Raman microscopy. Figure 5.7a is 2.2 pph cosurfactant and Figure 5.7b and 5.7c are 4.0 pph cosurfactant. Because of low resolving power of confocal Raman microscopy, 2.2 pph cosurfactant was not able to distinguish oil and surfactant from water background. However, 4.0 pph cosurfactant showed existence of the oil in the nanoemulsions. We assumed oil will reside in the gallery of the surfactant double layer, but was not able to observe it because of limit of resolution in confocal Raman microscopy.

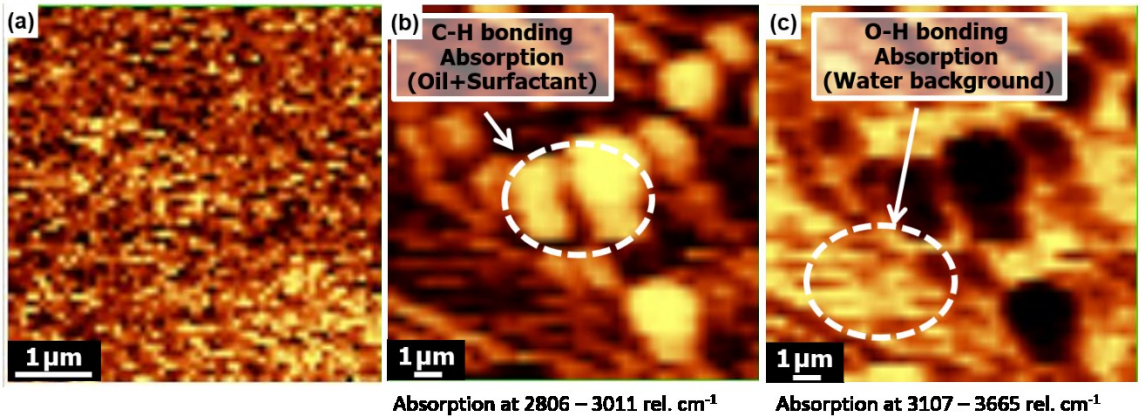

Figure 5.7. Representative confocal Raman micrographs of fresh nanoemulsions of H_2O/*n*-hexadecane/alkylphenol nonionic surfactants in (a) 2.2 parts per hundred (pph) and (b, c) 4.0 pph cosurfactant.

5.5 Conclusions

We have shown that long-lived nanoemulsions can be prepared by quenching and diluting microemulsions with a variety of *n*-alkanes as long as that microemulsion displays a high conductivity water-continuous structure, consistent with our earlier results for *n*-hexadecane. Small structures in the fresh nanoemulsion are again attributed to small, spherical unilamellar vesicles. Moreover, we confirmed that microemulsions with low conductivity (liquid lamellar) give quickly-separating nanoemulsions due to the formation of large, complex multilamellar structures in the fresh nanoemulsion. Finally, we demonstrate a similarity between the effect that the alkane chain length of the oil has on the process to the effect that the cosurfactant concentration has on the process.

Better understanding the principles of simple nanoemulsion production processes such as this one can lead to ease in engineering them for a variety of applications. Demonstration that the initially formed nanoemulsion structures can include simple small vesicles suggests the applicability of phase change emulsification processes for synthesis of nanocarrier drug delivery systems.

5.6 Supporting Information

Conductivity of *n*-dodecane microemulsions and characterization of nanoemulsion structure, varying the cosurfactant concentration

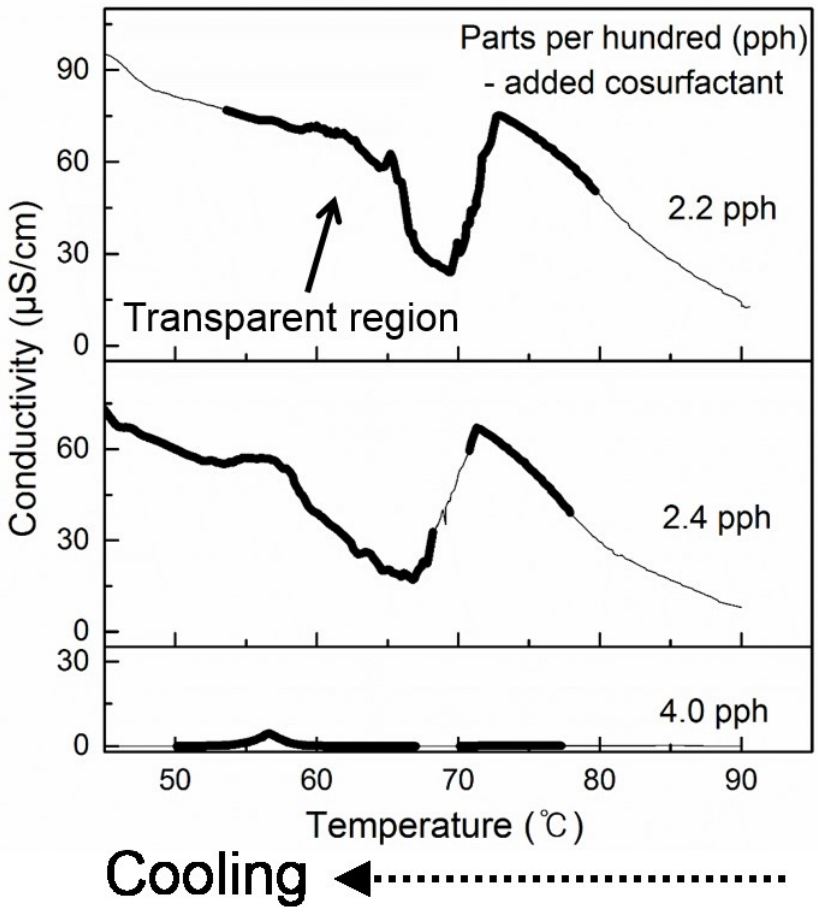

Figure 5.8. Temperature dependence of conductivity for H_2O/*n*-dodecane/alkylphenol nonionic surfactants. The concentration of add nonylphenol cosurfactant varied from 2.2 parts per hundred (pph) to 4.0 pph. Bold segments represent transparent microemulsion regions.

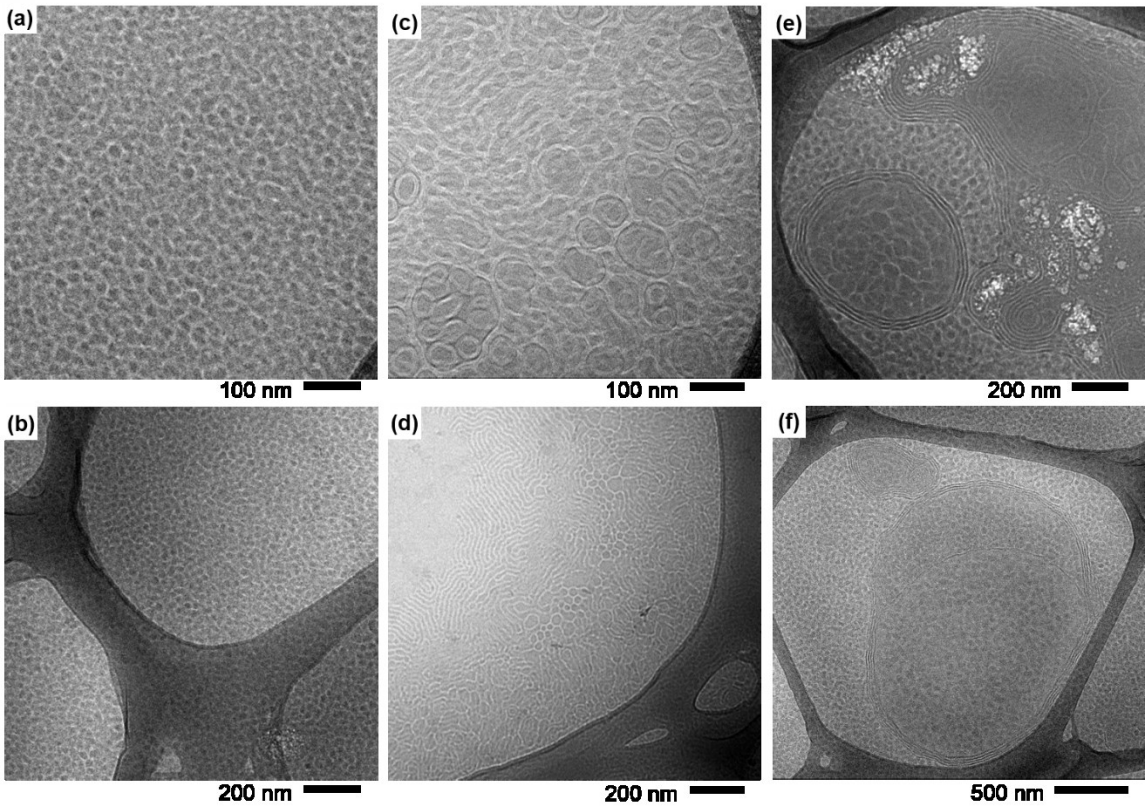

Figure 5.9. Representative cryo-TEM micrographs of fresh nanoemulsion sof H_2O/*n*-dodecane/alkylphenol nonionic surfactants with (a, b) 2.2 parts per hundred (pph), (c, d) 2.4 pph, and (e, f) 4.0 pph cosurfactant. Upper micrographs are high magnification and lower micrographs are low magnification (They are not necessarily same region.). In high magnification images, complex structures are observed starting in 2.4 pph cosurfactant.

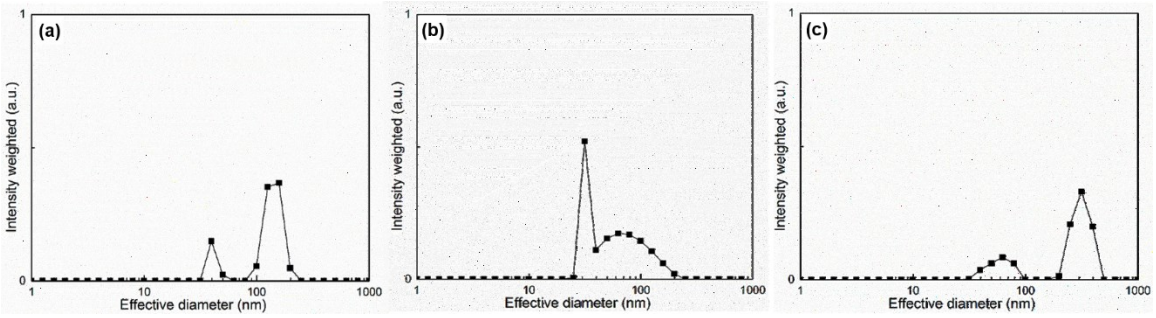

Figure 5.10. Intensity weighted effective diameter distribution of (a) 2.2 parts per hundred (pph), (b) 2.4 pph, and (c) 4.0 pph cosurfactant. The samples are fresh nanoemulsions of H_2O/*n*-dodecane/alkylphenol nonionic surfactants.

Conductivity of microemulsions with halogenated oils and characterization of halogenated oil nanoemulsion structure with 2.2 parts per hundred cosurfactant

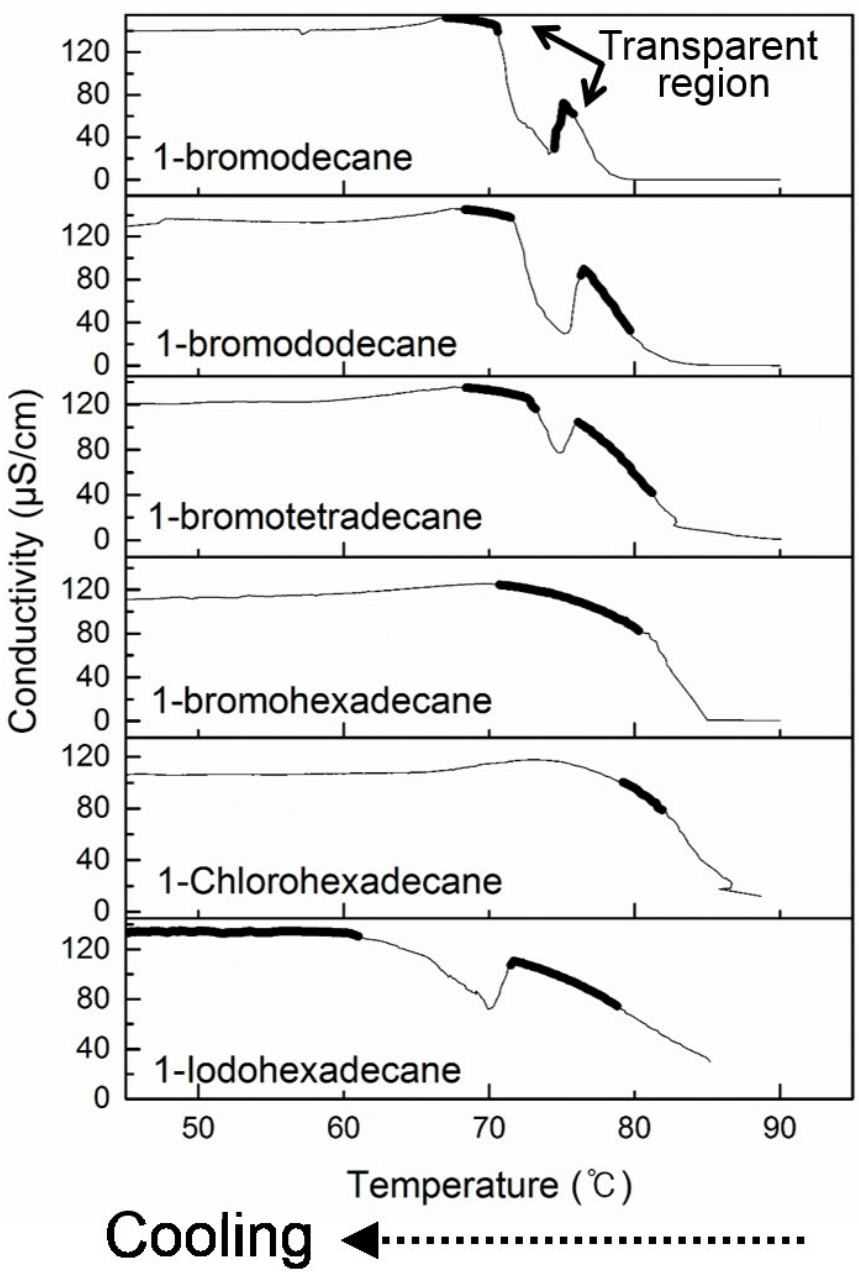

Figure 5.11. Temperature dependence of conductivity for H_2O/halogenated oil/alkylphenol nonionic surfactants with a fixed amount of 2.2 parts per hundred cosurfactant. Bold segments represent transparent microemulsion regions.

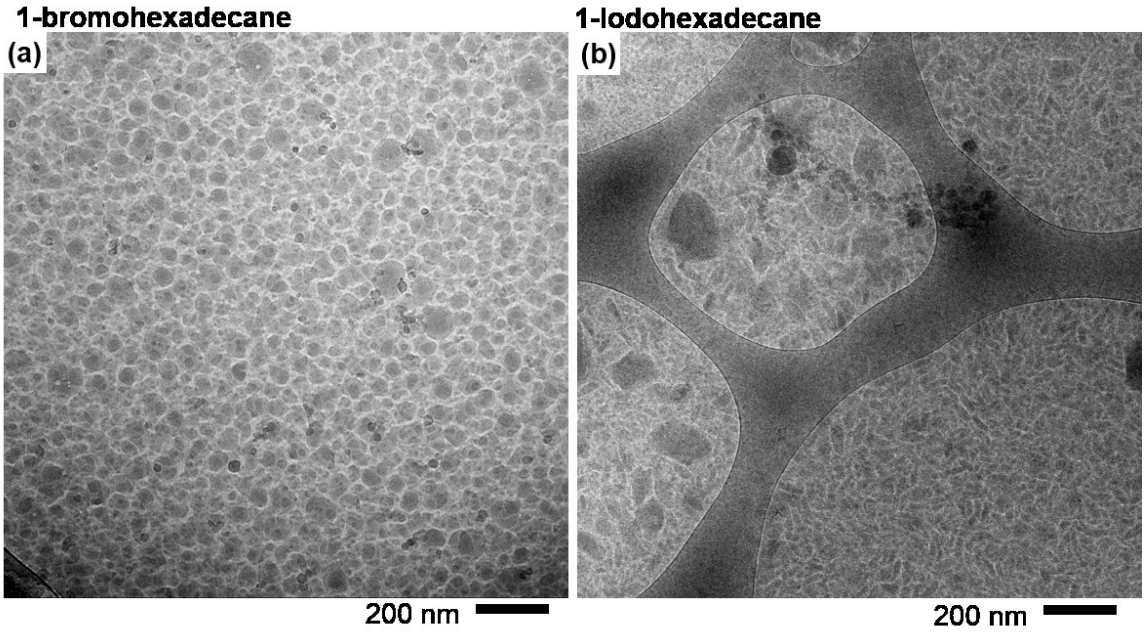

Figure 5.12. Representative cryo-TEM micrographs of fresh nanoemulsions of H_2O/halogenated hexadecanes/alkylphenol nonionic surfactants in 2.2 parts per hundred cosurfactant. (a) 1-bromohexadecane, (b) 1-iododhexadecane.

Selected hydrodynamic diameter of aged nanoemulsions

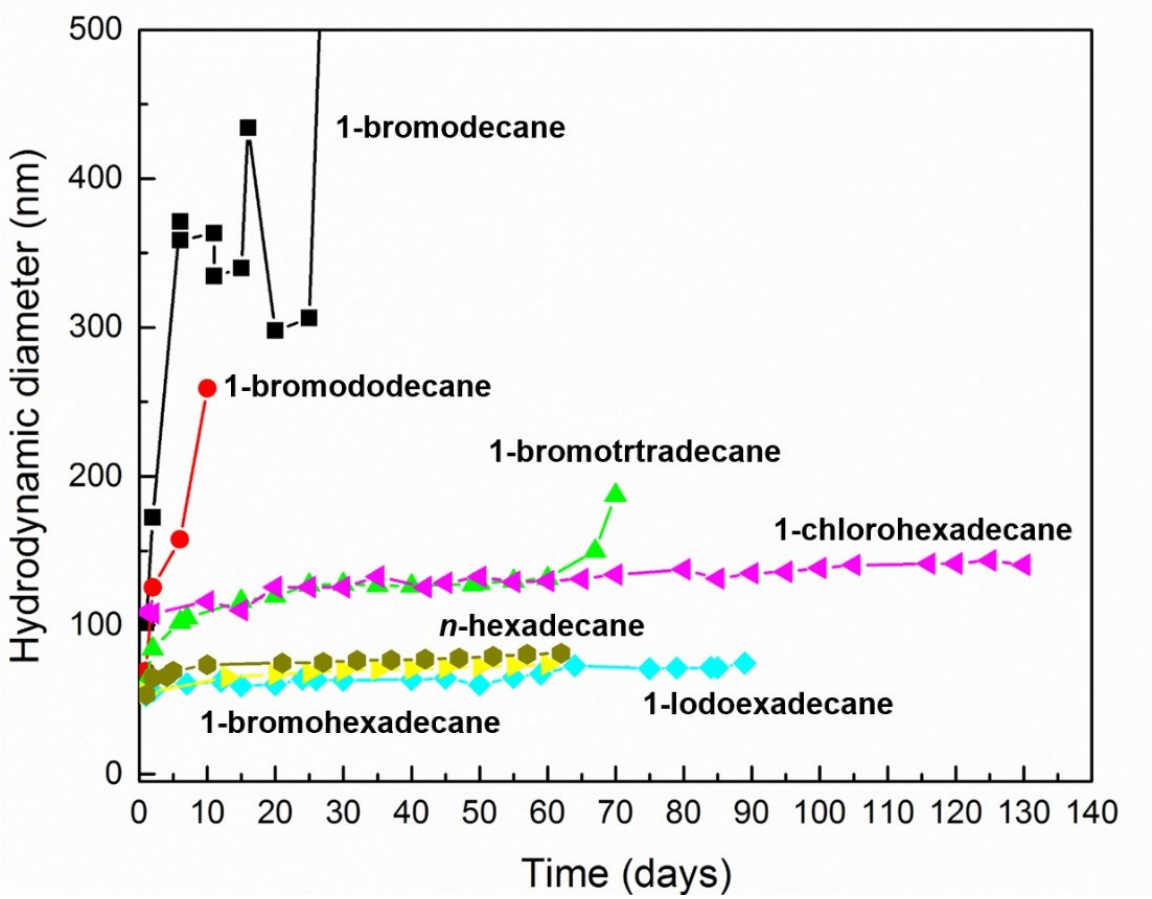

Figure 5.13. Selected hydrodynamic diameter of aged nanoemulsions with 2.2 parts per hundred cosurfactant.

Table 5.1. The approximate time to phase separation of selected nanoemulsions

Oil in nanoemulsions	Phase separation time (Days)		
	2.2 parts per hundred (pph)	2.4 pph	4.0 pph
n-octane	< 2 weeks	-	-
n-decane	> 2 months	> 2 months	< 1 week
n-dodecane	> 2 months	> 2 months	< 1 week
n-tetradecane	> 2 months	> 2 months	< 1 week
n-hexadecane	> 2 months	> 2 months	< 1 week
1-bromodecane	< 1 month	> 2 months	-
1-bromododecane	< 1 month	> 2 months	
1-bromotetradecane	> 2 months	-	-
1-bromohexadecane	> 2 months	-	-
1-chlorohexadecane	> 2 months	-	-
1-iodohexadecane	> 2 months	-	-

5.7 References

1. Tadros, T.; Izquierdo, P.; Esquena, J.; Solans, C. Formation and stability of nano-emulsions. *Adv. Colloid Interface Sci.* **2004,** *108-109*, 303-318.

2. Solans, C.; Izquierdo, P.; Nolla, J.; Azemar, N.; Garcia-Celma, M. J. Nano-emulsions. *Curr. Opin. Colloid Interface Sci.* **2005,** *10* (3-4), 102-110.

3. Nakajima, H.; Tomomasa, S.; Okabe, M. Preparation of Nano-emulsions. In *Proceedings of First Emulsion Conference*; EDS: Paris, 1993; Vol. 1, pp 1-11.

4. Feng, J.; Roche, M.; Vigolo, D.; Arnaudov, L. N.; Stoyanov, S. D.; Gurkov, T. D.; Tsutsumanova, G. G.; Stone, H. A. Nanoemulsions obtained via bubble-bursting at a compound interface. *Nat. Phys.* **2014,** *10* (8), 606-612.

5. Sadurní, N.; Solans, C.; Azemar, N.; García-Celma, M. J. Studies on the formation of O/W nano-emulsions, by low-energy emulsification methods, suitable for pharmaceutical applications. *Eur. J. Pharm. Sci.* **2005,** *26* (5), 438-445.

6. Srivastava, V. K.; Kini, G.; Rout, D. Detergency in spontaneously formed emulsions. *J. Colloid Interface Sci.* **2006,** *304* (1), 214-221.

7. Guglielmini, G. Nanostructured novel carrier for topical application. *Clin. Dermatol.* **2008,** *26* (4), 341-346.

8. Klang, V.; Matsko, N.; Raupach, K.; El-Hagin, N.; Valenta, C. Development of sucrose stearate-based nanoemulsions and optimisation through Î³-cyclodextrin. *Eur. J. Pharm. Biopharm.* **2011,** *79* (1), 58-67.

9. Ostertag, F.; Weiss, J.; McClements, D. J. Low-energy formation of edible nanoemulsions: Factors influencing droplet size produced by emulsion phase inversion. *J. Colloid Interface Sci.* **2012,** *388* (1), 95-102.

10. Saberi, A. H.; Fang, Y.; McClements, D. J. Fabrication of vitamin E-enriched nanoemulsions: Factors affecting particle size using spontaneous emulsification. *J. Colloid Interface Sci.* **2013,** *391*, 95-102.

11. Wang, L.; Dong, J.; Chen, J.; Eastoe, J.; Li, X. Design and optimization of a new self-nanoemulsifying drug delivery system. *J. Colloid Interface Sci.* **2009,** *330* (2), 443-448.

12. Taylor, P.; Ottewill, R. H. The formation and ageing rates of oil-in-water miniemulsions. *Colloids Surf., A* **1994,** *88* (2–3), 303-316.

13. Joos, A.; Weiss, J.; McClements, D. J. Fabrication of lipophilic nanoparticles by spontaneous emulsification: Stabilization by cosurfactants. *Food Biophys.* **2014**, 1-11.

14. Margulis, K.; Magdassi, S.; Lee, H. S.; Macosko, C. W. Formation of curcumin nanoparticles by flash nanoprecipitation from emulsions. *J. Colloid Interface Sci.* **2014,** *434*, 65-70.

15. Pouton, C. W. Formulation of self-emulsifying drug delivery systems. *Adv. Drug Delivery Rev.* **1997,** *25* (1), 47-58.

16. Zhou, H.; Yue, Y.; Liu, G.; Li, Y.; Zhang, J.; Gong, Q.; Yan, Z.; Duan, M. Preparation and characterization of a lecithin nanoemulsion as a topical delivery system. *Nanoscale Res. Lett.* **2009,** *5* (1), 224 - 230.

17. Fryd, M. M.; Mason, T. G. Nanoinclusions in cryogenically quenched nanoemulsions. *Langmuir* **2012,** *28* (33), 12015-12021.

18. Helgeson, M. E.; Gao, Y.; Moran, S. E.; Lee, J.; Godfrin, M.; Tripathi, A.; Bose, A.; Doyle, P. S. Homogeneous percolation versus arrested phase separation in attractively-driven nanoemulsion colloidal gels. *Soft Matter* **2014,** *10* (17), 3122-3133.

19. Delmas, T.; Piraux, H.; Couffin, A. C.; Texier, I.; Vinet, F.; Poulin, P.; Cates, M. E.; Bibette, J. How to prepare and stabilize very small nanoemulsions. *Langmuir* **2011,** *27* (5), 1683-1692.

20. Zhang, J.; Han, B.; Zhang, C.; Li, W.; Feng, X. Nanoemulsions induced by compressed gases. *Angew. Chem. Int. Ed.* **2008,** *47* (16), 3012-3015.

21. López-Montilla, J. C.; Herrera-Morales, P. E.; Shah, D. O. New method to quantitatively determine the spontaneity of the emulsification process. *Langmuir* **2002,** *18* (11), 4258-4262.

22. Rang, M.-J.; Miller, C. A. Spontaneous emulsification of oils containing hydrocarbon, nonionic surfactant, and oleyl alcohol. *J. Colloid Interface Sci.* **1999,** *209* (1), 179-192.

23. Kini, G. C.; Biswal, S. L.; Wong, M. S.; Miller, C. A. Characteristics of spontaneously formed nanoemulsions in octane/AOT/brine systems. *J. Colloid Interface Sci.* **2012,** *385* (1), 111-121.

24. Gutiérrez, J. M.; González, C.; Maestro, A.; Solè, I.; Pey, C. M.; Nolla, J. Nano-emulsions: New applications and optimization of their preparation. *Curr. Opin. Colloid Interface Sci.* **2008,** *13* (4), 245-251.

25. Porras, M.; Solans, C.; Gonzélez, C.; Martínez, A.; Guinart, A.; Gutiérrez, J. M. Studies of formation of W/O nano-emulsions. *Colloids Surf., A* **2004,** *249* (1-3), 115-118.

26. Roger, K.; Cabane, B.; Olsson, U. Emulsification through surfactant ydration: The PIC process revisited. *Langmuir* **2010,** *27* (2), 604-611.

27. Solè, I.; Solans, C.; Maestro, A.; González, C.; Gutiérrez, J. M. Study of nano-emulsion formation by dilution of microemulsions. *J. Colloid Interface Sci.* **2012,** *376* (1), 133-139.

28. Solans, C.; Solé, I. Nano-emulsions: Formation by low-energy methods. *Curr. Opin. Colloid Interface Sci.* **2012,** *17* (5), 246-254.

29. Langer, R. New methods of drug delivery. *Science* **1990,** *249* (4976), 1527-1533.

30. Langer, R. Drug delivery and targeting. *Nature* **1998,** *392* (6679), 5-10.

31. Zhang, L.; Gu, F. X.; Chan, J. M.; Wang, A. Z.; Langer, R. S.; Farokhzad, O. C. Nanoparticles in medicine: Therapeutic applications and developments. *Clin. Pharmacol. Ther.* **2008,** *83* (5), 761-769.

32. Chan, J. M.; Zhang, L.; Yuet, K. P.; Liao, G.; Rhee, J.-W.; Langer, R.; Farokhzad, O. C. PLGA–lecithin–PEG core–shell nanoparticles for controlled drug delivery. *Biomaterials* **2009,** *30* (8), 1627-1634.

33. Hoeller, S.; Sperger, A.; Valenta, C. Lecithin based nanoemulsions: A comparative study of the influence of non-ionic surfactants and the cationic phytosphingosine on physicochemical behaviour and skin permeation. *Int. J. Pharm.* **2009,** *370* (1-2), 181-186.

34. Rajera, R.; Nagpal, K.; Singh, S. K.; Mishra, D. N. Niosomes: A controlled and novel drug delivery system. *Biol. Pharm. Bull.* **2011,** *34* (7), 945-953.

35. McClements, D. J. Encapsulation, protection, and release of hydrophilic active components: Potential and limitations of colloidal delivery systems. *Adv. Colloid Interface Sci.* **2015,** *219*, 27-53.

36. Lee, H. S.; Morrison, E. D.; Frethem, C. D.; Zasadzinski, J. A.; McCormick, A. V. Cryogenic electron microscopy study of nanoemulsion formation from microemulsions. *Langmuir* **2014,** *30* (36), 10826-10833.

37. Solè, I.; Maestro, A.; Pey, C. M.; González, C.; Solans, C.; Gutiérrez, J. M. Nano-emulsions preparation by low energy methods in an ionic surfactant system. *Colloids Surf., A* **2006,** *288* (1-3), 138-143.

38. Uchiyama, H.; Acosta, E.; Tran, S.; Sabatini, D. A.; Harwell, J. H. Supersolubilization in chlorinated hydrocarbon microemulsions: Solubilization enhancement by lipophilic and hydrophilic linkers. *Ind. Eng. Chem. Res.* **2000,** *39* (8), 2704-2708.

39. Nishimi, T.; Miller, C. A. Spontaneous emulsification of oil in aerosol-OT/water/hydrocarbon systems. *Langmuir* **2000,** *16* (24), 9233-9241.

40. Miller, C. A. Spontaneous emulsification: Recent developments with emphasis on self-emulsification. In *Emulsions and emulsion stability*, Johan, S., Ed.; CRC Press: Boca Raton, 2006, pp 107-126.

41. Sabatini, D. A.; Acosta, E.; Harwell, J. H. Linker molecules in surfactant mixtures. *Curr. Opin. Colloid Interface Sci.* **2003,** *8* (4–5), 316-326.

42. Koppel, D. E. Analysis of macromolecular polydispersity in intensity correlation spectroscopy: The method of cumulants. *J. Chem. Phys.* **1972,** *57* (11), 4814-4820.

43. Hassan, P. A.; Rana, S.; Verma, G. Making sense of brownian motion: Colloid characterization by dynamic light scattering. *Langmuir* **2014,** *31* (1), 3-12.

44. Burauer, S.; Sachert, T.; Sottmann, T.; Strey, R. On microemulsion phase behavior and the monomeric solubility of surfactant. *Phys. Chem. Chem. Phys* **1999,** *1* (18), 4299-4306.

45. Sottmann, T.; Stubenrauch, C. Phase behaviour, interfacial tension and microstructure of microemulsions. In *Microemulsions*; John Wiley & Sons, Ltd, 2009, pp 1-47.

46. Bansal, V. K.; Shah, D. O.; O'Connell, J. P. Influence of alkyl chain length compatibility on microemulsion structure and solubilization. *J. Colloid Interface Sci.* **1980,** *75* (2), 462-475.

47. Anton, N.; Gayet, P.; Benoit, J. P.; Saulnier, P. Nano-emulsions and nanocapsules by the PIT method: An investigation on the role of the temperature cycling on the emulsion phase inversion. *Int. J. Pharm.* **2007,** *344* (1-2), 44-52.

48. Forgiarini, A.; Esquena, J.; González, C.; Solans, C. Formation and stability of nano-emulsions in mixed nonionic surfactant systems. *Prog. Colloid Polym. Sci.* **2001,** *118*, 184-189.

Chapter 6.
Lessons from Cryogenic Electron Microscopy*

6.1 Remark

The research investigated here presents microstructural characterization of soft materials using cryogenic electron microscopy (cryo-EM), small angle X-ray scattering and other techniques. Of these characterization techniques, the aim of cryo-EM is to keep liquid or liquid-like soft materials in a low vapor pressure status by lowering temperature so that they can be preserved in a high vacuum for cryo-EM. Although cryo-EM provides a direct structural analysis of materials, this technique can also create artifacts in the image.[1] Any microstructure which does not represent the original status of that soft material could be an artifact.

Careless handling of the sample during specimen preparation can alter the original status of the soft materials. To prevent artifact formation during the specimen preparation, it is important to achieve a complete vitrification by avoiding spinodal decomposition, crystal nucleation, and crystal growth in the sample. In addition, the sample should be minimally exposed to the atmosphere during sample transfer so that adsorption of moisture or contaminants to the surface of the cold specimen is prevented. Artifacts also could be produced by an interaction between the sample and an incoming electron beam. The soft material is very sensitive to high-energy beam, therefore it is central to suppress radiolytic effects by limiting the number of the incoming electrons which interact with the sample. Inexperience in cryo-EM can also damage the sample. Lastly, wrong interpretation of the micrograph can mislead. To correctly interpret micrographs, it is critical to train on how

* Portions of this chapter were done in collaboration with Dr. Benjamin Wong in the Zasadzinski research group in University of California, Santa Barbara and Prof. Zasadainski's collaborators in the Epand research group at McMaster University.

to distinguish the artifacts in the specimen. This chapter briefly describes sample fixation and common artifacts in cryo-EM.

Sample fixation

A correct sample preparation protocol is important to elucidate microstructure of soft materials in high vacuum (~ 10^{-9} Pa).[2, 3, 4] Chemical fixation or thermal (physical) fixation methods are used for EM characterization. Although chemical fixation is frequently used in histology to study animal or plant tissues, this method introduces compounds to the sample and can possibly disturb the original status of sample.[5, 6] Thermal fixation by freezing is an alternative way to overcome the drawbacks of the chemical fixation. In thermal fixation, cooling rate is fast enough to immobilize the sample, so the original status is preserved. There is no rearrangement of the microstructure in the sample because heat transport is faster than mass transport in the sample.

Vitrification of the sample and thickness control are two major factors in thermal fixation for cryogenic transmission electron microscopy (cryo-TEM) specimen. In order to prevent microstructural rearrangement in the sample, a rapid cooling rate (~10^5 °C/sec) should be attained in plunge freeze method.[7, 8] To successfully vitrify the sample, melting point of cryogen should be below the glass-transition temperature of the sample. The difference between the melting point and boiling point of the cryogen needs to be large enough to take out heat from the sample efficiently, preventing the Leidenfrost effect (formation of insulating vapor on the surface of the sample). The cryogen should have a large thermal conductivity and heat capacity, high density, and low viscosity. Extensive studies on the cryogen show liquid ethane is one of the most efficient cryogens.[9] Table 6.1 lists characteristics of the selected cryogens.[10, 11] In a manual plunge method, eutectic mixture of propane and ethane can be used to achieve lower temperature.[12]

Controlling the film thickness of the sample is another important factor in thermal fixation. The sample should be thin enough so that incident beam can transmit through the sample and produce an image. The thickness of the specimen is mainly controlled by two parameters: blotting offset (strength of blotting using filter paper) and blotting hold time. The optimum thickness suitable for cryo-TEM imaging is about 100–250 nm. The

thickness of the sample on the TEM grid can be determined by observing interference colors with stereomicroscope.[13] Typical Vitrobot parameters used in our studies are: -2–0 mm in blotting offset, 2–5 seconds in blotting time, 0–2 seconds in wait time (the time the sample loaded specimen in the chamber before blotting), and 0–3 seconds in drain time (the time the blotted grid is held in the chamber before plunging).

Table. 6.1. Characteristic of popular cryogens for cryo-EM experiment.[10]

Cryogen	Melting point (°C)	Boiling point (°C)	Density (g/cm^3)	Specific heat capacity (J/g-K)	Thermal conductivity (W/cm-K)	Viscosity (PaS)
Nitrogen	-210.0	-195.8	0.868	2.0	1.53	0.27
Ethane	-183.2	-88.6	0.655	2.27	2.4	0.9
Propane	-187.1	-42.1	0.8	1.92	1.92	1.9

Artifacts in cryo-TEM

Proper selection of cryogen is important for a complete vitrification of the specimen. Figure 6.1 shows typical artifacts of distilled water (polar) or *n*-octane (non-polar) quenched in liquid ethane and liquid nitrogen. Figure 6.1a shows successfully vitrified thin water film in the liquid ethane. However, Figure 6.1b shows hexagonal ice crystal artifacts developed as a result of slow cooling in liquid nitrogen. The bend contours in Figure. 6.1b are grain boundaries and stacking faults of the water crystal.[14] The hexagonal ice crystals are mobile structures with wave shape and rate of motion depending on the amount of electron dose they receive. The arrow in Figure 6.1c is *n*-octane quenched in the liquid ethane. The solubility of non-polar liquids in alkane cryogens is high at low temperature. As a result, *n*-octane is dissolved in liquid ethane cryogen and formed needle-shaped crystal structures. On the contrary, liquid nitrogen successfully vitrified liquid *n*-octane and a textured *n*-octane film is shown in Figure 6.1d. Bright spots on the bottom of Figure 6.1d indicate a hollow area (no film) and the rest of the micrograph (red arrow) shows a vitreous *n*-octane film. To minimize an incomplete vitrification or interaction between sample and cryogen, it is important to choose a suitable cryogen for physical fixation.

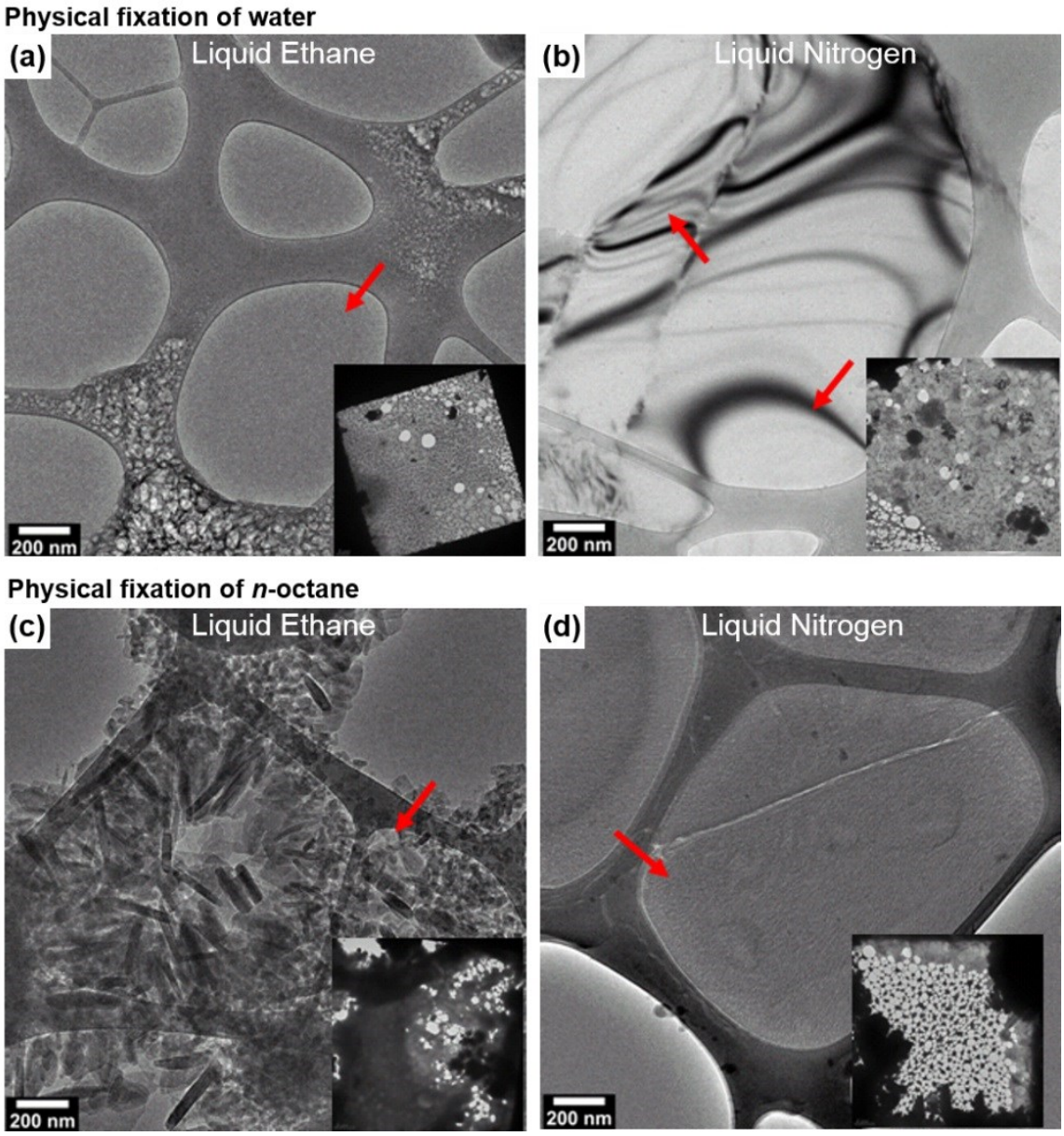

Figure 6.1. Typical cryo-TEM micrographs of distilled water and *n*-octane quenched in liquid nitrogen and liquid ethane, respectively. (a) Vitrification of distilled water in the liquid ethane. Red arrow indicates vitrified thin film. (b) Vitrification of distilled water quenched in the liquid nitrogen. Red arrows indicate hexagonal ice crystals. (c) Vitrification of *n*-octane quenched in the liquid ethane. Red arrow indicates result of interaction between *n*-octane and liquid ethane. (d) Vitrification of *n*-octane quenched in the liquid nitrogen. Red arrow indicates vitrified thin film. Insets (right below of each image) are low magnification images.

The physical fixation method also introduces another type of artifacts in the specimen. Figure 6.2 shows an example of third phase inclusion in the aqueous sample during quenching. The red arrow in Figure 6.2a shows deposited ethane on the grid. The aggregated ethane crusts are formed when the specimen is plunged into the liquid ethane. These artifacts quickly sublime because the frozen ethane has a high vapor in the high vacuum microscopy. Slow cooling also creates cubic ice crystals shown in Figure 6.2b. Hexagonal ice crystals in Figure 6.2c are formed because either impurities in the cryogen were deposited or vapors were condensed when the specimen is exposed in the atmosphere during sample transferring.[15, 16] The vitrified specimen is inevitably exposed to the atmosphere when it is transferred from the cryogen to a cryo-grid box. Inset in Figure 6.2c shows electron diffraction of hexagonal ice crystals.

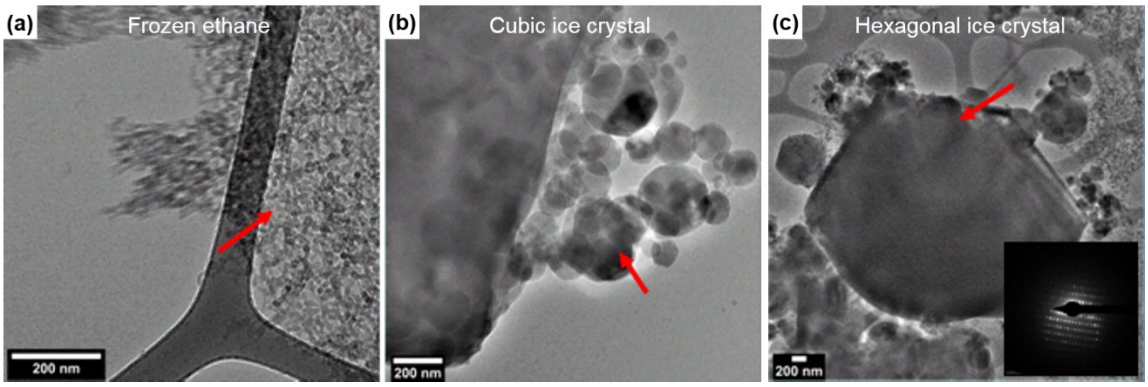

Figure 6.2. Typical cryo-TEM micrographs show artifacts. (a) Frozen ethane, (b) cubic ice crystal, and (c) hexagonal ice crystal.

Ice crystal artifacts on the grid are problematic because they disturb the original status of the sample and distort images. First, nucleation and growth of ice crystal segregates the aqueous matrix from other solutes because different melting temperature and thermal coefficients in the sample results phase/domain reconstruction or optical distortion. Second, the huge ice particles diffract incident electrons and, therefore, it results in optical alteration (e.g., contrast variation and moiré fringe). Finally, this diffracted electrons damage the microstructures located in the vicinity of the ice crystal artifacts.

Shearing effect occurs while the excess liquid sample is blotted on the grid. Filter papers remove the excess liquids from the thickness of 1–2 mm to that of 100–250 nm. The shear rate which is in the order of 10^5 s^{-1} causes the blotting flow to distort the microstructure of the soft materials.[17, 18, 19] The shear stress in the liquid or liquid-like sample can be released by allowing drain time before plunging into the cryogen.[20,21,22,23,24]

Thickness gradient in the blotted grid causes segregation of microstructure in the soft materials. The center of holey carbon grid is the thinnest part and periphery of the film (nearby the polymer carbon strut) is the thickest part due to surface tension effect. For this reason, microstructures are rearranged in the meniscus shaped film after the blotting. This behavior alters the original distribution of the soft materials. Figure 6.3a shows example of size segregation of nanoemulsions. In Figure 6.3b, sample is concentrated in the Quantifoil (Quantifoil Micro Tools, Jena, Germany) TEM grid and lost original status because of a space restriction in the TEM grid. The blotting process may exclude some structures in the sample larger than the thickness of the film. If they are not excluded, their original status may be severely distorted, resulting in a flattened or squeezed shape.

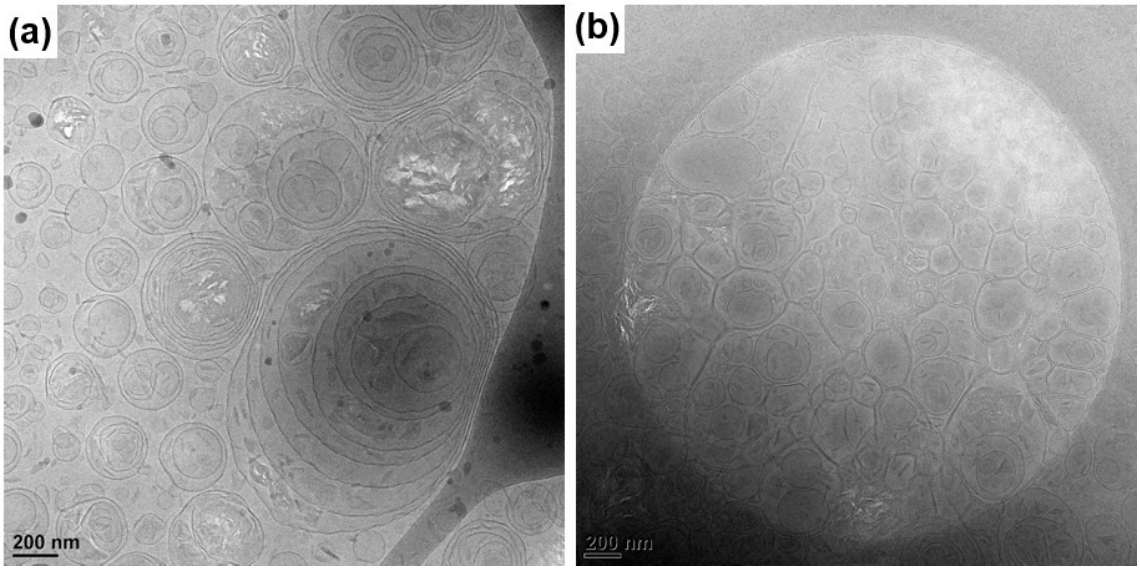

Figure 6.3. Representative cryo-TEM micrographs of fresh nanoemulsions of H_2O/*n*-hexadecane/alkylphenol nonionic surfactants microemulsions, showing size segregation because of meniscus shaped the blotted thin film. (a) Large structures are deformed and pushed to the edge of the film in 2.2 parts per hundred (pph) cosurfactant. (b) The microstructure of 4.0 pph cosurfactant is distorted because of space restriction in the TEM grid.

Beam damage artifacts can also appear during electron microscopy. The interaction between high-energy electrons and the sample leads to structural changes. Artifacts from electron beam damage in the microemulsions are mainly the result of primary events such as plasma excitation, ionization of valence electrons, and creation of electron-hole pairs.[25] These are described, for instance, in ref. 25. To summarize, first, the incoming beam interacts with the electrons in a shell level and generates a plasma excitation. This excitation generates heat energy and elevates the temperature of the surroundings (The cold finger connected to the liquid nitrogen reservoir in the cryo-holder may suppress local heating in the sample.). Second, the ionized valence electron can break weak interatomic bonding in the soft materials. Otherwise, the valence electrons are directly ionized by the incident beam. Lastly, the incoming electrons produce the electron-hole pairs. This generated exciton have a high stored energy and long lifetime. When the exciton transfers to the neighboring atom, it may dislocate the atom from its original position. This radiolysis process is enhanced by the presence of the ice crystals. The ice crystals are good source of free radicals in the soft materials. As a result, the sample suffers from the rearrangement of atomic structure and destruction. Figure 6.4 shows typical beam damaged micrograph of *n*-octane sample. Low dose imaging (typically, $<20\ e^{-}/Å^{2}$) can help to reduce beam damage of the sample.

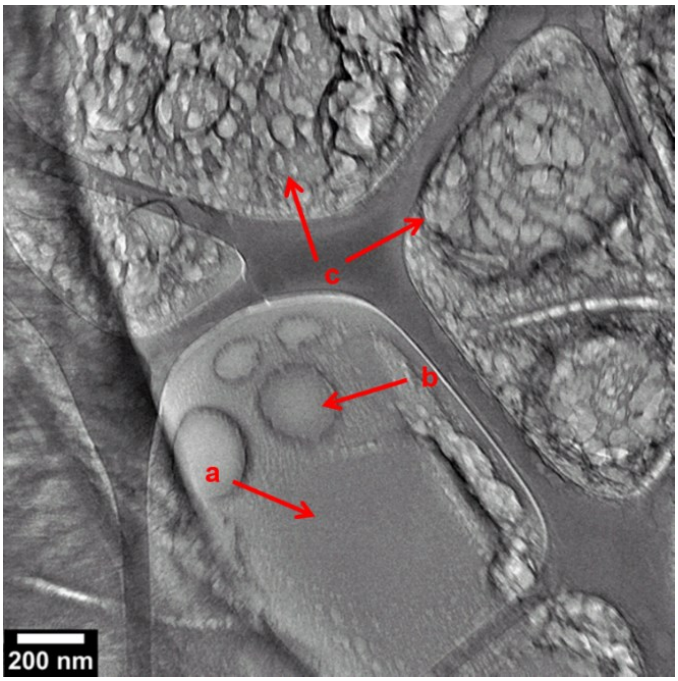

Figure 6.4. Typical cryo-TEM micrograph of beam-damaged *n*-octane. (a) No beam damage. (b) Initiation of beam damage. White bubble marks begin to appear in the sample. (c) Completion of beam damage. Blister-like structures form after beam irradiation.

The degree of destruction is related to the amount of electron exposure and the sample thickness. When the sample is thick enough to withstand the incoming electrons, the beam damage is observed as initiation of white bubble and development of blister-like structure. However, when the vitrified film is not strong enough to endure the incident beam, the film immediately disappears and this process is shown in Figure 6.5.

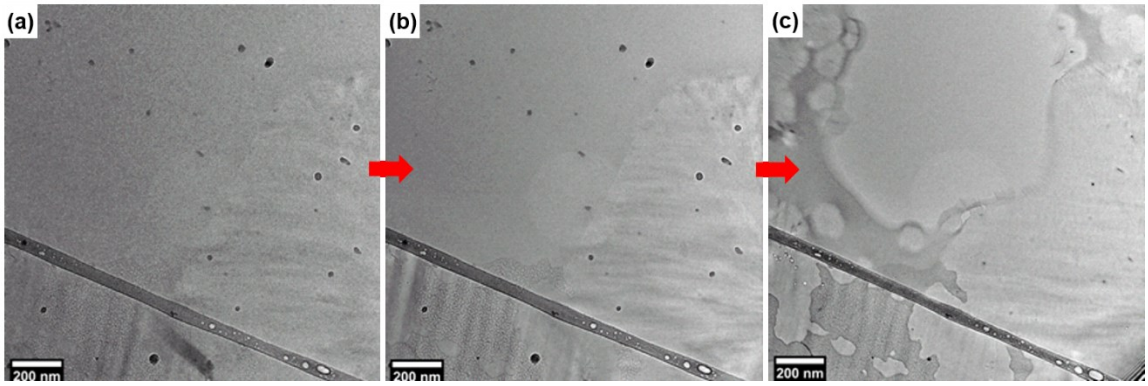

Figure 6.5. Typical cryo-TEM micrographs of oil-in-water type microemulsion of H_2O/*n*-octane/pentaethylene glycol monododecyl ether ($C_{12}E_5$), $\gamma_a = 0.022$, $w_B = 0.04$ at T = 26.1 °C. A series of micrograph shows development of beam damage in the film.

The low contrast (relative difference in intensity between the sample and its surrounding) in soft materials hard to image good micrographs without help of phase contrast. Therefore by defocusing the image, the formation of Fresnel fringes in different mass thickness part delineate the microstructure in the sample. The Fresnel fringes are bright lines in underfocused mode and are dark lines in overfocused mode. When the sample is in focus, there is no phase effects and therefore Fresnel fringes are gone. As long as the sample is not beam damaged, it is a good idea to acquire a series of focus images to observe microstructure of the sample (Figure A7). The nominal underfocus during imaging was 2–4 μm and the Cs (spherical aberration) value of the FEI Tecnai G^2 Spirit BioTWIN instrument was 6.3 mm.

Another tip in preparing cryo-TEM sample with the plunge freeze method is handling of the specimen. The prepared specimen in a cryo grid box (160−41, Ted Pella, Ltd., Redding, CA) is often stuck to the bottom of cryo grid box handling rod (160−46, Ted Pella, Ltd., Redding, CA). Electrostatic attraction between copper TEM grid and Teflon® handling rod mess up the order of TEM grid in the cryo grid box. To avoid sticking problem between Teflon based cryo-handling rod and the copper TEM grid, it is important to make sure the sample is fully inserted in the storage box or try a different sample storage box, cryo grid box with lid (160-40, Ted Pella, Ltd., Redding, CA). In addition, the sample could be misplaced or lost because of bubble from the bottom of the Gatan 626 cryo-transfer station. By putting a rolled filter paper in the hole of the cryo-transfer station, we can prevent loss of the sample.

Artifacts in cryo-SEM

Electrostatic charging on a surface of a sample is main artifact in cryo-SEM characterization (Hitachi S-900 In-Lens SEM). This is because we attempted SEM with non-conductive sample (though Pt is coated with electron sputtering) and charge neutrality on the surface is not maintained. As a result, when the electron from the specimen is not compensated, positive electron charges are accumulated onto the specimen. An advanced microscope can minimize electrical charging of the specimen by using a low acceleration voltage, short dwell times per pixel, high condenser number, and dissipation of the local charging by achieving neutrality (number of incoming electron = number of electrons emitted from the specimen).[26] Figure 6.6 shows electrical charged sample. The raster and very bright images represent charge buildup. Severely charged sample also can drift in the monitor.

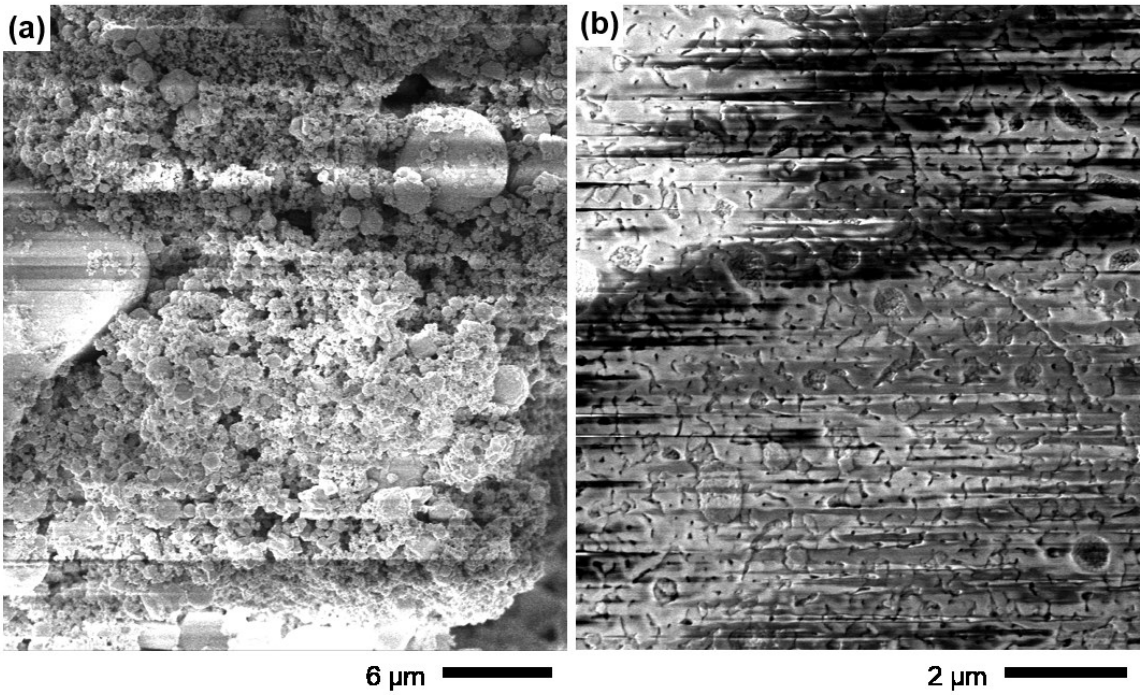

Figure 6.6. Typical cryo-SEM micrographs of electrically charged sample. The images are fresh nanoemulsions of H_2O/*n*-hexadecane/alkylphenol nonionic surfactants with 4.0 parts per hundred cosurfactant.

Ice crystal artifacts also observed in cryo-SEM. Aggregated spheres in Figure 6.6a and Figure 6.7b indicate ice crystals may be deposited on the fractured surface of the sample. Figure 6.7a shows ice crystals are formed during the cryo-holder transfer when it is exposed in the atmosphere.

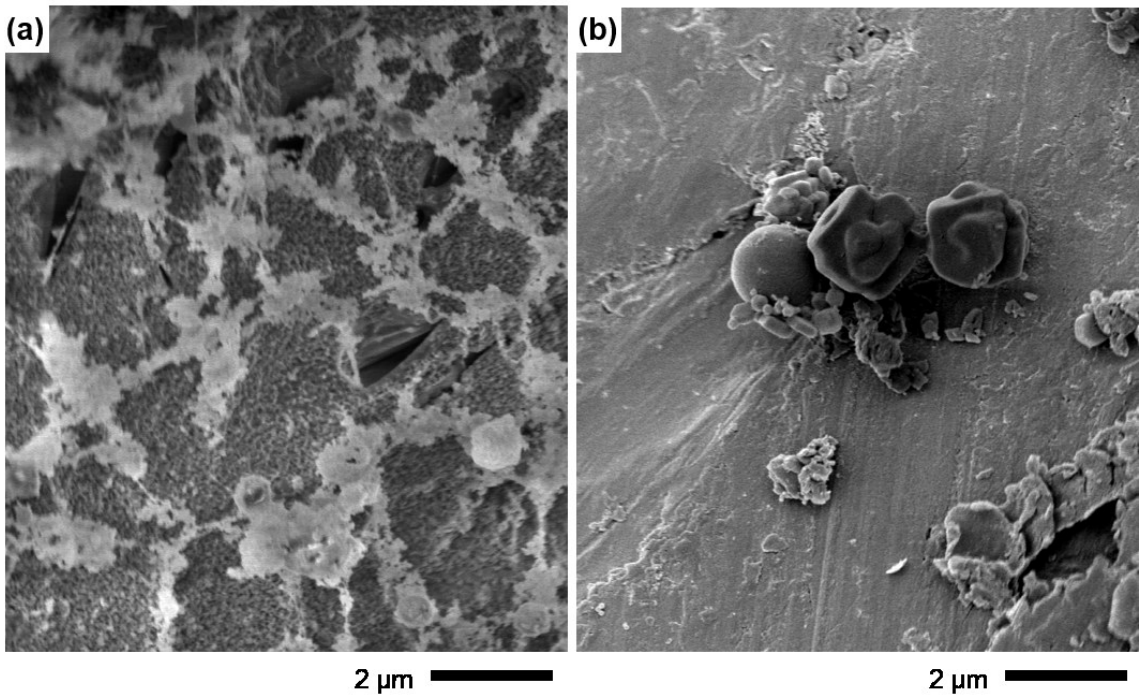

Figure 6.7. Typical cryo-SEM micrographs with ice crystal artifacts. (a) Fresh nanoemulsions of H_2O/*n*-hexadecane/alkylphenol nonionic surfactants with 2.2 parts per hundred cosurfactant. (b) Standard polystyrene (500 nm) nanoparticles.

An additional tip to minimize artifacts in cryo-SEM specimen preparation is applying sample in the copper planchette hat without allowing bubbles. Void space in the specimen assembly could potentially cause a phase separation during high pressure freeze. To avoid deposition or condensation of ice crystals on the fractured surface of the specimen, reduce the dwell time in the nitrogen liquid bath by quickly proceed to the next steps and minimize inflow of water vapor into the liquid nitrogen bath by wearing a surgical mask.

Sublimation is not always necessary to uncover the microstructure of the sample. If sublimation of the sample is required in the low temperature sputtering device, prepare a series of sample which is sublimed at different temperature or time. It is important all frozen samples should be maintained in the liquid nitrogen and minimize exposure to the atmosphere.

Artifacts in FF-TEM

Freeze fracture electron microscopy (FF-TEM) is preparing a replica of the sample by Pt-C sputtering in the low temperature.[7] Some representative and crucial artifacts are explained in following paragraphs. Figure 6.8a and 6.8b show possible artifacts arising from bare copper planchette surface when the sample is not completely coated on the surface of copper or oxidized layer of the copper planchettes is not completely etched with a nitric acid.

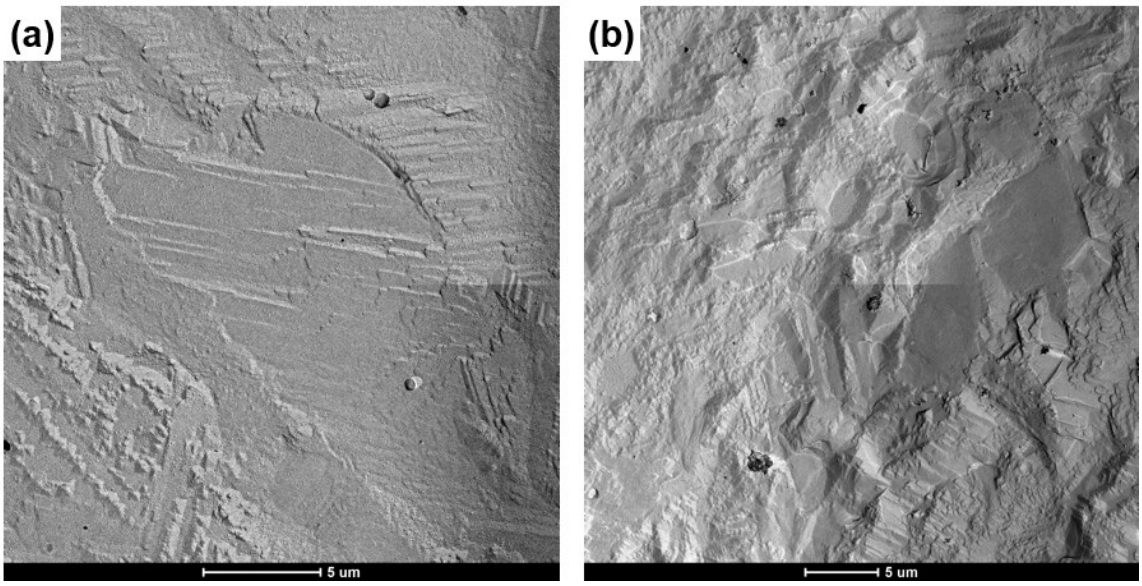

Figure 6.8. Typical FF-TEM micrographs of copper planchette. The images are replicas of bare copper planchette. Both images show textured surface and some knife marks from fracturing (repetitive oblique or straight line).

Water vapor or ice also can be deposited on the surface of the sample. Figure 6.9a shows ice inclusions and they appear as dark aggregates in the replica. Contaminant inclusion results from copper specimen carrier from adsorption of third phase during fracture, or attachment during replica processing are problematic in characterization of the sample. An example of contaminant (grey colored patches) is shown in Figure 6.9b.

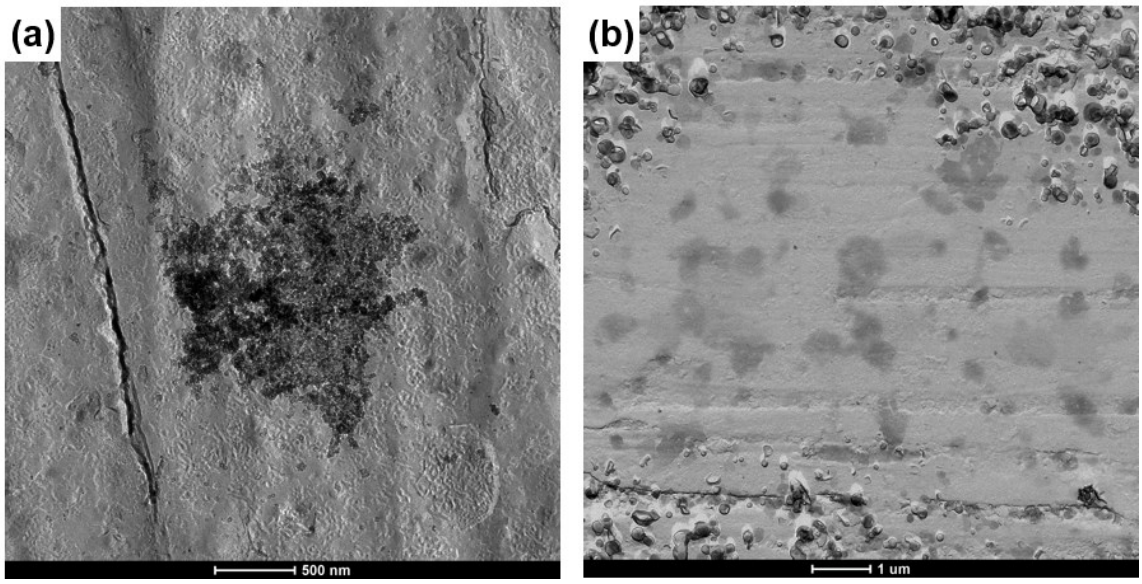

Figure 6.9. Typical FF-TEM micrographs of lipid vesicle. (a) Ice inclusion on the surface of the replica. (b) Grey patches are contaminants.

When bubbles are included with the sample, it is important to get rid of bubbles and excess sample by carefully blotting it with the edges of a filter paper on the both side of the specimen carrier. However, blotting for too long could adsorb entire sample. The bubble may disturb the sample and the example is shown in Figure 6.10a. In addition, incomplete adhesion between the sample and surface of copper planchette can cause rough surface as shown in Figure 6.10b. This makes it difficult to distinguish the microstructure of the sample from background.

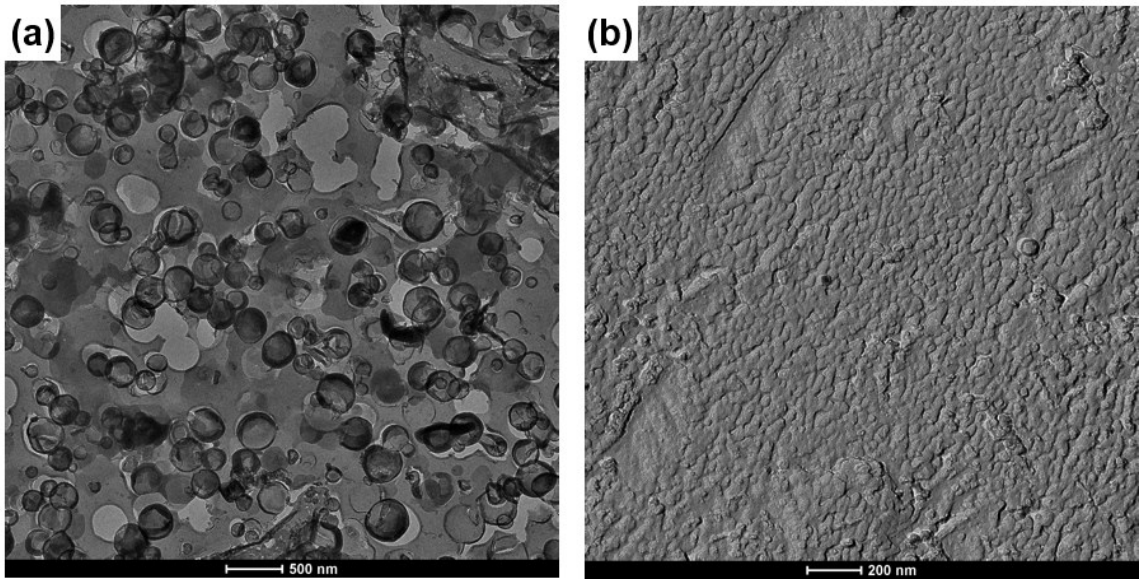

Figure 6.10. Typical FF-TEM micrographs show artifacts. (a) Bubbles in the surface of the replica of lipid vesicle. (b) Settling in pep-1, cell penetrating peptide.

Successfully prepared FF-TEM micrographs are shown in Figure 6.11. Figure 6.11a shows pep-1, cell penetrating peptide. The smooth background in Figure 6.11a is vitrified aqueous solution. It does not contain any ice crystals, bubbles or third phase inclusions, and the replica does not undergo rupture or folding during replica processing. Figure 6.11b shows fresh nanoemulsions with 4.0 parts per hundred cosurfactant. Excess nonylphenol cosurfactant gave complex and large nanoemulsions and the micrograph shows large structure represented as bumps, divots, and cross-fractured forms.

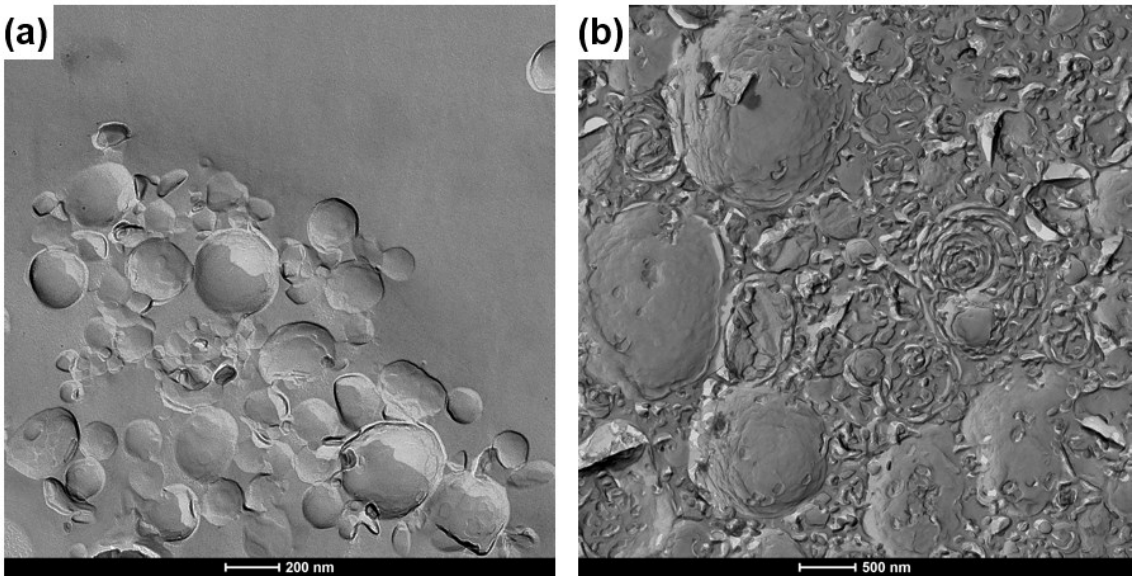

Figure 6.11. Typical FF-TEM micrographs. (a) Pep-1, cell penetrating peptide. (b) Fresh nanoemulsions of H_2O/*n*-hexadecane/alkylphenol nonionic surfactants with 4.0 parts per hundred cosurfactant.

6.2 References (Good references are marked with asterisk symbol)

1. Talmon, Y. Transmission electron miroscopy of complex fluids: The state of the art. *Ber. Bunsenges. physika. Chem.* **1996**, *100* (3), 364-372.*

2. Grassucci, R. A.; Taylor, D. J.; Frank, J. Preparation of macromolecular complexes for cryo-electron microscopy. *Nat. Protocols* **2007**, *2* (12), 3239-3246.*

3. Iancu, C. V.; Tivol, W. F.; Schooler, J. B.; Dias, D. P.; Henderson, G. P.; Murphy, G. E.; Wright, E. R.; Li, Z.; Yu, Z.; Briegel, A.; Gan, L.; He, Y.; Jensen, G. J. Electron cryotomography sample preparation using the Vitrobot. *Nat. Protocols* **2007**, *1* (6), 2813-2819.*

4. Grassucci, R. A.; Taylor, D. k.; Frank, J. Visualization of macromolecular complexes using cryo-electron microscopy with FEI Tecnai transmission electron microscopes. *Nat. Protocols* **2008**, *3* (2), 330-339.

5. Hayat, M. A. *Fixation for electron microscopy*; New York : Academic Press: New York, 1981.

6. Silva, M. T.; Carvalho Guerra, F.; Magalhães, M. M. The fixative action of uranyl acetate in electron microscopy. *Experientia* **1968**, *24* (10), 1074-1074.

7. Zasadzinski, J. A. N.; Bailey, S. M. Applications of freeze-fracture replication to problems in materials and colloid science. *J. Electron Micr. Tech.* **1989**, *13* (4), 309-334.

8. Echlin, P. *Low-temperature microscopy and analysis*; New York : Plenum Press: New York, 1992.

9. Siegel, D. P.; Green, W. J.; Talmon, Y. The mechanism of lamellar-to-inverted hexagonal phase transitions: A study using temperature-jump cryo-electron microscopy. *Biophys. J.* **1994**, *66* (2 Pt 1), 402-414.

10. *CRC handbook of chemistry and physics : A ready-reference book of chemical and physical data*; CRC Press: Boca Raton, Fla., 2009.

11. Cui, H.; Hodgdon, T. K.; Kaler, E. W.; Abezgauz, L.; Danino, D.; Lubovsky, M.; Talmon, Y.; Pochan, D. J. Elucidating the assembled structure of amphiphiles in solution via cryogenic transmission electron microscopy. *Soft Matter* **2007**, *3*, 945-955.*

12. Tivol, W. F.; Briegel, A.; Jensen, G. J. An improved cryogen for plunge freezing. *Microsc. Microanal.* **2008**, *14* (5), 375-379.

13. Bellare, J. R.; Davis, H. T.; Scriven, L. E.; Talmon, Y. Controlled environment vitrification system: An improved sample preparation technique. *J. Electron Microsc. Tech.* **1988**, *10* (1), 87-111.

14. Talmon, Y.; Davis, H. T.; Scriven, L. E.; Thomas, E. L. Cold-stage microscopy system for fast-frozen liquids. *Rev. Sci. Instrum.* **1979**, *50* (6), 698-704.

15. Dubochet, J.; McDowall, A. W. Vitrification of pure water for electron microscopy. *J. Microsc.* **1981**, *124* (3), 3-4.

16. Dubochet, J.; Lepault, J.; Freeman, R.; Berriman, J. A.; Homo, J. C. Electron microscopy of frozen water and aqueous solutions. *J. Microsc.* **1982**, *128* (3), 219-237.

17. Adrian, M.; Dubochet, J.; Lepault, J.; McDowall, A. W. Cryo-electron microscopy of viruses. *Nature* **1984**, *308* (5954), 32-36.

18. Bachmann, L.; Talmon, Y. Cryomicroscopy of liquid and semiliquid specimens: Direct imaging versus replication. *Ultramicroscopy* **1984**, *14* (3), 211-218.

19. Talmon, Y. Imaging surfactant dispersions by electron microscopy of vitrified specimens. *Colloids Surf.* **1986**, *19* (2–3), 237-248.*

20. Jain, S. Aqueous mixtures of block copolymer surfactants. Ph.D., University of Minnesota 2005.*

21. Roux, D. C.; Berret, J.-F.; Porte, G.; Peuvrel-Disdier, E.; Lindner, P. Shear-induced orientations and textures of nematic living polymers. *Macromolecules* **1995**, *28* (5), 1681-1687.

22. Wunderlich, I.; Hoffmann, H.; Rehage, H. Flow birefringence and rheological measurements on shear induced micellar structures. *Rheol. Acta* **1987**, *26* (6), 532-542.

23. Bates, F. S.; Koppi, K. A.; Tirrell, M.; Almdal, K.; Mortensen, K. Influence of shear on the hexagonal-to-disorder transition in a diblock copolymer melt. *Macromolecules* **1994**, *27* (20), 5934-5936.

24. Shahidzadeh, N.; Bonn, D.; Aguerre-Chariol, O.; Meunier, J. Large deformations of giant floppy vesicles in shear flow. *Phys. Rev. Lett.* **1998**, *81* (19), 4268-4271.

25. Talmon, Y. *Cryotechniques in biological electron microscopy*; Berlin, New York : Springer-Verlag: Berlin, New York, 1987.

26. Goldstein, J. I. *Scanning electron microscopy and X-ray microanalysis*; Third edition.. ed.; Boston, MA : Springer US: Boston, MA, 2003.

Bibliography

- Adrian, M.; Dubochet, J.; Lepault, J.; McDowall, A. W. Cryo-electron microscopy of viruses. *Nature* **1984**, *308* (5954), 32-36.
- Aggarwal, B. B.; Harikumar, K. B. Potential therapeutic effects of curcumin, the anti-inflammatory agent, against neurodegenerative, cardiovascular, pulmonary, metabolic, autoimmune and neoplastic diseases. *Int. J. Biochem. Cell Biol.* **2009,** *41* (1), 40-59.
- Allen, T. M.; Cullis, P. R. Drug delivery systems: Entering the mainstream. *Science* **2004,** *303* (5665), 1818-1822.
- Almgren, M.; Gimel, J. C.; Wang, K.; Karlsson, G.; Edwards, K.; Brown, W.; Mortensen, K. SDS micelles at high ionic strength. A light scattering, neutron scattering, fluorescence quenching, and cryoTEM investigation. *J. Colloid Interface Sci.* **1998,** *202* (2), 222-231.
- Akpinar, E.; Reis, D.; Figueiredo Neto, A. M. In *Investigation of the interaction of alkali ions with surfactant head groups for the formation of lyotropic biaxial nematic phase via optical birefringence measurements*, Society of Photo-Optical Instrumentation Engineers, San Francisco, California, USA, February 2, 2013; 2013; SPIE, pp 864203-864208.
- Anton, N.; Gayet, P.; Benoit, J. P.; Saulnier, P. Nano-emulsions and nanocapsules by the PIT method: An investigation on the role of the temperature cycling on the emulsion phase inversion. *Int. J. Pharm.* **2007,** *344* (1-2), 44-52.
- Anton, N.; Vandamme, T. F. The universality of low-energy nano-emulsification. *Int. J. Pharm.* **2009,** *377* (1-2), 142-147.
- Atkins, P. W.; De Paula, J. *Atkins' Physical Chemistry*; Oxford University Press 2002.
- Bachmann, L.; Talmon, Y. Cryomicroscopy of liquid and semiliquid specimens: Direct imaging versus replication. *Ultramicroscopy* **1984**, *14* (3), 211-218

- Bales, B. L.; Benrraou, M.; Zana, R. Krafft temperature and micelle ionization of aqueous solutions of cesium dodecyl sulfate. *J. Phys. Chem. B* **2002,** *106* (35), 9033-9035.
- Bansal, V. K.; Shah, D. O.; O'Connell, J. P. Influence of alkyl chain length compatibility on microemulsion structure and solubilization. *J. Colloid Interface Sci.* **1980,** *75* (2), 462-475.
- Bates, F. S.; Koppi, K. A.; Tirrell, M.; Almdal, K.; Mortensen, K. Influence of shear on the hexagonal-to-disorder transition in a diblock copolymer melt. *Macromolecules* **1994**, *27* (20), 5934-5936.
- Bellare, J. R.; Davis, H. T.; Scriven, L. E.; Talmon, Y. Controlled environment vitrification system: An improved sample preparation technique. *J. Electron Microsc. Tech.* **1988**, *10* (1), 87-111.
- Bellare, J. R.; Kaneko, T.; Evans, D. F. Seeing micelles. *Langmuir* **1988,** *4* (4), 1066-1067.
- Bellare, J. R. Cryo-electron and optical microscopy of surfactant microstructures. Ph. D., University of Minnesota 1988.
- Benrraou, M.; Bales, B. L.; Zana, R. Effect of the nature of the counterion on the properties of anionic surfactants. 1. Cmc, ionization degree at the cmc and aggregation number of micelles of sodium, cesium, tetramethylammonium, tetraethylammonium, tetrapropylammonium, and tetrabutylammonium dodecyl sulfates. *J. Phys. Chem. B* **2003,** *107* (48), 13432-13440.
- Bilbao-Sáinz, C.; Avvena-Bustillos, R. J.; Wood, D. F.; Williams, T. G.; McHugh, T. H. Nanoemulsions prepared by a low-energy emulsification method applied to edible films. *J. Agric. Food Chem.* **2010,** *58* (22), 11932-11938.
- Binks, B. P. *Modern aspects of emulsion science*; Royal Society of Chemistry: Cambridge, 1998.
- Bisht, S.; Maitra, A. Dextran–doxorubicin/chitosan nanoparticles for solid tumor therapy. *Wiley Interdiscip. Rev. Nanomed. Nanobiotechnol.:* **2009,** *1* (4), 415-425

- Blackburn, J. C.; Kilpatrick, P. K. Transitional liquid crystalline phases between the hexagonal and lamellar phases in ternary cesium *n*-tetradecanoate-water-additive mixtures. *J. Colloid Interface Sci.* **1993,** *157* (1), 88-99.
- Bogner, A.; Jouneau, P. H.; Thollet, G.; Basset, D.; Gauthier, C. A history of scanning electron microscopy developments: Towards "wet-STEM" imaging. *Micron* **2007,** *38* (4), 390-401.
- Bollmann, W.; Spreadborough, J. Action of graphite as a lubricant. *Nature* **1960,** *186* (4718), 29-30.
- Burauer, S.; Belkoura, L.; Stubenrauch, C.; Strey, R. Bicontinuous microemulsions revisited: A new approach to freeze fracture electron microscopy (FFEM). *Colloids Surf., A* **2003,** *228* (1-3), 159-170.
- Burauer, S.; Sachert, T.; Sottmann, T.; Strey, R. On microemulsion phase behavior and the monomeric solubility of surfactant. *Phys. Chem. Chem. Phys* **1999,** *1* (18), 4299-4306.
- Cao, G. *Nanostructures and nanomaterials - Synthesis, properties and applications*; Imperial College Press: London, 2004.
- Chan, J. M.; Zhang, L.; Yuet, K. P.; Liao, G.; Rhee, J.-W.; Langer, R.; Farokhzad, O. C. PLGA–lecithin–PEG core–shell nanoparticles for controlled drug delivery. *Biomaterials* **2009,** *30* (8), 1627-1634.
- *CRC handbook of chemistry and physics : A ready-reference book of chemical and physical data*; CRC Press: Boca Raton, Fla., 2009.
- Cui, H.; Hodgdon, T. K.; Kaler, E. W.; Abezgauz, L.; Danino, D.; Lubovsky, M.; Talmon, Y.; Pochan, D. J. Elucidating the assembled structure of amphiphiles in solution via cryogenic transmission electron microscopy. *Soft Matter* **2007,** *3*, 945-955.
- Date, A. A.; Nagarsenker, M. S. Design and evaluation of self-nanoemulsifying drug delivery systems (SNEDDS) for cefpodoxime proxetil. *Int. J. Pharm.* **2007,** *329* (1–2), 166-172.
- Davis, K. P. Role of molecular architecture in amphiphilic dispersions. Ph.D., University of Minnesota 2009.

- Delmas, T.; Piraux, H.; Couffin, A. C.; Texier, I.; Vinet, F.; Poulin, P.; Cates, M. E.; Bibette, J. How to prepare and stabilize very small nanoemulsions. *Langmuir* **2011,** *27* (5), 1683-1692.
- Di Biasio, A.; Cametti, C.; Codastefano, P.; Tartaglis, P.; Rouch, J.; Chen, S. H. Phase behavior of dense three-component ionic microemulsions and electrical conductivity in the lamellar phase. *Phys. Rev. E* **1993,** *47* (6), 4258-4264.
- Dubochet, J.; Lepault, J.; Freeman, R.; Berriman, J. A.; Homo, J. C. Electron microscopy of frozen water and aqueous solutions. *J. Microsc.* **1982**, *128* (3), 219-237.
- Dubochet, J.; McDowall, A. W. Vitrification of pure water for electron microscopy. *J. Microsc.* **1981**, *124* (3), 3-4
- Duncan, R. Polymer conjugates as anticancer nanomedicines. *Nat. Rev. Cancer* **2006,** *6* (9), 688-701.
- Echlin, P. *Low-temperature microscopy and analysis*; New York : Plenum Press: New York, 1992.
- Falls, A. H. Electron microscopy and molecular theory of microstructured fluids (ice, frozen). Ph.D., University of Minnesota 1982.
- Feng, J.; Roche, M.; Vigolo, D.; Arnaudov, L. N.; Stoyanov, S. D.; Gurkov, T. D.; Tsutsumanova, G. G.; Stone, H. A. Nanoemulsions obtained via bubble-bursting at a compound interface. *Nat. Phys.* **2014,** *10* (8), 606-612.
- Fernandez, P.; André, V.; Rieger, J.; Kühnle, A. Nano-emulsion formation by emulsion phase inversion. *Colloids Surf., A* **2004,** *251* (1-3), 53-58.
- Ferrari, M. Cancer nanotechnology: Opportunities and challenges. *Nat. Rev. Cancer* **2005,** *5* (3), 161-171.
- Forgiarini, A.; Esquena, J.; González, C.; Solans, C. Formation and stability of nano-emulsions in mixed nonionic surfactant systems. *Prog. Colloid Polym. Sci.* **2001,** *118*, 184-189.
- Forgiarini, A.; Esquena, J.; González, C.; Solans, C. Formation of nano-emulsions by low-energy emulsification methods at constant temperature. *Langmuir* **2001,** *17* (7), 2076-2083.

- Frank, S.; Poncharal, P.; Wang, Z. L.; Heer, W. A. d. Carbon nanotube quantum resistors. *Science* **1998,** *280* (5370), 1744-1746.
- Fryd, M. M.; Mason, T. G. Nanoinclusions in cryogenically quenched nanoemulsions. *Langmuir* **2012,** *28* (33), 12015-12021.
- Gennes, P.-G. d. *The physics of liquid crystals*; Oxford : Clarendon Press New York : Oxford University Press: Oxford : New York, 1979.
- Gindy, M. E.; Panagiotopoulos, A. Z.; Prud'homme, R. K. Composite block copolymer stabilized nanoparticles: Simultaneous encapsulation of organic actives and inorganic nanostructures. *Langmuir* **2008,** *24* (1), 83-90.
- Goldstein, J. I. *Scanning electron microscopy and X-ray microanalysis*; Third edition.. ed.; Boston, MA : Springer US: Boston, MA, 2003.
- Graciaa, A.; Lachaise, J.; Cucuphat, C.; Bourrel, M.; Salager, J. L. Improving solubilization in microemulsions with additives. 1. The lipophilic linker role. *Langmuir* **1993,** *9* (3), 669-672.
- Graciaa, A.; Lachaise, J.; Cucuphat, C.; Bourrel, M.; Salager, J. L. Improving solubilization in microemulsions with additives. 2. Long chain alcohols as lipophilic linkers. *Langmuir* **1993,** *9* (12), 3371-3374.
- Grassucci, R. A.; Taylor, D. J.; Frank, J. Preparation of macromolecular complexes for cryo-electron microscopy. *Nat. Protocols* **2007**, *2* (12), 3239-3246.
- Grassucci, R. A.; Taylor, D. k.; Frank, J. Visualization of macromolecular complexes using cryo-electron microscopy with FEI Tecnai transmission electron microscopes. *Nat. Protocols* **2008**, *3* (2), 330-339.
- Gref, R.; Minamitake, Y.; Peracchia, M.; Trubetskoy, V.; Torchilin, V.; Langer, R. Biodegradable long-circulating polymeric nanospheres. *Science* **1994,** *263* (5153), 1600-1603.
- Grillo, I. Small-angle neutron scattering and applications in soft condensed matter. In *Soft Matter Characterization*, Borsali, R.; Pecora, R., Eds.; Springer Netherlands, 2008, pp 723-782.
- Guglielmini, G. Nanostructured novel carrier for topical application. *Clin. Dermatol.* **2008,** *26* (4), 341-346.

- Guinier, A.; Fournet, G. *Small-angle scattering of X-rays*; Wiley 1955.
- Gutiérrez, J. M.; González, C.; Maestro, A.; Solè, I.; Pey, C. M.; Nolla, J. Nano-emulsions: New applications and optimization of their preparation. *Curr. Opin. Colloid Interface Sci.* **2008,** *13* (4), 245-251.
- Han, J.; Zhu, Z.; Qian, H.; Wohl, A. R.; Beaman, C. J.; Hoye, T. R.; Macosko, C. W. A simple confined impingement jets mixer for flash nanoprecipitation. *J. Pharm. Sci.* **2012,** *101* (10), 4018-4023.
- Han, J.; Michel, A. R.; Lee, H. S.; Kalscheuer, S.; Wohl, A. R.; McCormick, A. V.; Panyam, J; Hoye, T. R.; Macosko, C. W. Nanoparticles containing high loads of paclitaxel silicate prodrugs: Formulation, drug release, and anitcancer efficacy. *manuscript in preparation*.
- Hansen, J.-P.; Hayter, J. B. A rescaled MSA structure factor for dilute charged colloidal dispersions. *Mol. Phys.* **1982,** *46* (3), 651-656.
- Hassan, P. A.; Fritz, G.; Kaler, E. W. Small angle neutron scattering study of sodium dodecyl sulfate micellar growth driven by addition of a hydrotropic salt. *J. Colloid Interface Sci.* **2003,** *257* (1), 154-162.
- Hassan, P. A.; Rana, S.; Verma, G. Making sense of brownian motion: Colloid characterization by dynamic light scattering. *Langmuir* **2014,** *31* (1), 3-12.
- Hatfield, J. C. Freeze-fracture electron microscopy and electrical conductivity of microemulsions. Ph.D., University of Minnesota 1978.
- Hayat, M. A. *Fixation for electron microscopy*; New York : Academic Press: New York, 1981.
- Hayter, J. B.; Penfold, J. An analytic structure factor for macroion solutions. *Mol. Phys.* **1981,** *42* (1), 109-118.
- Helgeson, M. E.; Gao, Y.; Moran, S. E.; Lee, J.; Godfrin, M.; Tripathi, A.; Bose, A.; Doyle, P. S. Homogeneous percolation versus arrested phase separation in attractively-driven nanoemulsion colloidal gels. *Soft Matter* **2014,** *10* (17), 3122-3133.

- Helgeson, M. E.; Moran, S. E.; An, H. Z.; Doyle, P. S. Mesoporous organohydrogels from thermogelling photocrosslinkable nanoemulsions. *Nat. Mater.* **2012,** *11* (4), 344-352.
- Heunemann, P.; Prevost, S.; Grillo, I.; Marino, C. M.; Meyer, J.; Gradzielski, M. Formation and structure of slightly anionically charged nanoemulsions obtained by the phase inversion concentration (PIC) method. *Soft Matter* **2011,** *7*, 5697-5710.
- Hiemenz, P. C.; Lodge, T. P. *Polymer Chemistry*; CRC Press, Boca Raton, FL, 2007; pp 354-355.
- Hiemenz, P. C.; Paul, C. H. Principles of colloid and surface chemistry; 3rd ed.; CRC Press, Boca Raton, FL, 2007; pp 237-240.
- Hu, C.-M. J.; Zhang, L.; Aryal, S.; Cheung, C.; Fang, R. H.; Zhang, L. Erythrocyte membrane-camouflaged polymeric nanoparticles as a biomimetic delivery platform. *Proc. Natl. Acad. Sci.* **2011**, 108 *(27)*, 10980-10985.
- Hoeller, S.; Sperger, A.; Valenta, C. Lecithin based nanoemulsions: A comparative study of the influence of non-ionic surfactants and the cationic phytosphingosine on physicochemical behaviour and skin permeation. *Int. J. Pharm.* **2009,** *370* (1-2), 181-186.
- Iancu, C. V.; Tivol, W. F.; Schooler, J. B.; Dias, D. P.; Henderson, G. P.; Murphy, G. E.; Wright, E. R.; Li, Z.; Yu, Z.; Briegel, A.; Gan, L.; He, Y.; Jensen, G. J. Electron cryotomography sample preparation using the Vitrobot. *Nat. Protocols* **2007**, *1* (6), 2813-2819.
- Israelachvili, J. N.; Mitchell, D. J.; Ninham, B. W. Theory of self-assembly of hydrocarbon amphiphiles into micelles and bilayers *J. Chem. Soc., Faraday Trans. 2* **1975,** *72*, 1525-1568.
- Israelachvili, J. N. *Intermolecular and surface forces*; Burlington, MA : Academic Press: Burlington, MA, 2011.
- Issman, L.; Talmon, Y. Cryo-SEM specimen preparation under controlled temperature and concentration conditions. *J. Microsc.* **2012,** *246* (1), 60-99.

- Izquierdo, P.; Esquena, J.; Tadros, T. F.; Dederen, C.; Garcia, M. J.; Azemar, N.; Solans, C. Formations and Stability of Nano-Emulsions Prepared using the Phase Inversion Temperature Method. *Langmuir* **2002,** *18* (1), 26-30.
- Izquierdo, P.; Esquena, J.; Tadros, T. F.; Dederen, J. C.; Feng, J.; Garcia-Celma, M. J.; Azemar, N.; Solans, C. Phase Behavior and Nano-emulsion Formation by the Phase Inversion Temperature Method. *Langmuir* **2004,** *20* (16), 6594-6598.
- Jacobs, D. S.; Boissy, Y. L.; Lindberg, S. E. Low temperature SEM as a tool for understanding dynamic events in consumer products research manufacture and use. *Microscopy and Microanalysis* **2002,** *8* (SupplementS02), 786-787.
- Jain, S.; Bates, F. S. On the origins of morphological complexity in block copolymer surfactants. *Science* **2003,** *300* (5618), 460-464.
- Jain, S. Aqueous mixtures of block copolymer surfactants. Ph.D., University of Minnesota 2005.
- Jaromír, J. Regularized positive exponential sum (REPES) program - A way of inverting laplace transform data obtained by dynamic light scattering. *Collect. Czech. Chem. Commun.* **1995,** *60*, 1781-1797.
- Johnson, B. K.; Prud'homme, R. K. Flash nanoprecipitation of organic actives and block copolymers using a confined impinging jets mixer. *Aust. J. Chem.* **2003,** *56* (10), 1021-1024.
- Johnson, B. K.; Prud'homme, R. K. Chemical processing and micromixing in confined impinging jets. *AIChE Journal* **2003,** *49* (9), 2264-2282.
- Joshi, J. V.; Aswal, V. K.; Bahadur, P.; Goyal, P. S. Role of counterion of the surfactant molecule on the micellar structure in aqueous solution. *Curr. Sci.* **2002,** *83* (1), 47-49.
- Joshi, J. V.; Aswal, V. K.; Goyal, P. S. Combined SANS and SAXS studies on alkali metal dodecyl sulphate micelles. *J. Phys.: Condens. Matter* **2007,** *19* (19), 196219.
- Joos, A.; Weiss, J.; McClements, D. J. Fabrication of lipophilic nanoparticles by spontaneous emulsification: Stabilization by cosurfactants. *Food Biophys.* **2014**, 1-11.

- Kanungo, S.; Narayanan, J.; Aswal, V. K.; Bellare, J. R.; Goyal, P. S. Study of core–shell structure of cesium dodecylsulfate micelles using small-angle X-ray and neutron scattering. *J. Mol. Liq.* **2012,** *175*, 38-43.
- Kataoka, K.; Harada, A.; Nagasaki, Y. Block copolymer micelles for drug delivery: design, characterization and biological significance. *Adv. Drug Deliv. Rev.* **2001,** *47* (1), 113-131.
- Kim, J.; Gao, Y.; Hebebrand, C.; Peirtsegaele, E.; Helgeson, M. E. Polymer-surfactant complexation as a generic route to responsive viscoelastic nanoemulsions. *Soft Matter* **2013,** *9* (29), 6897-6910.
- Kini, G. C.; Biswal, S. L.; Wong, M. S.; Miller, C. A. Characteristics of spontaneously formed nanoemulsions in octane/AOT/brine systems. *J. Colloid Interface Sci.* **2012,** *385* (1), 111-121.
- Klang, V.; Matsko, N.; Raupach, K.; El-Hagin, N.; Valenta, C. Development of sucrose stearate-based nanoemulsions and optimisation through Î³-cyclodextrin. *Eur. J. Pharm. Biopharm.* **2011,** *79* (1), 58-67.
- Koppel, D. E. Analysis of macromolecular polydispersity in intensity correlation spectroscopy: The method of cumulants. *J. Chem. Phys.* **1972,** *57* (11), 4814-4820.
- Langer, R. New methods of drug delivery. *Science* **1990,** *249* (4976), 1527-1533.
- Langer, R. Drug delivery and targeting. *Nature* **1998,** *392* (6679), 5-10.
- Lawrence, M. J.; Rees, G. D. Microemulsion-based media as novel drug delivery systems. *Adv. Drug Deliv. Rev.* **2000,** *45* (1), 89-121.
- Lee, H. S.; Morrison, E. D.; Frethem, C. D.; Zasadzinski, J. A.; McCormick, A. V. Cryogenic electron microscopy study of nanoemulsion formation from microemulsions. *Langmuir* **2014,** *30* (36), 10826-10833.
- Lee, S. Structure and dynamics of block copolymer based soft materials. Ph.D., University of Minnesota 2011.
- Li, X. Phase behavior, microstructure and transitions in self-assembled colloidal systems. Ph.D., University of Minnesota 1996.

- Lin, Z. Microstructure and phase behavior of surfactants in solution. Ph.D., University of Minnesota 1993.
- Lin, Z.; Cai, J. J.; Scriven, L. E.; Davis, H. T. Spherical-to-wormlike micelle transition in CTAB solutions. *J. Phys. Chem.* **1994,** *98* (23), 5984-5993.
- Liu, Y. C.; Ku, C. Y.; LoNostro, P.; Chen, S. H. Ion correlations in a micellar solution studied by small-angle neutron and X-ray scattering. *Phys. Rev. E* **1995,** *51* (5), 4598-4607.
- Livsey, I. Neutron scattering from concentric cylinders. Intraparticle interference function and radius of gyration. *J. Chem. Soc., Faraday Trans. 2* **1987,** *83* (8), 1445-1452.
- Lodge, T. P. A unique platform for materials design. *Science* **2008,** *321* (5885), 50-51.
- López-Montilla, J. C.; Herrera-Morales, P. E.; Pandey, S.; Shah, D. O. Spontaneous emulsification: Mechanisms, physicochemical aspects, modeling, and applications. *J. Dispersion Sci. Technol.* **2002,** *23* (1-3), 219-268.
- López-Montilla, J. C.; Herrera-Morales, P. E.; Shah, D. O. New method to quantitatively determine the spontaneity of the emulsification process. *Langmuir* **2002,** *18* (11), 4258-4262.
- Maeda, H.; Wu, J.; Sawa, T.; Matsumura, Y.; Hori, K. Tumor vascular permeability and the EPR effect in macromolecular therapeutics: a review. *J. Control. Release* **2000,** *65* (1–2), 271-284.
- Margulis, K.; Magdassi, S.; Lee, H. S.; Macosko, C. W. Formation of curcumin nanoparticles by flash nanoprecipitation from emulsions. *J. Colloid Interface Sci.* **2014,** *434*, 65-70.
- Mason, T. G.; Graves, S. M.; Wilking, J. N.; Lin, M. Y. Extreme emulsification: formation and structure of nanoemulsions. *Condens. Matter Phys.* **2006,** *9* (1), 193-199.
- Mason, T. G.; Wilking, J. N.; Meleson, K.; Chang, C. B.; Graves, S. M. Nanoemulsions: Formation, structure, and physical properties. *J. Phys.: Condens. Matter* **2006,** *18* (41), R635-R666.

- McClements, D. J. Encapsulation, protection, and release of hydrophilic active components: Potential and limitations of colloidal delivery systems. *Adv. Colloid Interface Sci.* **2015,** *219*, 27-53.
- Meyer, J.; Polak, G.; Scheuermann, R. Preparing PIC emulsions with a very fine particle size. *Cosmetics & Toiletries* **2007,** *122* (1), 61-70.
- *Microemulsions : properties and applications*; Boca Raton : CRC Press: Boca Raton, Florida, 2009.
- Miller, C. A. Spontaneous emulsification produced by diffusion - A review. *Colloids Surf.* **1988,** *29* (1), 89-102.
- Miller, C. A. Spontaneous emulsification: Recent developments with emphasis on self-emulsification. In *Emulsions and emulsion stability*, Johan, S., Ed.; CRC Press: Boca Raton, 2006, pp 107-126.
- Missel, P. J.; Mazer, N. A.; Carey, M. C.; Benedek, G. B. Influence of alkali-metal counterion identity on the sphere-to-rod transition in alkyl sulfate micelles. *J. Phys. Chem.* **1989,** *93* (26), 8354-8366.
- Morales, D.; Gutiérrez, J. M.; García-Celma, M. J.; Solans, Y. C. A study of the relation between bicontinuous microemulsions and oil/water nano-emulsion Formation. *Langmuir* **2003,** *19* (18), 7196-7200.
- Nakajima, H.; Tomomasa, S.; Okabe, M. Preparation of Nano-emulsions. In *Proceedings of First Emulsion Conference*; EDS: Paris, 1993; Vol. 1, pp 1-11.
- Nishimi, T.; Miller, C. A. Spontaneous emulsification of oil in aerosol-OT/water/hydrocarbon systems. *Langmuir* **2000,** *16* (24), 9233-9241.
- Oh, K. S.; Song, J. Y.; Cho, S. H.; Lee, B. S.; Kim, S. Y.; Kim, K.; Jeon, H.; Kwon, I. C.; Yuk, S. H. Paclitaxel-loaded pluronic nanoparticles formed by a temperature-induced phase transition for cancer therapy. *J. Control. Release* **2010,** *148* (3), 344-350.
- Ostertag, F.; Weiss, J.; McClements, D. J. Low-energy formation of edible nanoemulsions: Factors influencing droplet size produced by emulsion phase inversion. *J. Colloid Interface Sci.* **2012,** *388* (1), 95-102.

- Peer, D.; Karp, J. M.; Hong, S.; Farokhzad, O. C.; Margalit, R.; Langer, R. Nanocarriers as an emerging platform for cancer therapy. *Nat. Nano.* **2007,** *2* (12), 751-760.
- Pey, C. M.; Maestro, A.; Solé, I.; González, C.; Solans, C.; Gutiérrez, J. M. Optimization of nano-emulsions prepared by low-energy emulsification methods at constant temperature using a factorial design study. *Colloids Surf., A* **2006,** *288* (1-3), 144-150.
- Pons, R.; Carrera, I.; Caelles, J.; Rouch, J.; Panizza, P. Formation and properties of miniemulsions formed by microemulsions dilution. *Adv. Colloid and Interface Sci.* **2003,** *106* (1-3), 129-146.
- Porras, M.; Solans, C.; Gonzélez, C.; Martínez, A.; Guinart, A.; Gutiérrez, J. M. Studies of formation of W/O nano-emulsions. *Colloids Surf., A* **2004,** *249* (1-3), 115-118.
- Pouton, C. W. Formulation of self-emulsifying drug delivery systems. *Adv. Drug Delivery Rev.* **1997,** *25* (1), 47-58.
- Pustulka, K. M.; Wohl, A. R.; Lee, H. S.; Michel, A. R.; Han, J.; Hoye, T. R.; McCormick, A. V.; Panyam, J.; Macosko, C. W. Flash nanoprecipitation: Particle structure and stability. *Mol. Pharmaceutics* **2013,** *10* (11), 4367-4377.
- Qian, H.; Wohl, A. R.; Crow, J. T.; Macosko, C. W.; Hoye, T. R. A Strategy for control of "Random" copolymerization of lactide and glycolide: Application to synthesis of PEG-*b*-PLGA block polymers having narrow dispersity. *Macromolecules* **2011,** *44* (18), 7132-7140.
- Rajera, R.; Nagpal, K.; Singh, S. K.; Mishra, D. N. Niosomes: A controlled and novel drug delivery system. *Biol. Pharm. Bull.* **2011,** *34* (7), 945-953.
- Rang, M.-J.; Miller, C. A. Spontaneous emulsification of oils containing hydrocarbon, nonionic surfactant, and oleyl alcohol. *J. Colloid Interface Sci.* **1999,** *209* (1), 179-192.
- Raghavan, S. R.; Kaler, E. W. Highly viscoelastic wormlike micellar solutions formed by cationic surfactants with long unsaturated tails. *Langmuir* **2000,** *17* (2), 300-306.

- Rao, J.; McClements, D. J. Formation of flavor oil microemulsions, nanoemulsions and emulsions: Influence of composition and preparation method. *J. Agric. Food. Chem.* **2011,** *59* (9), 5026-5035.
- Roger, K.; Cabane, B.; Olsson, U. Emulsification through surfactant ydration: The PIC process revisited. *Langmuir* **2010,** *27* (2), 604-611.
- Roux, D. C.; Berret, J.-F.; Porte, G.; Peuvrel-Disdier, E.; Lindner, P. Shear-induced orientations and textures of nematic living polymers. *Macromolecules* **1995**, *28* (5), 1681-1687.
- Sabatini, D. A.; Acosta, E.; Harwell, J. H. Linker molecules in surfactant mixtures. *Curr. Opin. Colloid Interface Sci.* **2003,** *8* (4–5), 316-326.
- Saberi, A. H.; Fang, Y.; McClements, D. J. Fabrication of vitamin E-enriched nanoemulsions: Factors affecting particle size using spontaneous emulsification. *J. Colloid Interface Sci.* **2013,** *391*, 95-102.
- Sadurní, N.; Solans, C.; Azemar, N.; García-Celma, M. J. Studies on the formation of O/W nano-emulsions, by low-energy emulsification methods, suitable for pharmaceutical applications. *Eur. J. Pharm. Sci.* **2005,** *26* (5), 438-445.
- Sajjadi, S. Nanoemulsion formation by phase inversion emulsification: On the nature of inversion. *Langmuir* **2006,** *22* (13), 5597-5603.
- Saupe, A.; Gordon, K. C.; Rades, T. Structural investigations on nanoemulsions, solid lipid nanoparticles and nanostructured lipid carriers by cryo-field emission scanning electron microscopy and Raman spectroscopy. *Int. J. Pharm.* **2006,** *314* (1), 56-62.
- Schryver, S. B.; Ramsden, W.; Cross, C. F.; Schidrowitz, P.; Dreaper, W. P.; McBain, J. W.; Turner, T.; Worley, F. P.; Martin, C. J.; Bousfield, W. R.; Morse, H. N.; Henri, V.; Freundlich, H.; The, C.; Ostwald, W.; Chapman, C.; Senter, G. Discussion. *Trans. Faraday Soc.* **1913,** *9*, 93-107.
- Schwarz, J. C.; Kählig, H.; Matsko, N. B.; Kratzel, M.; Husa, M.; Valenta, C. Decrease of liposomal size and retarding effect on fluconazole skin permeation by lysine derivatives. *J. Pharm. Sci.* **2011,** *100* (7), 2911-2919.

- Shahidzadeh, N.; Bonn, D.; Aguerre-Chariol, O.; Meunier, J. Large deformations of giant floppy vesicles in shear flow. *Phys. Rev. Lett.* **1998**, *81* (19), 4268-4271.
- Shen, H.; Jacobs, D.; Burns, J.; Boissy, Y.; Domaschko, D. Modern electron microscopy applications in the consumer products industry. *Microscopy and Microanalysis* **2003,** *9* (SupplementS02), 156-157.
- Sheu, E. Y.; Wu, C. F.; Chen, S. H. Effects of ion sizes on the aggregation and surface charge of ionic micelles in 1:1 electrolyte solutions. *J. Phys. Chem.* **1986,** *90* (17), 4179-4187.
- Siegel, D. P.; Green, W. J.; Talmon, Y. The mechanism of lamellar-to-inverted hexagonal phase transitions: A study using temperature-jump cryo-electron microscopy. *Biophys. J.* **1994**, *66* (2 Pt 1), 402-414.
- Silva, M. T.; Carvalho Guerra, F.; Magalhães, M. M. The fixative action of uranyl acetate in electron microscopy. *Experientia* **1968**, *24* (10), 1074-1074.
- Solans, C.; Izquierdo, P.; Nolla, J.; Azemar, N.; Garcia-Celma, M. J. Nano-emulsions. *Curr. Opin. Colloid Interface Sci.* **2005,** *10* (3-4), 102-110.
- Solans, C.; Solé, I. Nano-emulsions: Formation by low-energy methods. *Curr. Opin. Colloid Interface Sci.* **2012,** *17* (5), 246-254.
- Solè , I.; Maestro, A.; González, C.; Solans, C.; Gutiérrez, J. M. Optimization of nano-emulsion preparation by low-energy methods in an ionic surfactant system. *Langmuir* **2006,** *22* (20), 8326-8332.
- Solè, I.; Maestro, A.; Pey, C. M.; González, C.; Solans, C.; Gutiérrez, J. M. Nano-emulsions preparation by low energy methods in an ionic surfactant system. *Colloids Surf., A* **2006,** *288* (1-3), 138-143.
- Solè, I.; Solans, C.; Maestro, A.; González, C.; Gutiérrez, J. M. Study of nano-emulsion formation by dilution of microemulsions. *J. Colloid Interface Sci.* **2012,** *376* (1), 133-139.
- Sonneville-Aubrun, O.; Simonnet, J. T.; L'Alloret, F. Nanoemulsions: A new vehicle for skincare products. *Adv. Colloid and Interface Sci.* **2004,** *108-109*, 145-149.

- Sottmann, T.; Stubenrauch, C. Phase behaviour, interfacial tension and microstructure of microemulsions. In *Microemulsions*; John Wiley & Sons, Ltd, 2009, pp 1-47.
- Srivastava, V. K.; Kini, G.; Rout, D. Detergency in spontaneously formed emulsions. *J. Colloid Interface Sci.* **2006,** *304* (1), 214-221.
- Stewart, B. W.; Wild, C. P. *World cancer report 2014*; World Health Organization Press: Geneva, 2014. p 630.
- Tadros, T.; Izquierdo, P.; Esquena, J.; Solans, C. Formation and stability of nano-emulsions. *Adv. Colloid Interface Sci.* **2004,** *108-109*, 303-318.
- Tadros, T. F. Surfactants in Nano-Emulsions. Wiley-VCH: Weinheim, 2005, pp 285-308.
- Talmon, Y.; Davis, H. T.; Scriven, L. E.; Thomas, E. L. Cold-stage microscopy system for fast-frozen liquids. *Rev. Sci. Instrum.* **1979**, *50* (6), 698-704.
- Talmon, Y. Fluid microstructure: Cold stage electron microscopy and theoretical modeling. Ph.D., University of Minnesota 1979.
- Talmon, Y. Imaging surfactant dispersions by electron microscopy of vitrified specimens. *Colloids Surf.* **1986**, *19* (2–3), 237-248.
- Talmon, Y. *Cryotechniques in biological electron microscopy*; Berlin, New York : Springer-Verlag: Berlin, New York, 1987.
- Talmon, Y. Transmission electron microscopy of complex fluids: The state of the art. *Berichte der Bunsengesellschaft für physikalische Chemie* **1996,** *100* (3), 364-372.
- Tan, G.; Ford, C.; John, V. T.; He, J.; McPherson, G. L.; Bose, A. Surfactant solubilization and the direct encapsulation of interfacially active phenols in mesoporous silicas. *Langmuir* **2008,** *24* (3), 1031-1036.
- Taylor, P.; Ottewill, R. H. The formation and ageing rates of oil-in-water miniemulsions. *Colloids Surf., A* **1994,** *88* (2–3), 303-316.
- Tivol, W. F.; Briegel, A.; Jensen, G. J. An improved cryogen for plunge freezing. *Microsc. Microanal.* **2008**, *14* (5), 375-379.

- Torchilin, V. P. Recent advances with liposomes as pharmaceutical carriers. *Nat. Rev. Drug Discov.* **2005,** *4* (2), 145-160.
- Uchiyama, H.; Acosta, E.; Tran, S.; Sabatini, D. A.; Harwell, J. H. Supersolubilization in chlorinated hydrocarbon microemulsions: Solubilization enhancement by lipophilic and hydrophilic linkers. *Ind. Eng. Chem. Res.* **2000,** *39* (8), 2704-2708.
- Usón, N.; Garcia, M. J.; Solans, C. Formation of water-in-oil (W/O) nano-emulsions in a water/mixed non-ionic surfactant/oil systems prepared by a low-energy emulsification method. *Colloids Surf., A* **2004,** *250* (1-3), 415-421.
- Vagias, A. N. Cesium dodecyl sulphate phase behavior in aqueous solutions and comparision with the sodium dodecyl sulphate/water phase diagram. M.S. Thesis, University of Minnesota 2010.
- Vass, S.; Pleštil, J.; Laggner, P.; Gilányi, T.; Borbély, S.; Kriechbaum, M.; Jákli, G.; Décsy, Z.; Abuja, P. M. Models of micellar structure tested by SANS and SAXS (from a Kratky camera) in cesium dodecyl sulfate solution. *J. Phys. Chem. B* **2003,** *107* (46), 12752-12761.
- Vinson , P. K. Cryo-electron microscopy of microstructures in complex liquids. Ph. D., University of Minnesota 1990.
- Vlachy, N.; Jagoda-Cwiklik, B.; Vácha, R.; Touraud, D.; Jungwirth, P.; Kunz, W. Hofmeister series and specific interactions of charged headgroups with aqueous ions. *Adv. Colloid Interface Sci* **2009,** *146* (1–2), 42-47.
- Wadle, A.; Förster, T.; von Rybinski, W. Influence of the microemulsion phase structure on the phase inversion temperature emulsification of polar oils. *Colloids Surf., A* **1993,** *76*, 51-57.
- Wang, L.; Li, X.; Zhang, G.; Dong, J.; Eastoe, J. Oil-in-water nanoemulsions for pesticide formulations. *J. Colloid Interface Sci.* **2007,** *314* (1), 230-235.
- Wang, L.; Mutch, K. J.; Eastoe, J.; Heenan, R. K.; Dong, J. Nanoemulsions prepared by a two-step low-energy process. *Langmuir* **2008,** *24* (12), 6092-6099.

- Wang, L.; Dong, J.; Chen, J.; Eastoe, J.; Li, X. Design and optimization of a new self-nanoemulsifying drug delivery system. *J. Colloid Interface Sci.* **2009,** *330* (2), 443-448.
- Wang, L.; Tabor, R.; Eastoe, J.; Li, X.; Heenan, R. K.; Dong, J. Formation and stability of nanoemulsions with mixed ionic-nonionic surfactants. *Phys. Chem. Chem. Phys.* **2009,** *11*, 9772-9778.
- Wang, Z. L. Transmission electron microscopy of shape-controlled nanocrystals and their assemblies. *The Journal of Physical Chemistry B* **2000,** *104* (6), 1153-1175.
- Wang, Z.; Larson, R. G. Molecular dynamics simulations of threadlike cetyltrimethylammonium chloride micelles: Effects of sodium chloride and sodium salicylate salts. *J. Phys. Chem. B* **2009,** *113* (42), 13697-13710.
- Wani, M. C.; Taylor, H. L.; Wall, M. E.; Coggon, P.; McPhail, A. T. Plant antitumor agents. VI. Isolation and structure of taxol, a novel antileukemic and antitumor agent from Taxus brevifolia. *J. Am. Chem. Soc.* **1971,** *93* (9), 2325-2327.
- Watanabe, K.; Klein, M. L. Shape fluctuations in ionic micelles. *J. Phys. Chem.* **1989,** *93* (19), 6897-6901.
- Weiss, R. B.; Donehower, R. C.; Wiernik, P. H.; Ohnuma, T.; Gralla, R. J.; Trump, D. L.; Baker, J. R.; Van Echo, D. A.; Von Hoff, D. D.; Leyland-Jones, B. Hypersensitivity reactions from taxol. *J. Clin. Oncol.* **1990,** *8* (7), 1263-1268.
- Williams, D. B.; Carter, C. B. The Transmission electron microscope. In *Transmission Electron Microscopy*; Springer, 1996, pp 3-17.
- Wohl, A. R.; Michel, A. R.; Kalscheuer, S.; Macosko, C. W.; Panyam, J.; Hoye, T. R. Silicate esters of paclitaxel and docetaxel: Synthesis, hydrophobicity, hydrolytic stability, cytotoxicity, and prodrug potential. *J. Med. Chem.* **2014,** *57* (6), 2368-2379.
- Won, Y.-Y. Block copolymer micelles in water. Ph.D., University of Minnesota 2000.

- Wunderlich, I.; Hoffmann, H.; Rehage, H. Flow birefringence and rheological measurements on shear induced micellar structures. *Rheol. Acta* **1987**, *26* (6), 532-542.
- Ying, G.-G.; Williams, B.; Kookana, R. Environmental fate of alkylphenols and alkylphenol ethoxylates—a review. *Envirom. Int.* **2002,** *28* (3), 215-226.
- Zasadzinski, J. A. N. Liquid crystal structure by electron microscopy (liposomes, vesicles, surfctants). Ph.D., University of Minnesota 1985.
- Zasadzinski, J. A. N.; Bailey, S. M. Applications of freeze-fracture replication to problems in materials and colloid science. *J. Electron Micr. Tech.* **1989,** *13* (4), 309-334.
- Zemb, T.; Charpin, P. Micellar structure from comparison of X-ray and neutron small-angle scattering. *J. Phys. France* **1985,** *46* (2), 249-256.
- Zhang, J.; Han, B.; Zhang, C.; Li, W.; Feng, X. Nanoemulsions induced by compressed gases. *Angew. Chem. Int. Ed.* **2008,** *47* (16), 3012-3015.
- Zhang, L.; Gu, F. X.; Chan, J. M.; Wang, A. Z.; Langer, R. S.; Farokhzad, O. C. Nanoparticles in Medicine: Therapeutic applications and developments. *Clin. Pharmacol. Ther.* **2008,** *83* (5), 761-769.
- Zhao, Y.; Zhang, J.; Wang, Q.; Li, J.; Han, B. Water-in-oil-in-water double nanoemulsion induced by CO_2. *Phys. Chem. Chem. Phys.* **2011,** *13* (2), 684-689.
- Zheng, Y. Cryo-electron microscopy of microstructures in self-assembled colloidal systems. Ph.D., University of Minnesota 2000.
- Zheng, Y.; Lin, Z.; Zakin, J. L.; Talmon, Y.; Davis, H. T.; Scriven, L. E. Cryo-TEM imaging the flow-induced transition from vesicles to threadlike micelles. *J. Phys. Chem. B* **2000,** *104* (22), 5263-5271.
- Zhou, H.; Yue, Y.; Liu, G.; Li, Y.; Zhang, J.; Gong, Q.; Yan, Z.; Duan, M. Preparation and characterization of a lecithin nanoemulsion as a topical delivery system. *Nanoscale Res. Lett.* **2009,** *5* (1), 224 - 230.

Appendix A.

Supplemental information of CsDS aqueous solution

I. SAXS intensity profiles as a function of temperature
    -Figures A1 – A3
II. Cryo-TEM images of CsDS aqueous solution from 0.2 wt % to 8.1 wt %
    - Figures A4 – A20
III. FF-TEM images of CsDS aqueous solution from 5.0 wt % to 8.1 wt %
    - Figures A18 – A24
IV. FF-TEM images of bare copper planchette
    - Figure A25

I. SAXS intensity profiles as a function of temperature

Figures 2.23 to 2.25 show SAXS intensity profiles as a function of temperature on 2.0, 5.0, and 8.1 wt % CsDS solutions, respectively.

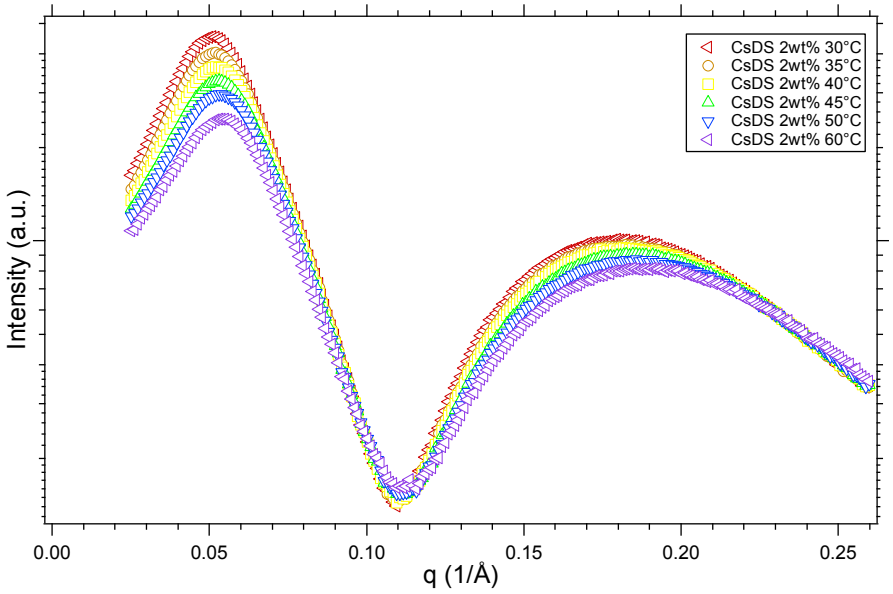

Figure A1. SAXS patterns obtained from 2.0 wt % cesium dodecyl sulfate in aqueous solution showing the mild effect of temperature.

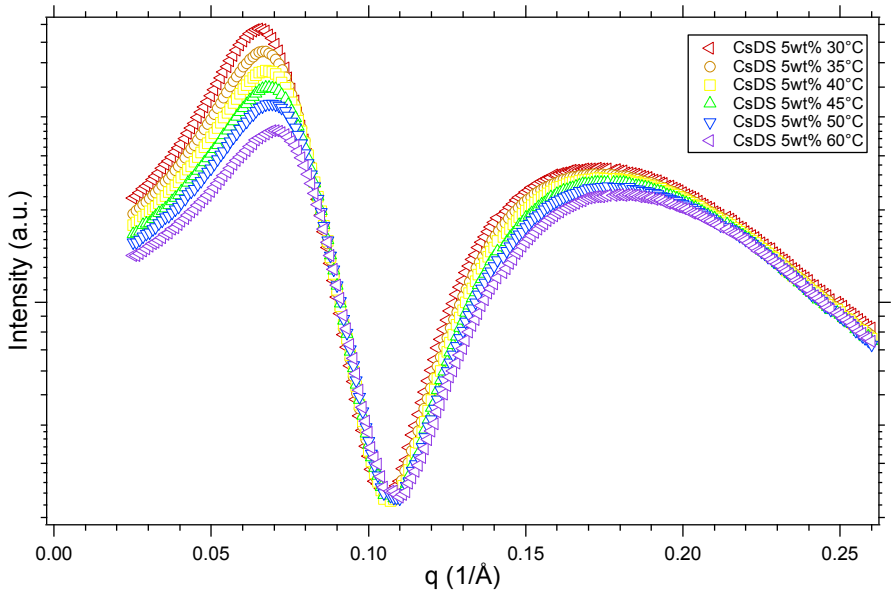

Figure A2. SAXS patterns obtained from 5.0 wt % cesium dodecyl sulfate in aqueous solution showing the mild effect of temperature.

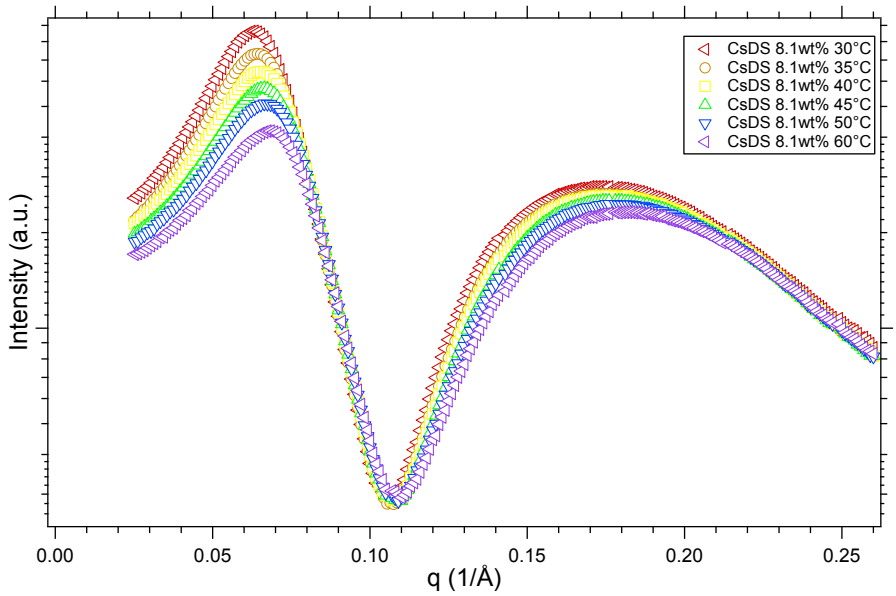

Figure A3. SAXS patterns obtained from 8.1 wt % cesium dodecyl sulfate in aqueous solution showing the mild effect of temperature.

II. Cryo-TEM images of CsDS aqueous solution from 0.2 wt % to 8.1 wt %

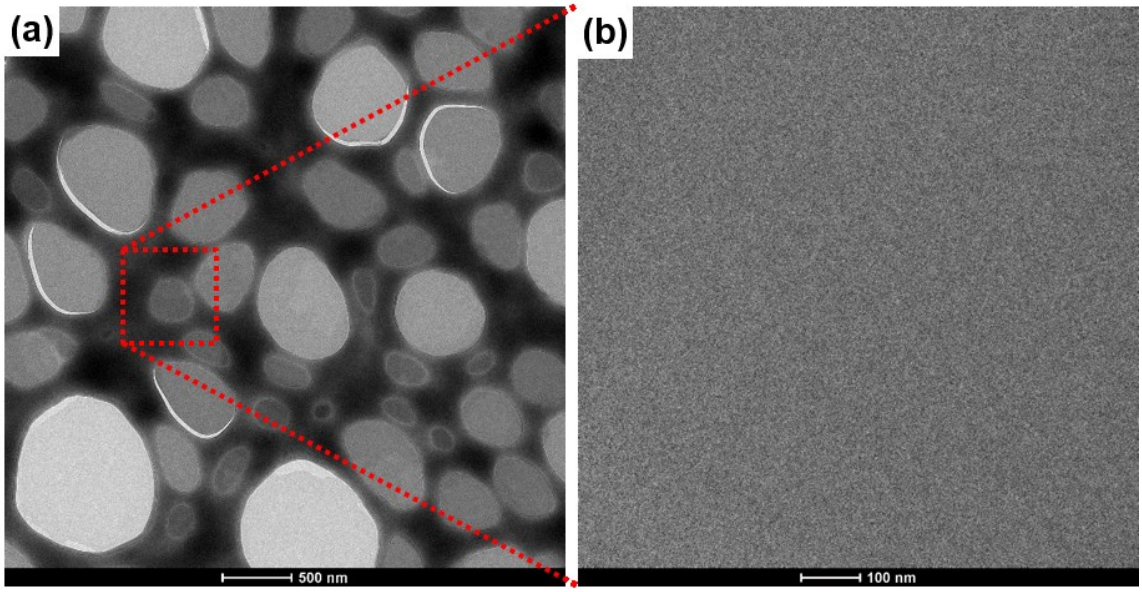

Figure A4. Typical cryo-TEM micrographs obtained from a 0.2 wt % cesium dodecyl sulfate (CsDS) aqueous solution at 40 °C. (a) Low magnification of CsDS aqueous solution. (b) High magnification of CsDS aqueous solution from red square of (a).

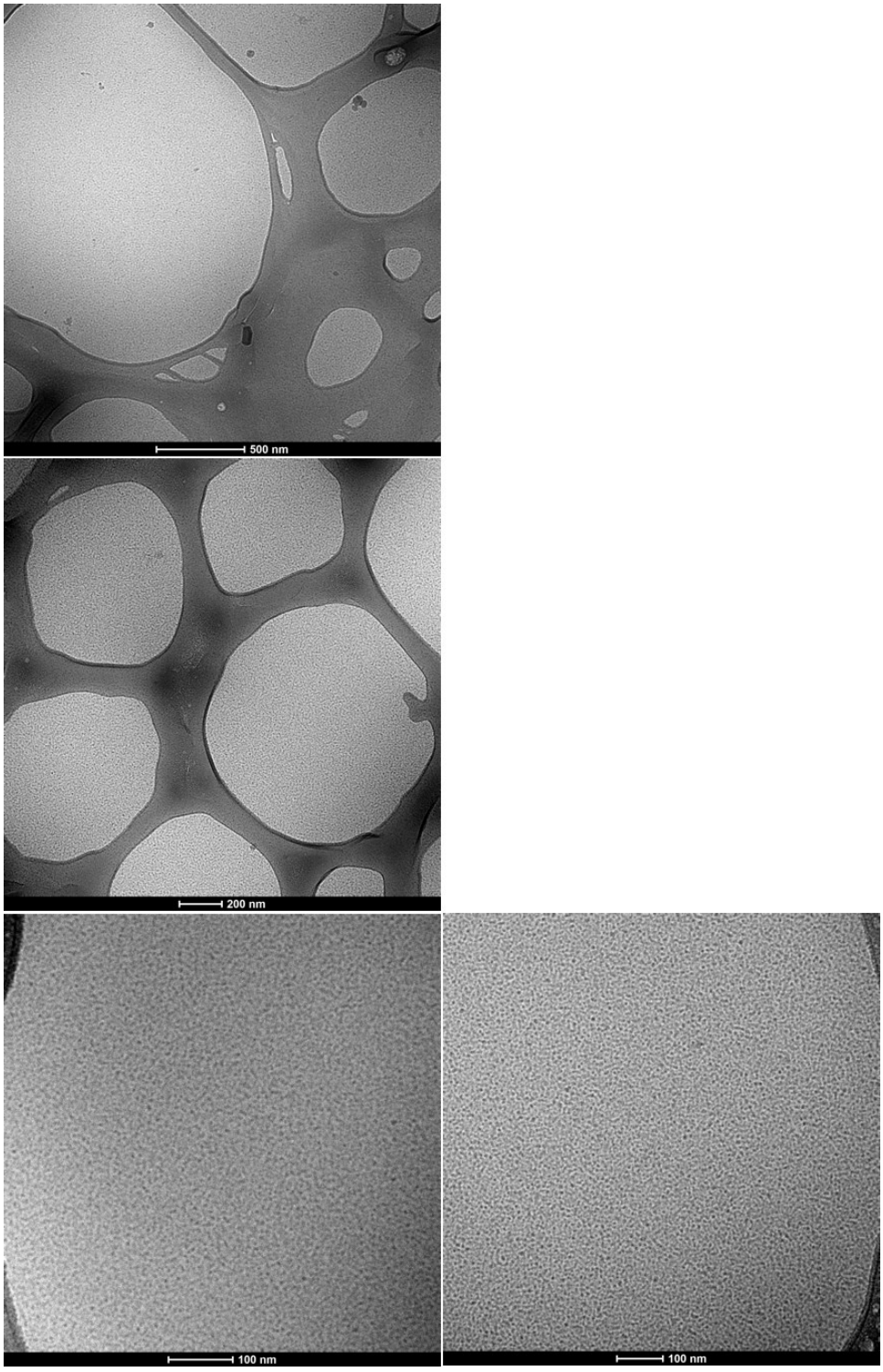

Figure A5. Typical cryo-TEM micrographs obtained from a 1.0 wt % cesium dodecyl sulfate aqueous solution at 40 °C.

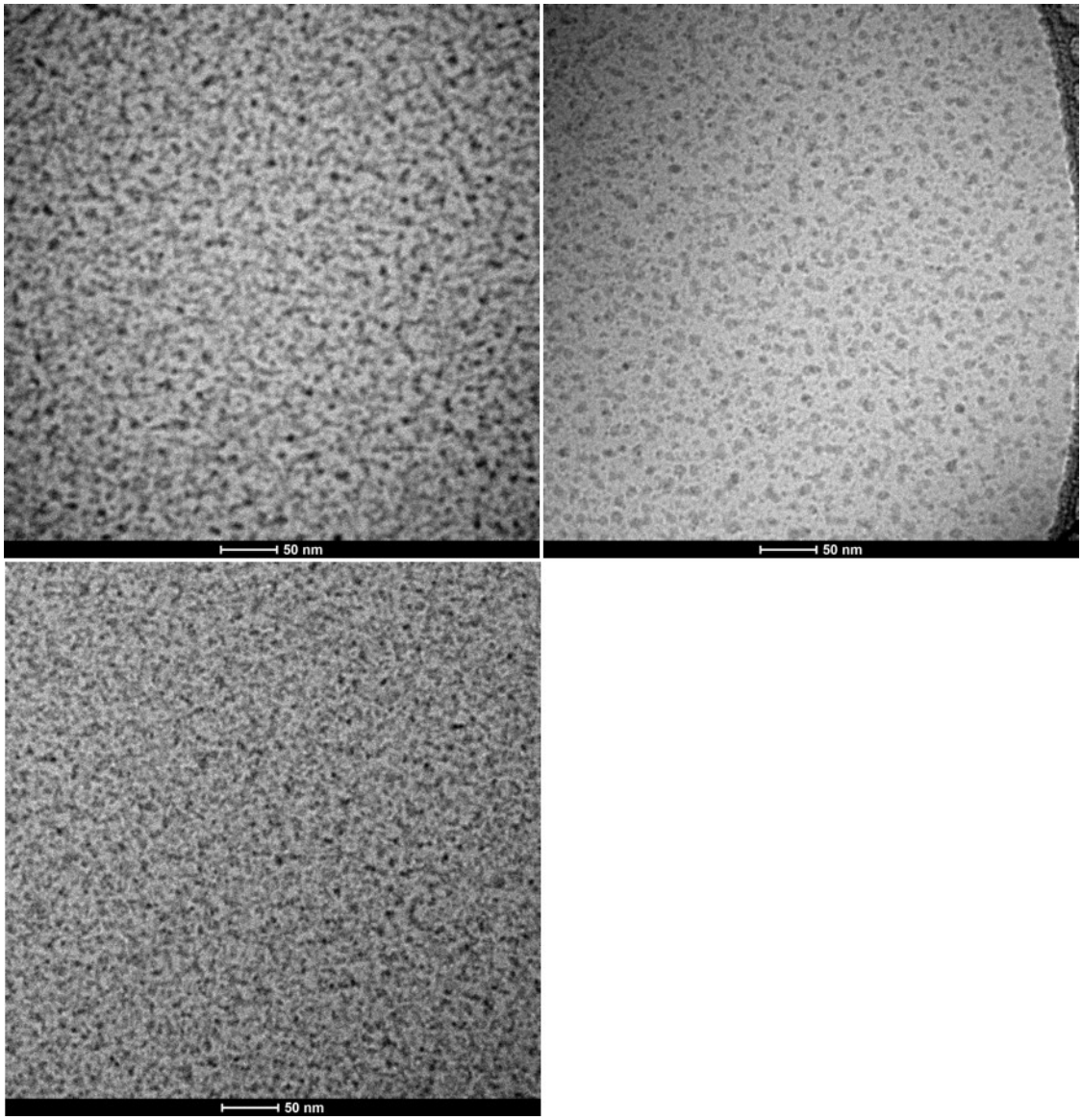

Figure A6. Typical cryo-TEM micrographs obtained from a 1.0 wt % cesium dodecyl sulfate aqueous solution at 40 °C.

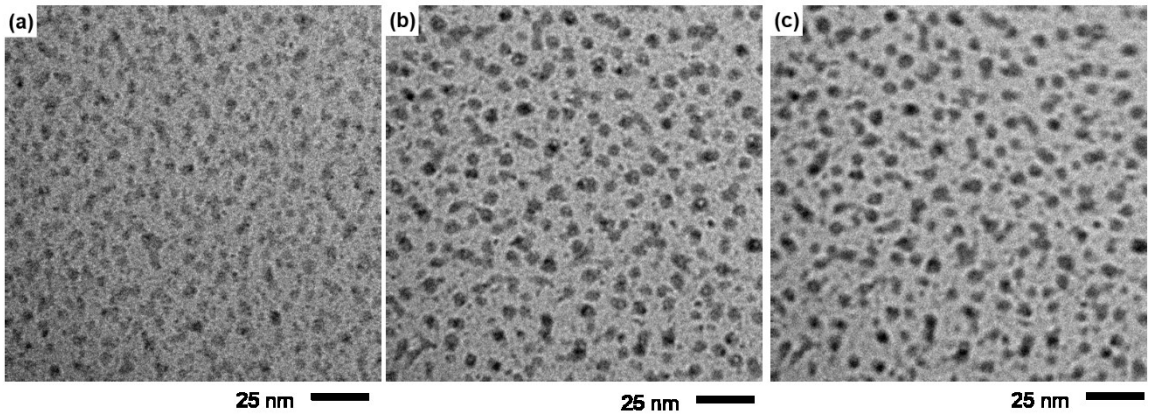

Figure A7. Typical cryo-TEM micrographs of same region obtained from a 2.0 wt % cesium dodecyl sulfate aqueous solution at 40 °C, showing through focus series at the same magnification (a) 0.1 μm, (b) 0.5 μm, and (c) 1.0 μm of nominal underfocus value.

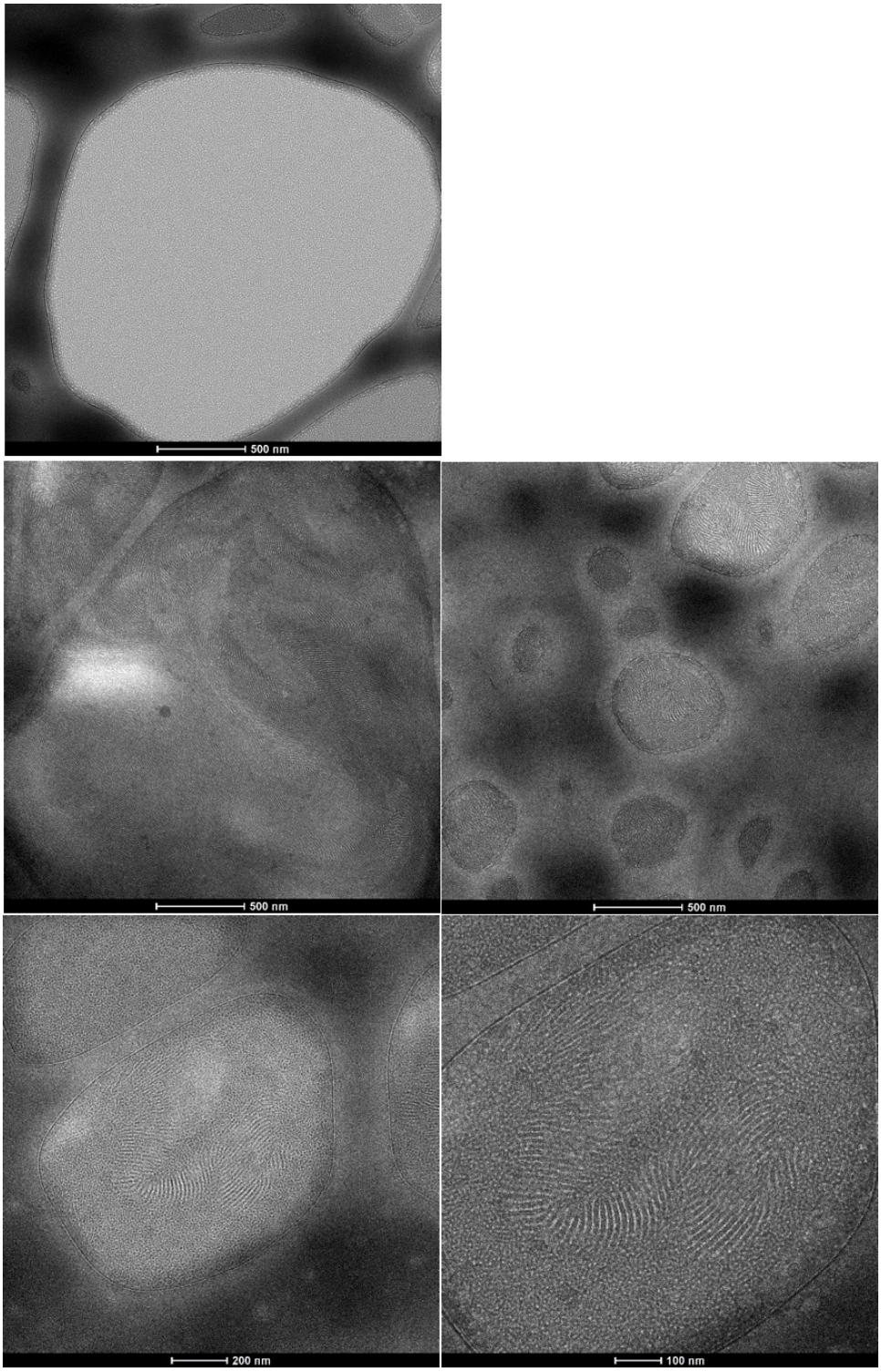

Figure A8. Typical cryo-TEM micrographs obtained from a 5.0 wt % cesium dodecyl sulfate aqueous solution at 40 °C.

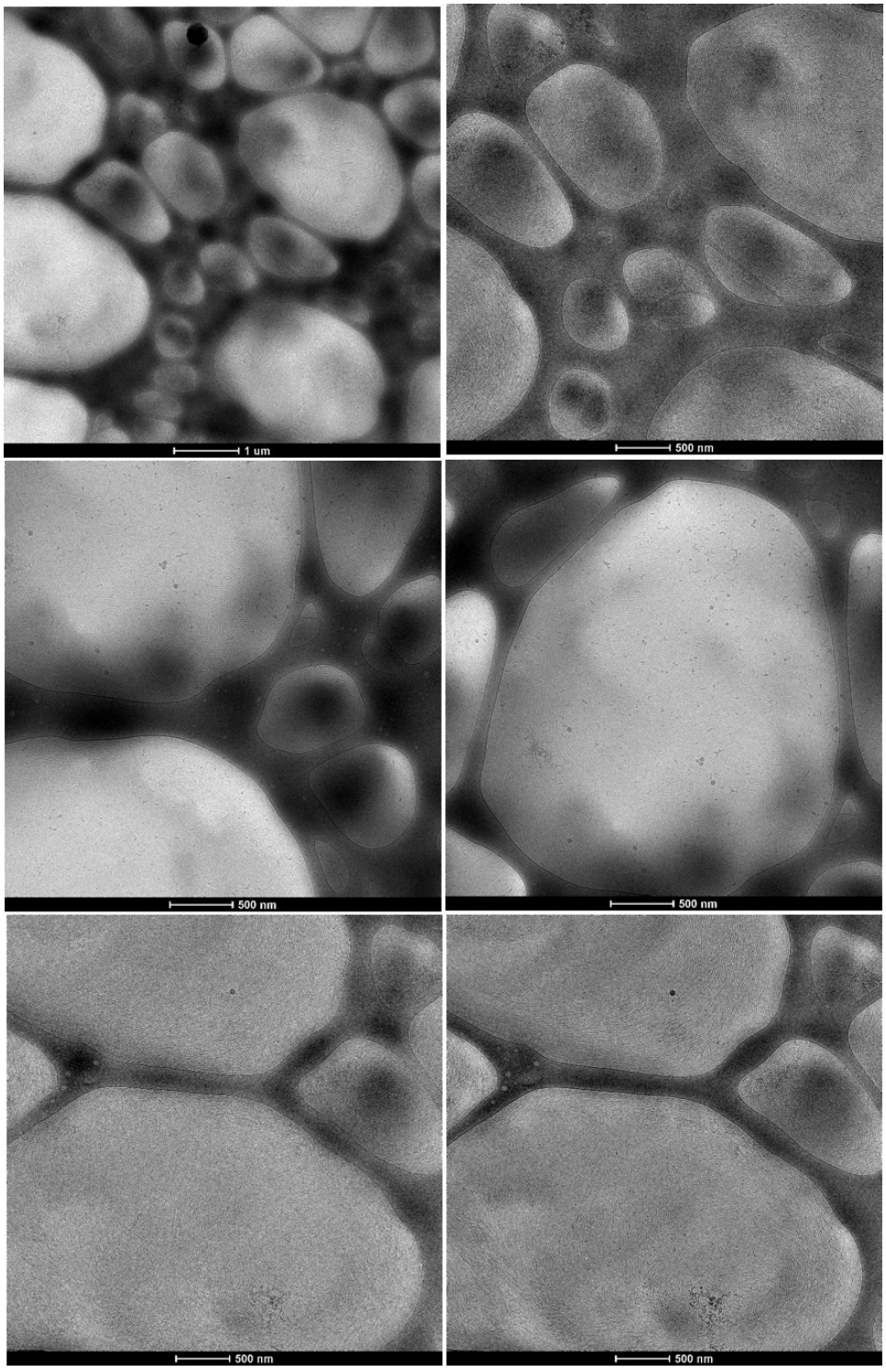

Figure A9. Typical cryo-TEM micrographs obtained from a 5.0 wt % cesium dodecyl sulfate aqueous solution at 40 °C.

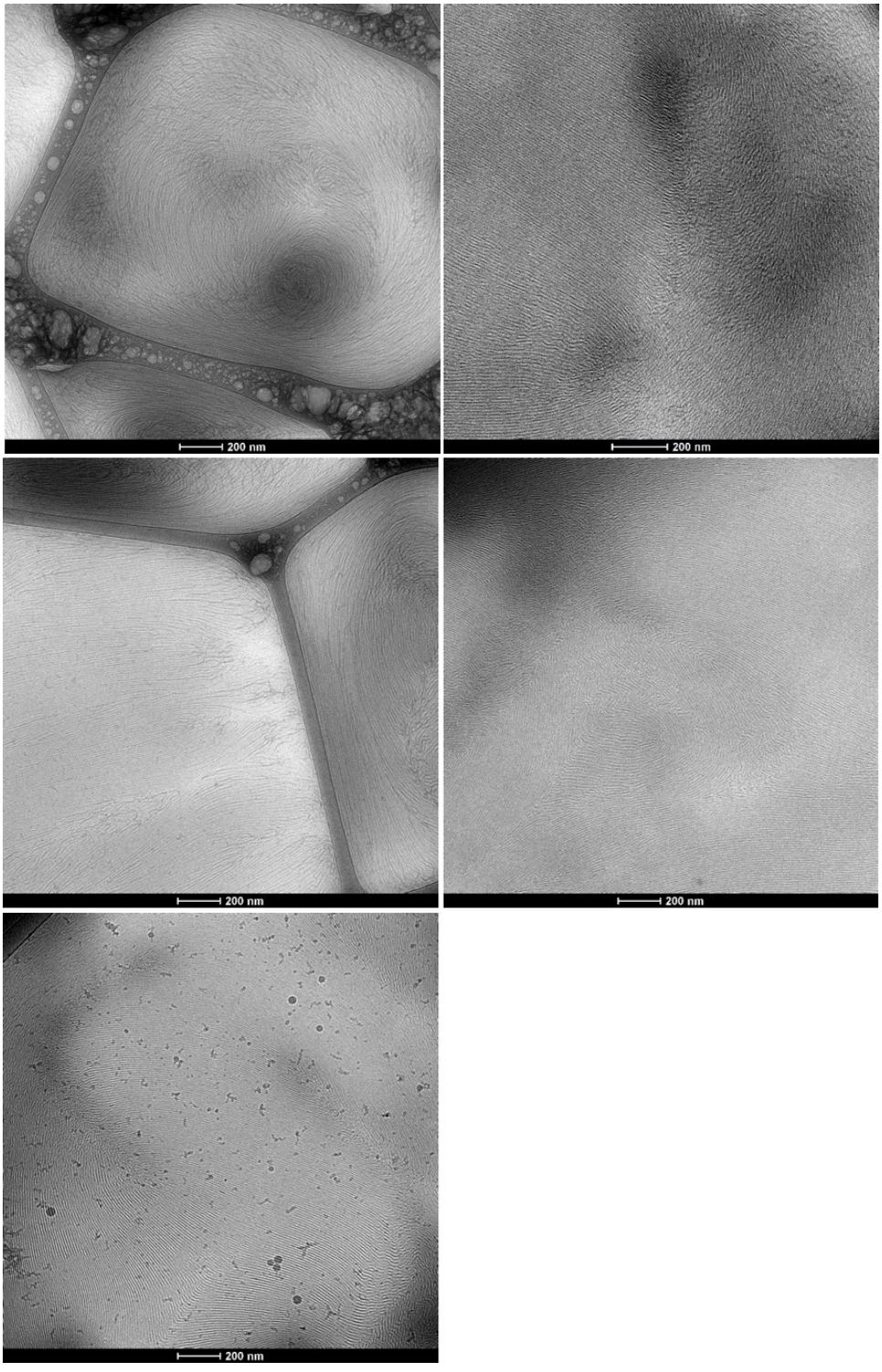

Figure A10. Typical cryo-TEM micrographs obtained from a 5.0 wt % cesium dodecyl sulfate aqueous solution at 40 °C.

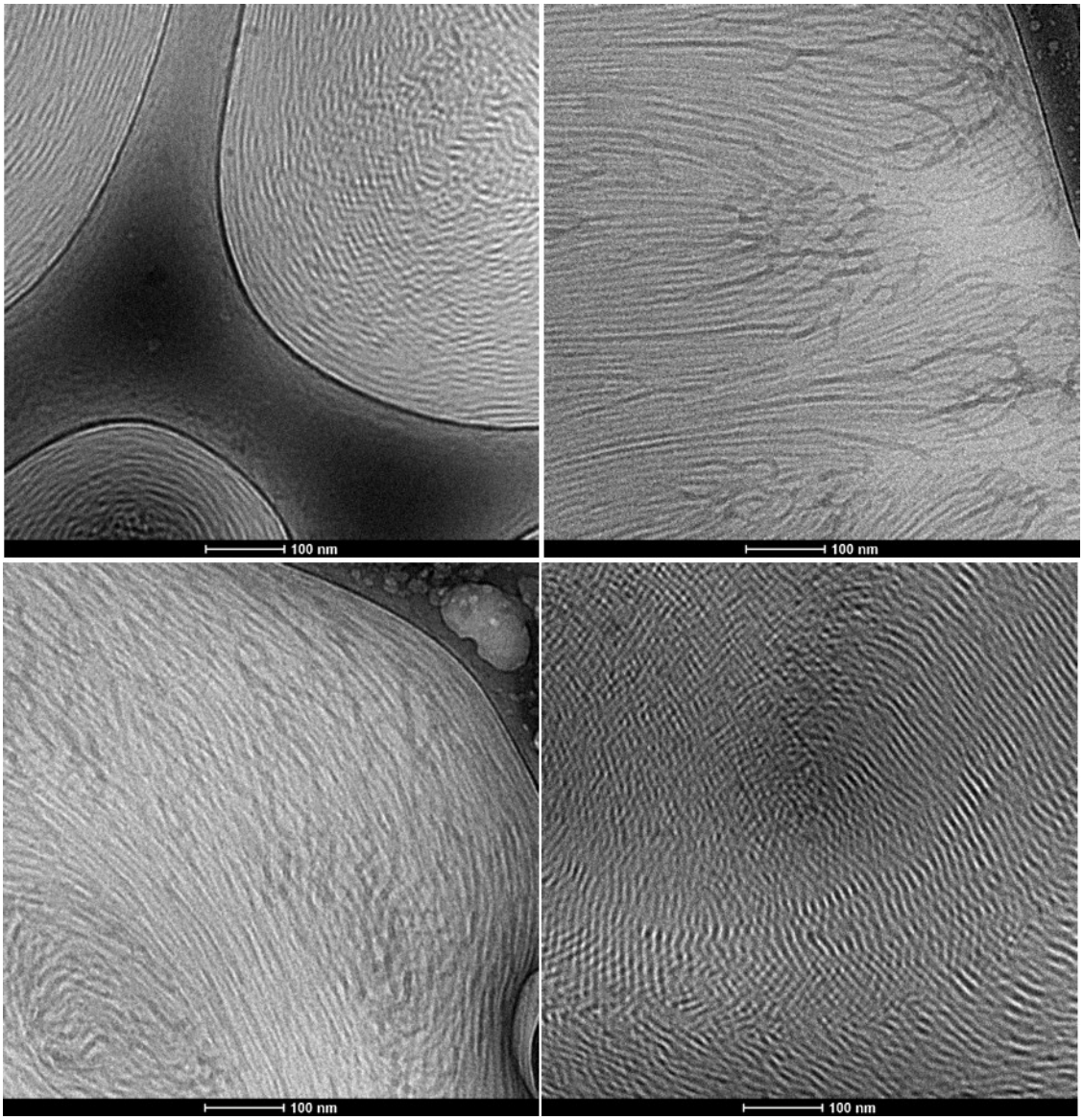

Figure A11. Typical cryo-TEM micrographs obtained from a 5.0 wt % cesium dodecyl sulfate aqueous solution at 40 °C.

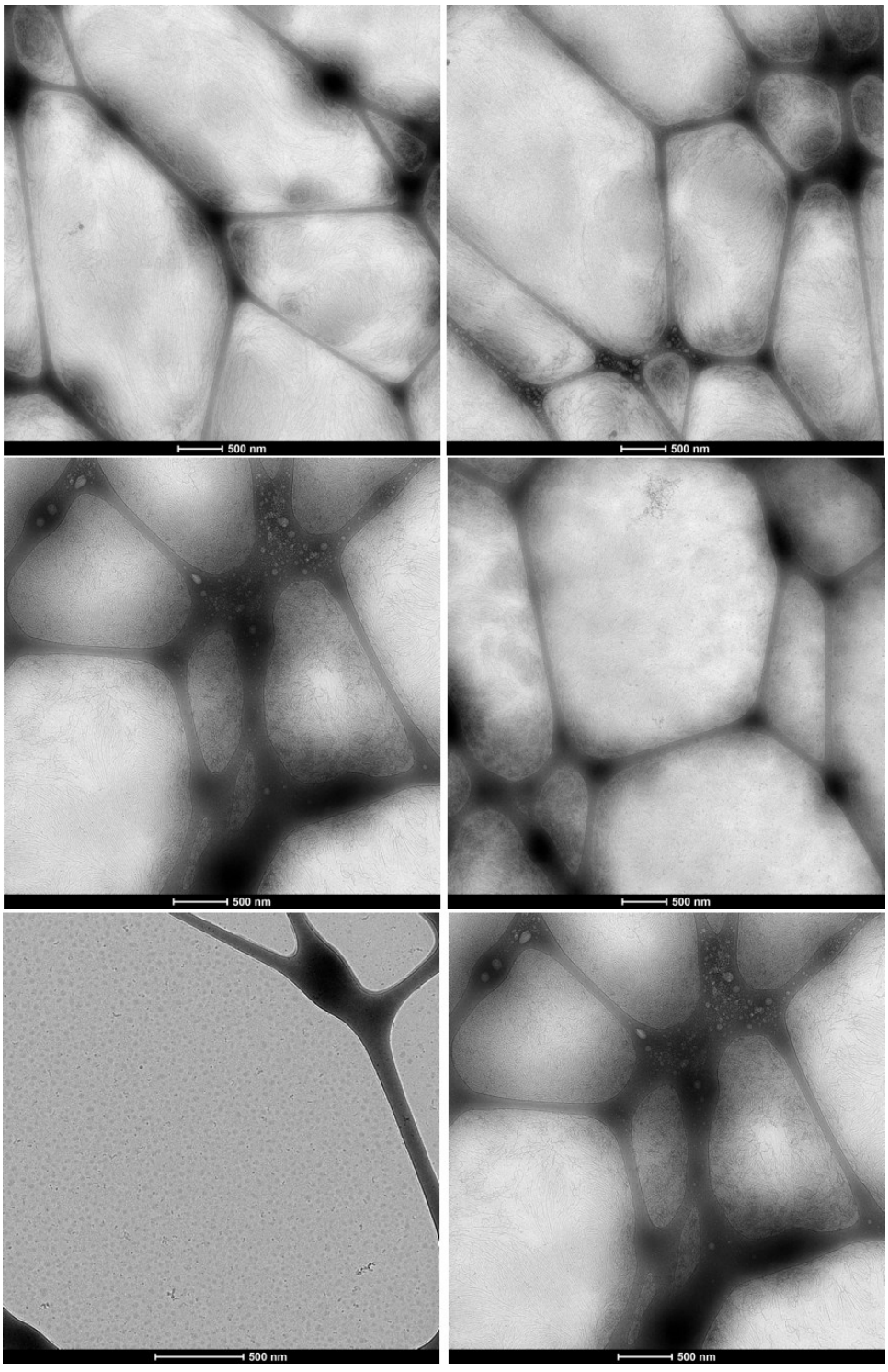

Figure A12. Typical cryo-TEM micrographs obtained from a 5.0 wt % cesium dodecyl sulfate aqueous solution at 40 °C.

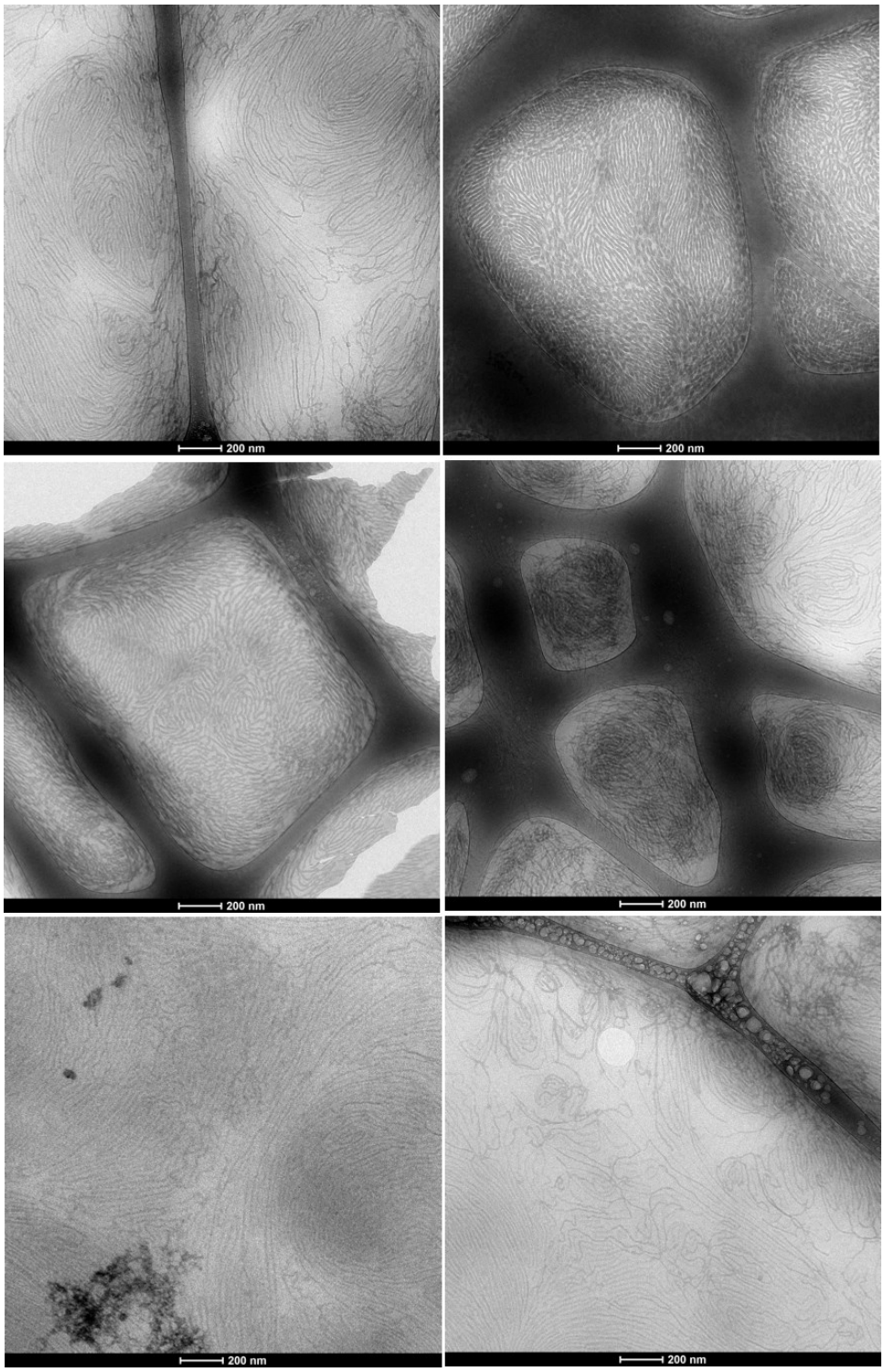

Figure A13. Typical cryo-TEM micrographs obtained from a 5.0 wt % cesium dodecyl sulfate aqueous solution at 40 °C.

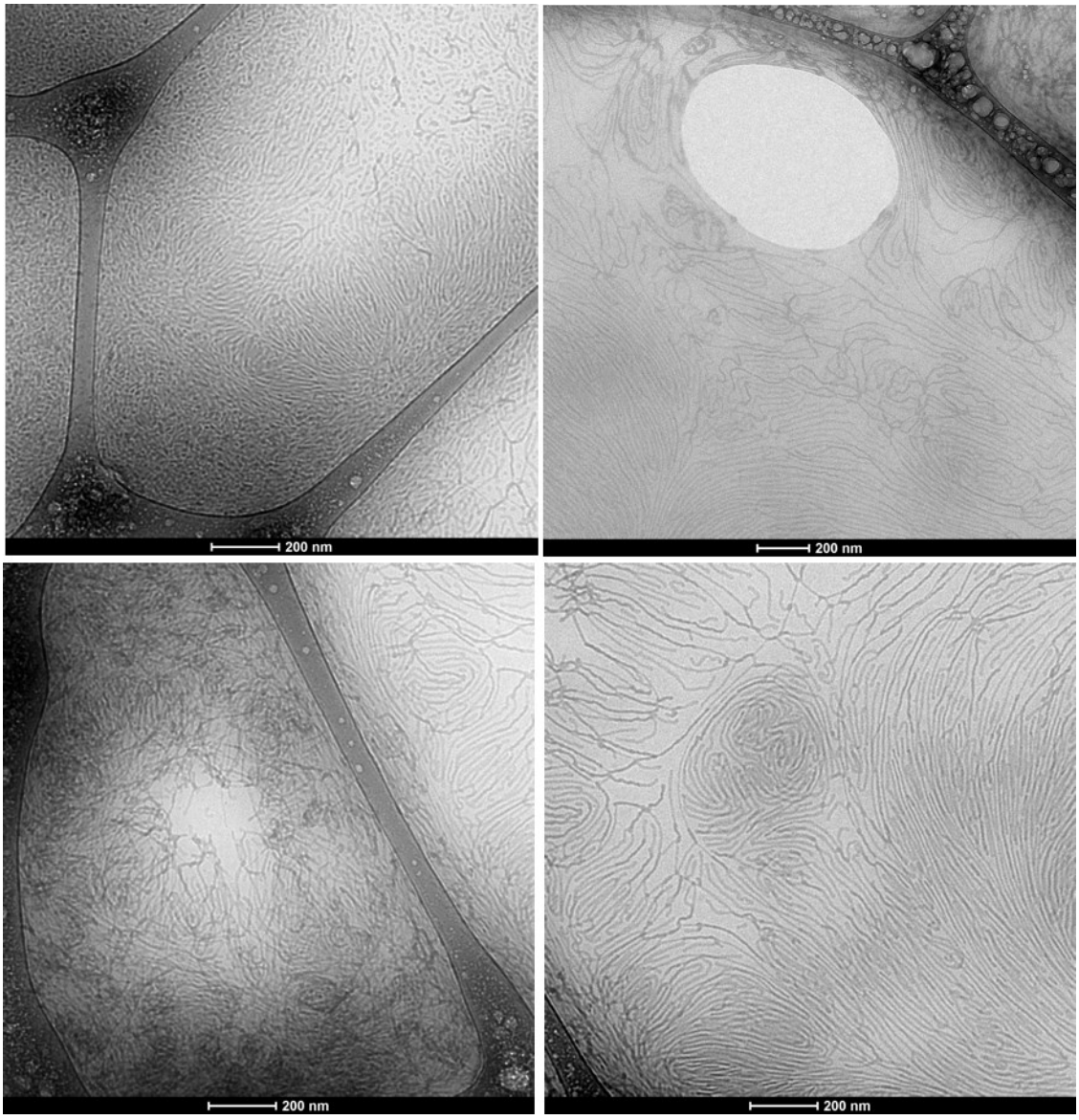

Figure A14. Typical cryo-TEM micrographs obtained from a 5.0 wt % cesium dodecyl sulfate aqueous solution at 40 °C.

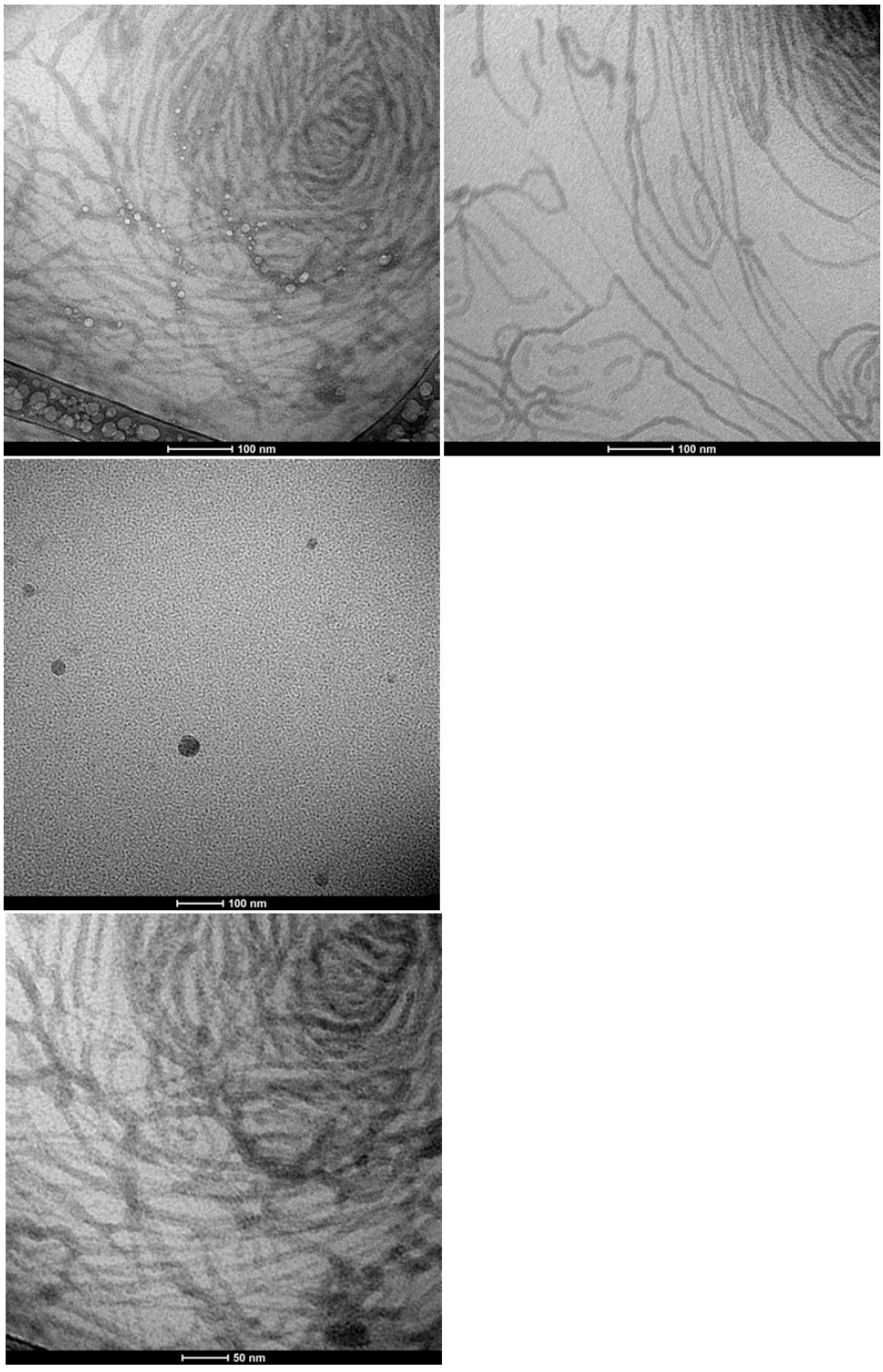

Figure A15. Typical cryo-TEM micrographs obtained from a 5.0 wt % cesium dodecyl sulfate aqueous solution at 40 °C.

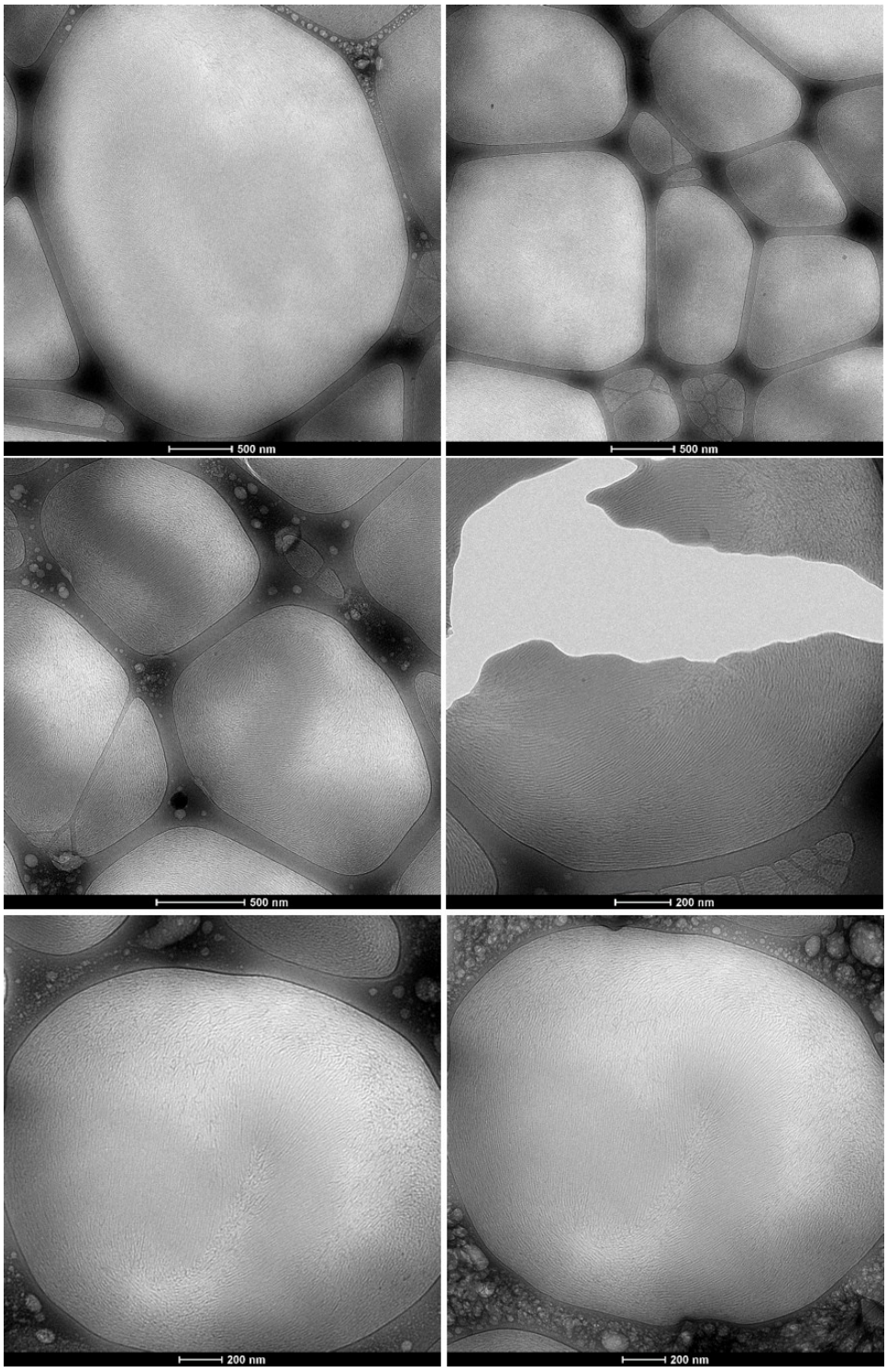

Figure A16. Typical cryo-TEM micrographs obtained from a 8.1 wt % cesium dodecyl sulfate aqueous solution at 35 °C.

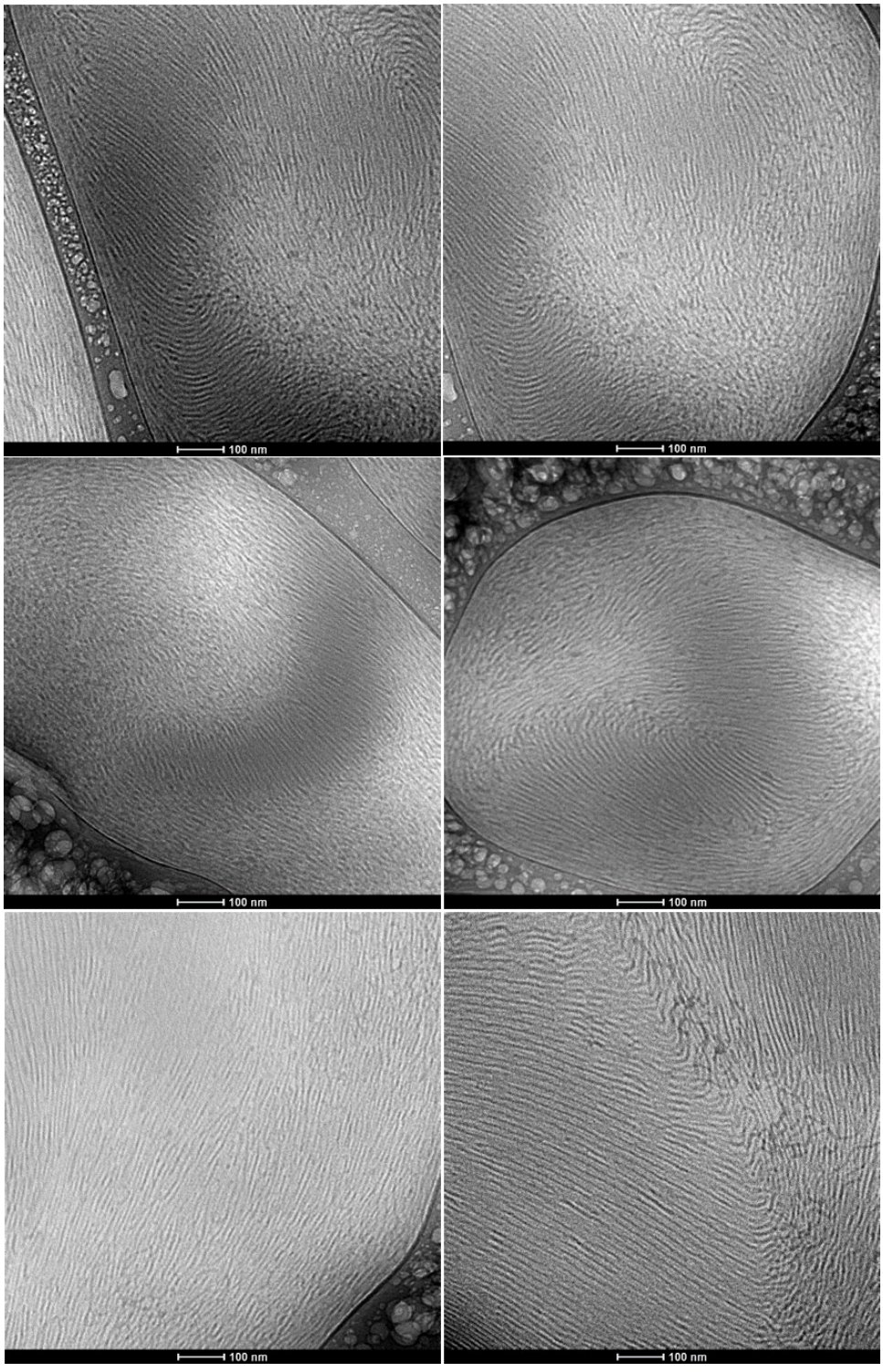

Figure A17. Typical cryo-TEM micrographs obtained from a 8.1 wt % cesium dodecyl sulfate aqueous solution at 35 °C.

III. FF-TEM images of CsDS aqueous solution from 5.0 wt % to 8.1 wt %

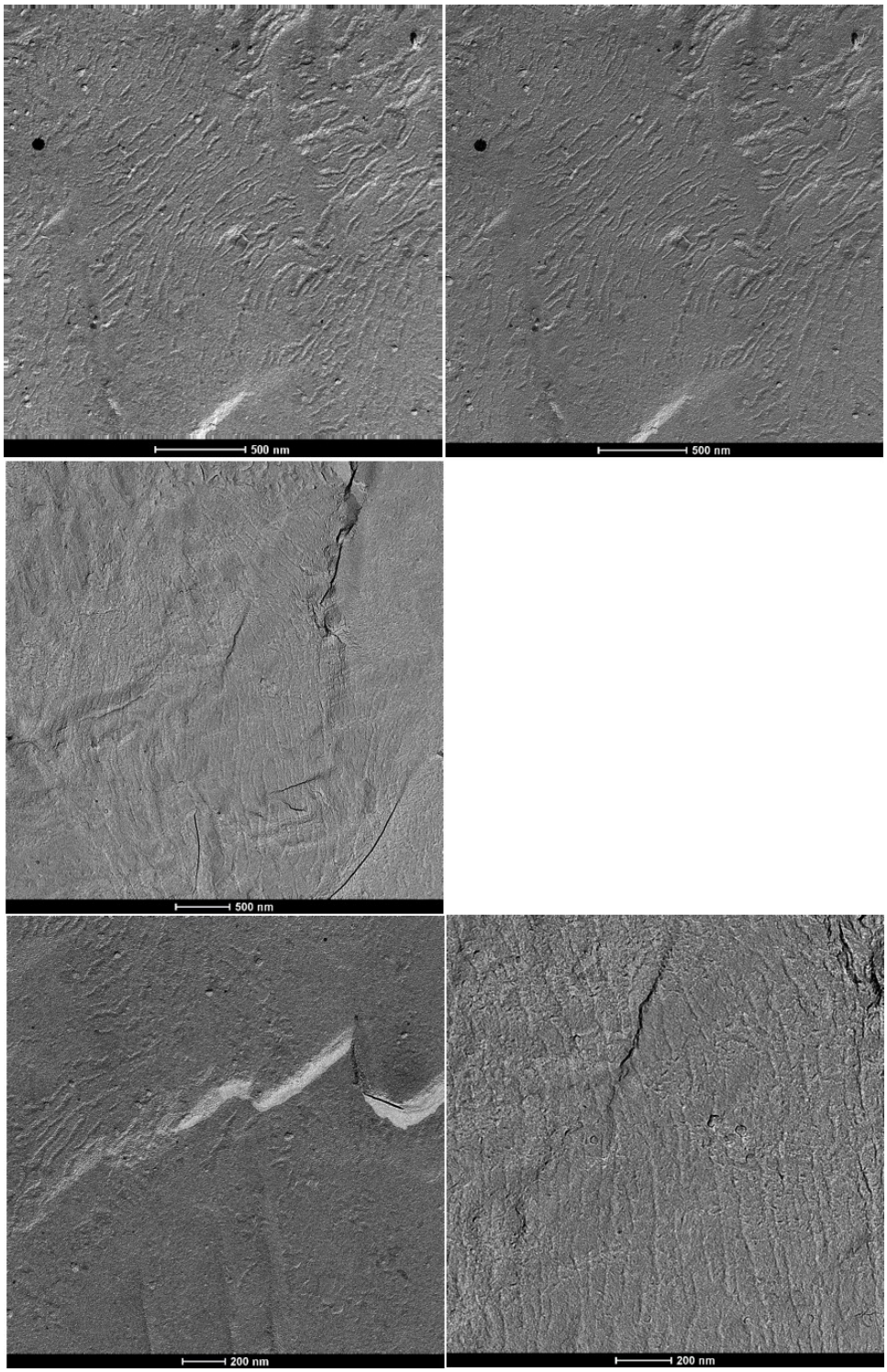

Figure A18. Typical FF-TEM micrographs obtained from a 5.0 wt % cesium dodecyl sulfate aqueous solution at 40 °C.

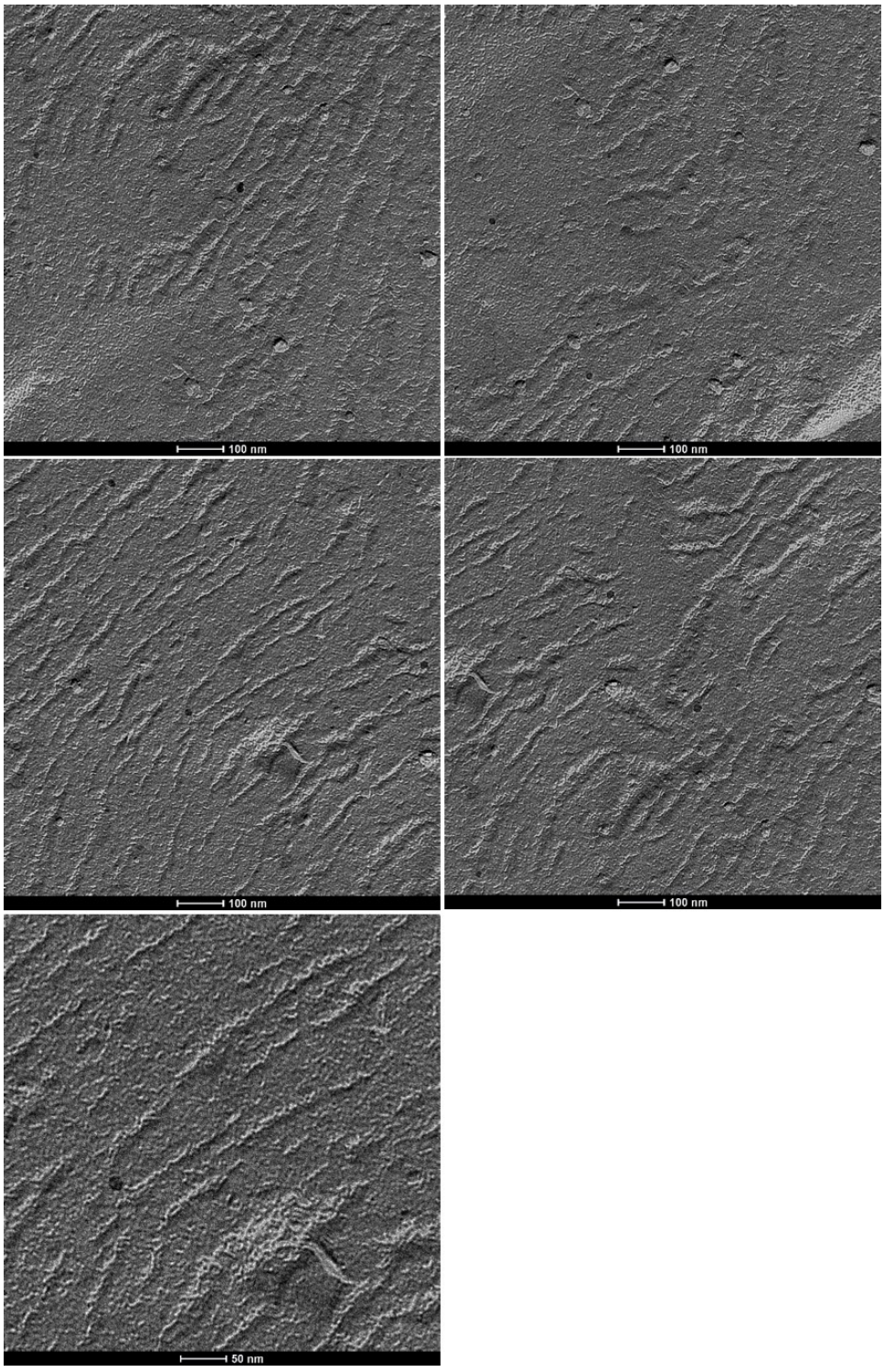

Figure A19. Typical FF-TEM micrographs obtained from a 5.0 wt % cesium dodecyl sulfate aqueous solution at 40 °C.

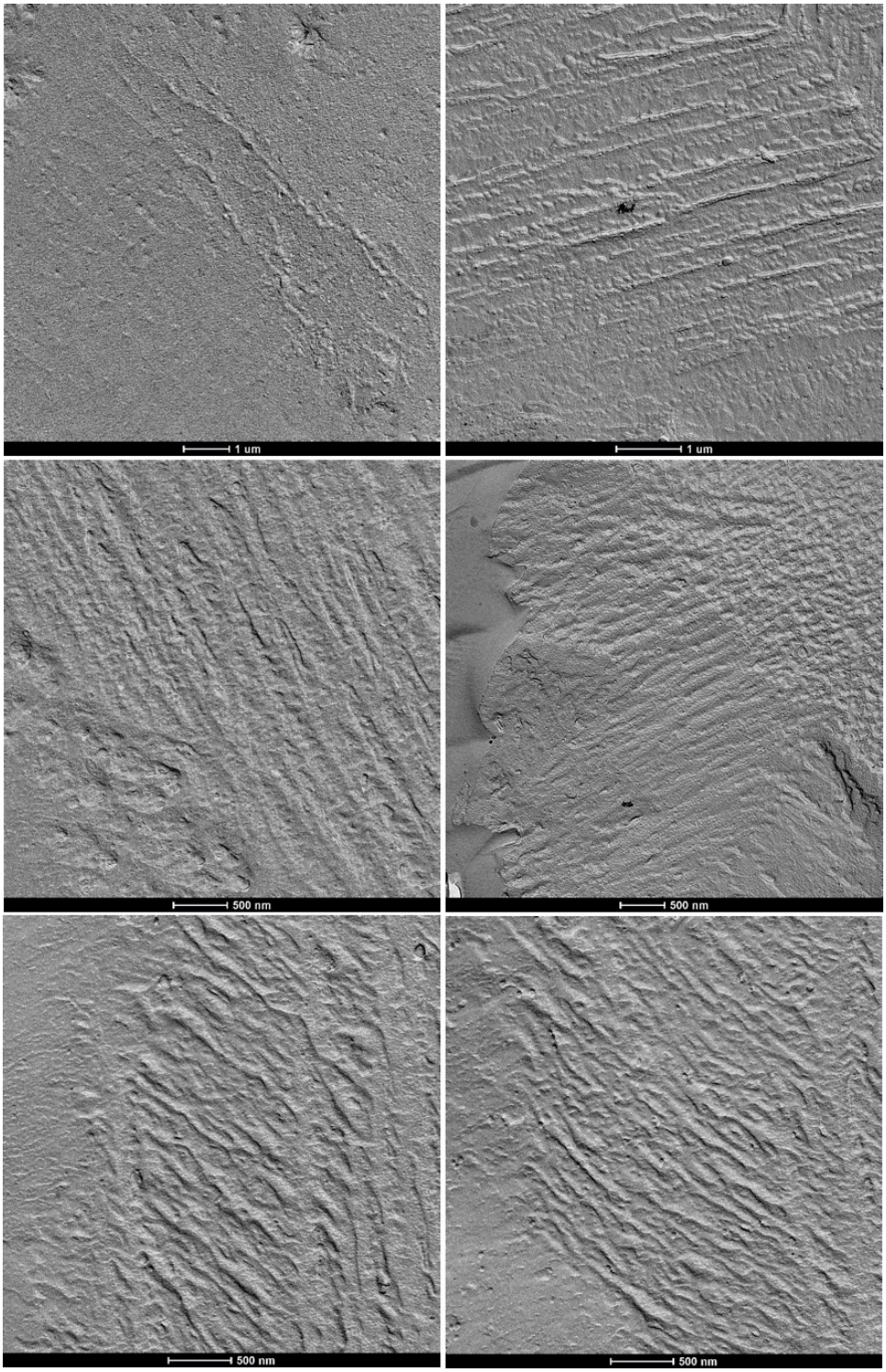

Figure A20. Typical FF-TEM micrographs obtained from a 5.0 wt % cesium dodecyl sulfate aqueous solution at 40 °C.

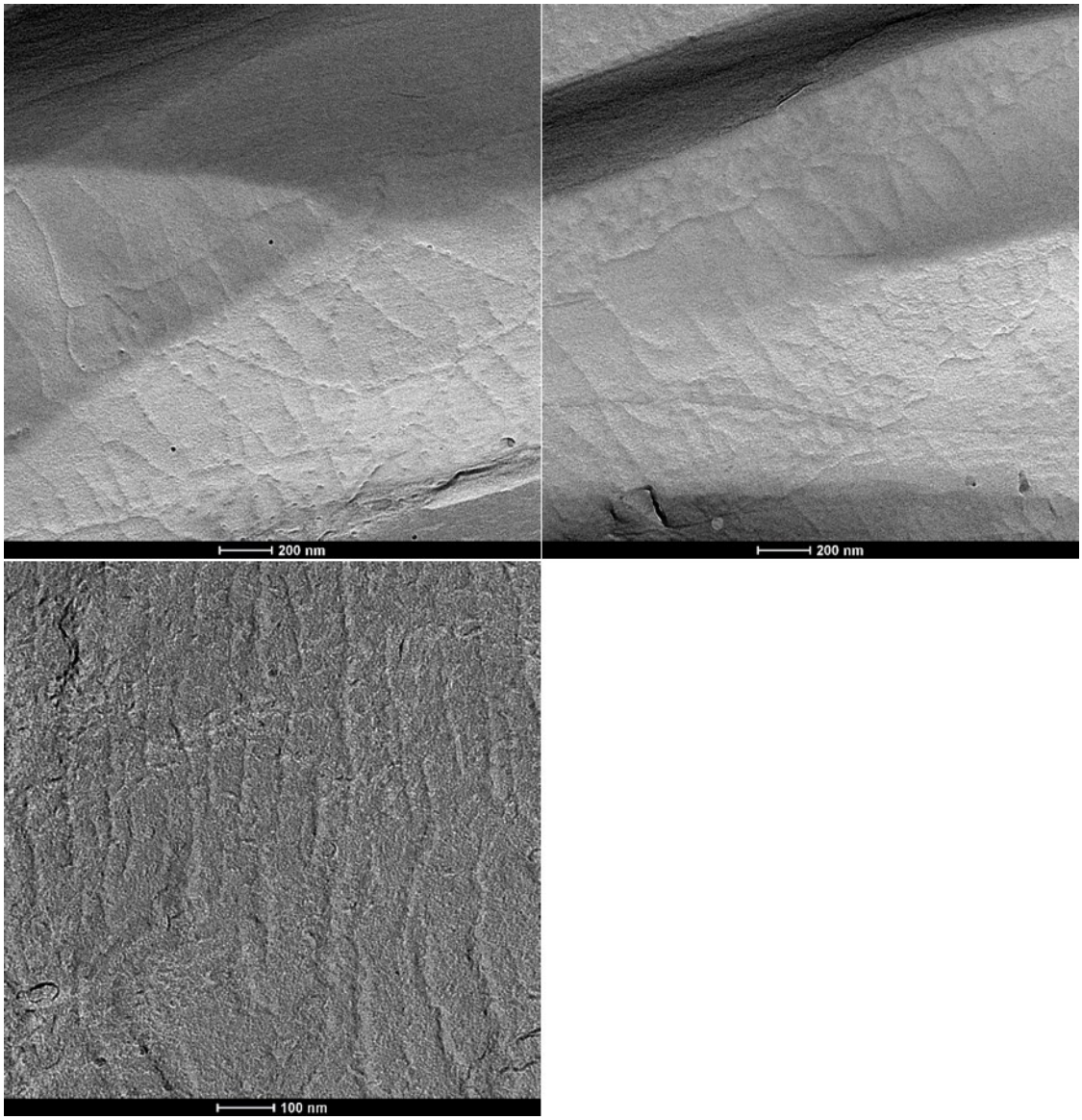

Figure A21. Typical FF-TEM micrographs obtained from a 5.0 wt % cesium dodecyl sulfate aqueous solution at 40 °C.

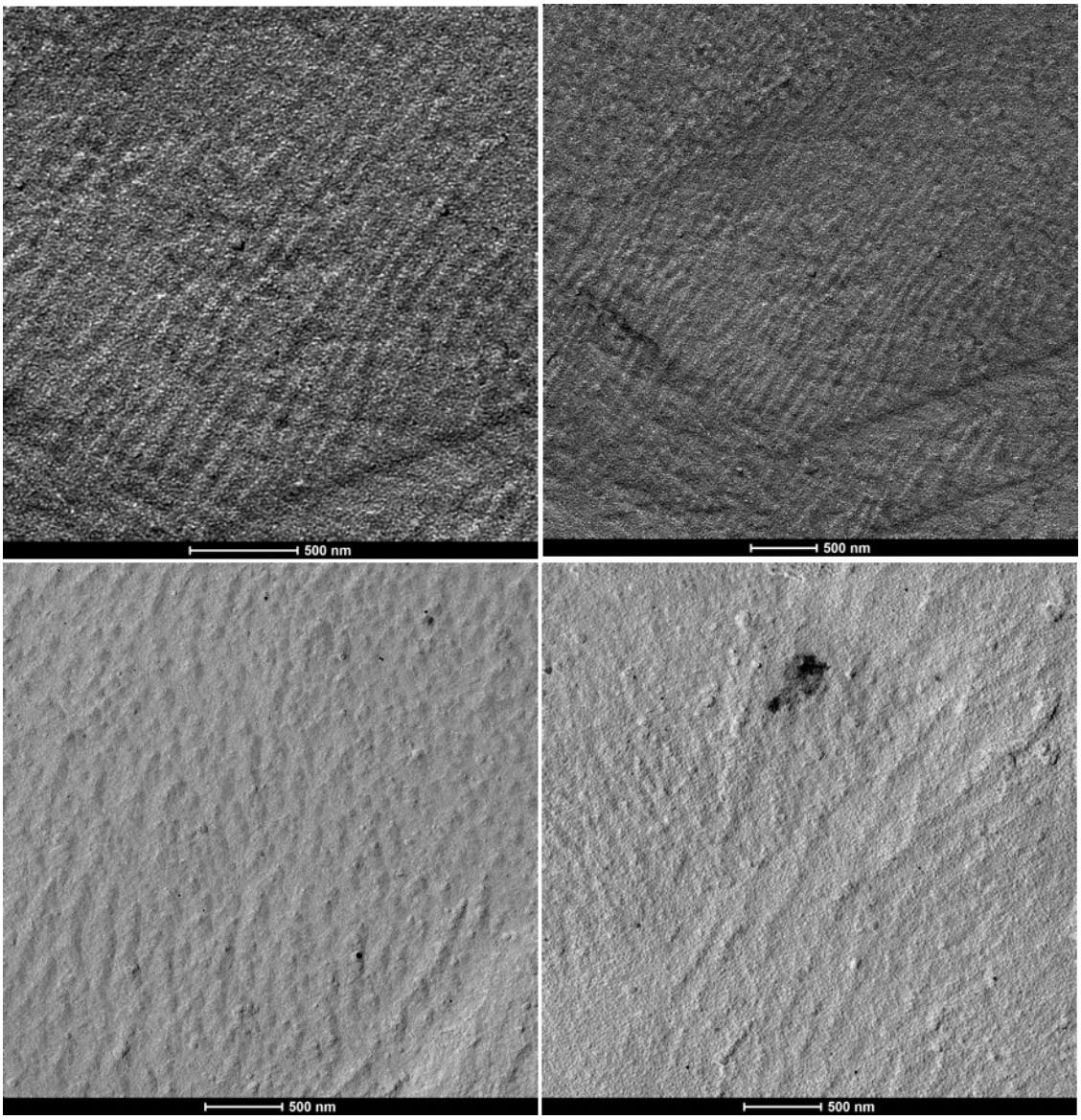

Figure A22. Typical FF-TEM micrographs obtained from a 5.0 wt % cesium dodecyl sulfate aqueous solution at 40 °C.

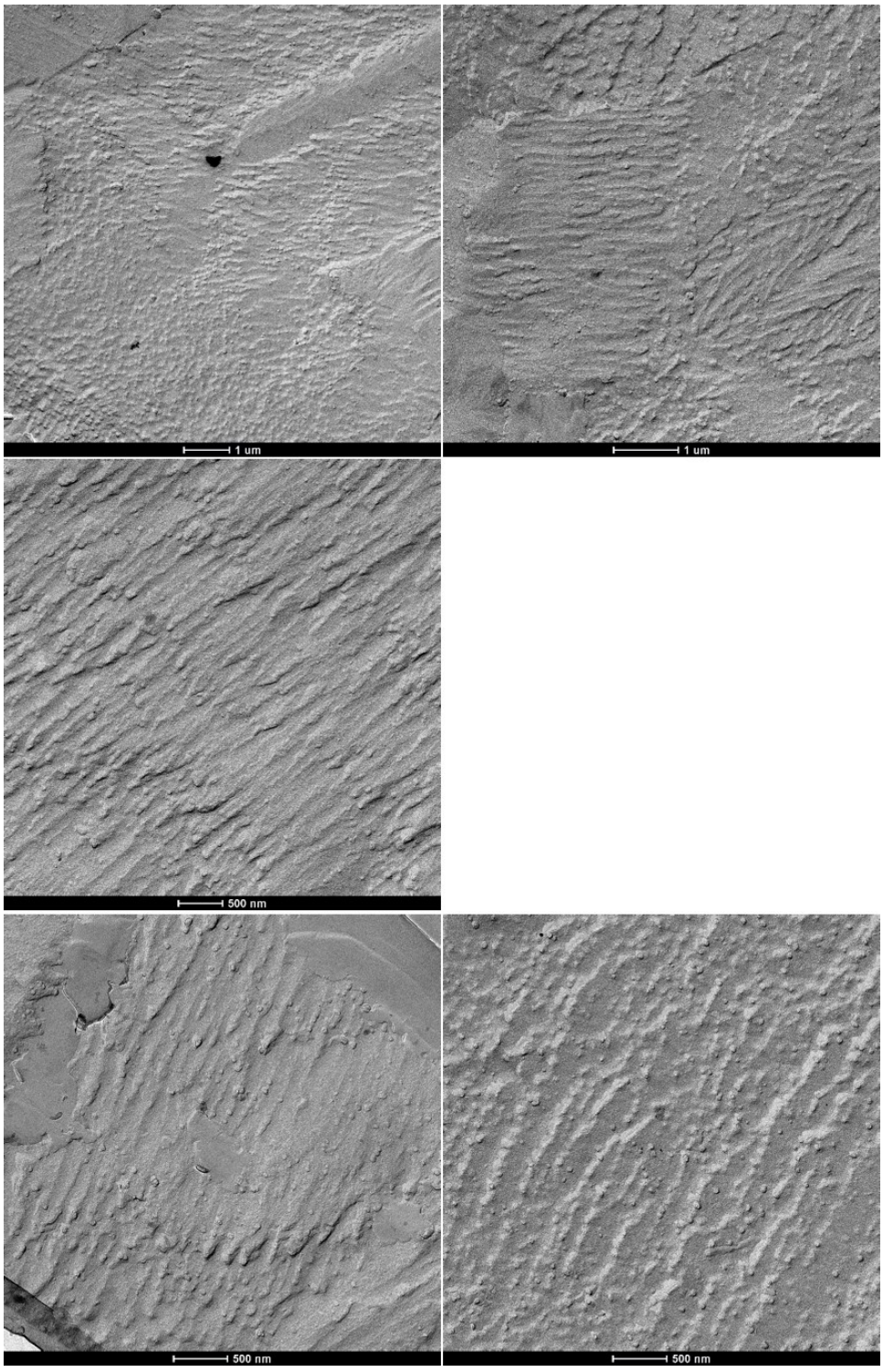

Figure A23. Typical FF-TEM micrographs obtained from a 8.1 wt % cesium dodecyl sulfate aqueous solution at 35 °C.

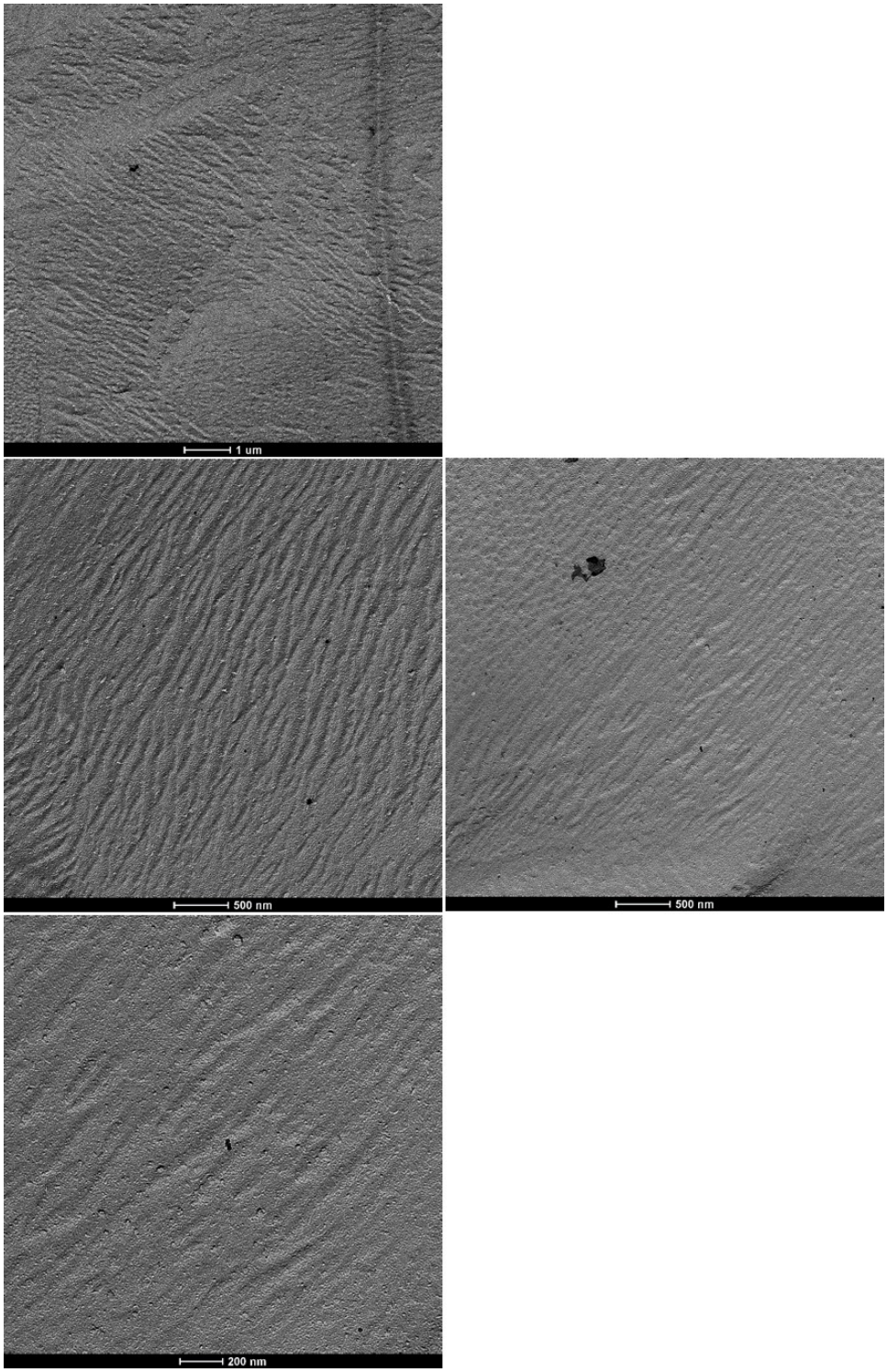

Figure A24. Typical FF-TEM micrographs obtained from a 8.1 wt % cesium dodecyl sulfate aqueous solution at 35 °C.

IV. FF-TEM images of bare copper planchette

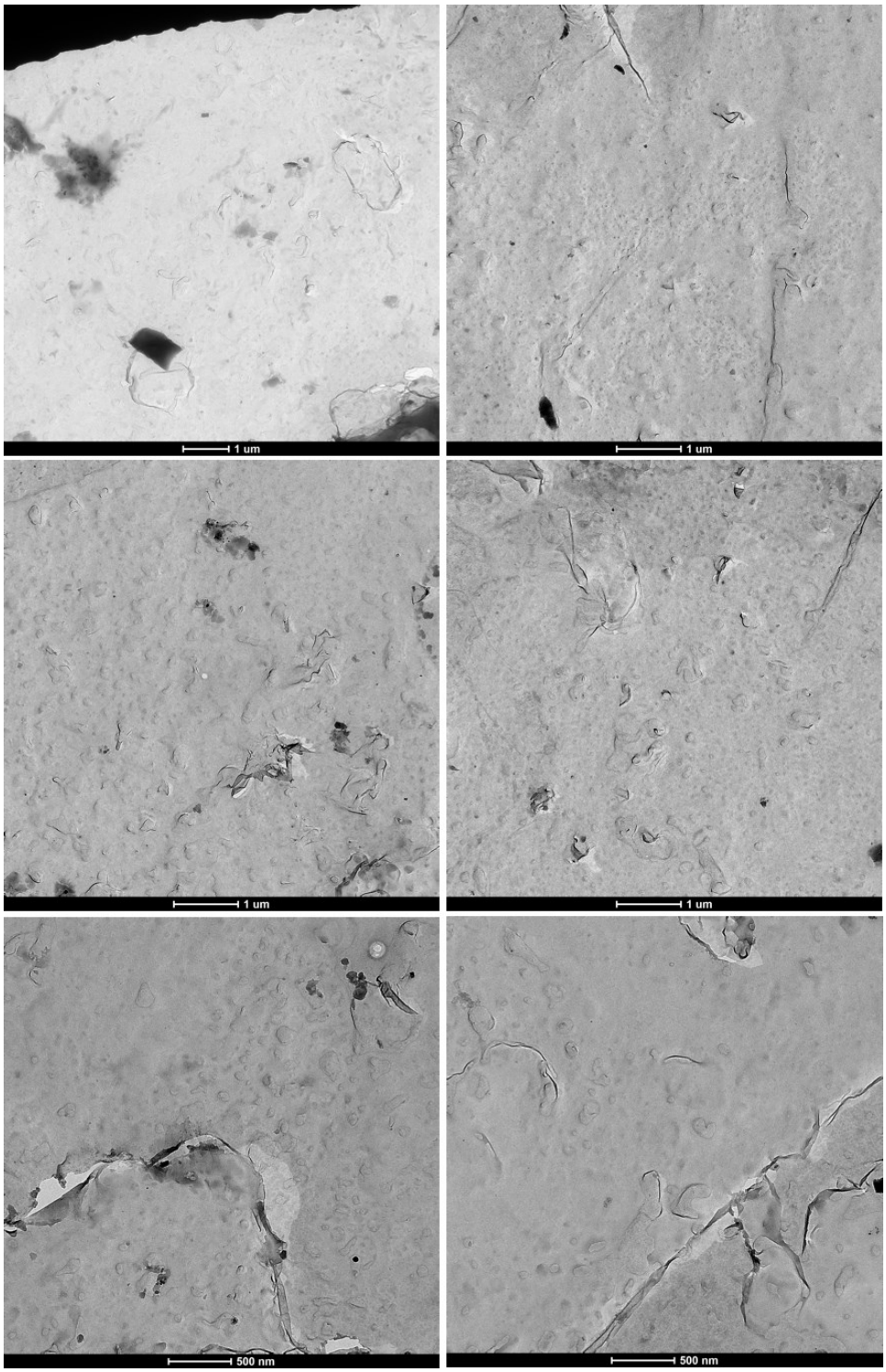

Figure A25. Typical FFT-EM micrographs obtained from a bare copper planchette.

Appendix B.

Cryo-TEM images of drug nanoparticles

I. Cryo-TEM images of 5K-10K poly(ethylene glycol)-*b*-poly(lactic-co-glycolic acid) (PEG-*b*-PLGA) diblock copolymer
- Figures B1 – B2

II. Cryo-TEM images of dried paclitaxel from DI-water suspension
- Figure B3

III. Collaborative work with Kevin Pustulka
- Figures B4 – B8

IV. Collaborative work with Andrew Michel
- Figures B9 – B13

V. Collaborative work with Adam Wohl and Jing Han. (5K-10K poly(ethylene glycol)-*b*-poly(lactic-co-glycolic acid) (PEG-*b*-PLGA) with 2′,7-tri-ethoxy paclitaxel silicate nanoparticles.)
- Figures B14 – B29

VI. Collaborative work with Andrew Michel and Jing Han
- Figures B30 – B49

I. Cryo-TEM images of 5K-10K poly(ethylene glycol)-*b*-poly(lactic-co-glycolic acid) (PEG-*b*-PLGA) diblock copolymer

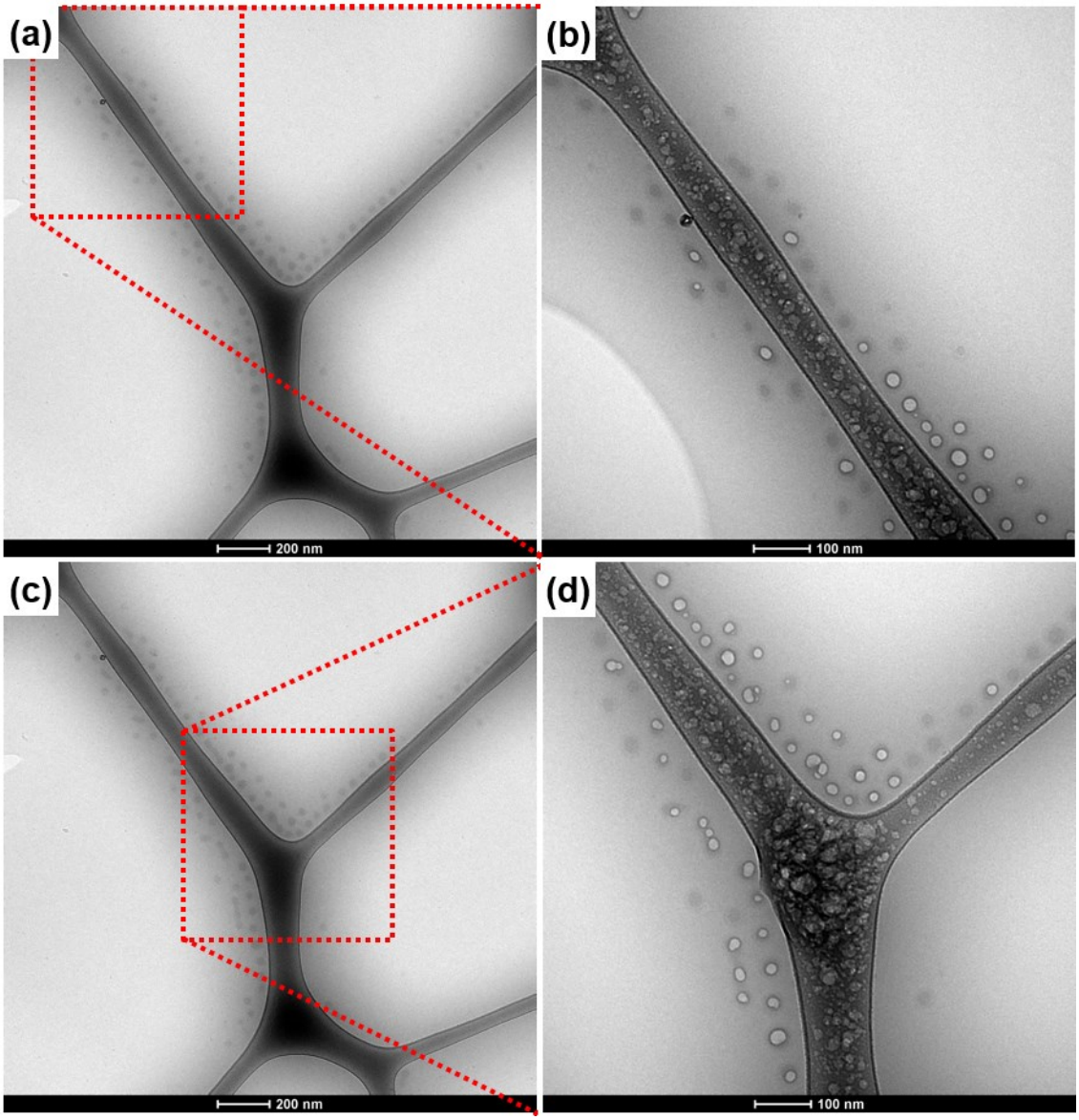

Figure B1. Typical cryo-TEM micrographs obtained from poly(ethylene glycol)-*b*-poly(lactic-co-glycolic acid) (PEG-*b*-PLGA) diblock copolymer. (a) is low magnification of (b, c) are low magnification of (d). (b, d) show some beam damaged block copolymer nanoparticles. Core in dark contrast may suggest PLGA and shell (halos) in the undamaged nanoparticles in (b, d) may show PEG corona.

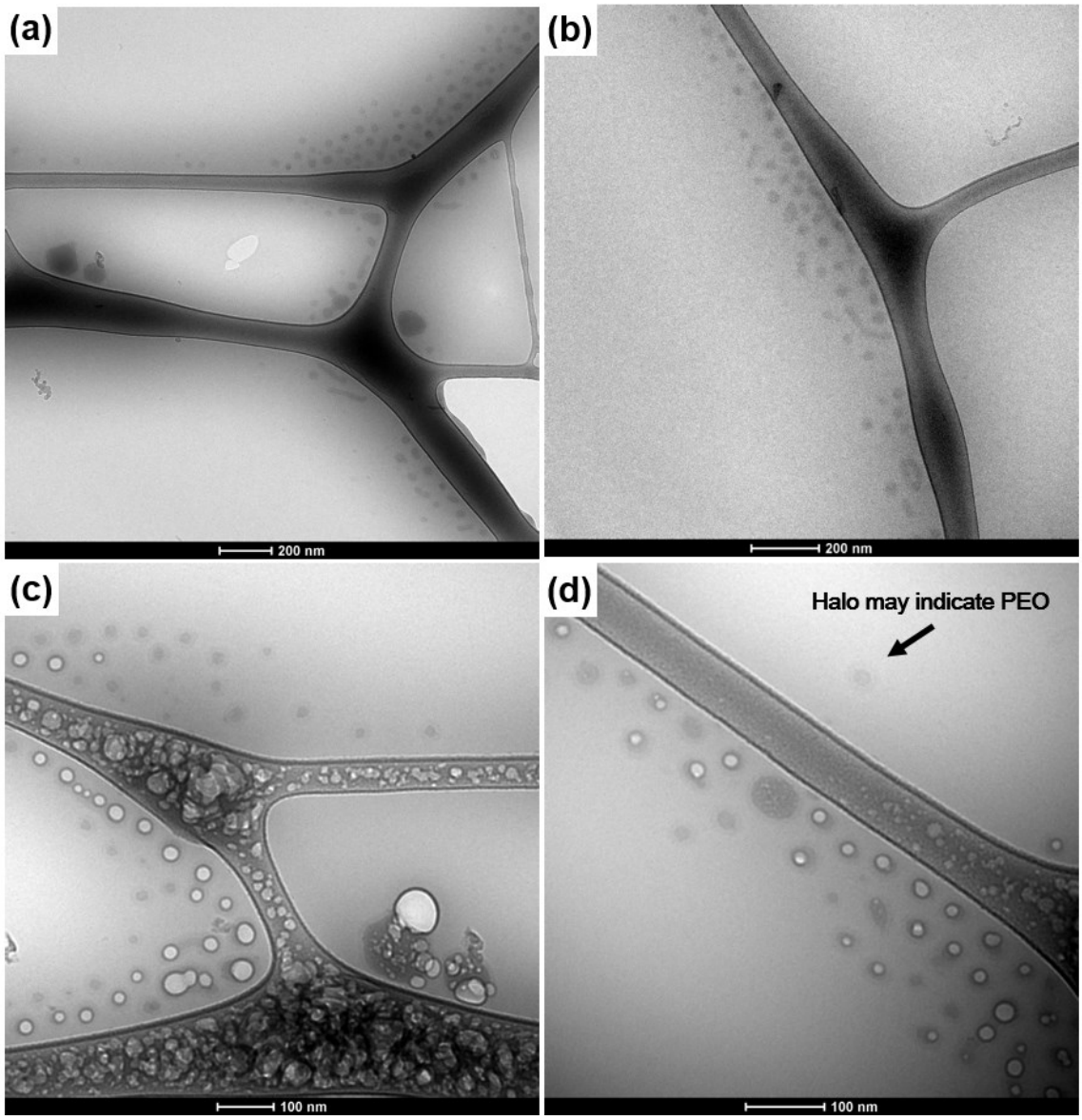

Figure B2. Typical cryo-TEM micrographs obtained from poly(ethylene glycol)-*b*-poly(lactic-co-glycolic acid) (PEG-*b*-PLGA) diblock copolymer. (a, b) are low magnification of diblock copolymer with no beam damage. (c, d) are high magnification of diblock copolymer with beam damage. Undamaged diblock copolymer may show core (PLGA) and shell (PEG) structure.

II. Cryo-TEM images of dried paclitaxel from DI-water suspension

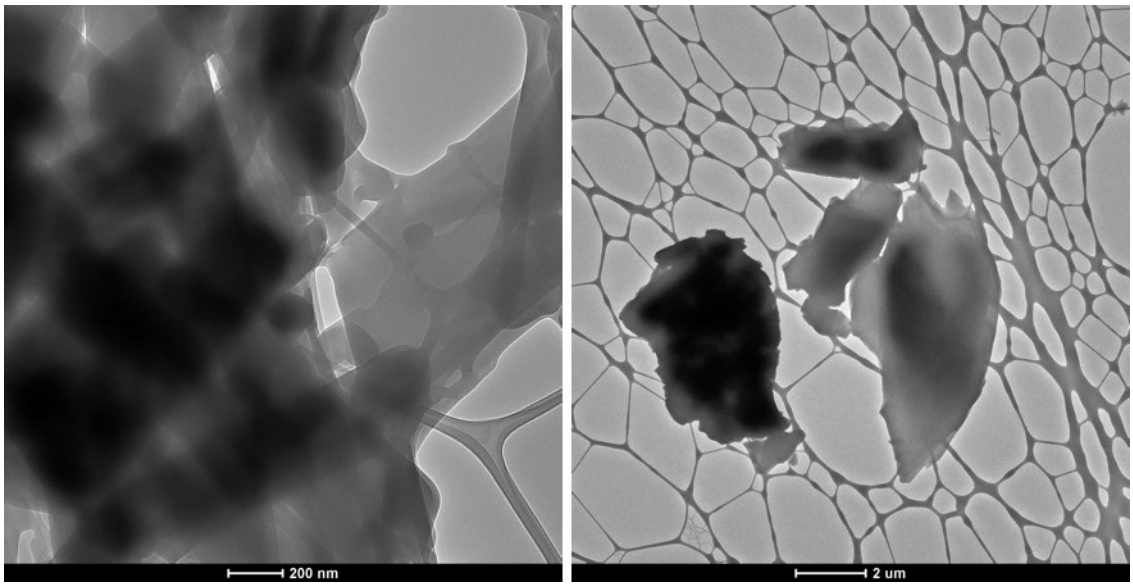

Figure B3. Typical cryo-TEM micrographs obtained from DI-water suspended paclitaxel.

III. Collaborative work with Kevin Pustulka

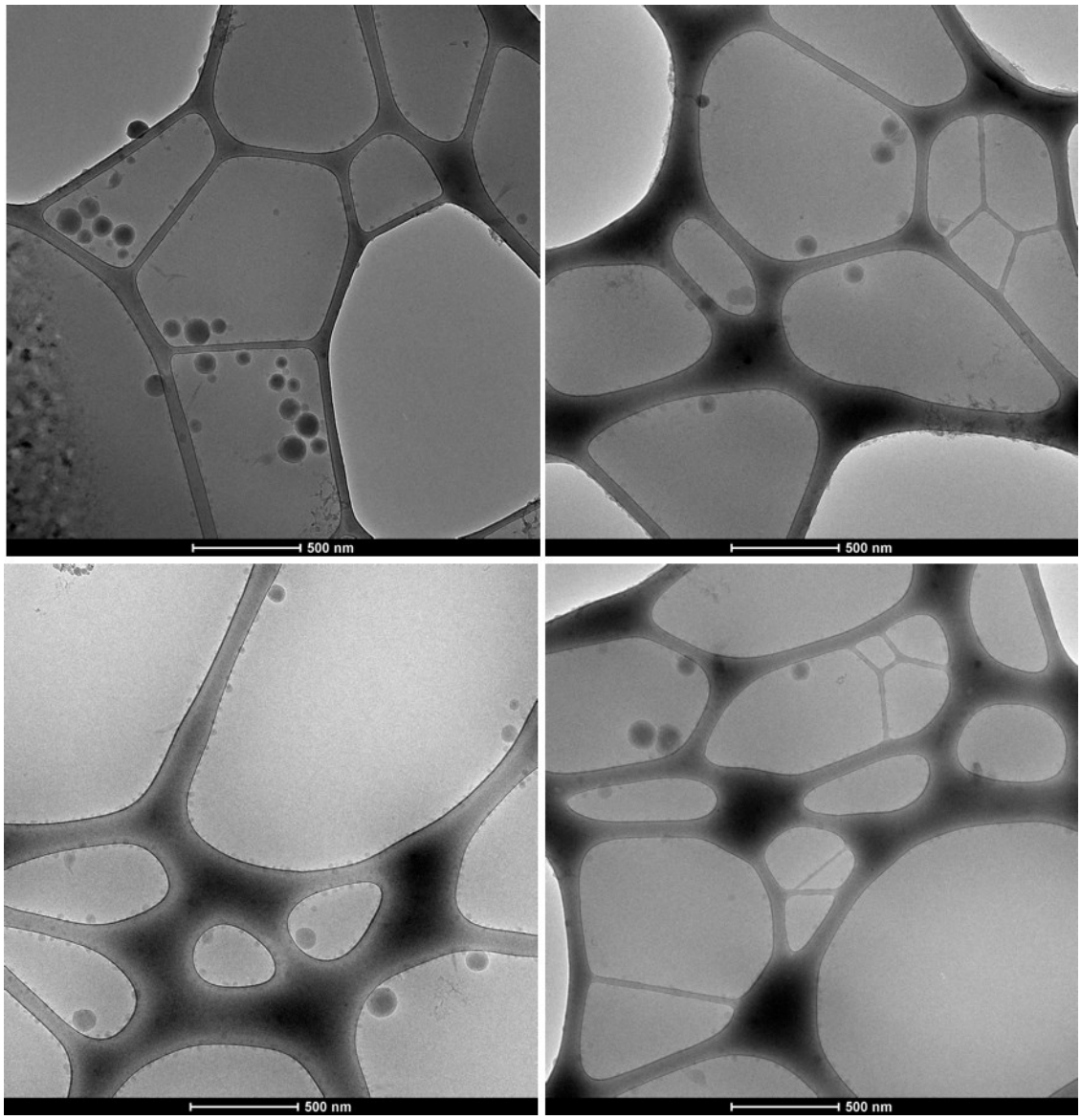

Figure B4. Typical cryo-TEM micrographs obtained from 5K-10K PEG-*b*-PLGA/bis-triethylsilicate paclitaxel prodrug (0.1 wt % loaded) stained with 2 wt % uranyl acetate. Sample is provided by Kevin Pustulka.

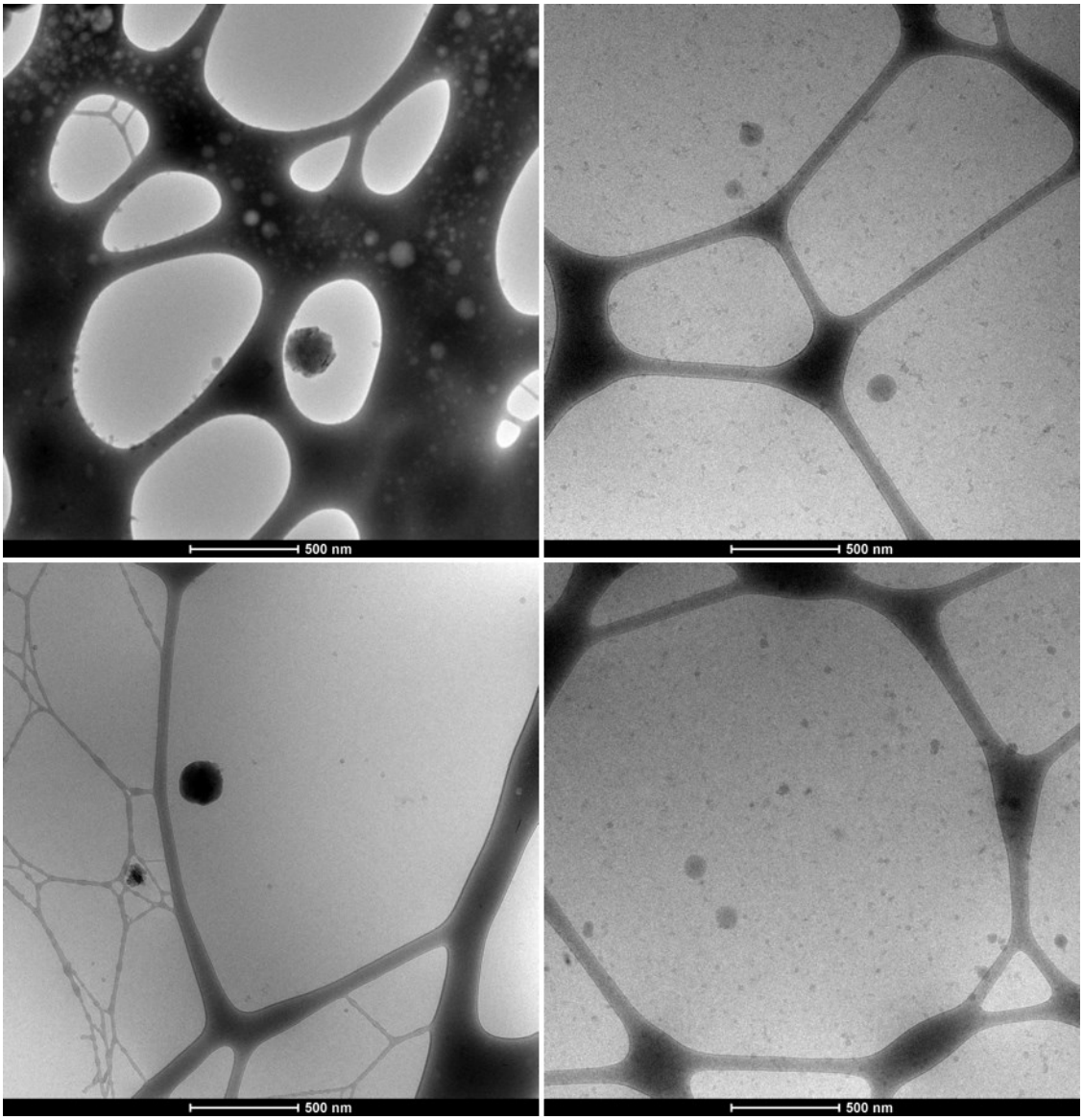

Figure B5. Typical cryo-TEM micrographs obtained from 5K-10K PEG-*b*-PLGA/bis-triethylsilicate paclitaxel prodrug (0.1 wt % loaded) stained with 0.135 M osmium tetroxide. Sample is provided by Kevin Pustulka.

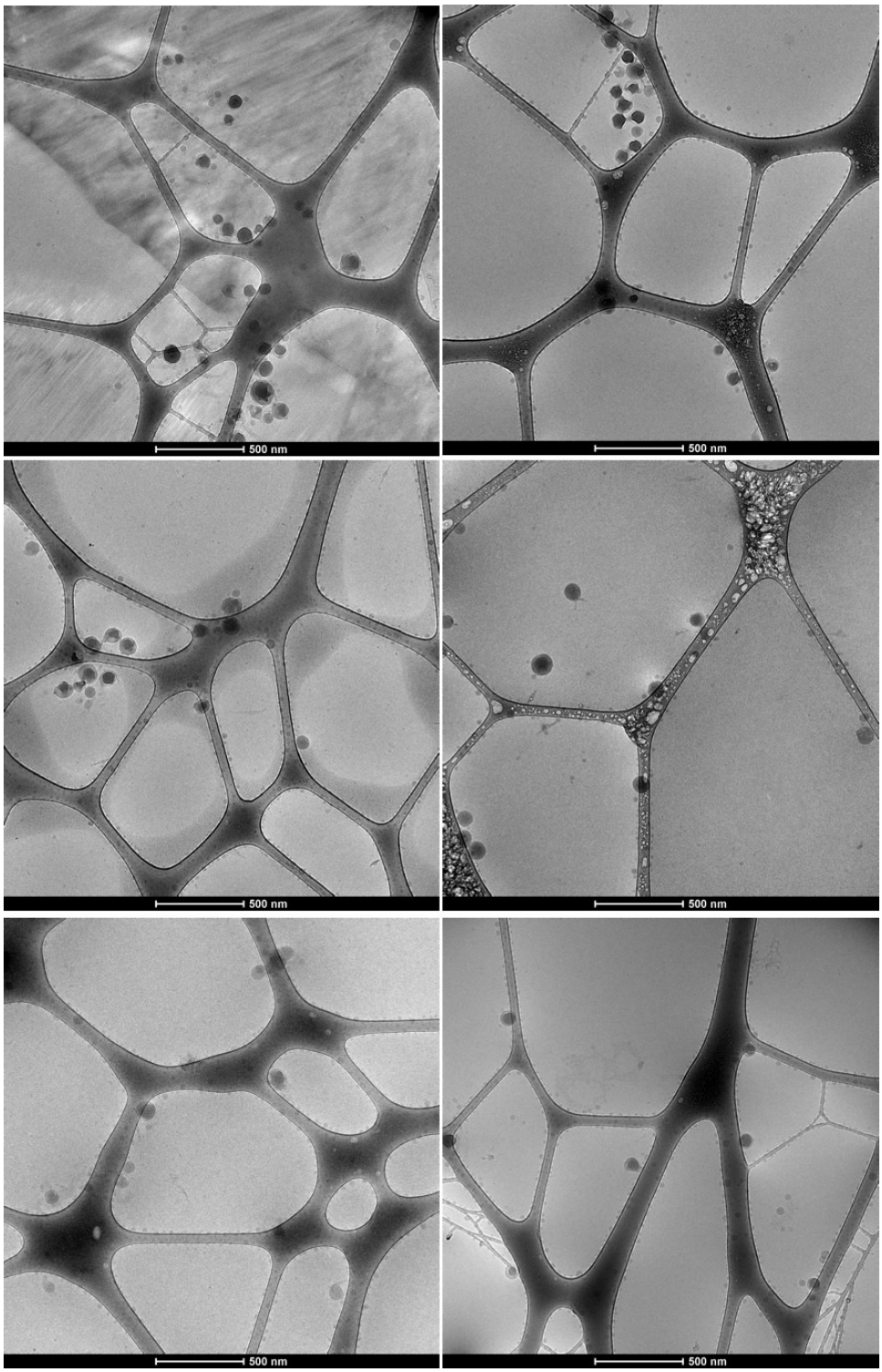

Figure B6. Typical cryo-TEM micrographs obtained from 5K-10K PEG-*b*-PLGA/bis-triethylsilicate paclitaxel prodrug (0.1 wt % loaded) stained with 0.135 M osmium tetroxide and 2 wt % uranyl acetate. Sample is provided by Kevin Pustulka.

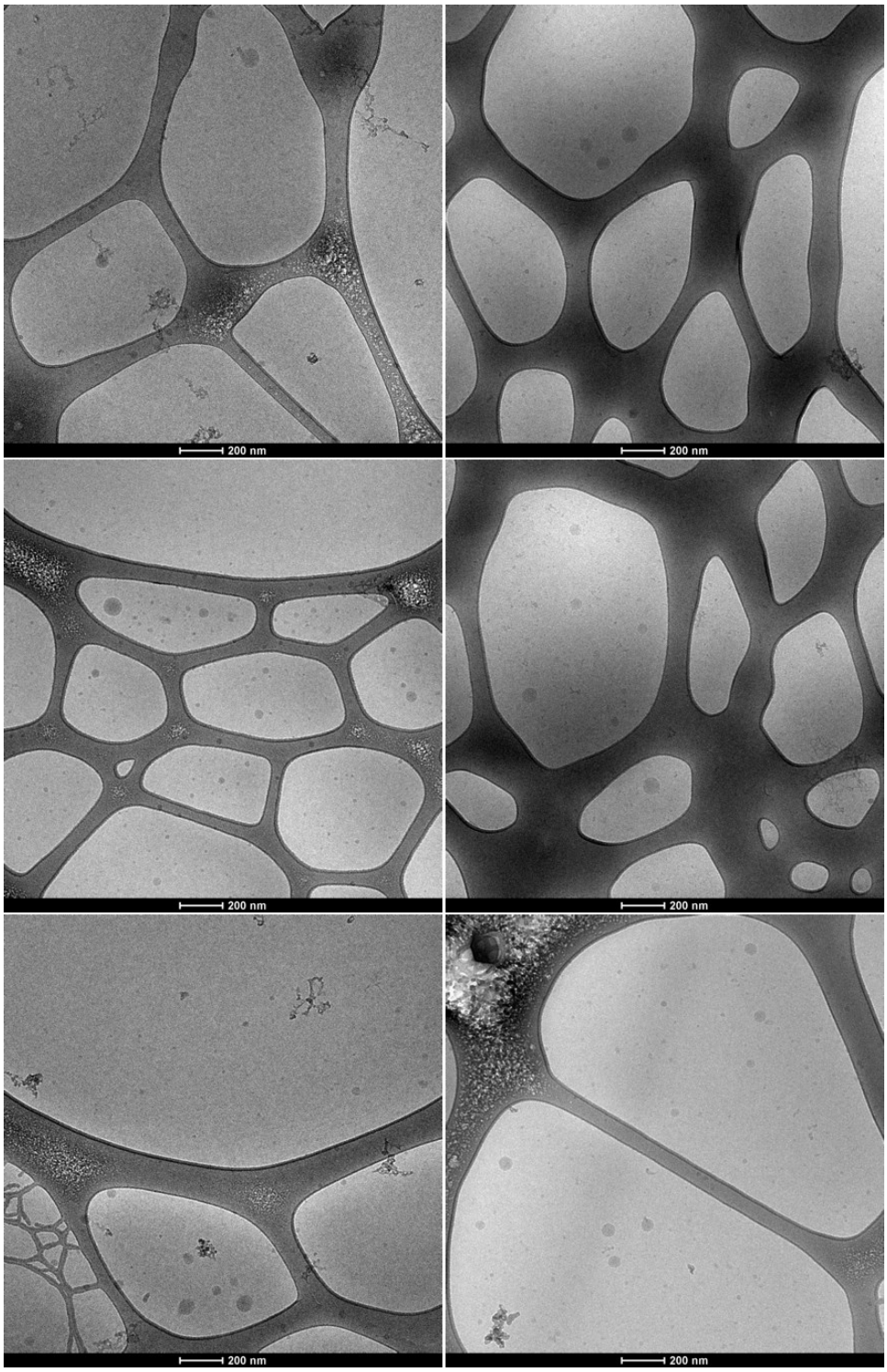

Figure B7. Typical cryo-TEM micrographs obtained from 5K-10K PEG-*b*-PLGA/tetramenthoxysilicate (50%). Sample is provided by Kevin Pustulka.

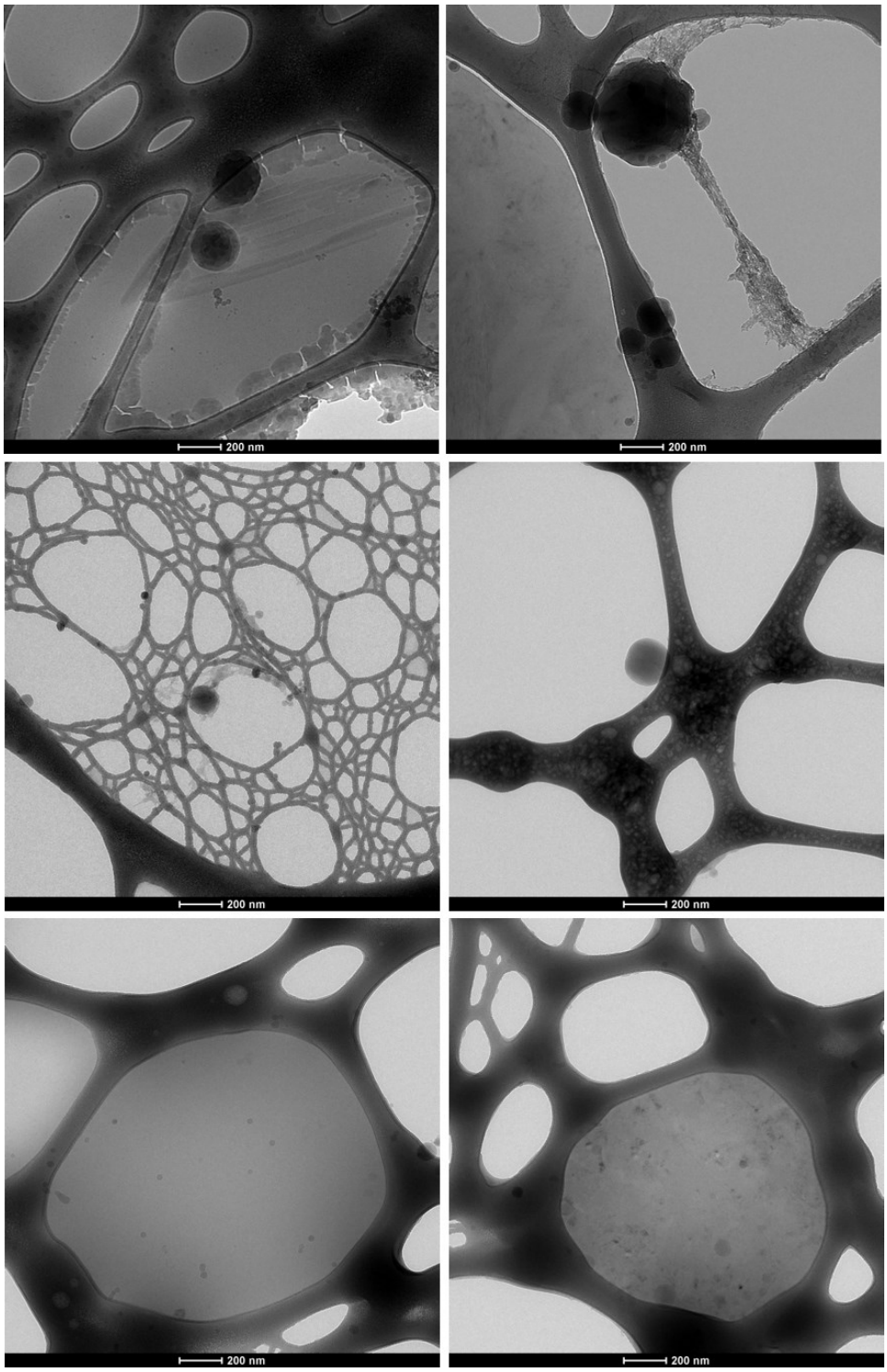

Figure B8. Typical cryo-TEM micrographs obtained from 5K-10K PEG-*b*-PLGA/tetramenthoxysilicate (90%). Sample is provided by Kevin Pustulka.

IV. Collaborative work with Andrew Michel

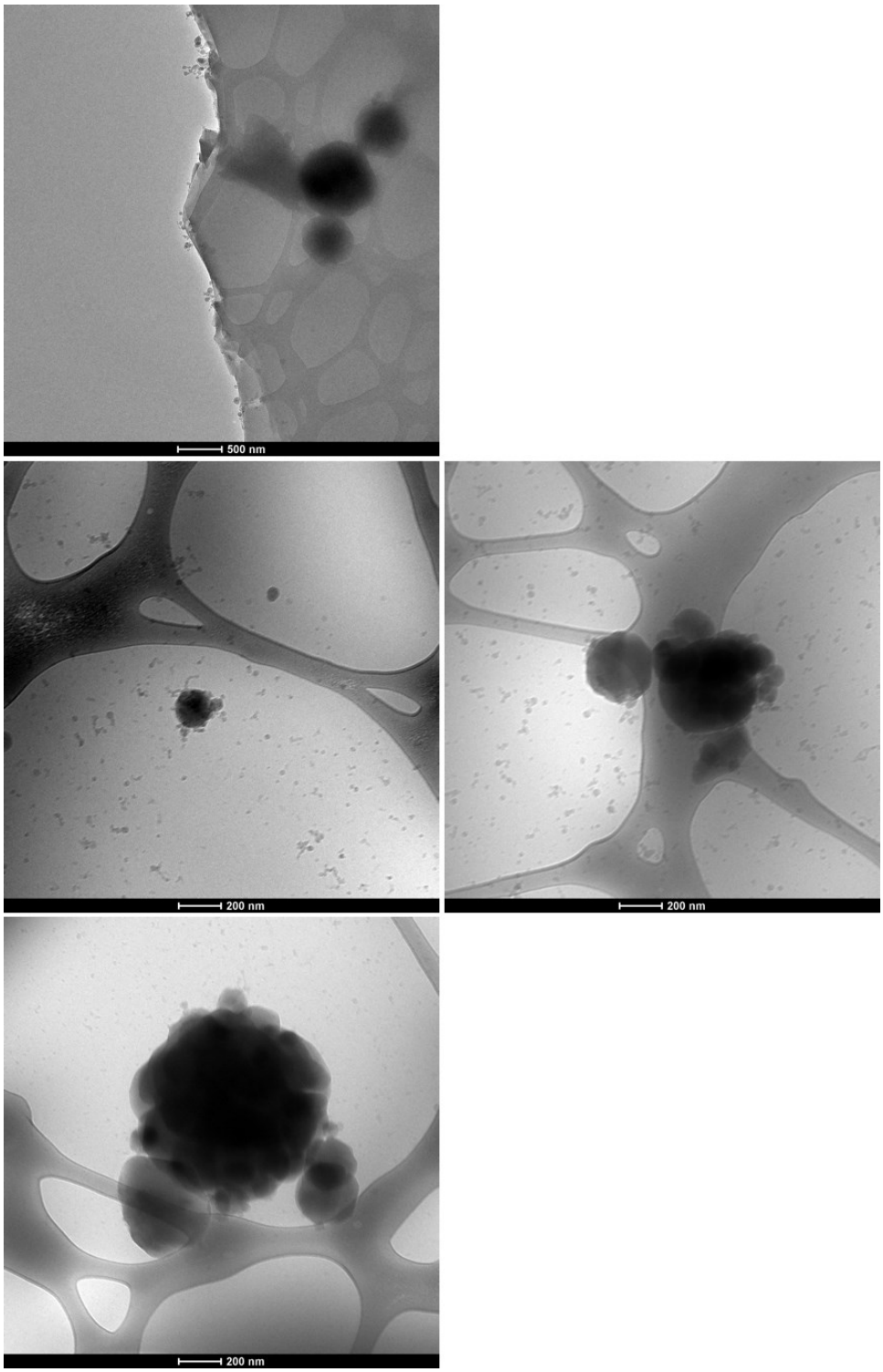

Figure B9. Typical cryo-TEM micrographs obtained from 5K-10K PEG-*b*-PLGA/triiodiphenol paclitaxel prodrug. Sample is provided by Andrew Michel.

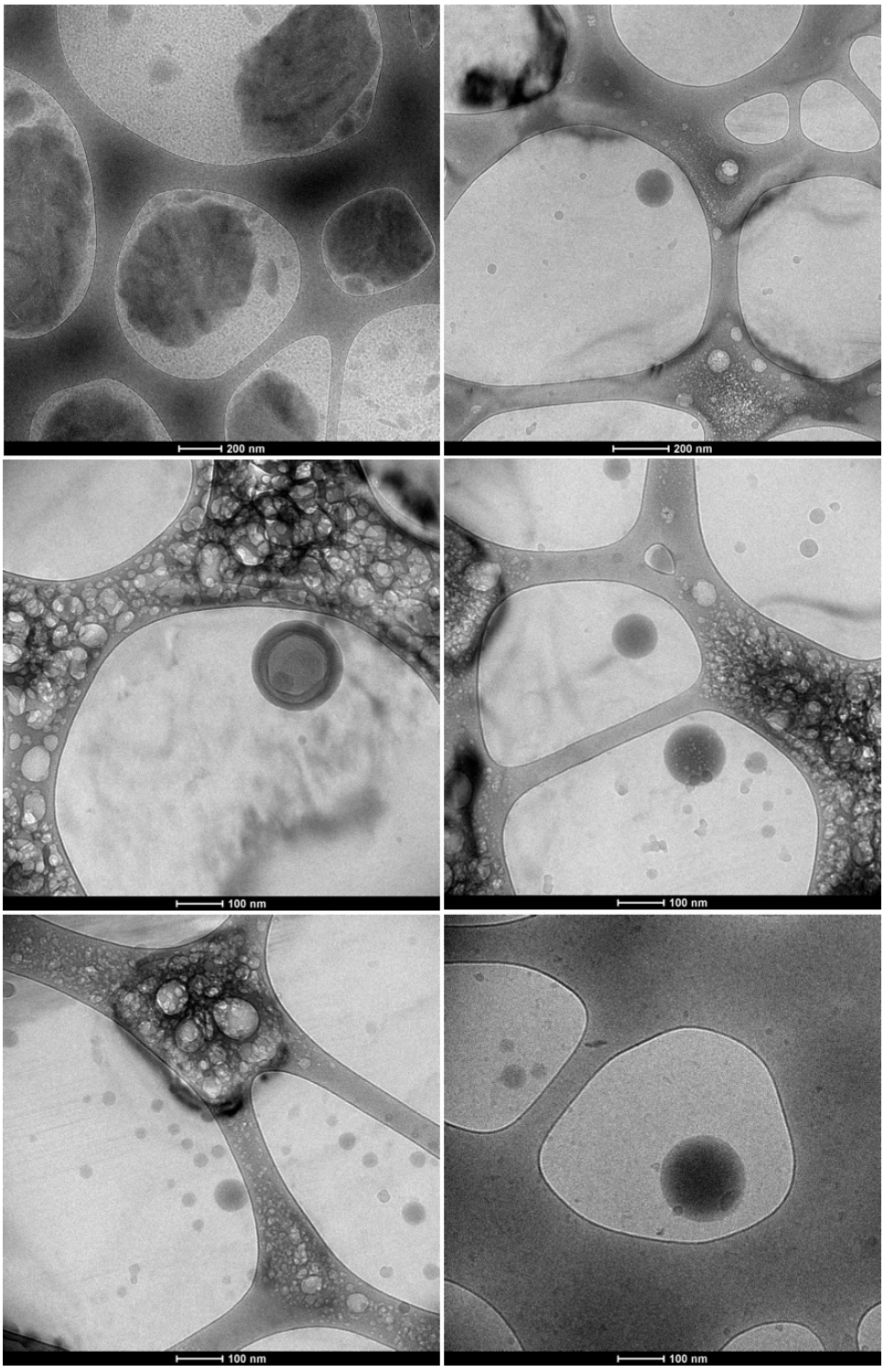

Figure B10. Typical cryo-TEM micrographs obtained from 5K-10K PEG-*b*-PLGA/iodosilicate paclitaxel prodrug. Sample is provided by Andrew Michel.

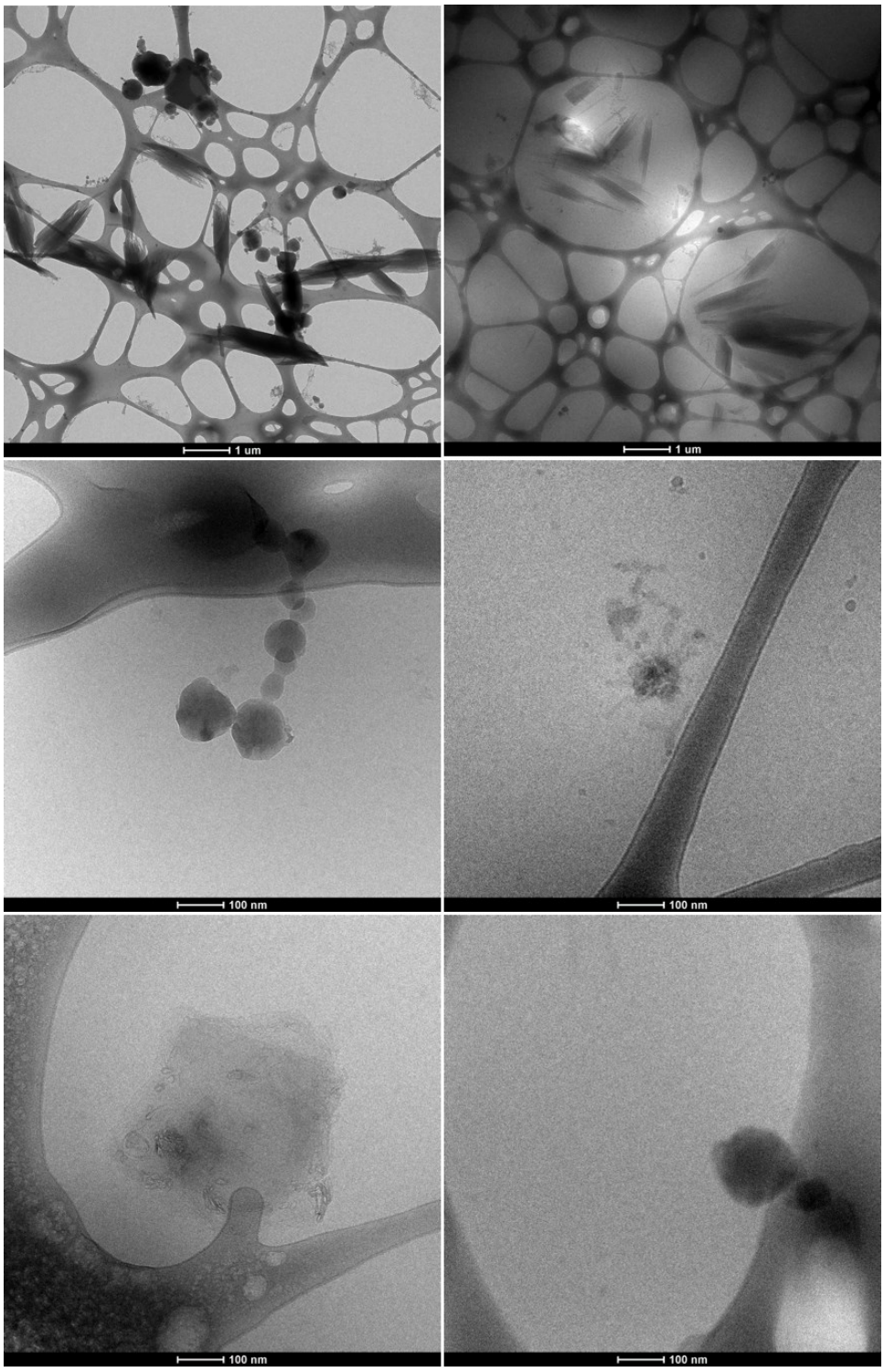

Figure B11. Typical cryo-TEM micrographs obtained from 5K-10K PEG-*b*-PLGA/2′,7-tri-ethoxy paclitaxel silicate prodrug (fresh nanoparticle with tetrahydrofuran). Sample is provided by Andrew Michel.

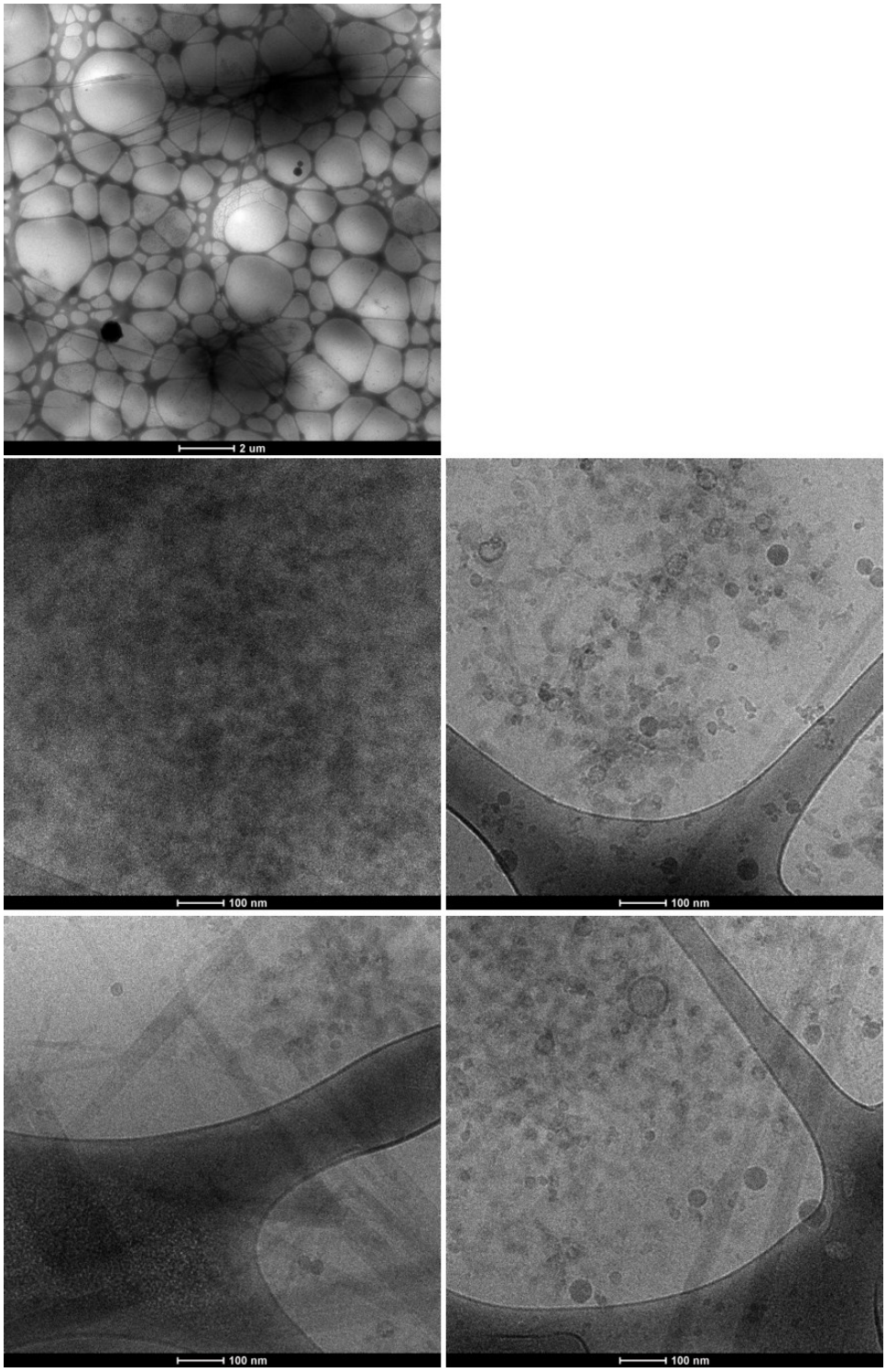

Figure B12. Typical cryo-TEM micrographs obtained from 5K-10K PEG-*b*-PLGA/2′,7-tri-ethoxy paclitaxel silicate prodrug (freeze-dried and sonicated nanoparticle). Sample is provided by Andrew Michel.

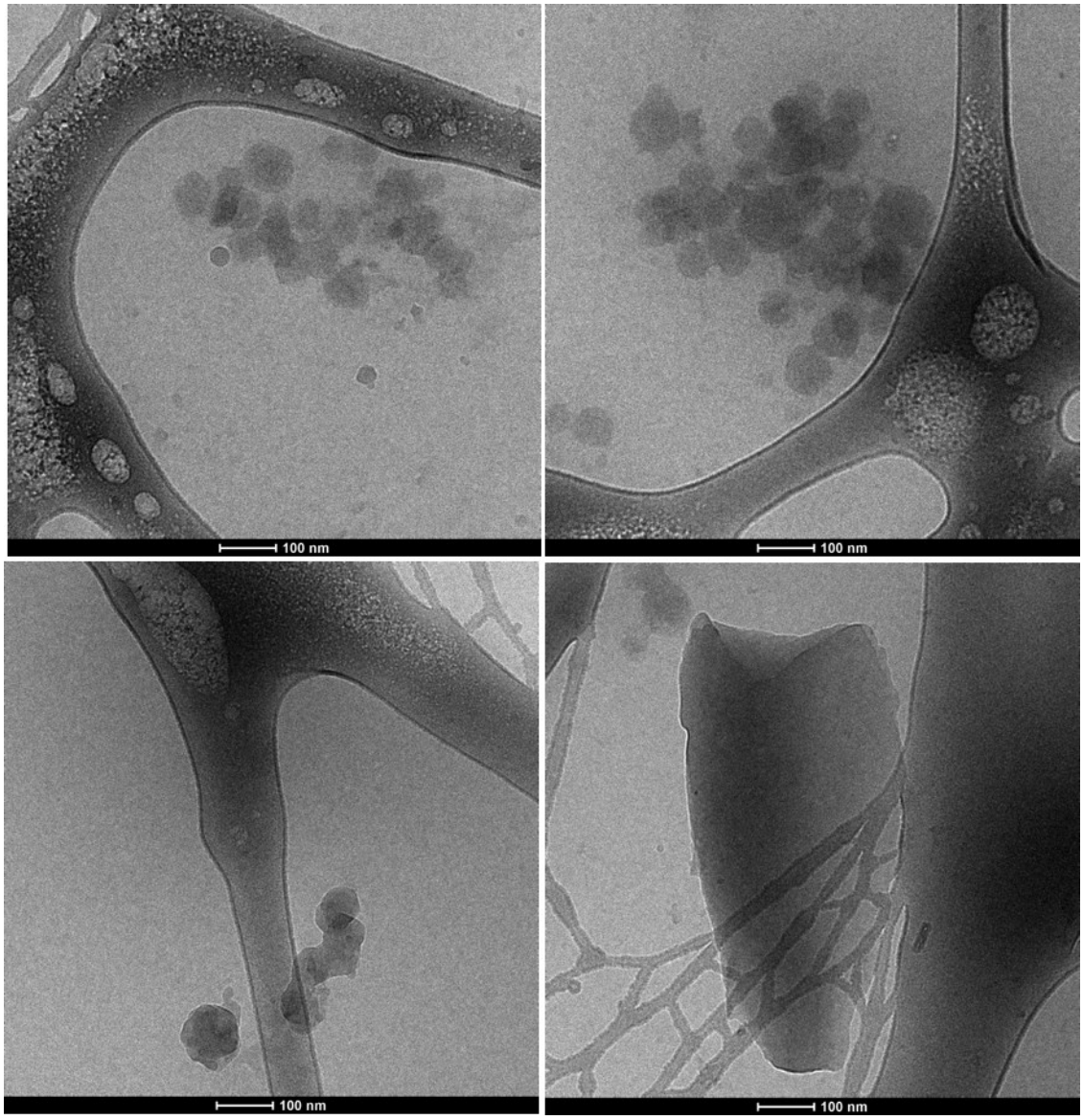

Figure B13. Typical cryo-TEM micrographs obtained from 5K-10K PEG-*b*-PLGA/2′,7-tri-ethoxy paclitaxel silicate prodrug (concentrator sonicated sample). Sample is provided by Andrew Michel.

V. Collaborative work with Adam Wohl and Jing Han (5K-10K poly(ethylene glycol)-*b*-poly(lactic-co-glycolic acid) (PEG-*b*-PLGA) with 2′,7-tri-ethoxy paclitaxel silicate prodrug nanoparticles)

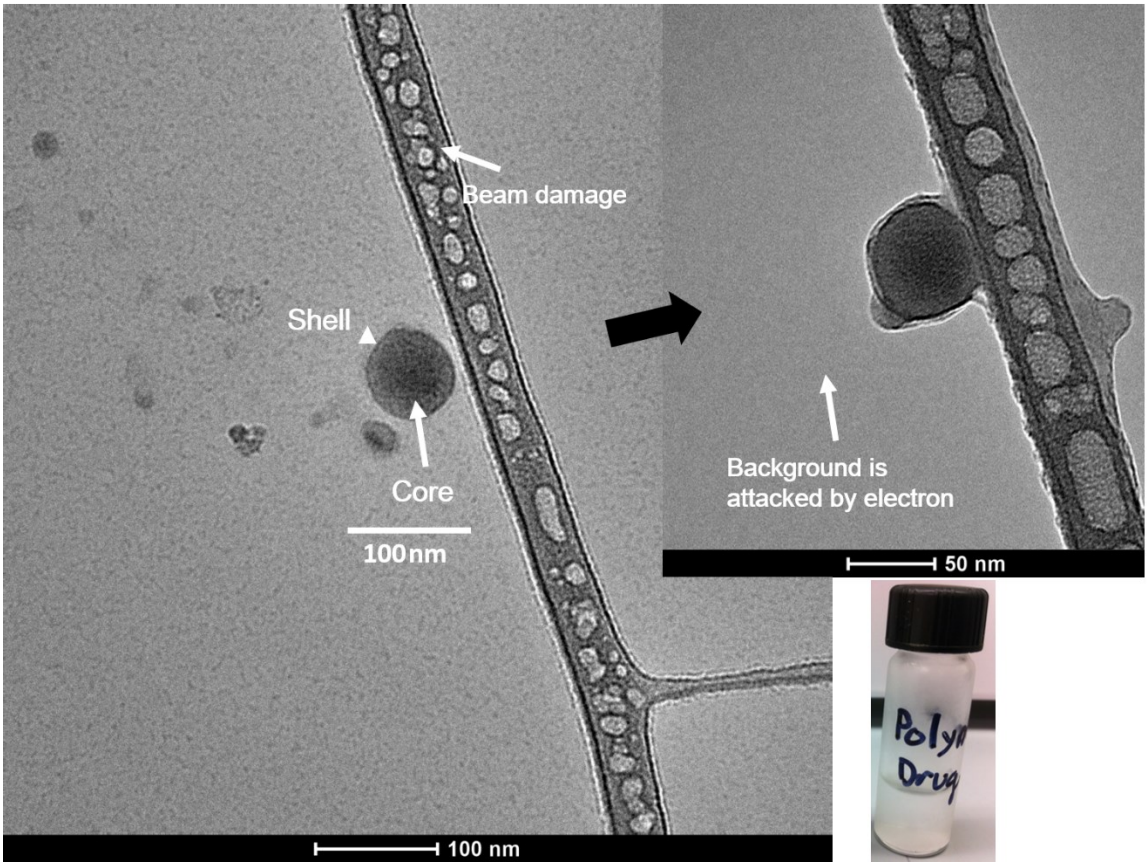

Figure B14. Typical cryo-TEM micrographs obtained from 5K-10K PEG-*b*-PLGA/2′,7-tri-ethoxy paclitaxel silicate prodrug (0.1 wt %, no freeze-dried sample) and image of the sample. Sample is provided by Adam Wohl and Jing Han.

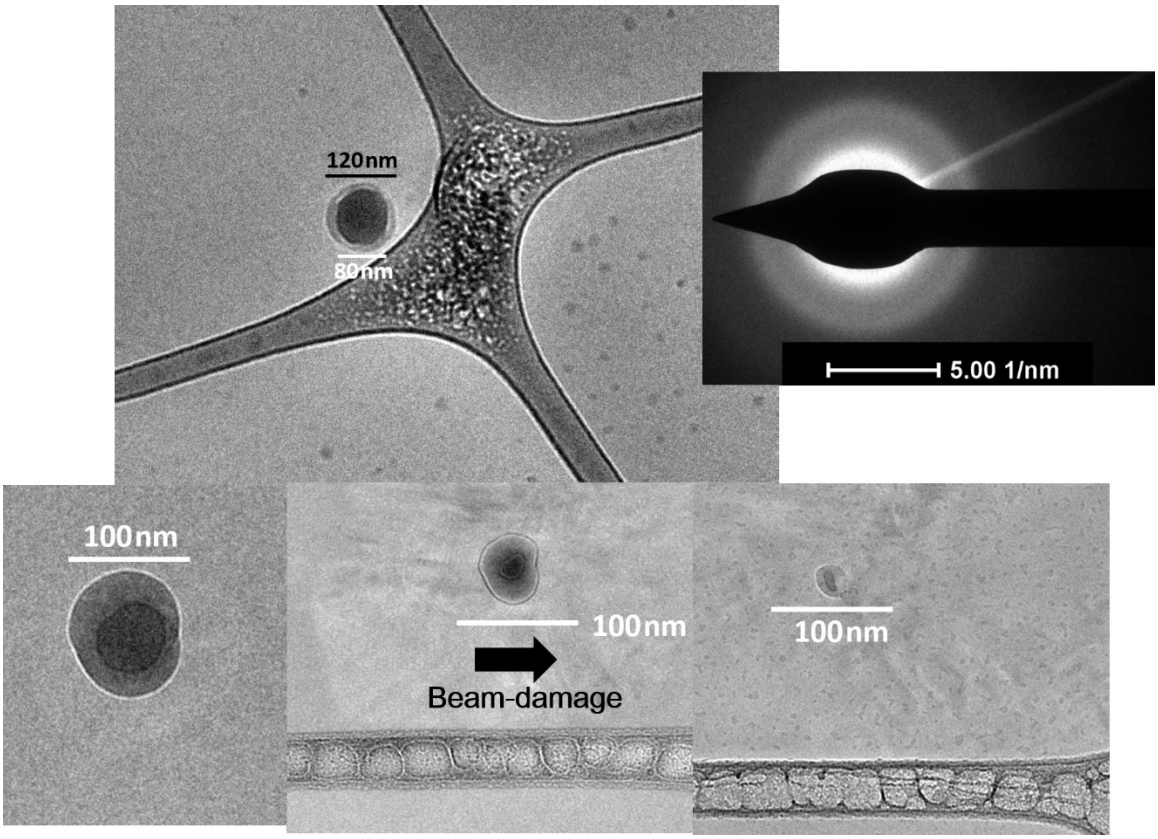

Figure B15. Typical cryo-TEM micrographs obtained from 5K-10K PEG-*b*-PLGA/2′,7-tri-ethoxy paclitaxel silicate prodrug (0.1 wt %, no freeze-dried sample), diffraction pattern, and beam damage process. Sample is provided by Adam Wohl and Jing Han.

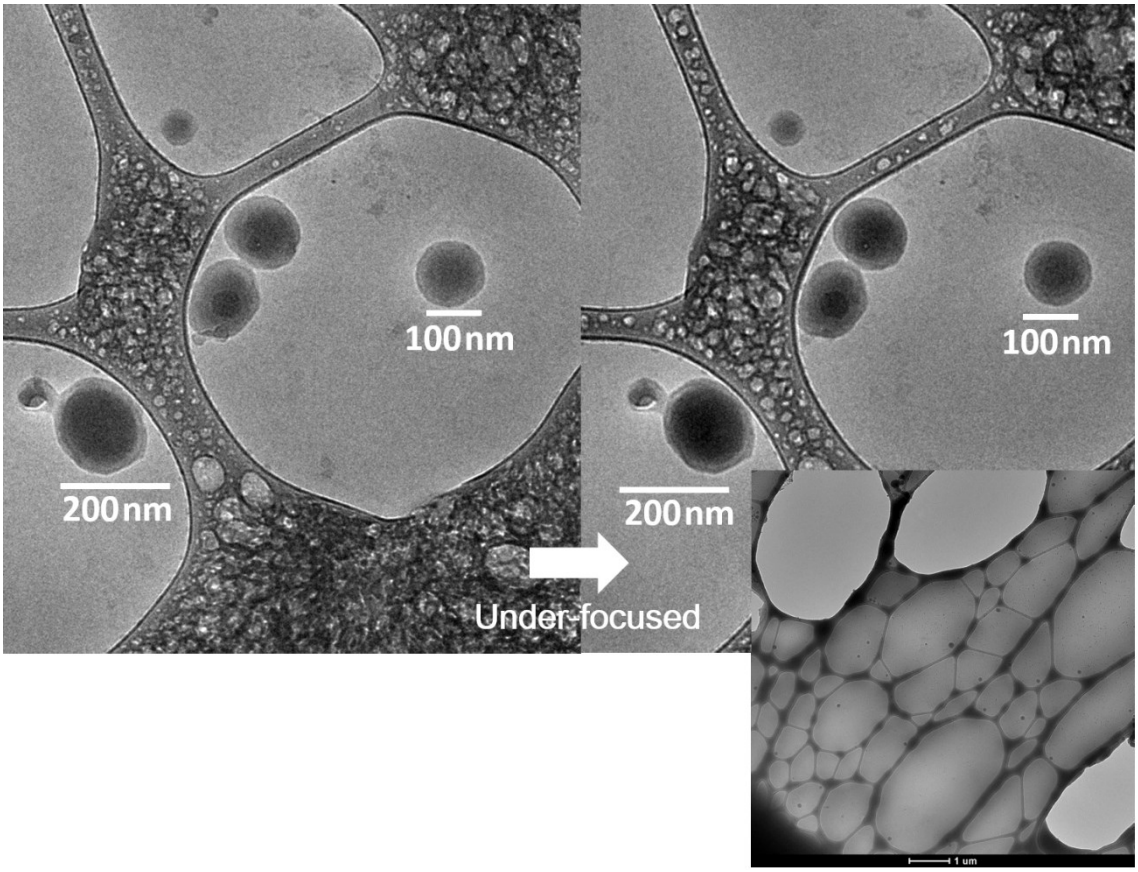

Figure B16. Typical cryo-TEM micrographs obtained from 5K-10K PEG-*b*-PLGA/2′,7-tri-ethoxy paclitaxel silicate prodrug (0.1 wt %, no freeze-dried sample). Sample is provided by Adam Wohl and Jing Han.

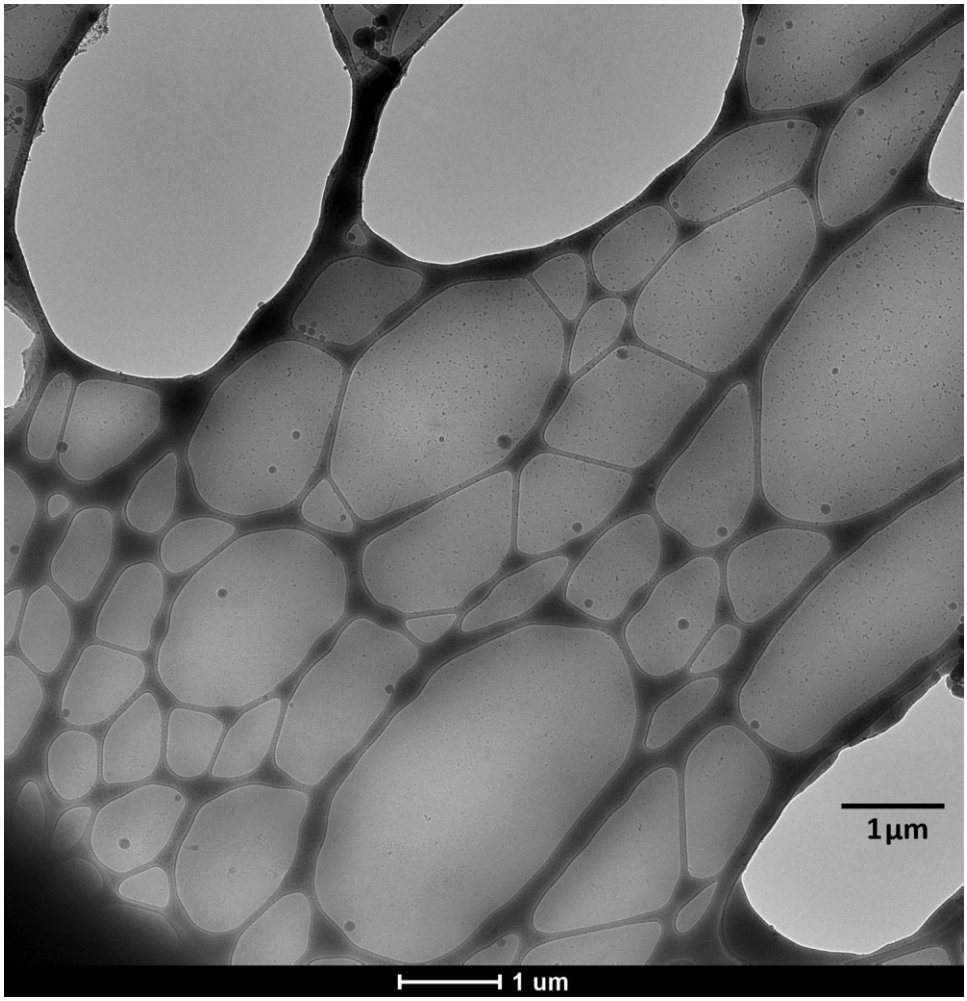

Figure B17. Typical cryo-TEM micrograph obtained from 5K-10K PEG-*b*-PLGA/2′,7-tri-ethoxy paclitaxel silicate prodrug (0.1 wt %, no freeze-dried sample). Sample is provided by Adam Wohl and Jing Han.

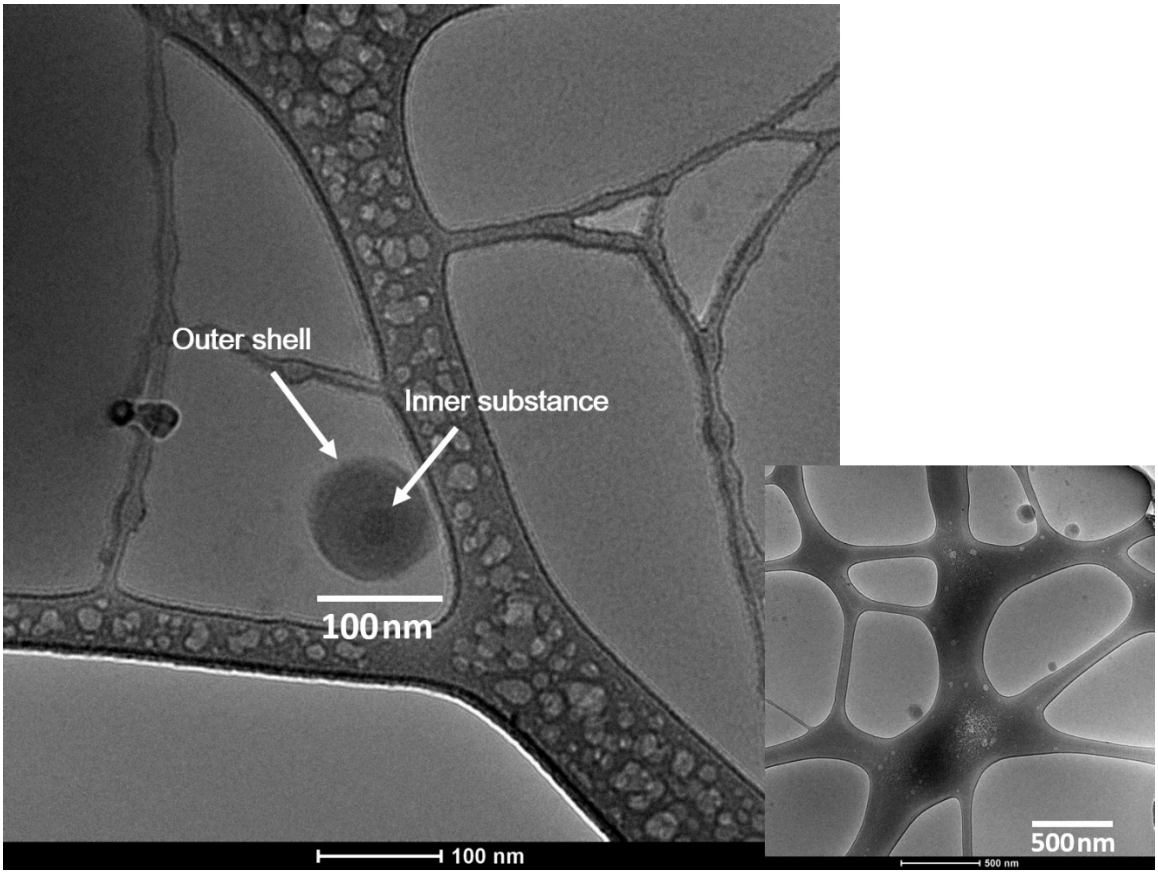

Figure B18. Typical cryo-TEM micrographs obtained from 5K-10K PEG-*b*-PLGA/2′,7-tri-ethoxy paclitaxel silicate prodrug (0.1 wt %, no freeze-dried sample). Sample is provided by Adam Wohl and Jing Han.

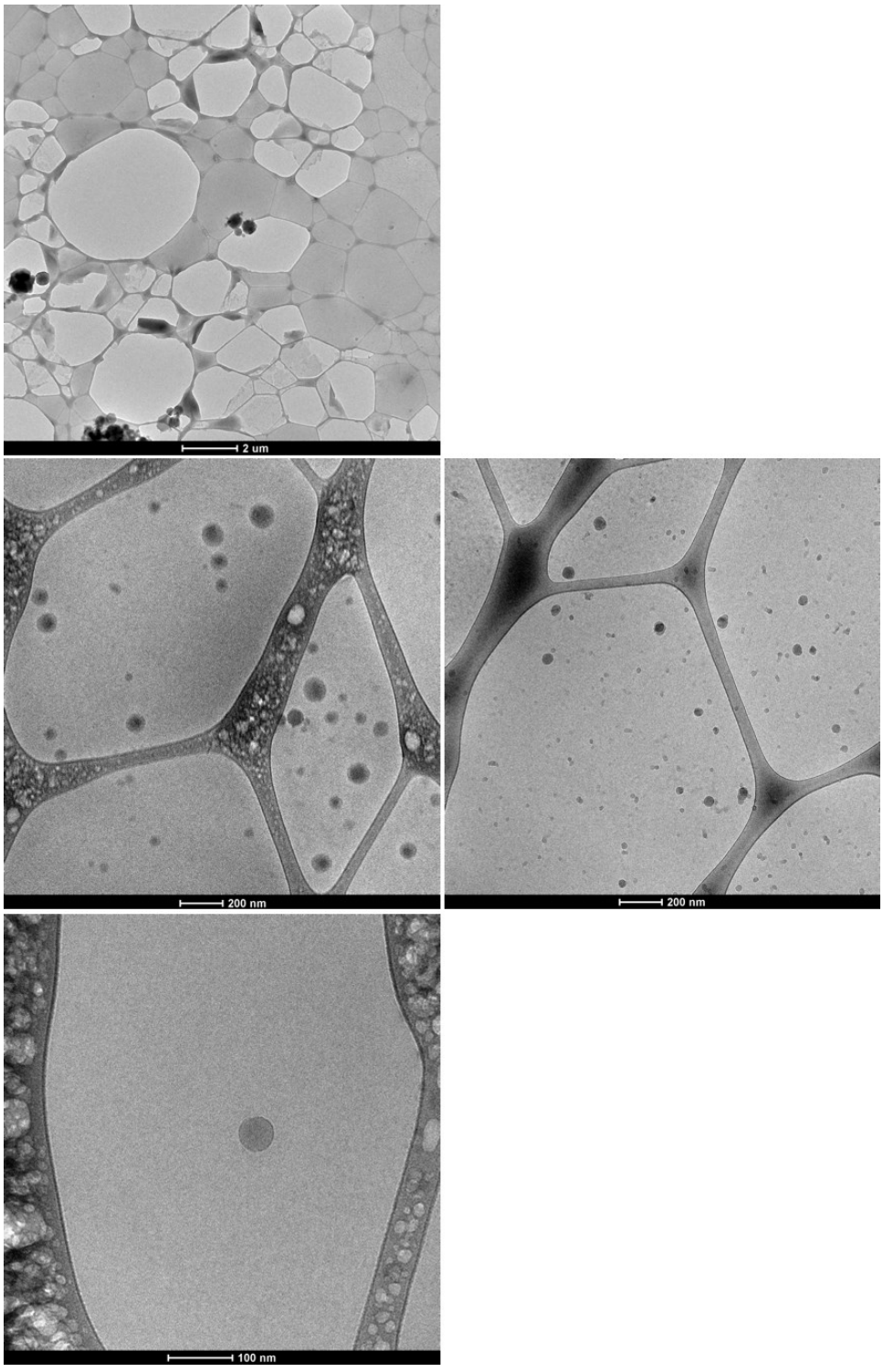

Figure B19. Typical cryo-TEM micrographs obtained from 5K-10K PEG-*b*-PLGA/2′,7-tri-ethoxy paclitaxel silicate prodrug (0.1 wt %, no freeze-dried sample). Sample is provided by Adam Wohl and Jing Han.

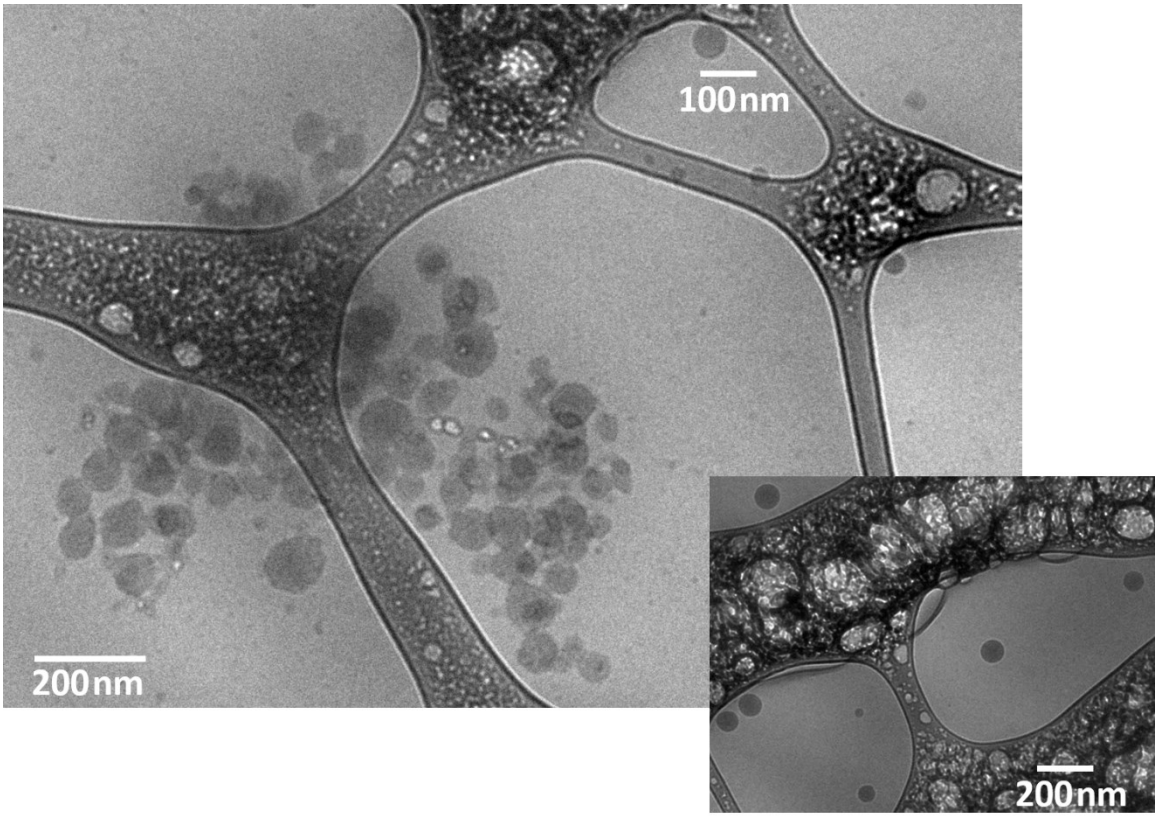

Figure B20. Typical cryo-TEM micrographs obtained from 5K-10K PEG-*b*-PLGA/2′,7-tri-ethoxy paclitaxel silicate prodrug (0.1 wt %, freeze-dried sample). Sample is provided by Adam Wohl and Jing Han.

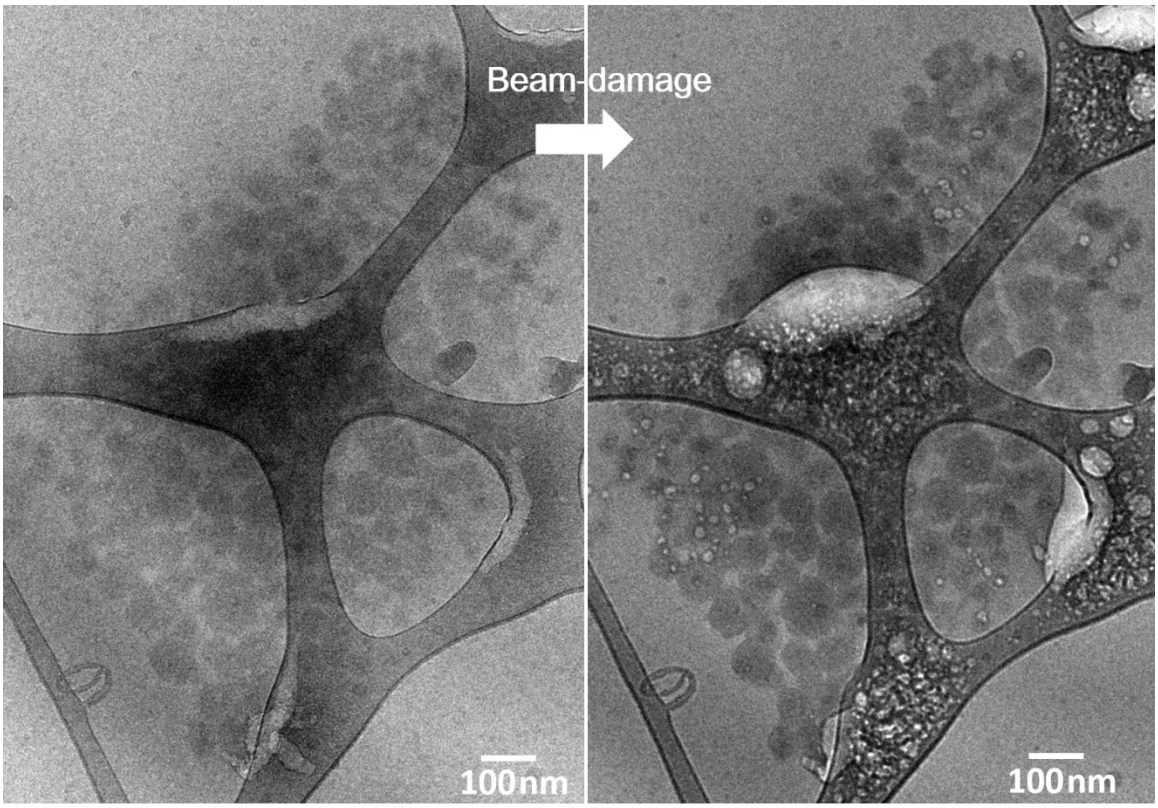

Figure B21. Typical cryo-TEM micrographs obtained from 5K-10K PEG-*b*-PLGA/2′,7-tri-ethoxy paclitaxel silicate prodrug (0.1 wt %, freeze-dried sample) show beam damage. Sample is provided by Adam Wohl and Jing Han.

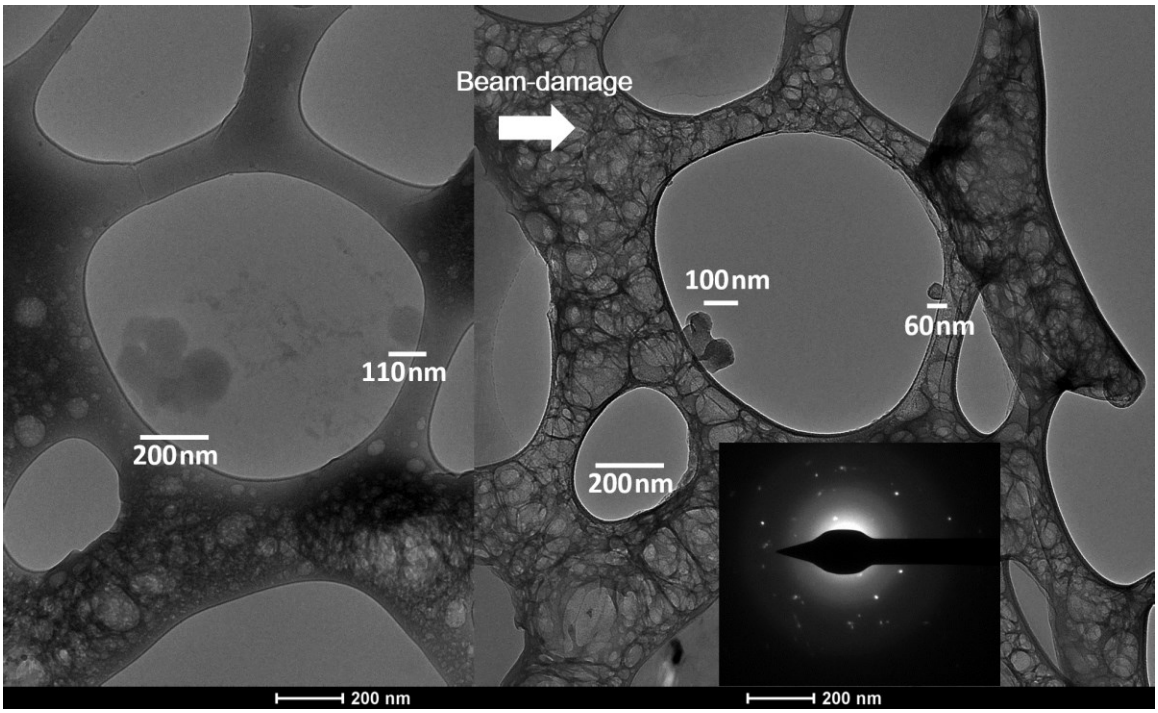

Figure B22. Typical cryo-TEM micrographs obtained from 5K-10K PEG-*b*-PLGA/2′,7-tri-ethoxy paclitaxel silicate prodrug (0.1 wt %, freeze-dried sample) show beam damage. Sample is provided by Adam Wohl and Jing Han.

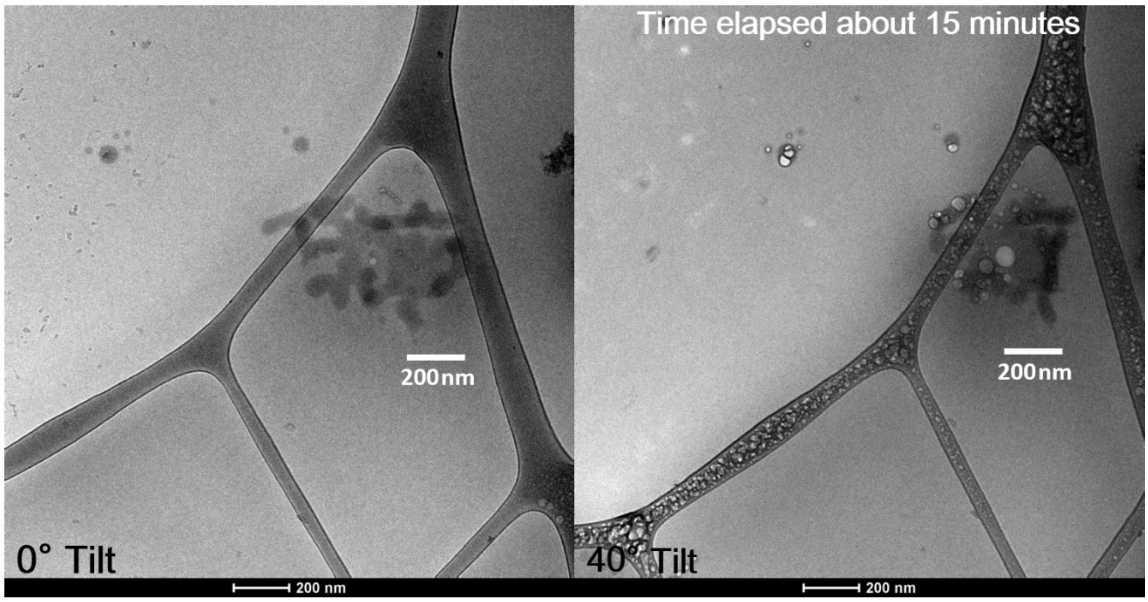

Figure B23. Typical cryo-TEM micrographs obtained from 5K-10K PEG-*b*-PLGA/2′,7-tri-ethoxy paclitaxel silicate prodrug (0.1 wt %, freeze-dried sample) show tilted images. Sample is provided by Adam Wohl and Jing Han.

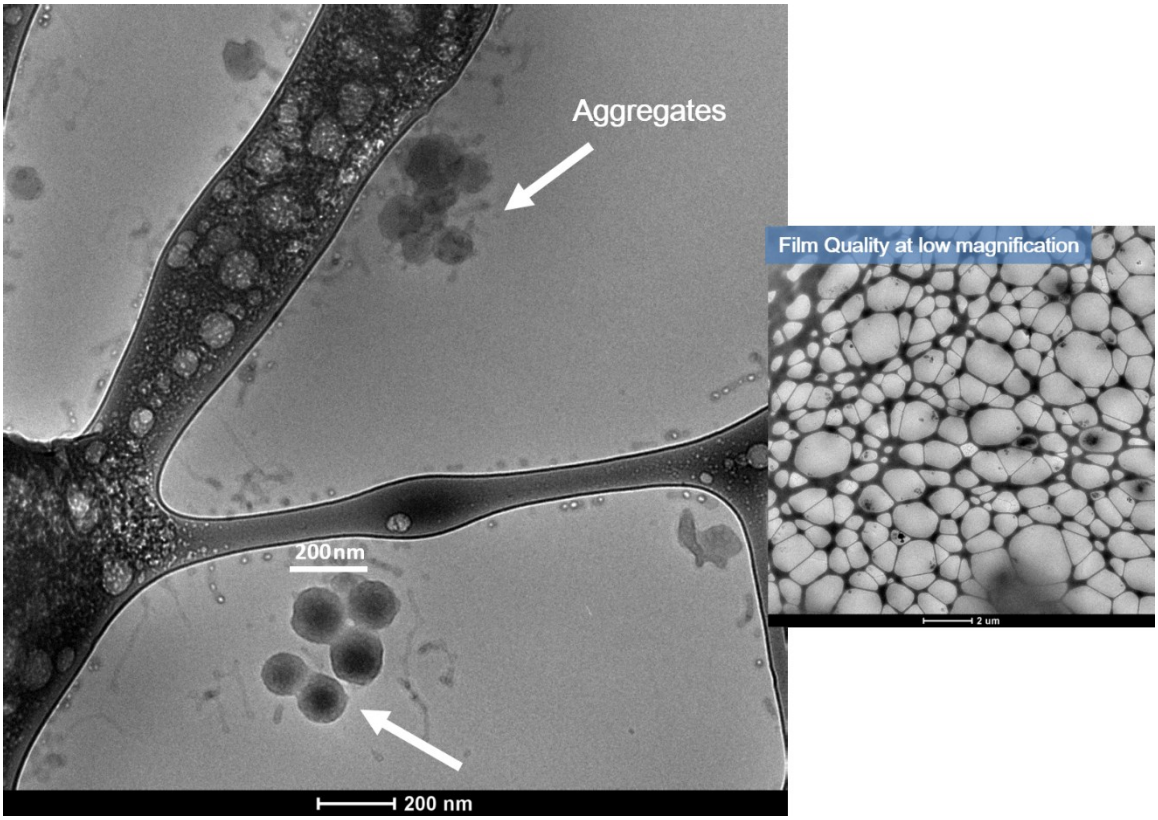

Figure B24. Typical cryo-TEM micrographs obtained from 5K-10K PEG-*b*-PLGA/2′,7-tri-ethoxy paclitaxel silicate prodrug (1.0 wt %, animal injected sample). Sample is provided by Adam Wohl and Jing Han.

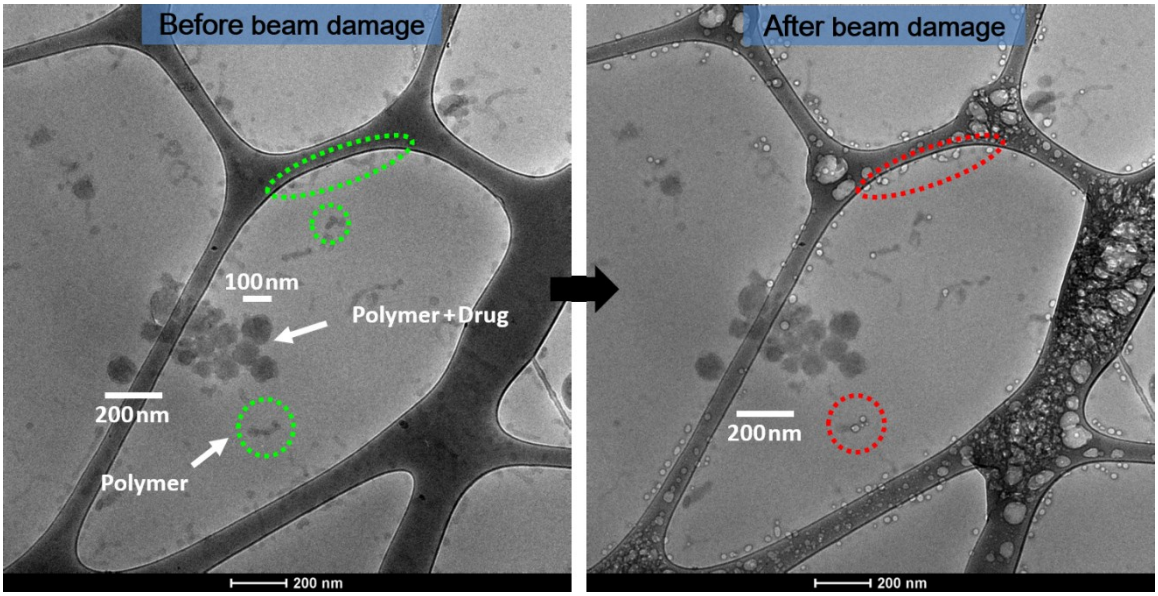

Figure B25. Typical cryo-TEM micrographs obtained from 5K-10K PEG-*b*-PLGA/2′,7-tri-ethoxy paclitaxel silicate prodrug (1.0 wt %, animal injected sample) show beam damages. Sample is provided by Adam Wohl and Jing Han.

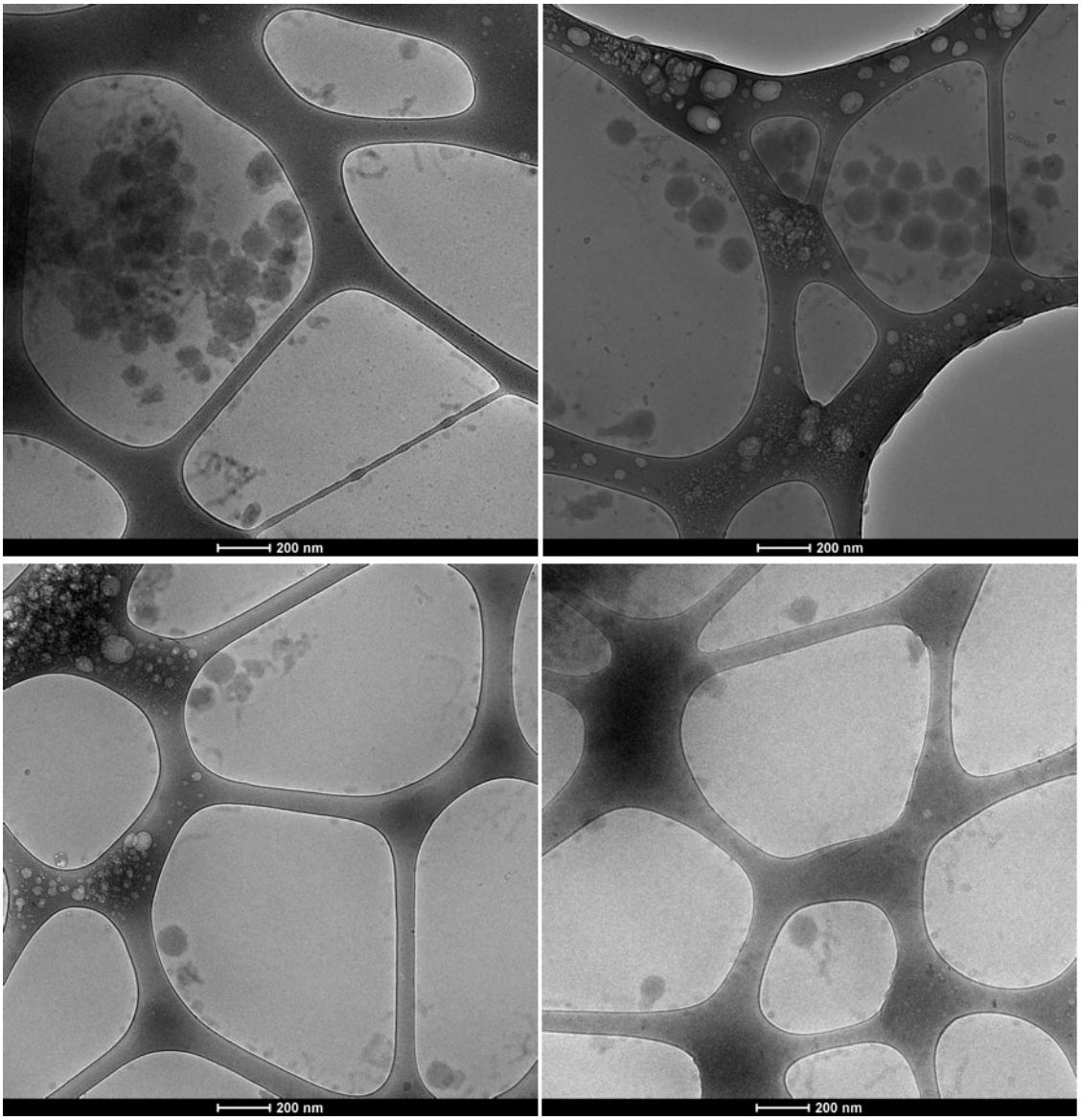

Figure B26. Typical cryo-TEM micrographs obtained from 5K-10K PEG-*b*-PLGA/2′,7-tri-ethoxy paclitaxel silicate prodrug (1.0 wt %, animal injected sample). Sample is provided by Adam Wohl and Jing Han.

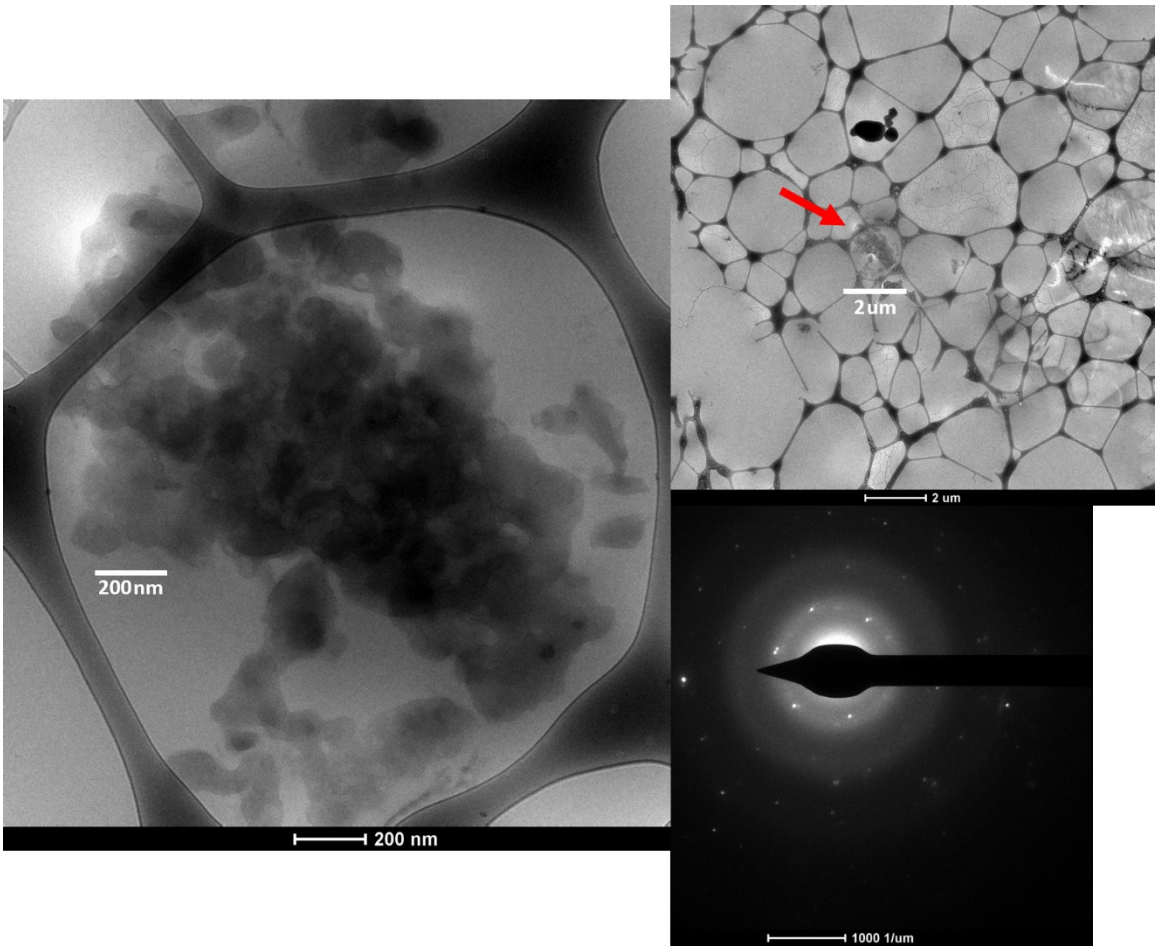

Figure B27. Typical cryo-TEM micrographs obtained from 5K-10K PEG-*b*-PLGA/2′,7-tri-ethoxy paclitaxel silicate prodrug (3.0 wt %). Sample is provided by Adam Wohl and Jing Han.

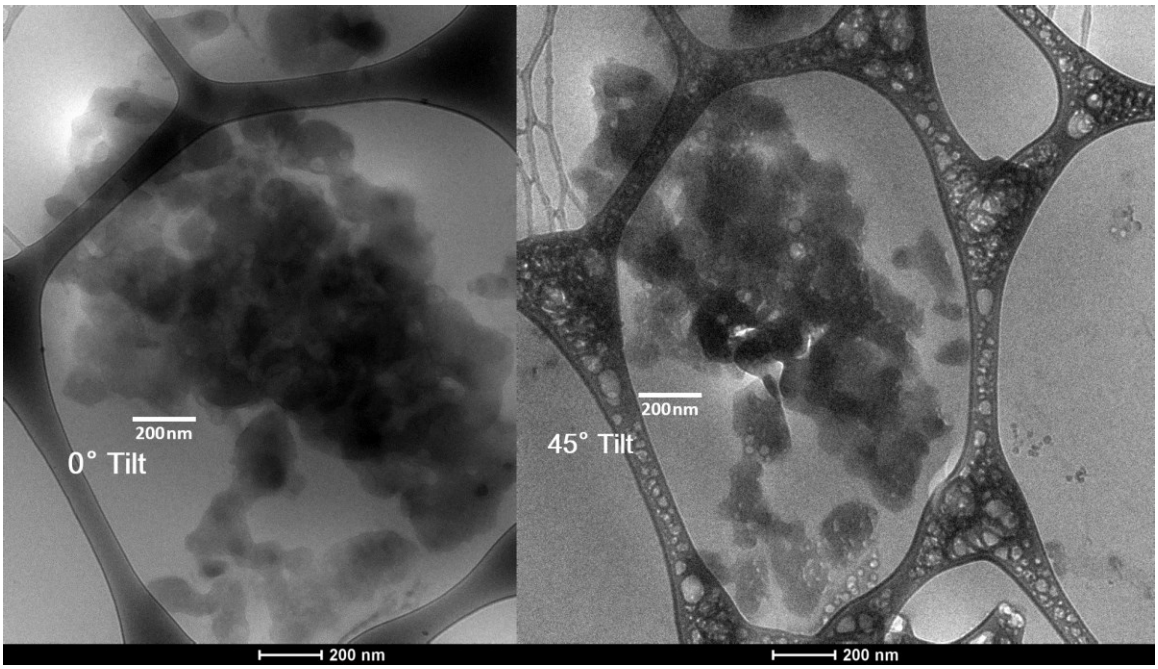

Figure B28. Typical cryo-TEM micrographs obtained from 5K-10K PEG-*b*-PLGA/2′,7-tri-ethoxy paclitaxel silicate prodrug (3.0 wt %) show tilted images. Sample is provided by Adam Wohl and Jing Han.

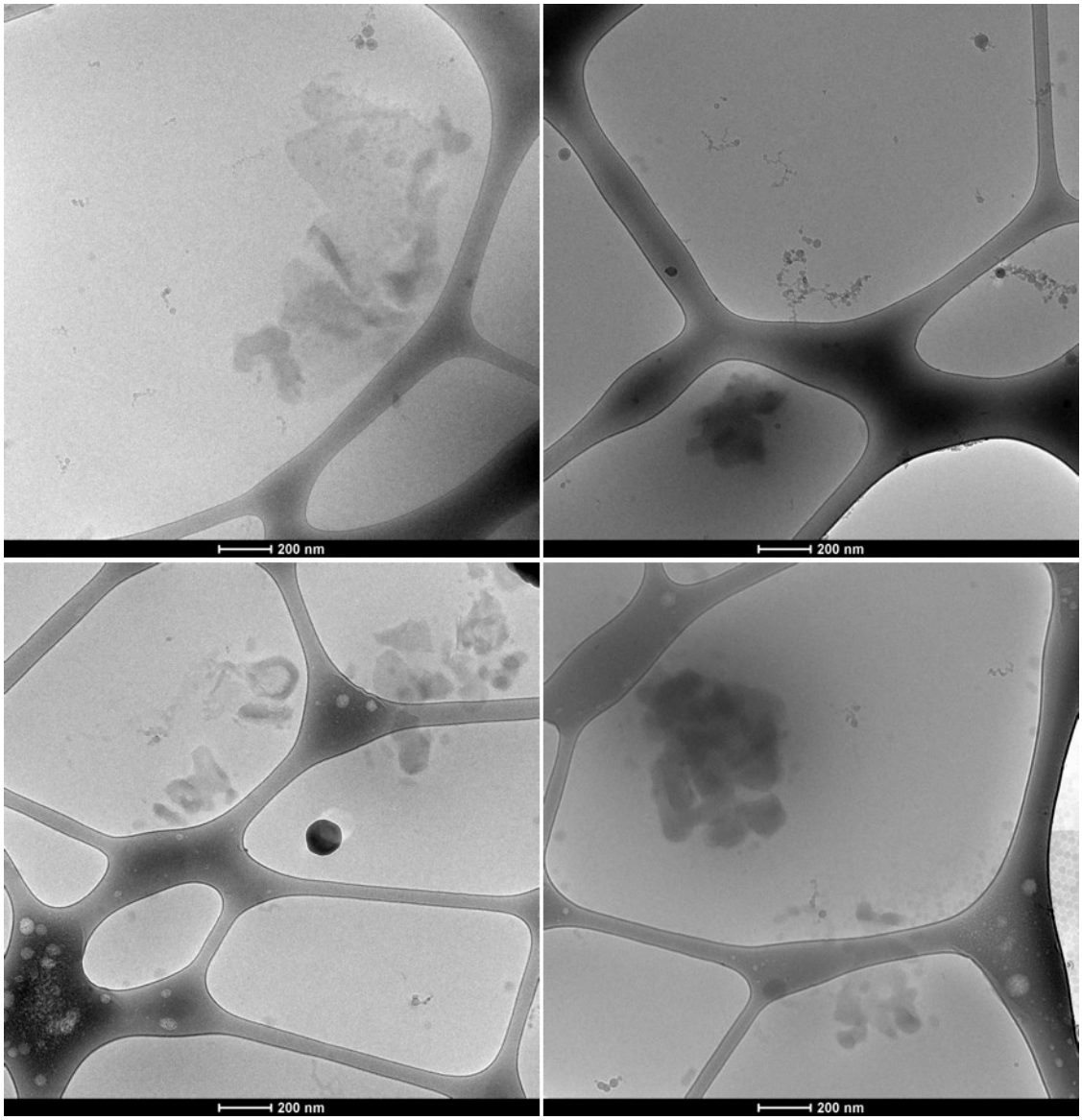

Figure B29. Typical cryo-TEM micrographs obtained from 5K-10K PEG-*b*-PLGA/2′,7-tri-ethoxy paclitaxel silicate prodrug (3.0 wt %). Sample is provided by Adam Wohl and Jing Han.

VI. Collaborative work with Andrew Michel and Jing Han

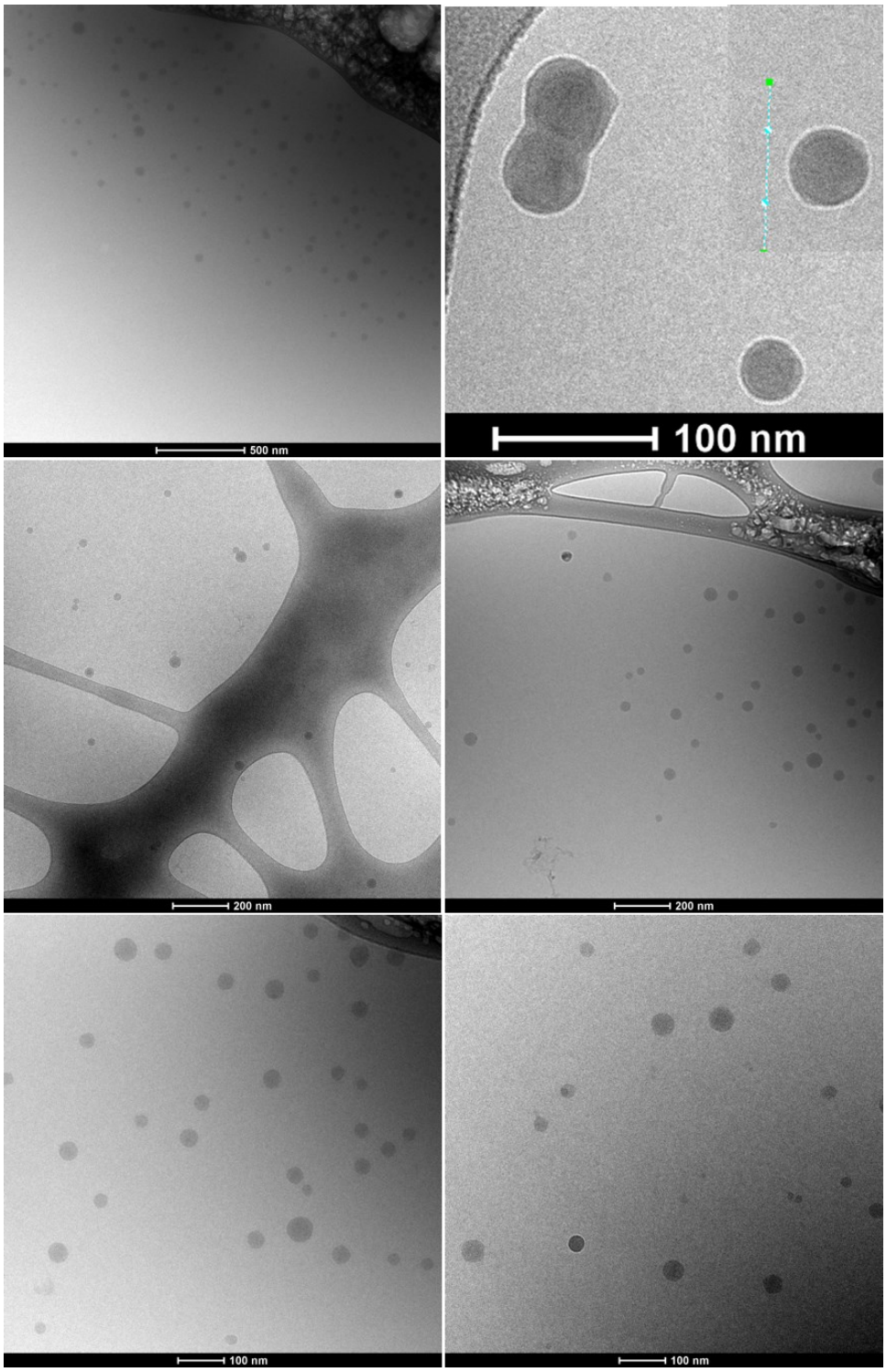

Figure B30. Typical cryo-TEM micrographs obtained from 5K-10K PEG-*b*-PLGA/2´-tri-octoxy paclitaxel silicate prodrug. Sample is provided by Adam Wohl and Jing Han.

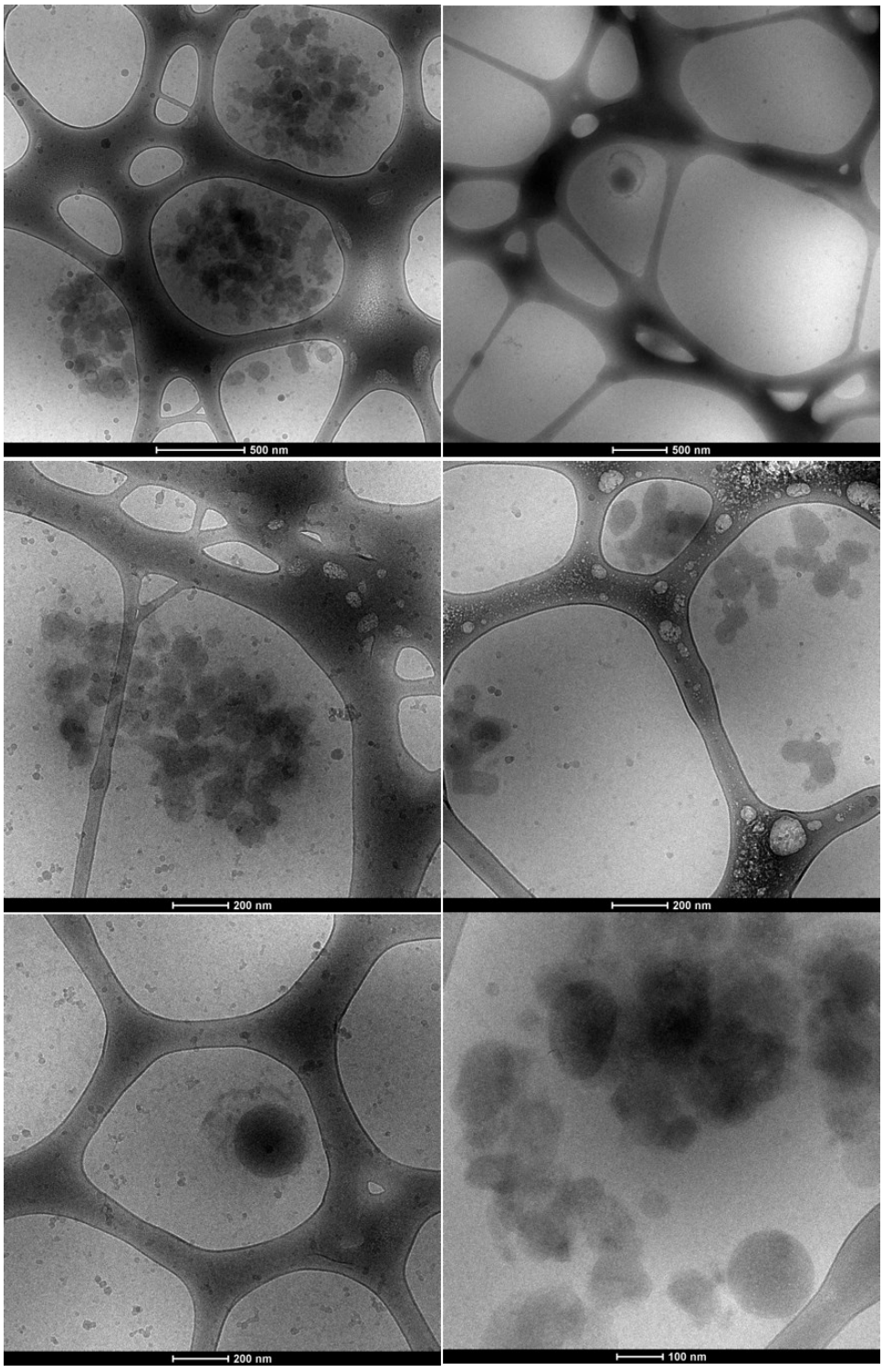

Figure B31. Typical cryo-TEM micrographs obtained from 5K-10K PEG-*b*-PLGA/2′-tri-octoxy paclitaxel silicate prodrug (freeze-dried sample). Sample is provided by Adam Wohl and Jing Han.

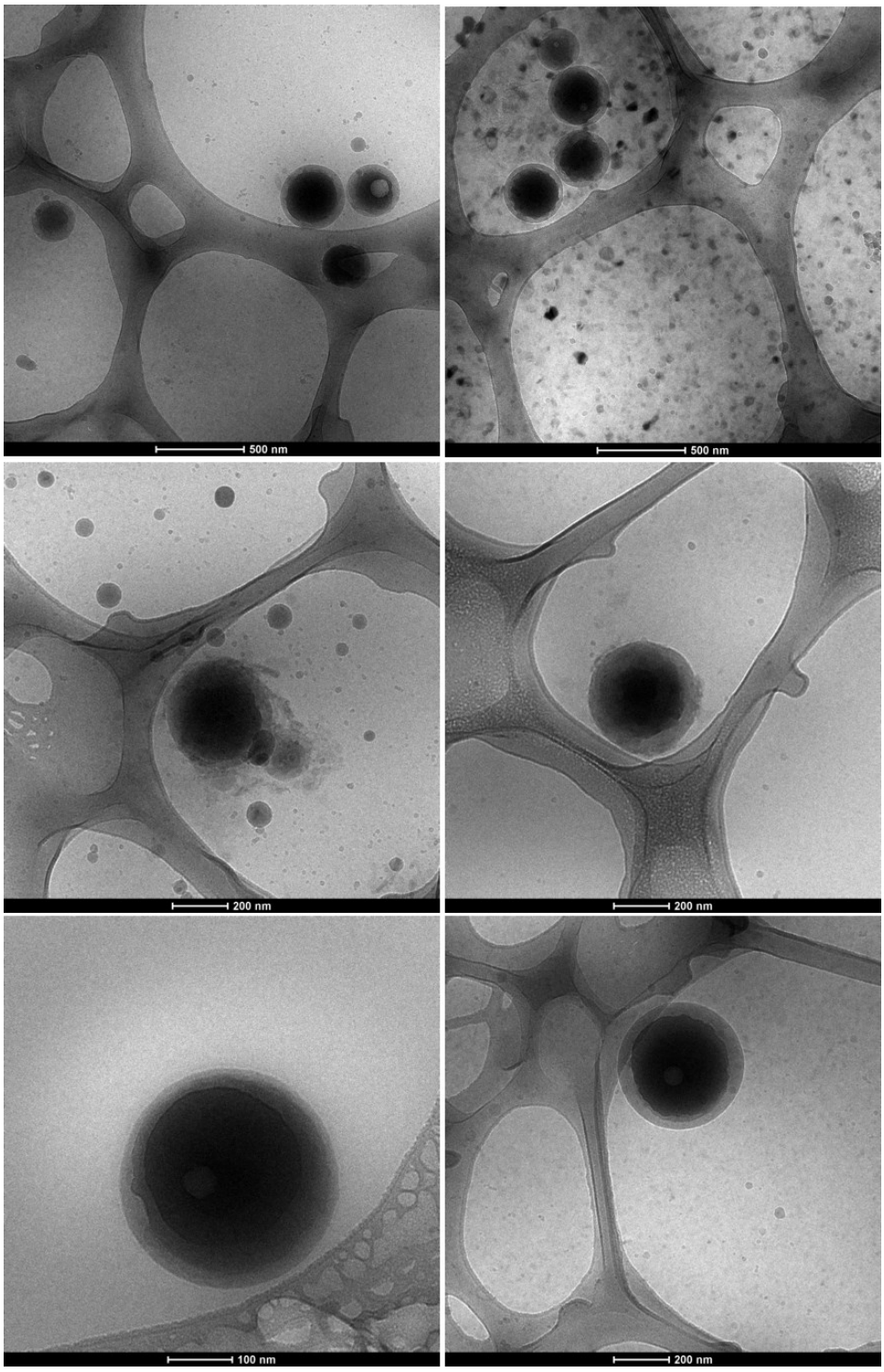

Figure B32. Typical cryo-TEM micrographs obtained from 5K-10K PEG-*b*-PLGA/2′-tri-isopropoxy paclitaxel silicate prodrug. Sample is provided by Adam Wohl and Jing Han.

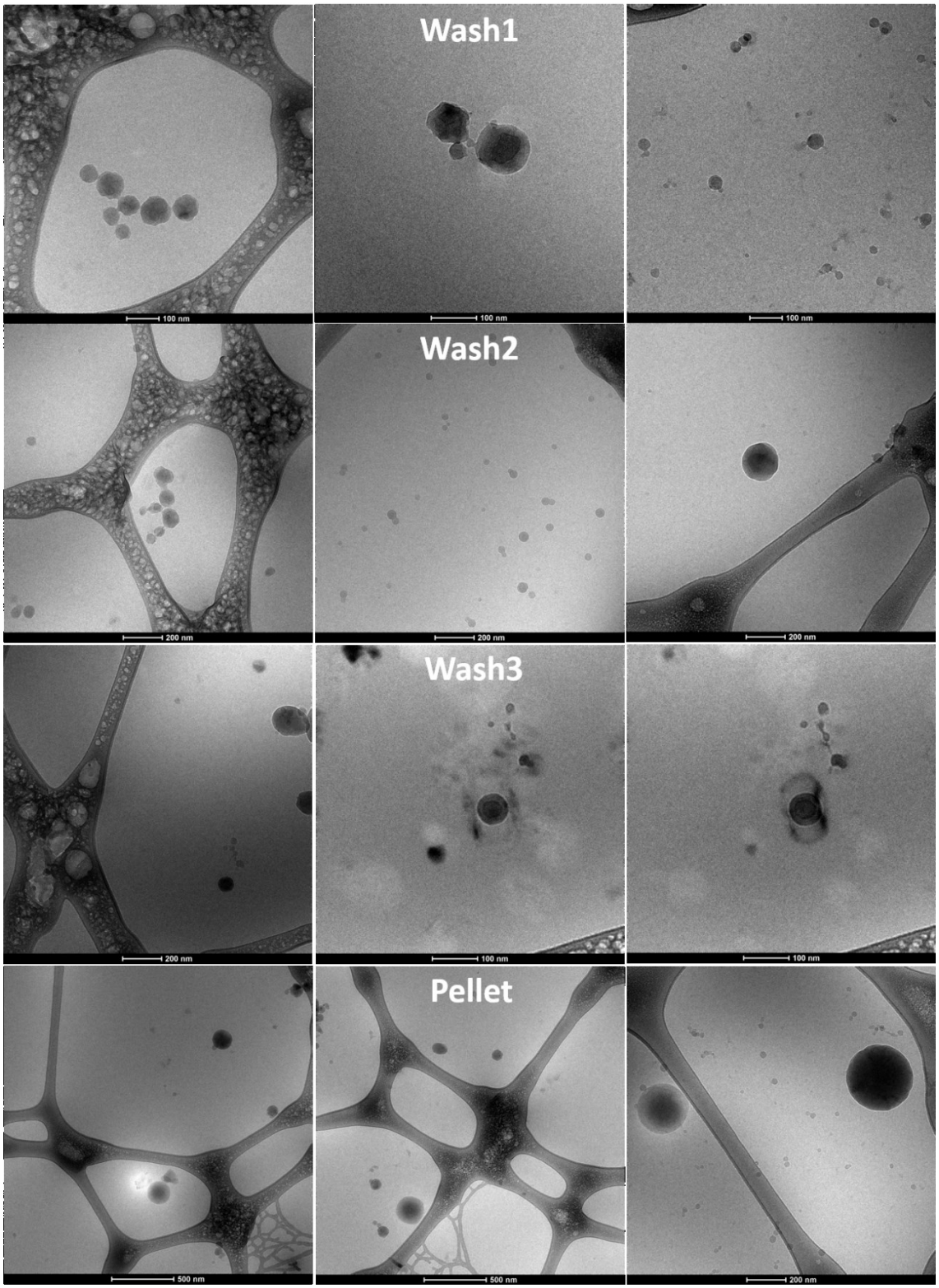

Figure B33. Typical cryo-TEM micrographs obtained from 5K-10K PEG-*b*-PLGA/2′-tri-isopropoxy paclitaxel silicate prodrug (Ultracentrifuged (washed) sample). Sample is provided by Adam Wohl and Jing Han.

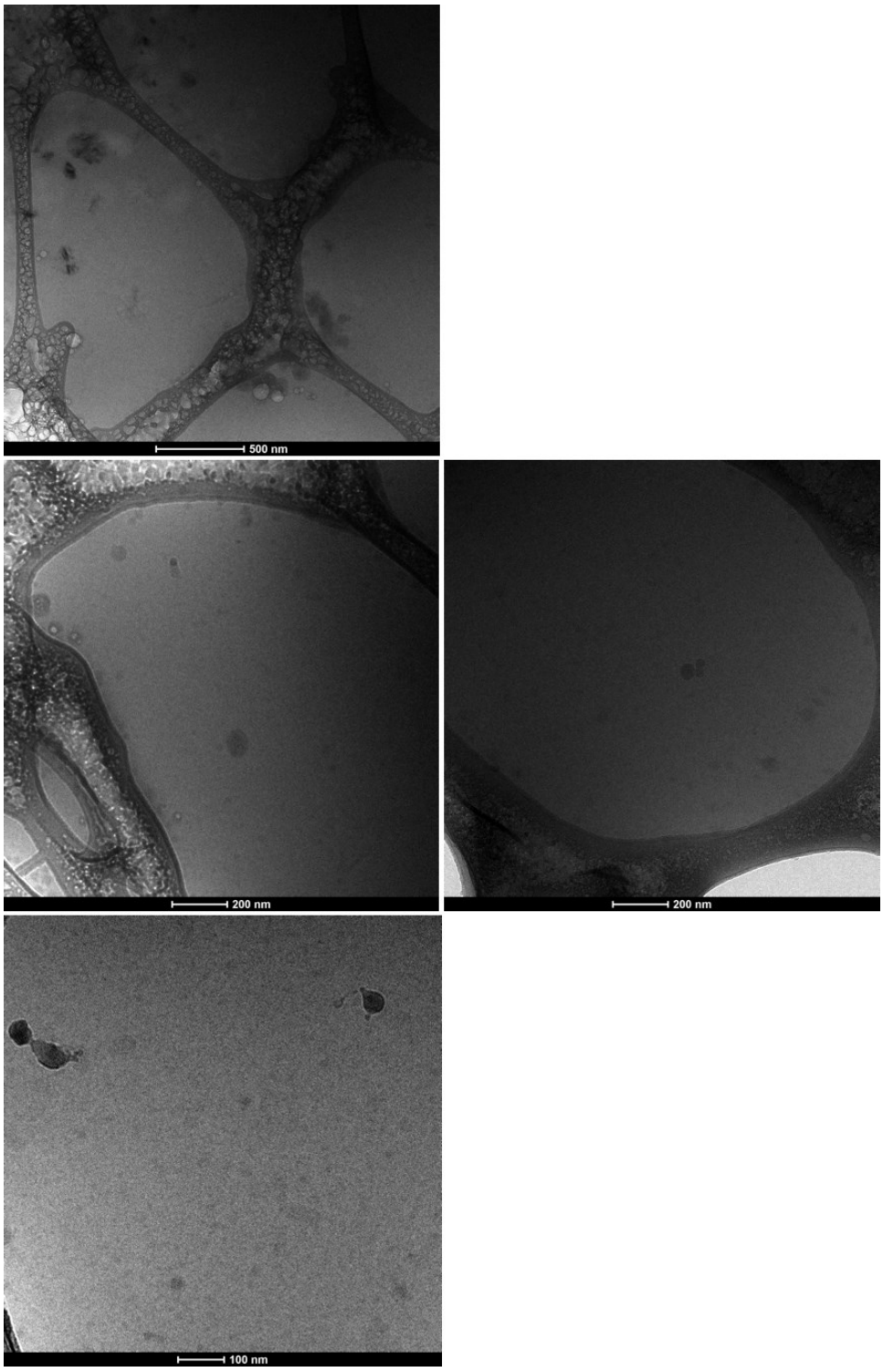

Figure B34. Typical cryo-TEM micrographs obtained from 5K-10K PEG-*b*-PLGA/2′-tri-isopropoxy paclitaxel silicate prodrug (24 hours release). Sample is provided by Adam Wohl and Jing Han.

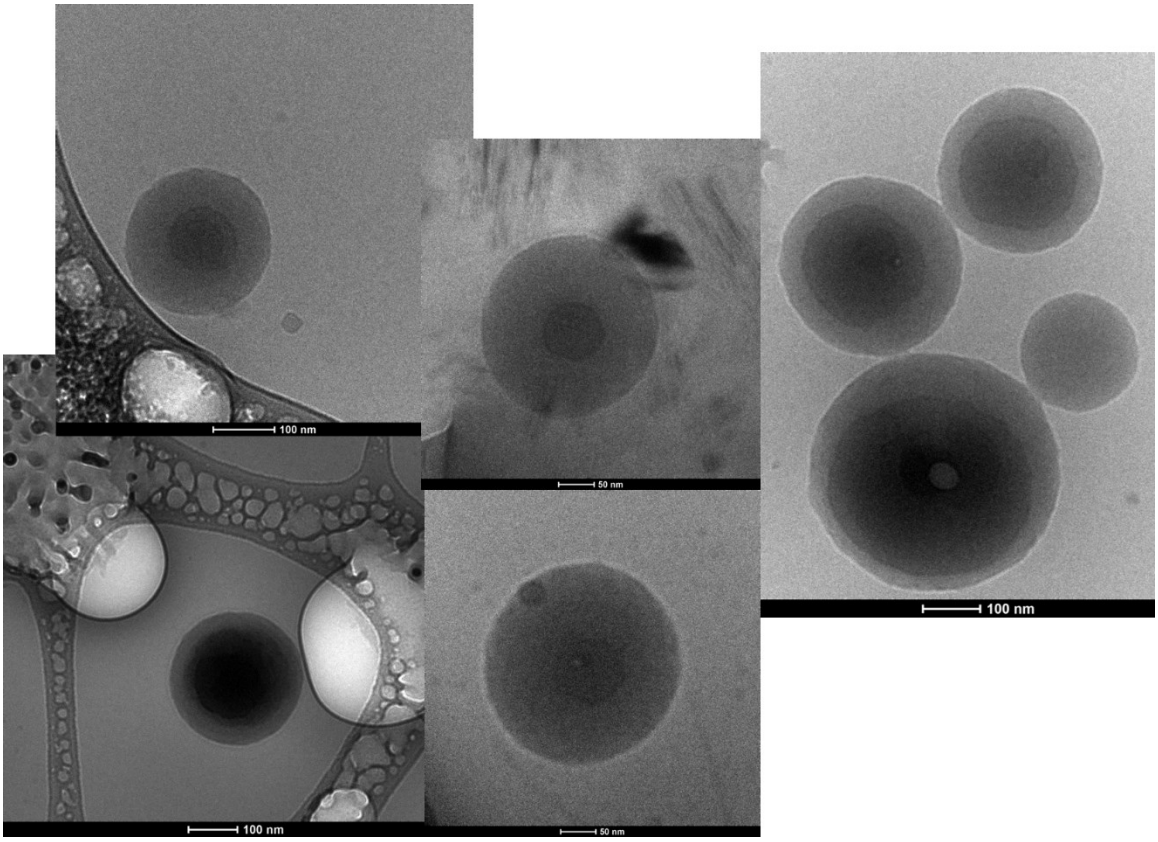

Figure B35. Typical cryo-TEM micrographs obtained from 5K-10K PEG-*b*-PLGA/2′-tri-ethoxy paclitaxel silicate prodrug. Sample is provided by Adam Wohl and Jing Han.

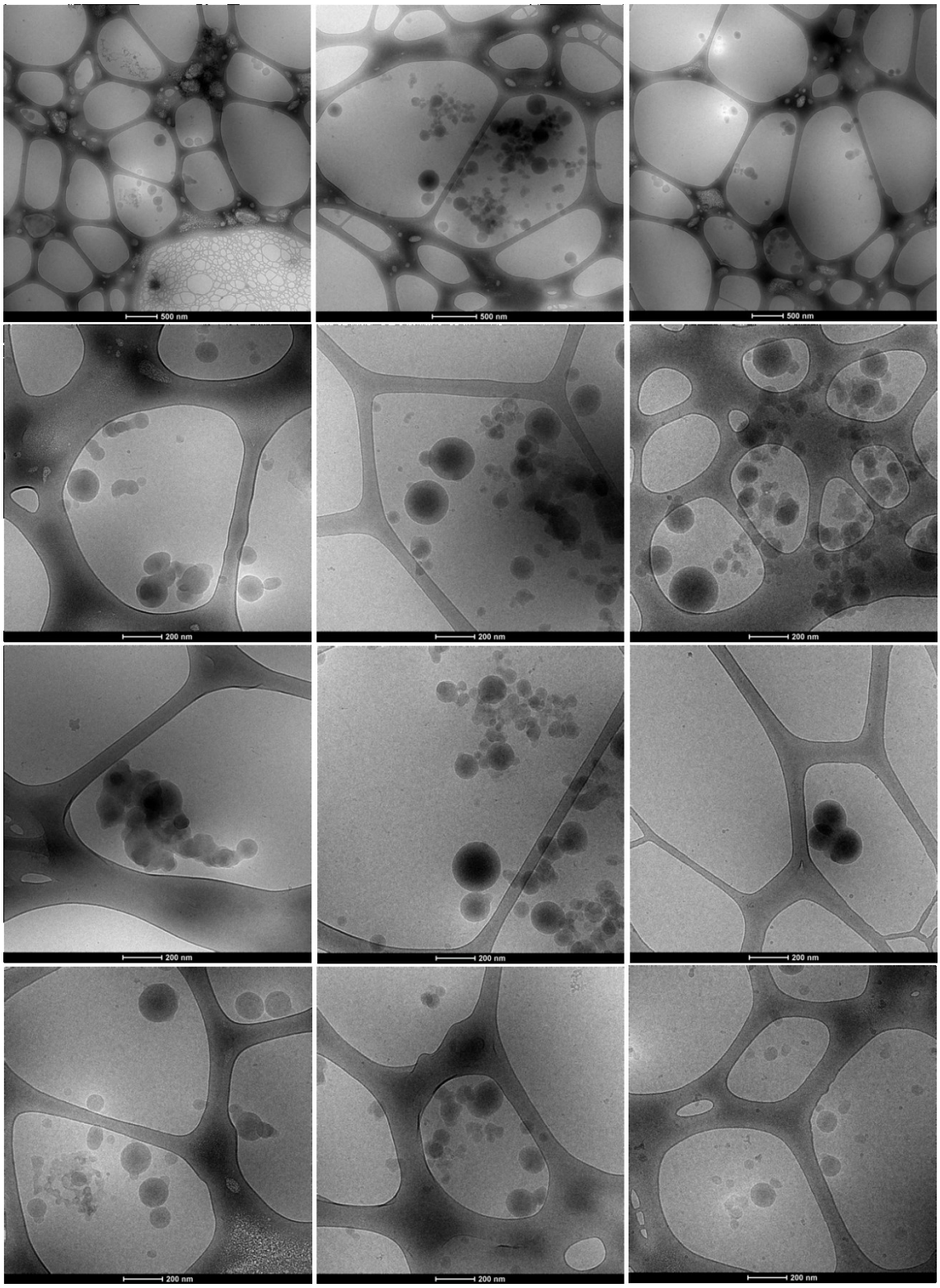

Figure B36. Typical cryo-TEM micrographs obtained from 5K-10K PEG-*b*-PLGA/2′-tri-ethoxy paclitaxel silicate prodrug (0 hour release). Sample is provided by Adam Wohl and Jing Han.

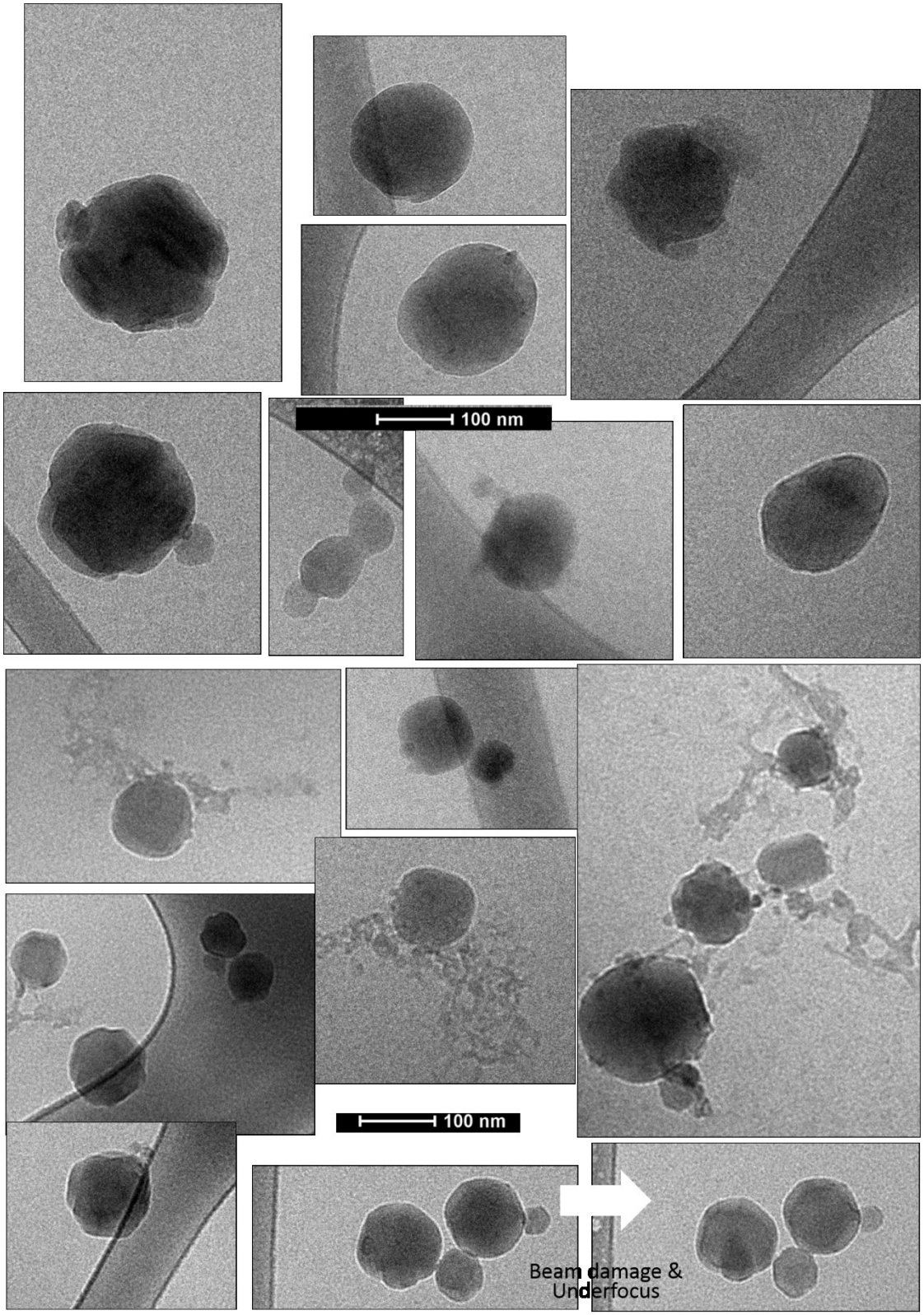

Figure B37. Typical cryo-TEM micrographs obtained from 5K-10K PEG-*b*-PLGA/2´-tri-ethoxy paclitaxel silicate prodrug (24 hours release). Sample is provided by Adam Wohl and Jing Han.

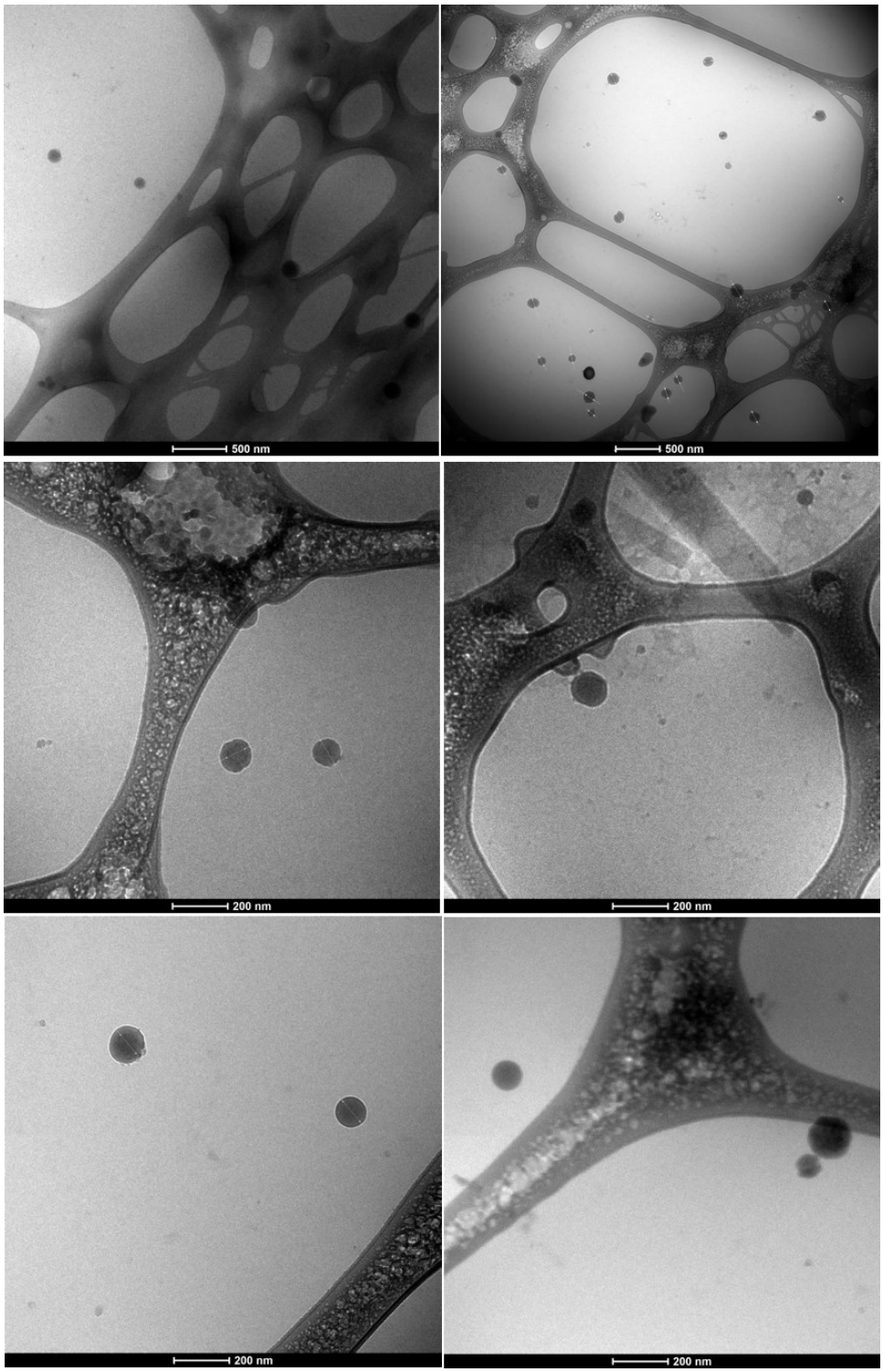

Figure B38. Typical cryo-TEM micrographs obtained from 5K-10K PEG-*b*-PLGA/2,7′-tri-ethoxy paclitaxel silicate prodrug. Sample is provided by Adam Wohl and Jing Han.

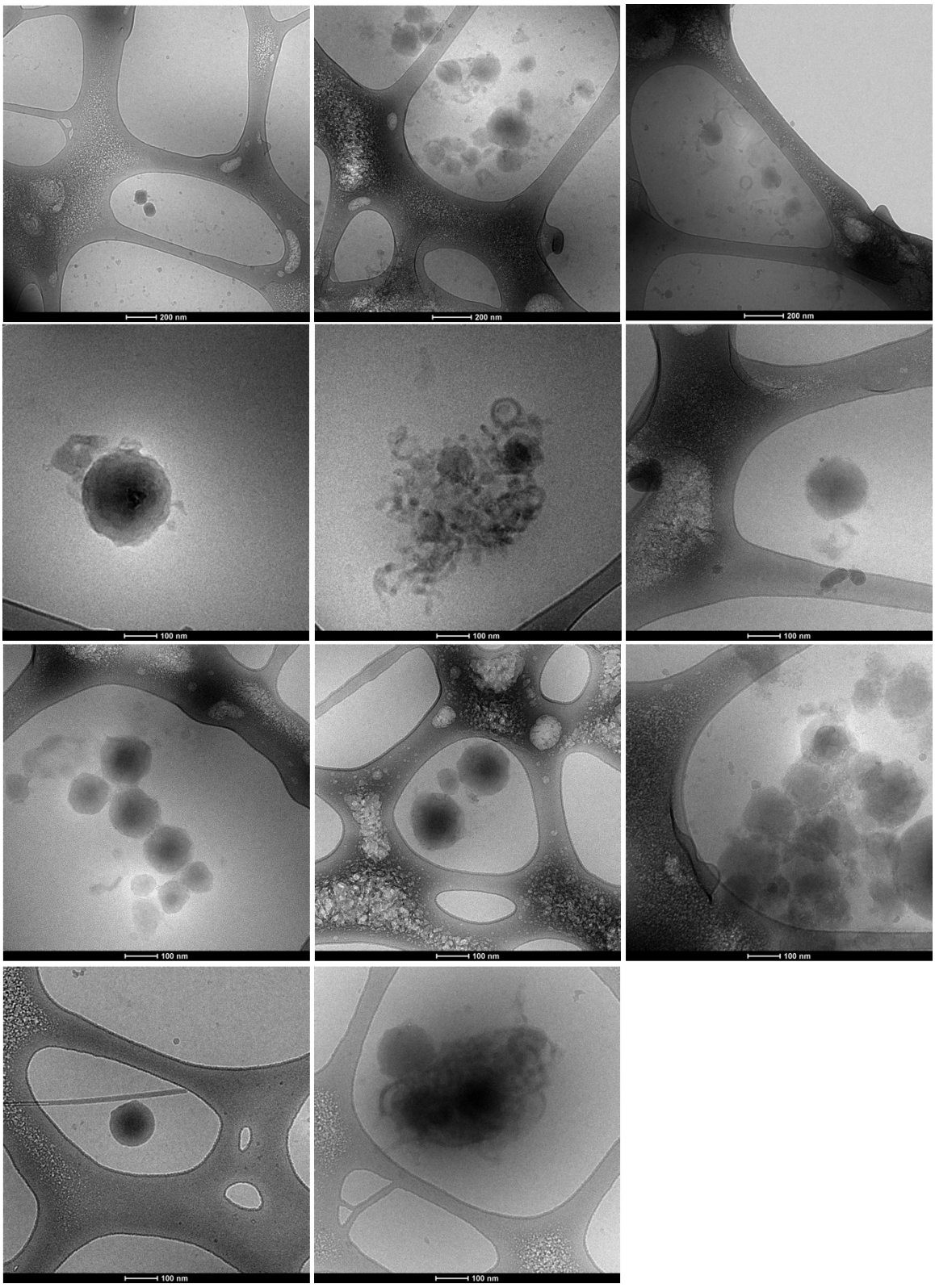

Figure B39. Typical cryo-TEM micrographs obtained from 5K-10K PEG-*b*-PLGA/2,7´-tri-ethoxy paclitaxel silicate prodrug (0 hour release). Sample is provided by Adam Wohl and Jing Han.

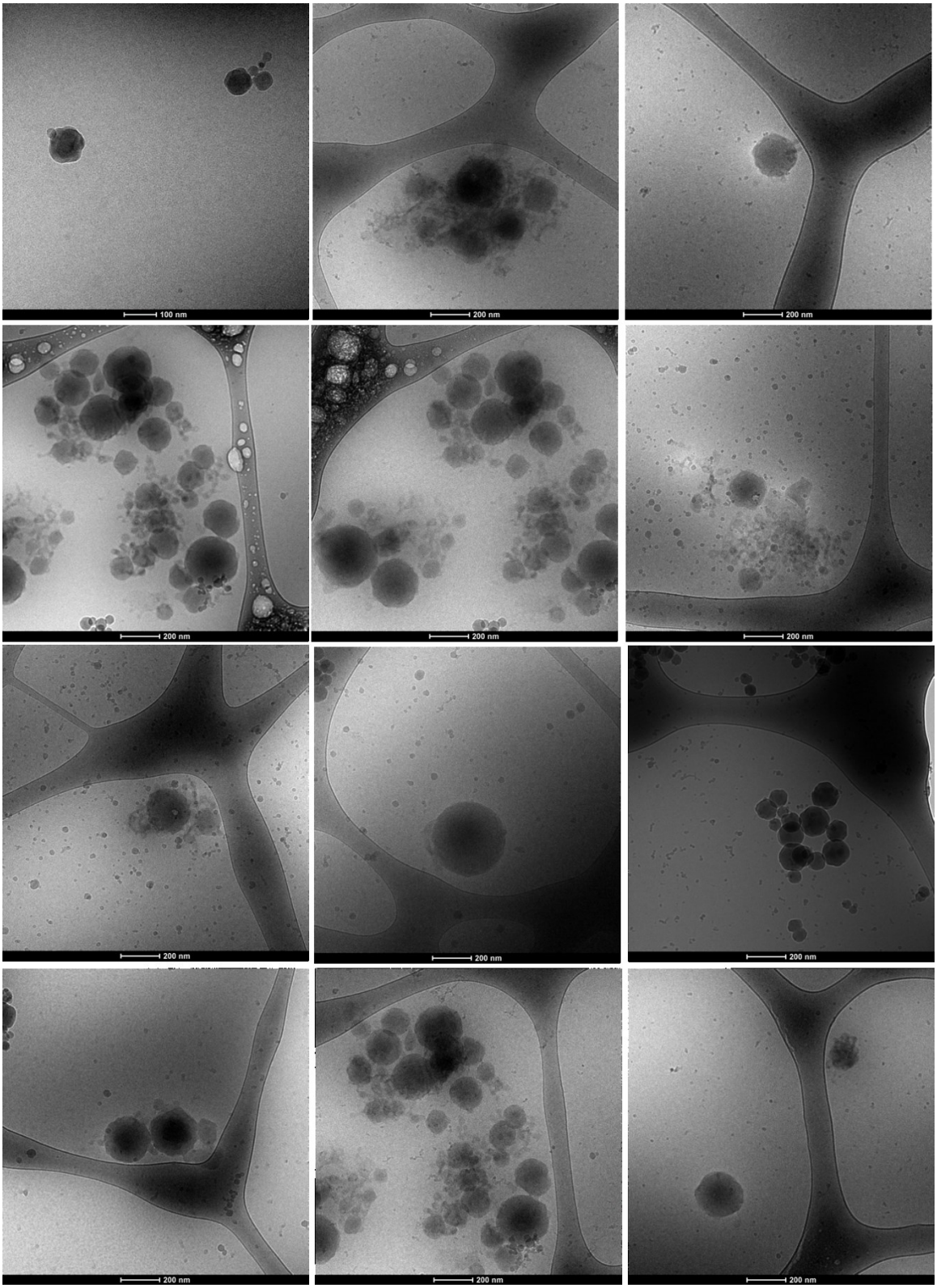

Figure B40. Typical cryo-TEM micrographs obtained from 5K-10K PEG-*b*-PLGA/2,7′-tri-ethoxy paclitaxel silicate prodrug (24 hours release). Sample is provided by Adam Wohl and Jing Han.

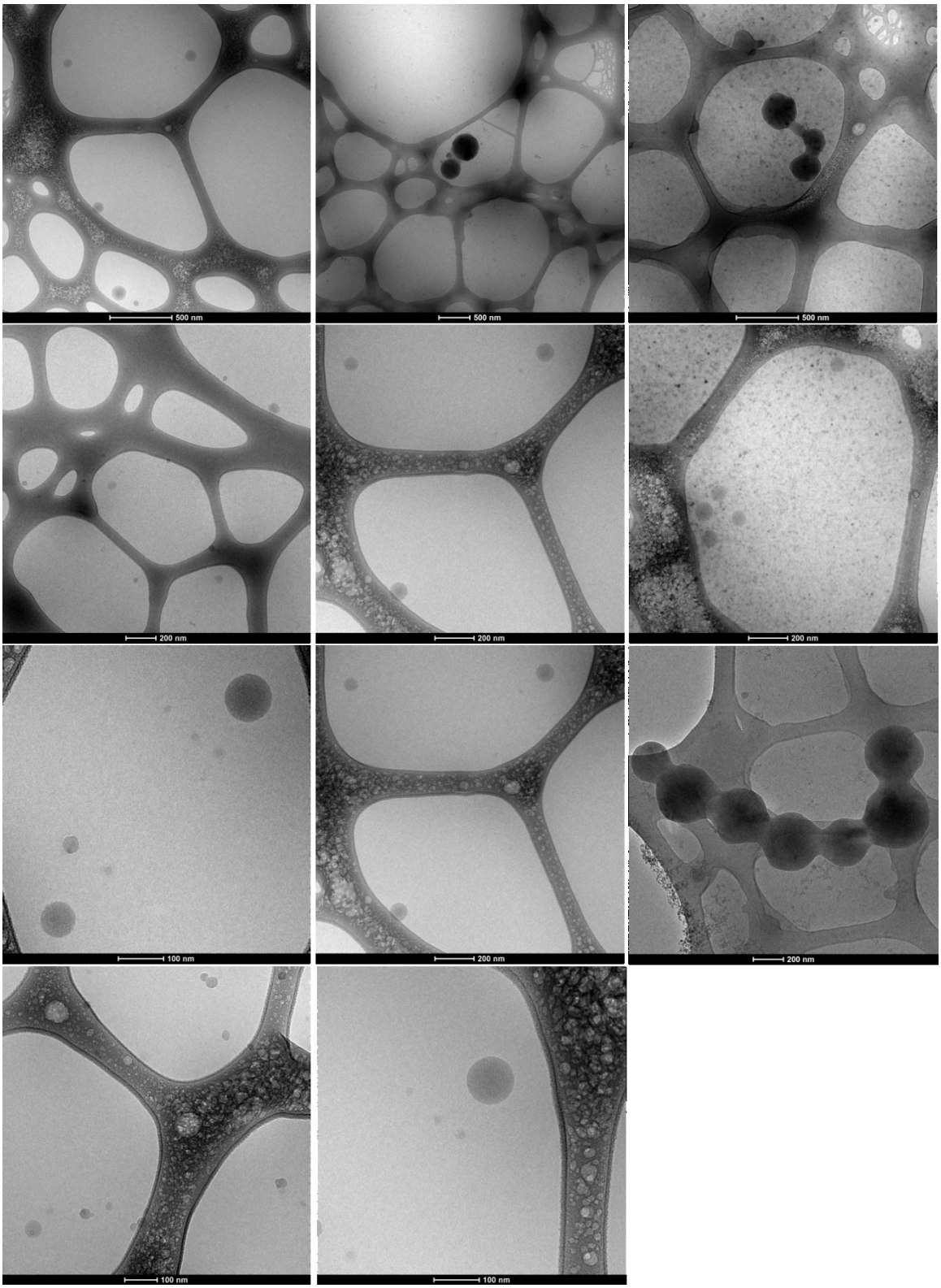

Figure B41. Typical cryo-TEM micrographs obtained from 5K-10K PEG-*b*-PLGA/2′-di-tert butoxy/ethoxy paclitaxel silicate prodrug. Sample is provided by Adam Wohl and Jing Han.

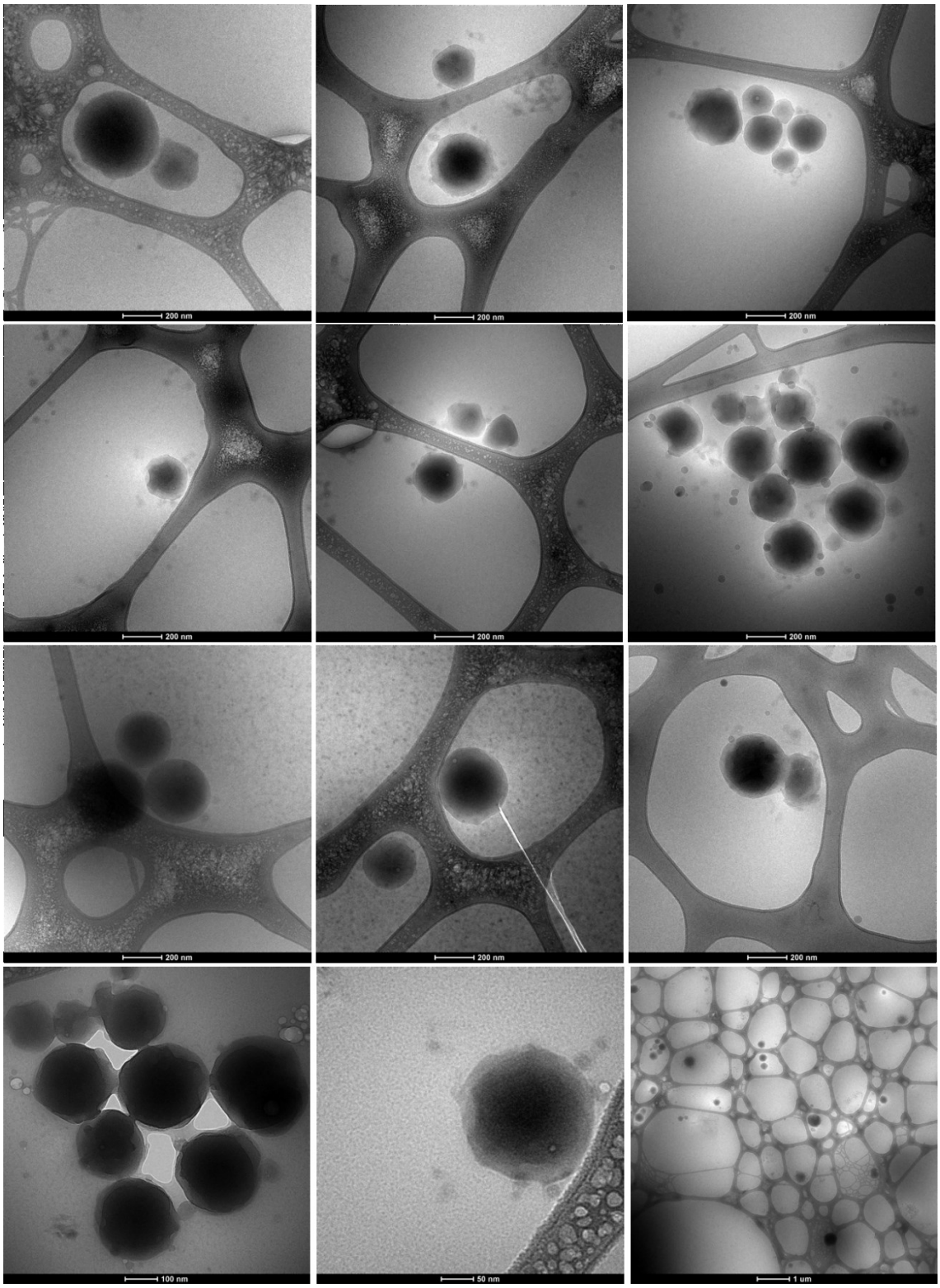

Figure B42. Typical cryo-TEM micrographs obtained from 5K-10K PEG-*b*-PLGA/2′-di-tert butoxy/ethoxy paclitaxel silicate prodrug (0 hour release). Sample is provided by Adam Wohl and Jing Han.

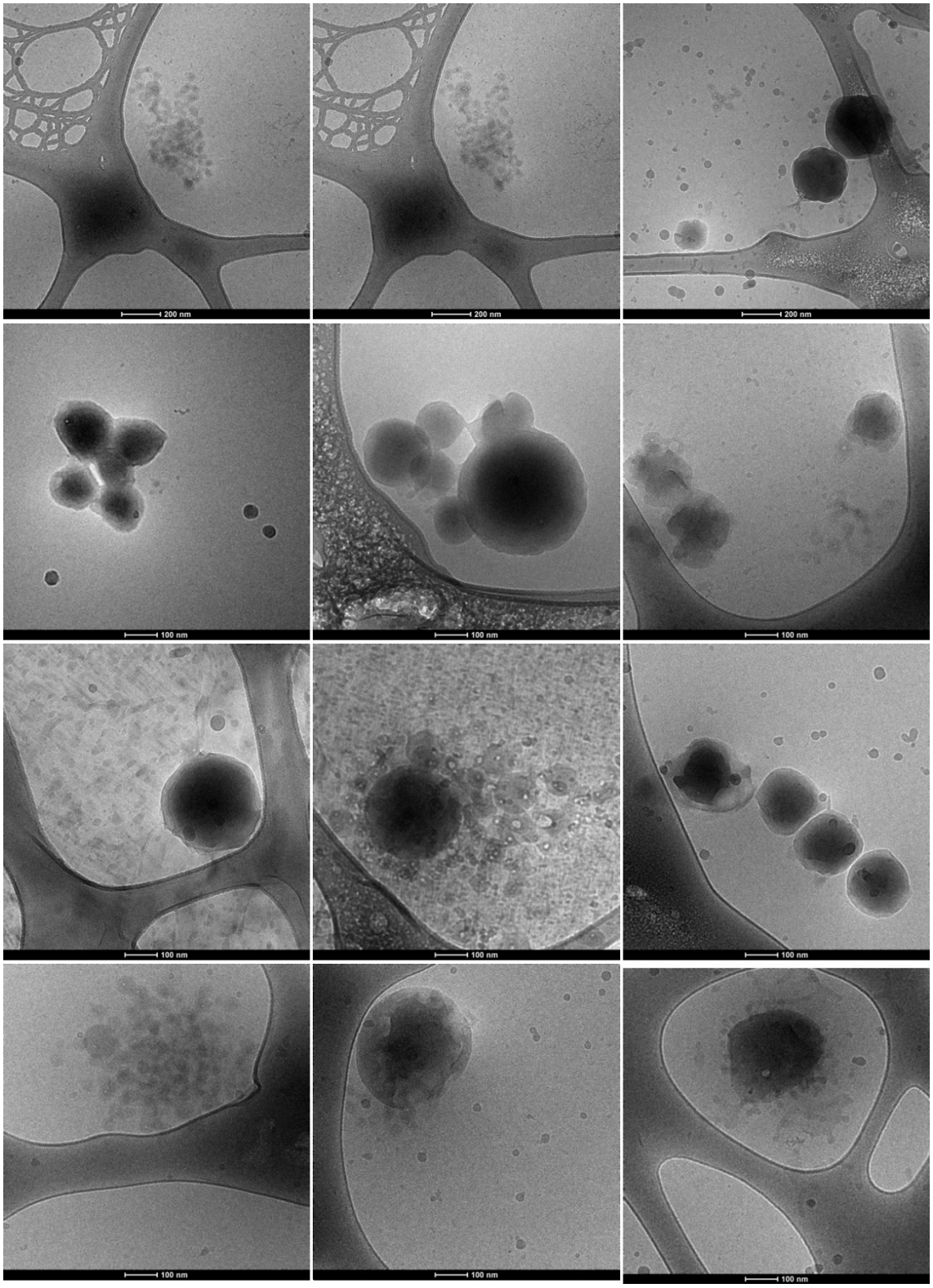

Figure B43. Typical cryo-TEM micrographs obtained from 5K-10K PEG-*b*-PLGA/2′-di-tert butoxy/ethoxy paclitaxel silicate prodrug (24 hours release). Sample is provided by Adam Wohl and Jing Han.

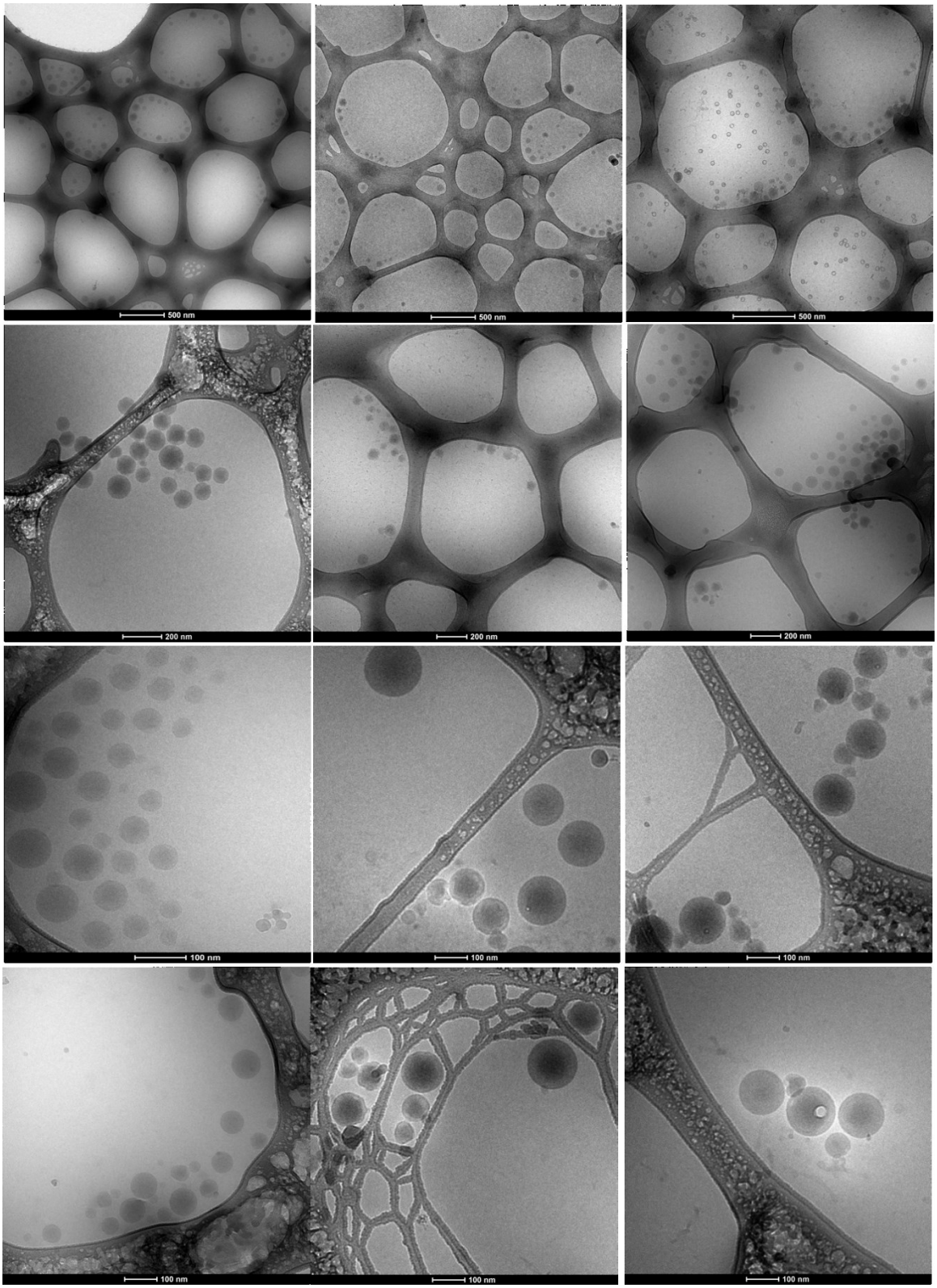

Figure B44. Typical cryo-TEM micrographs obtained from 5K-10K PEG-*b*-PLGA/2′-tri-menthoxy paclitaxel silicate prodrug. Sample is provided by Adam Wohl and Jing Han.

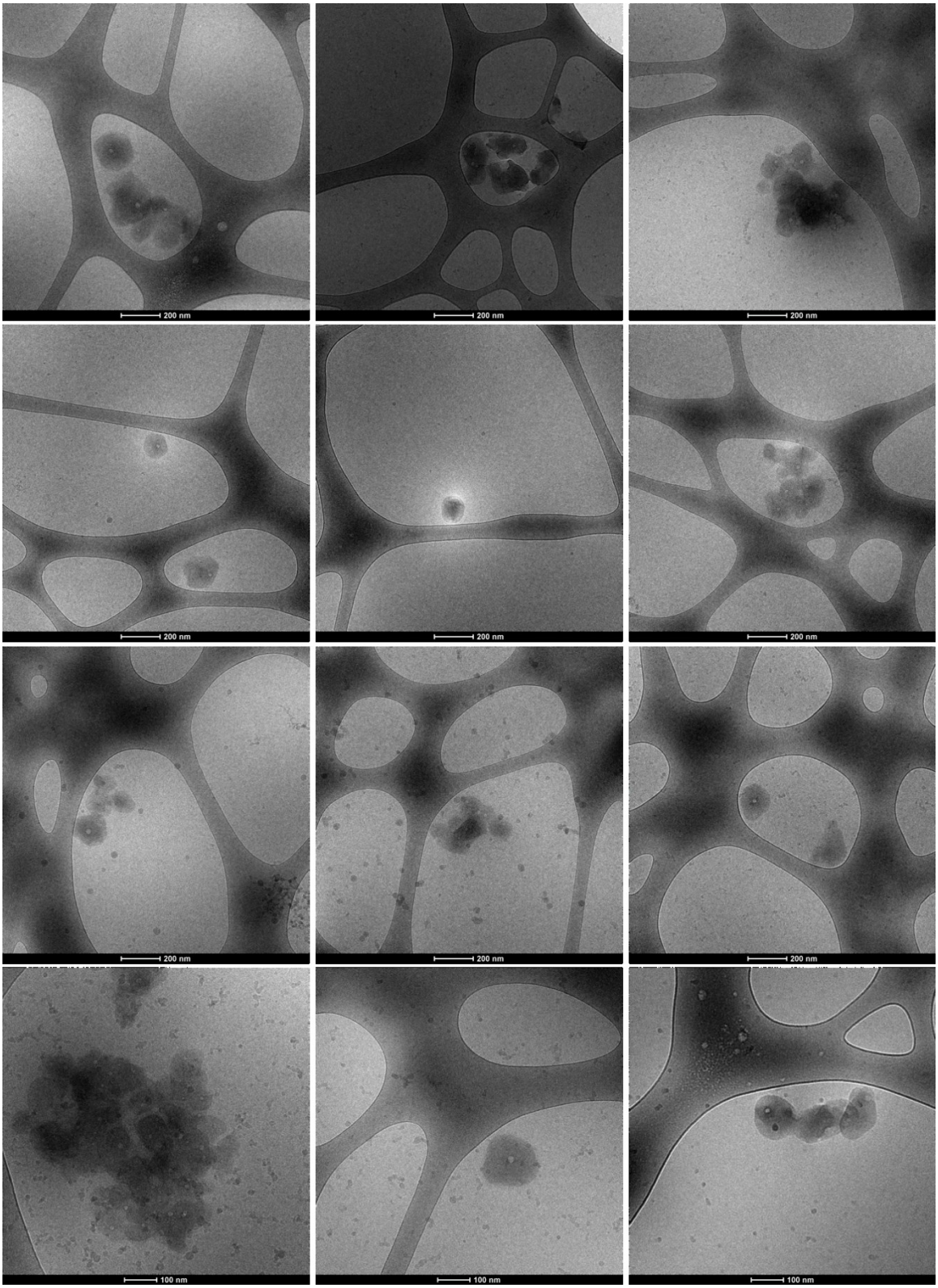

Figure B45. Typical cryo-TEM micrographs obtained from 5K-10K PEG-*b*-PLGA/2′-tri-menthoxy paclitaxel silicate prodrug (0 hour release). Sample is provided by Adam Wohl and Jing Han.

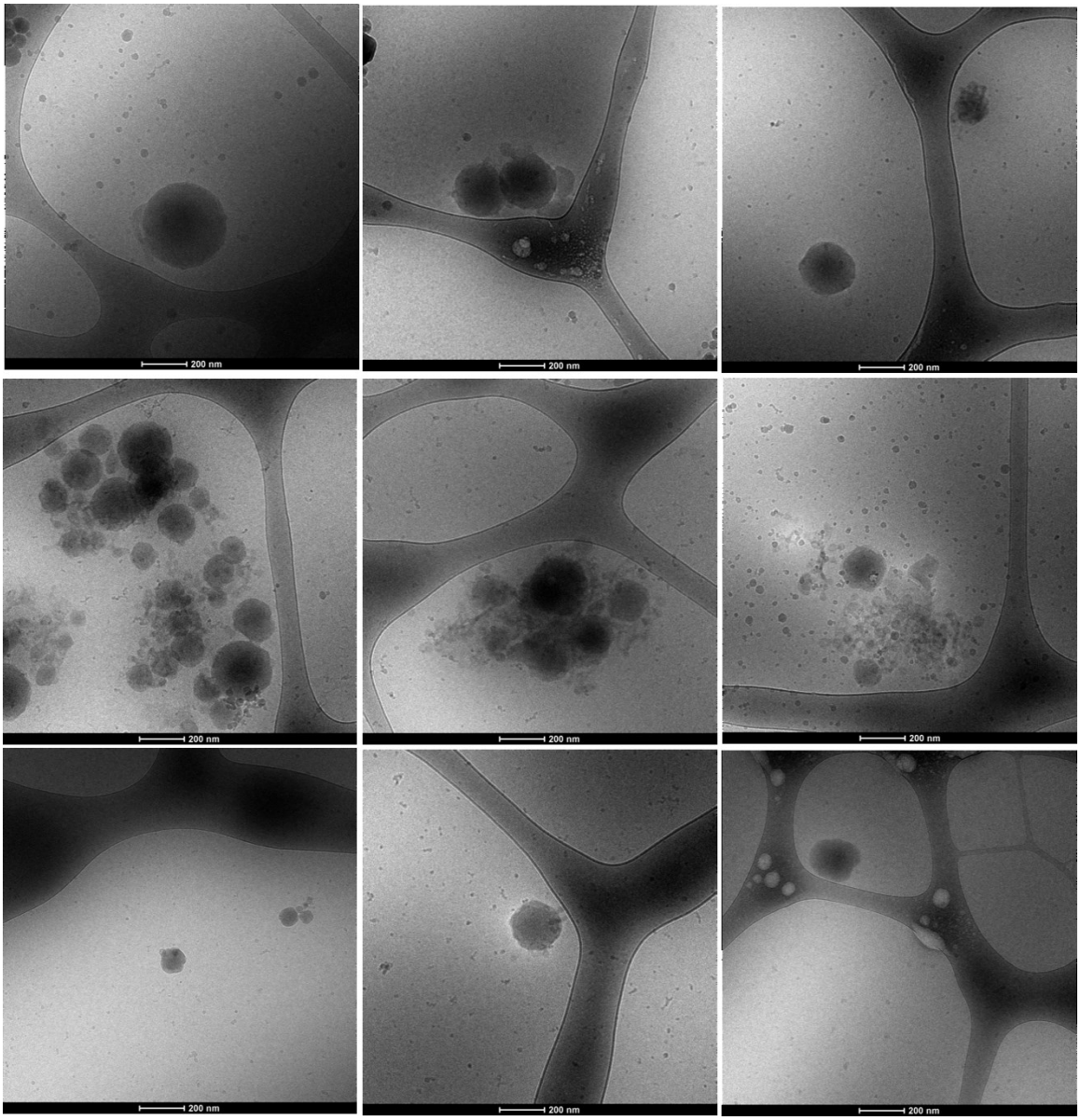

Figure B46. Typical cryo-TEM micrographs obtained from 5K-10K PEG-*b*-PLGA/2′-tri-menthoxy paclitaxel silicate prodrug (24 hours release). Sample is provided by Adam Wohl and Jing Han.

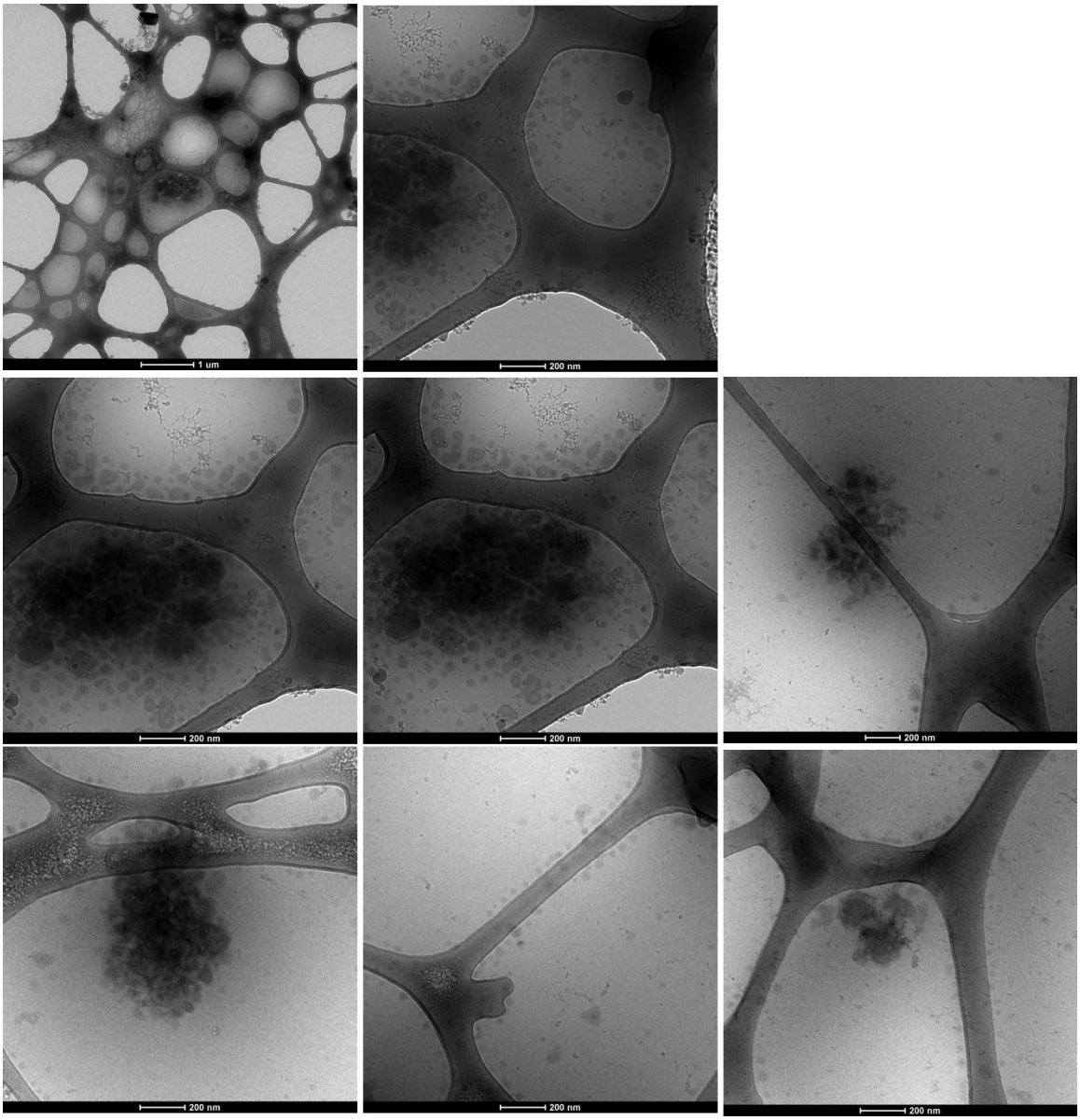

Figure B47. Typical cryo-TEM micrographs obtained from 5K-10K PEG-*b*-PLGA/2′-tri-ethoxy/butoxy (coloading) paclitaxel silicate prodrug. Sample is provided by Adam Wohl and Jing Han.

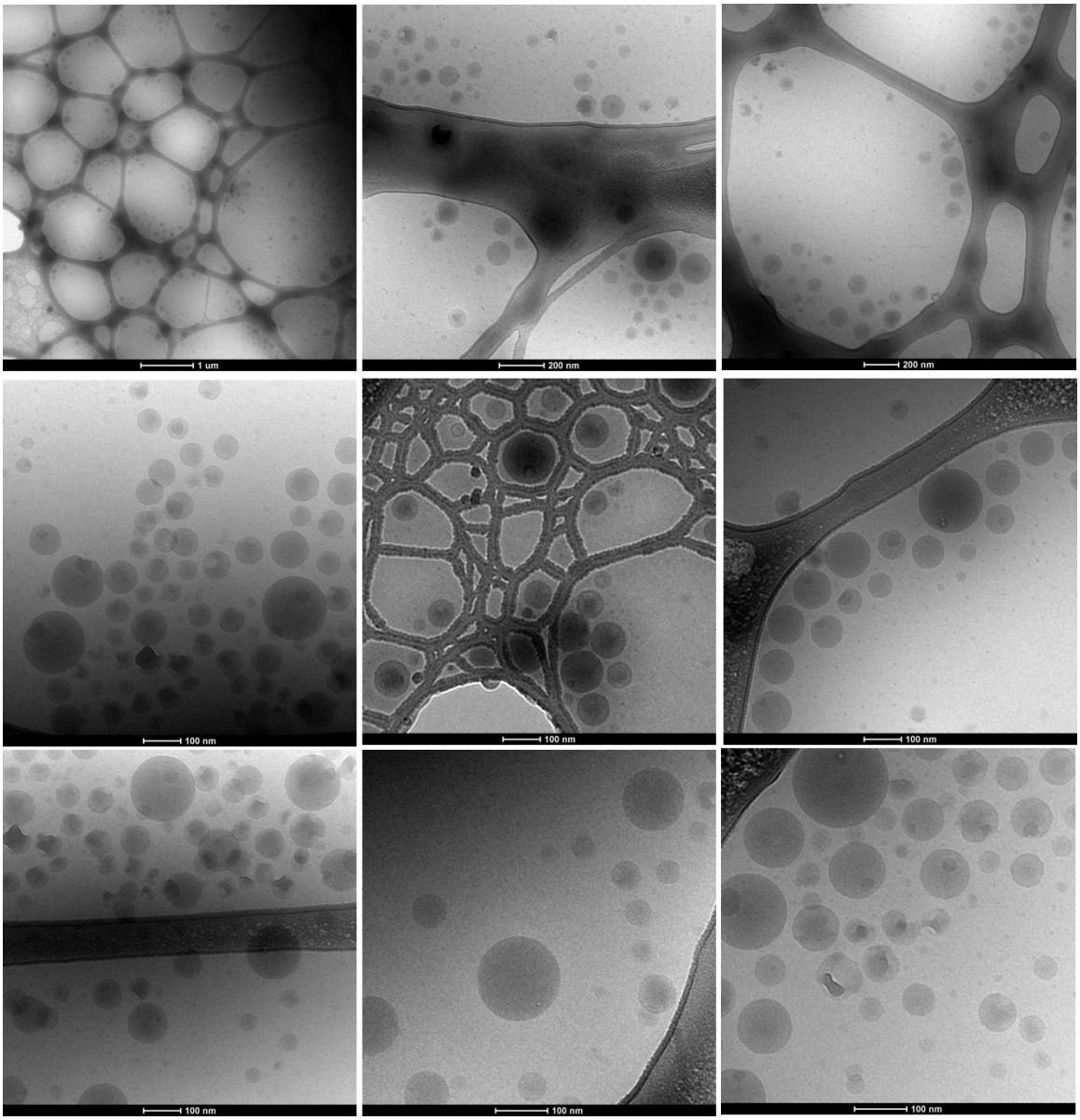

Figure B48. Typical cryo-TEM micrographs obtained from 5K-10K PEG-*b*-PLGA/60% 2′-tri-menthoxy paclitaxel silicate prodrug. Sample is provided by Adam Wohl and Jing Han.

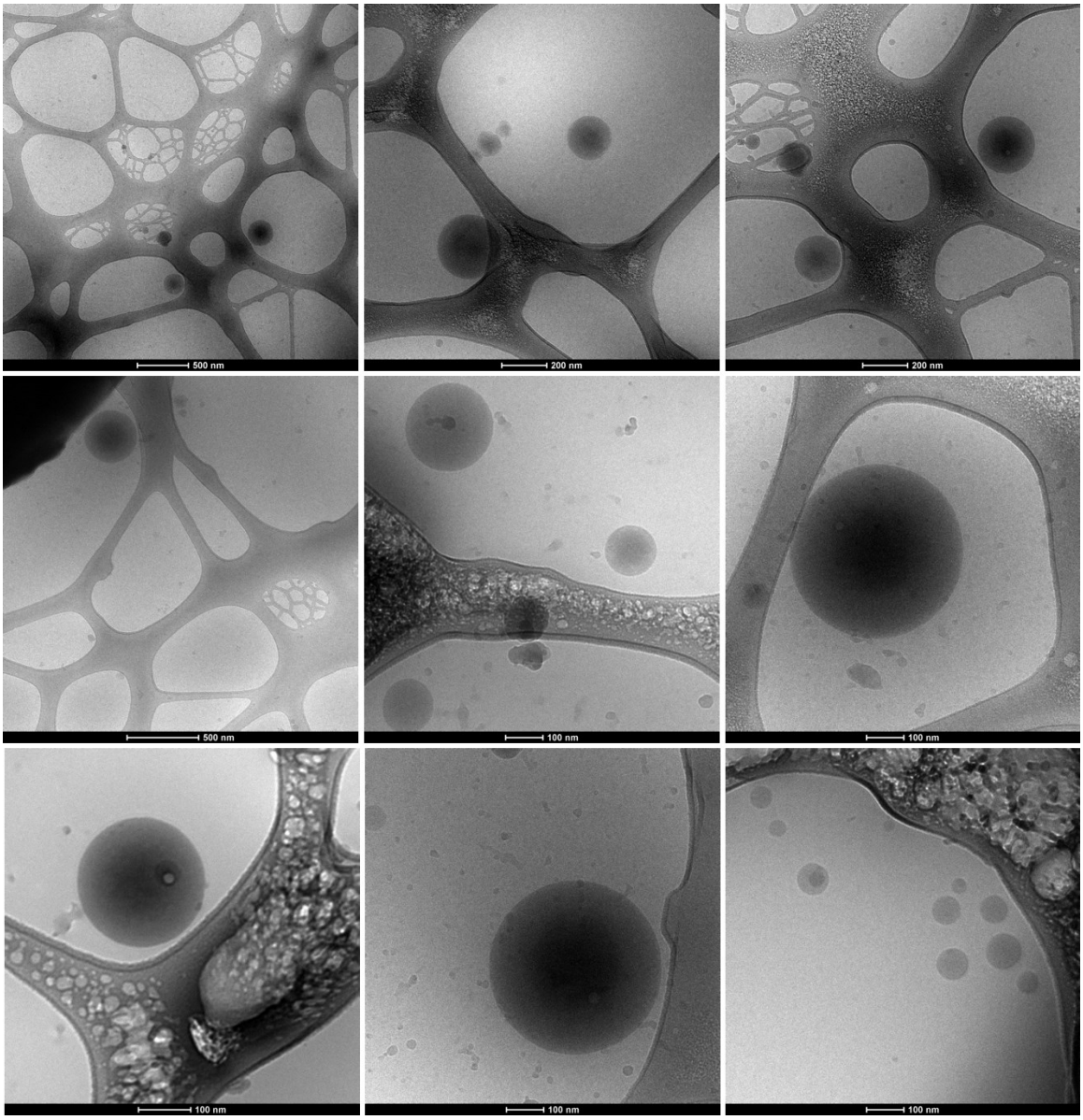

Figure B49. Typical cryo-TEM micrographs obtained from 5K-10K PEG-*b*-PLGA/80% 2′-tri-menthoxy paclitaxel silicate prodrug. Sample is provided by Adam Wohl and Jing Han.

Appendix C.

EM images of nanoemulsion formation from microemulsions

I. EM images of H_2O/*n*-hexadecane/alkylphenol nonionic surfactants, 2.2 parts per hundred cosurfactant
    - Figures C1 – C4

II. EM images of H_2O/*n*-hexadecane/alkylphenol nonionic surfactants, 2.4 parts per hundred cosurfactant
    - Figures C5 – C6

III. EM images of H_2O/*n*-hexadecane/alkylphenol nonionic surfactants, 4.0 parts per hundred cosurfactant.
    - Figures C7 – C8

IV. Cryo-TEM images of uranyl acetated stained nanoemulsions
    - Figures C9

V. Cross polarized of microemulsions of H_2O/*n*-hexadecane/alkylphenol nonionic surfactants, 4.0 parts per hundred cosurfactant
    - Figures C10

I. EM images of H_2O/*n*-hexadecane/alkylphenol nonionic surfactants, 2.2 parts per hundred cosurfactant

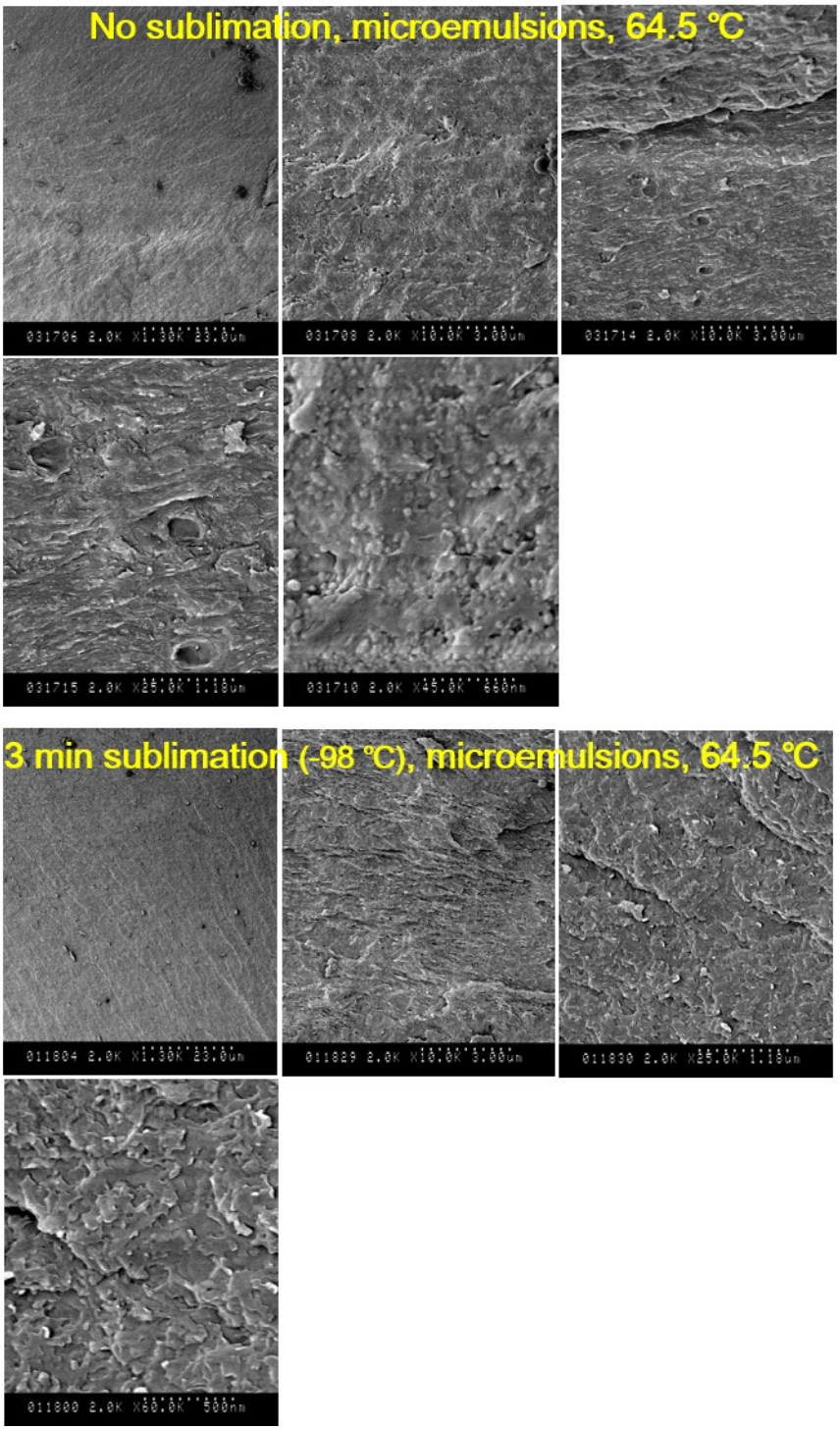

Figure C1. Typical cryo-SEM micrographs obtained from H_2O/*n*-hexadecane/alkylphenol nonionic surfactants with 2.2 parts per hundred cosurfactant.

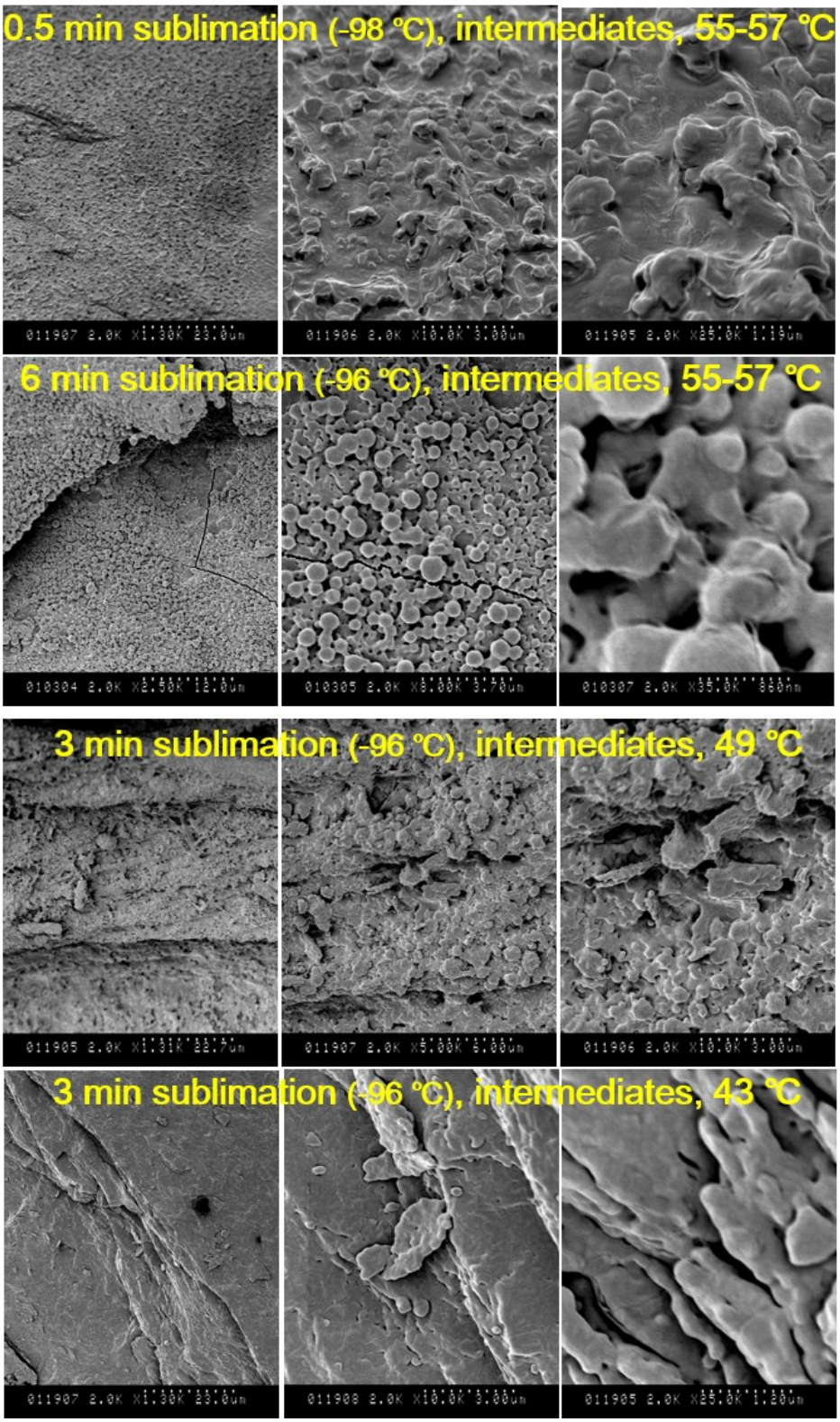

Figure C2. Typical cryo-SEM micrographs obtained from H_2O/*n*-hexadecane/alkylphenol nonionic surfactants with 2.2 parts per hundred cosurfactant.

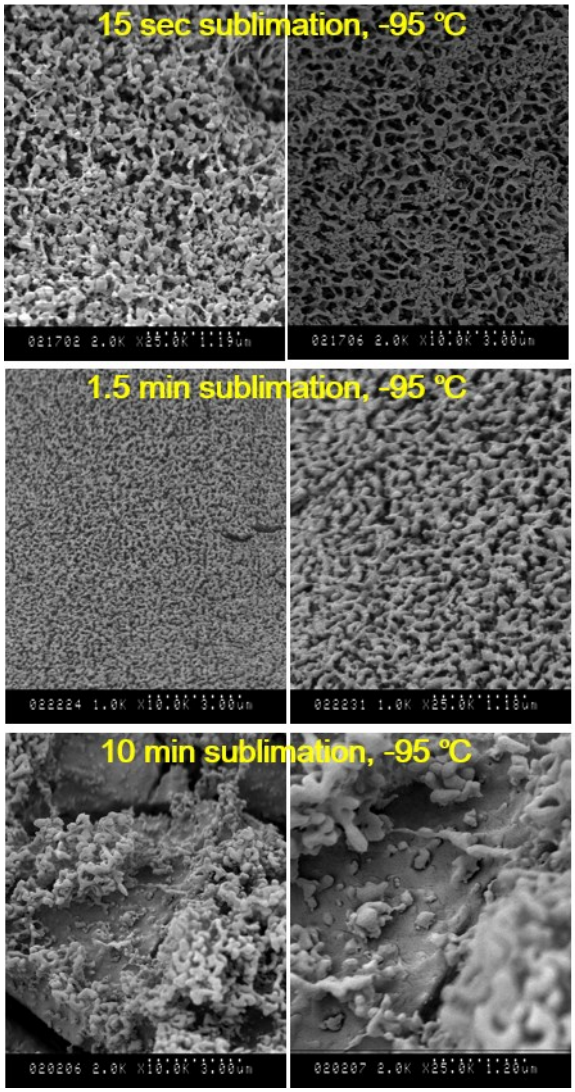

Figure C3. Typical cryo-SEM micrographs obtained from H_2O/*n*-hexadecane/alkylphenol nonionic surfactants. Nanoemulsions with 2.2 parts per hundred cosurfactant.

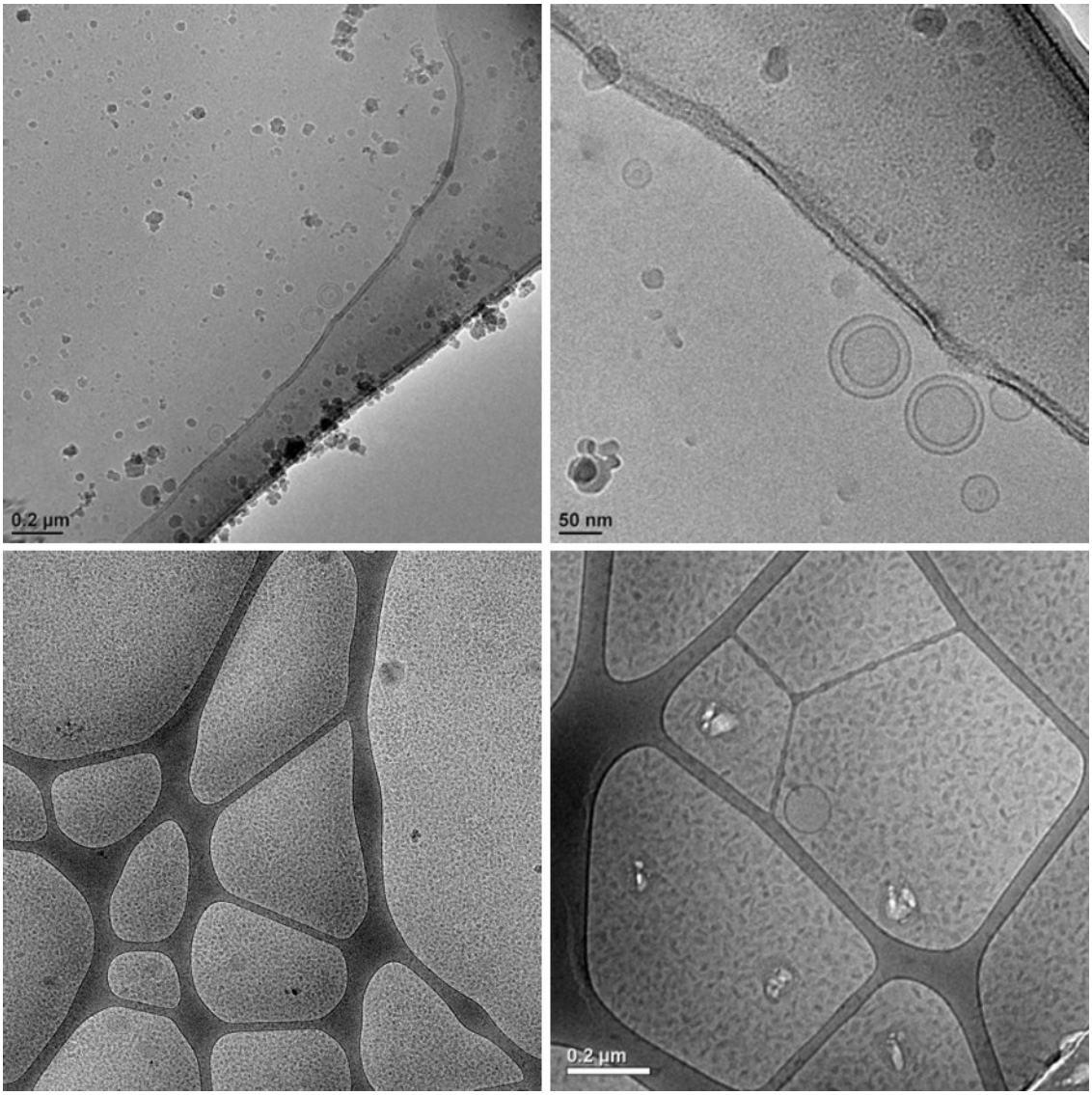

Figure C4. Typical cryo-TEM micrographs obtained from H_2O/*n*-hexadecane/alkylphenol nonionic surfactants. Nanoemulsions with 2.2 parts per hundred cosurfactant.

II. EM images of H_2O/*n*-hexadecane/alkylphenol nonionic surfactants, 2.4 parts per hundred cosurfactant

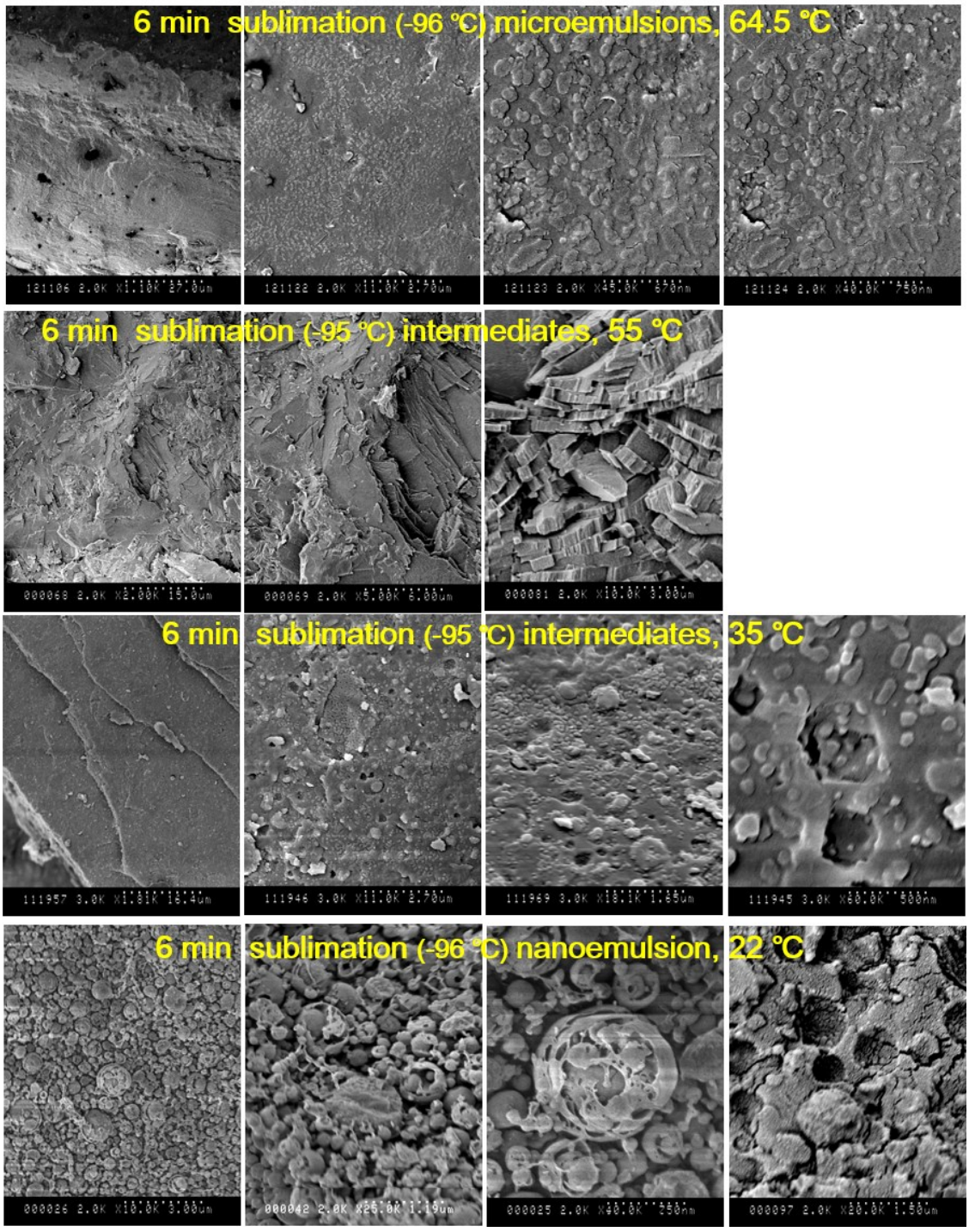

Figure C5. Typical cryo-SEM micrographs obtained from H_2O/*n*-hexadecane/alkylphenol nonionic surfactants with 2.4 parts per hundred cosurfactant.

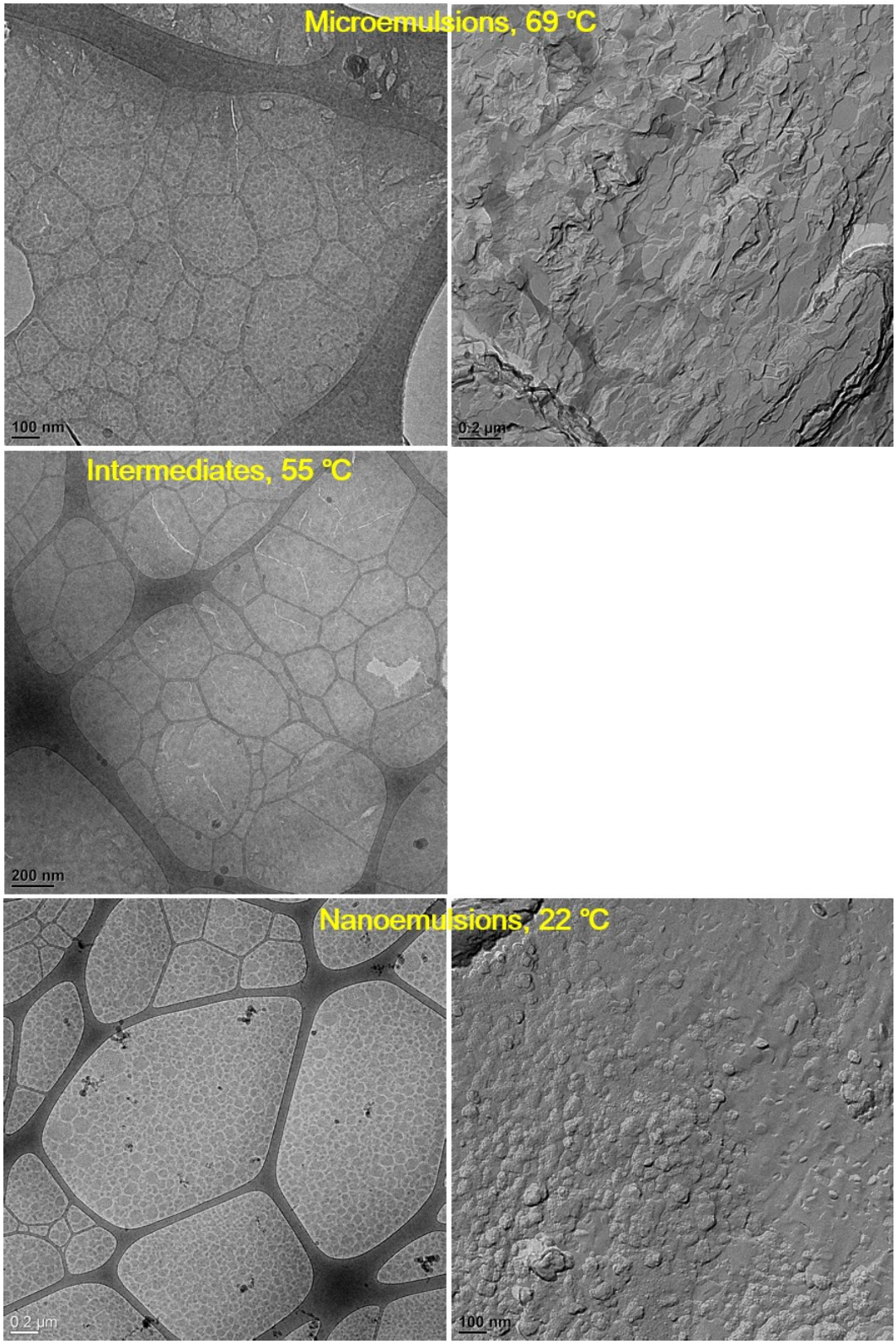

Figure C6. Typical cryo-TEM and FF-TEM micrographs obtained from H_2O/*n*-hexadecane/alkylphenol nonionic surfactants with 2.4 parts per hundred cosurfactant.

III. EM images of H_2O/*n*-hexadecane/alkylphenol nonionic surfactants, 4.0 parts per hundred cosurfactant

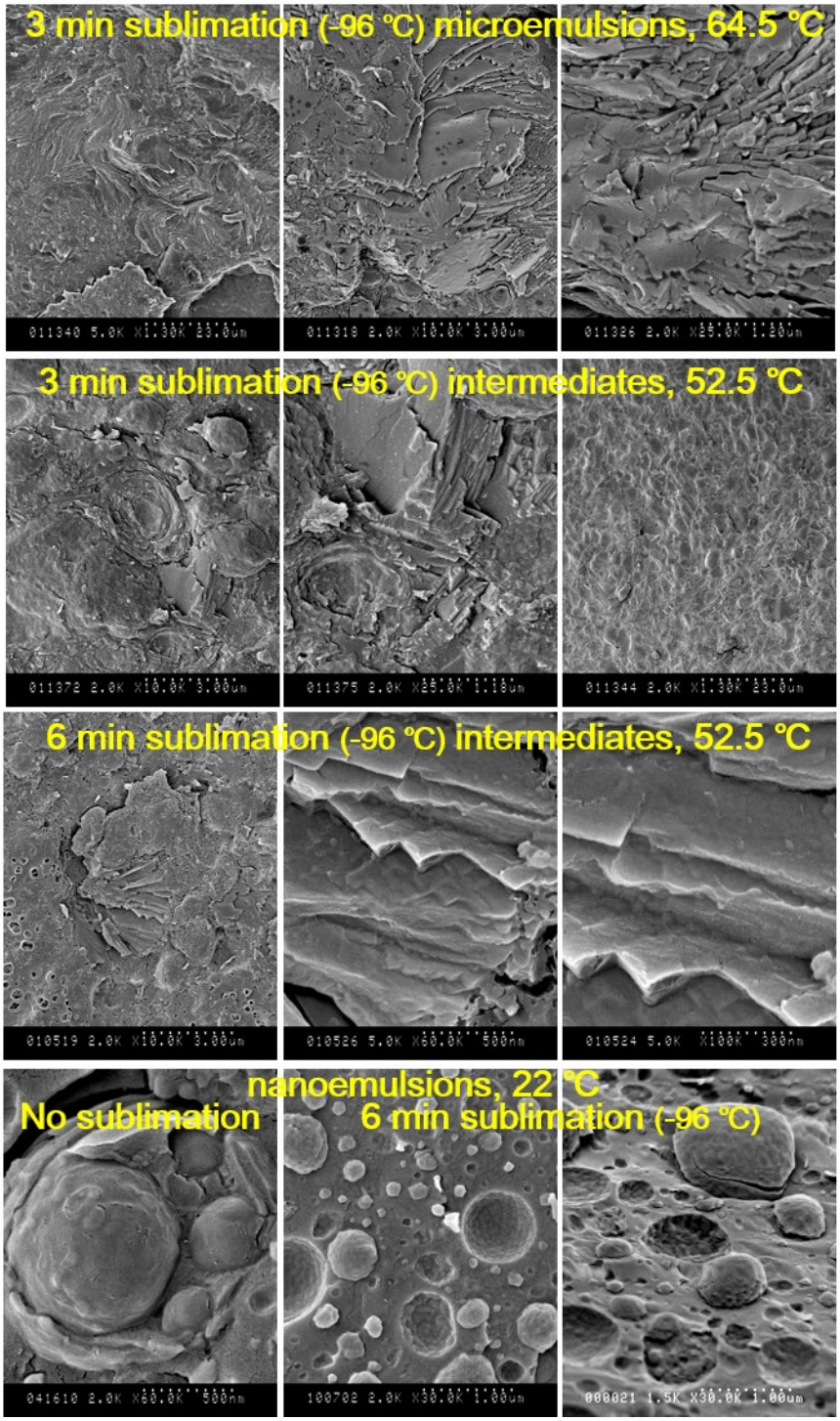

Figure C7. Typical cryo-SEM micrographs obtained from H_2O/*n*-hexadecane/alkylphenol nonionic surfactants with 4.0 parts per hundred cosurfactant.

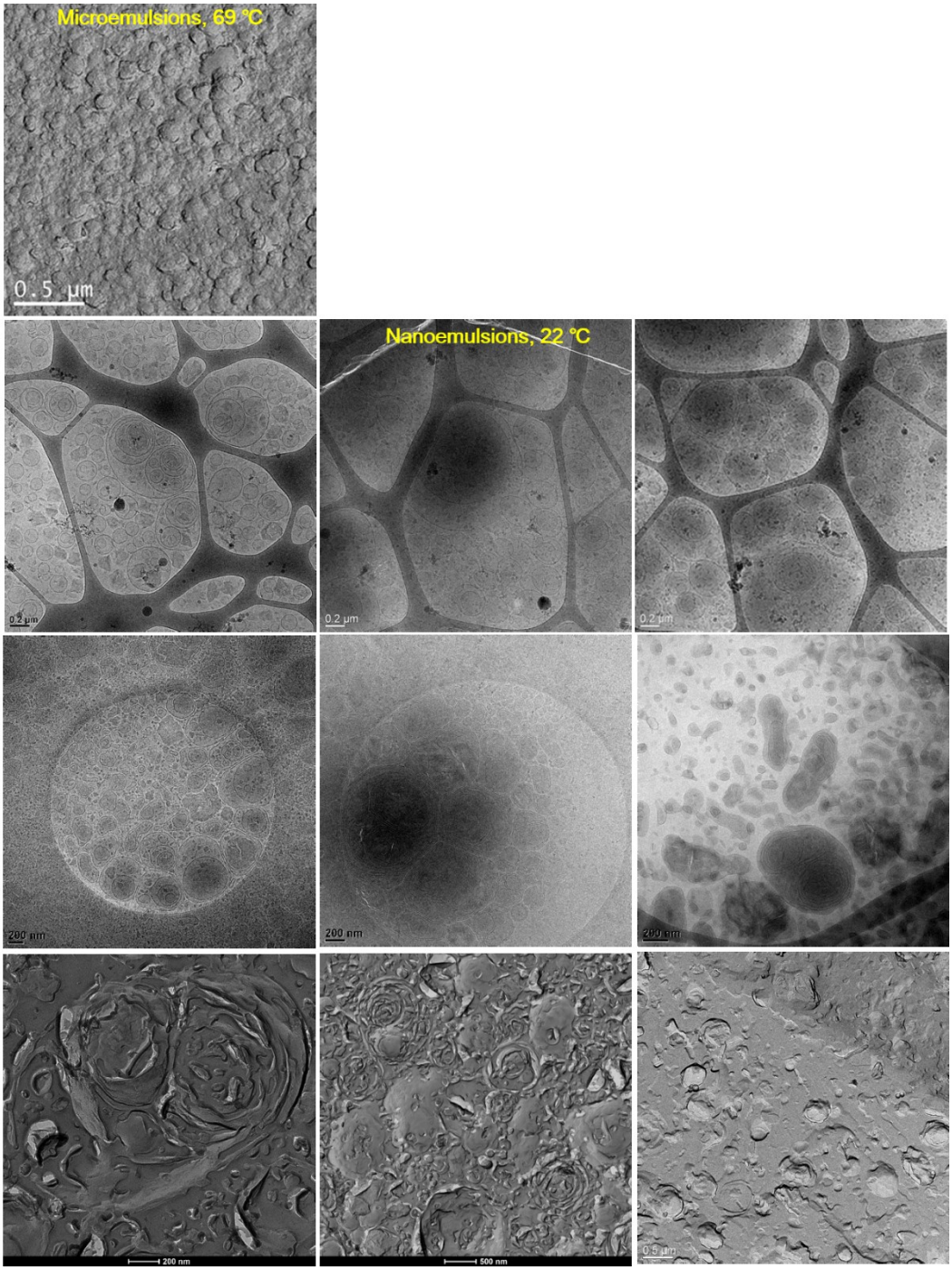

Figure C8. Typical cryo-TEM and FF-TEM micrographs obtained from H_2O/*n*-hexadecane/alkylphenol nonionic surfactants with 4.0 parts per hundred cosurfactant.

IV. Cryo-TEM images of uranyl acetated stained nanoemulsions

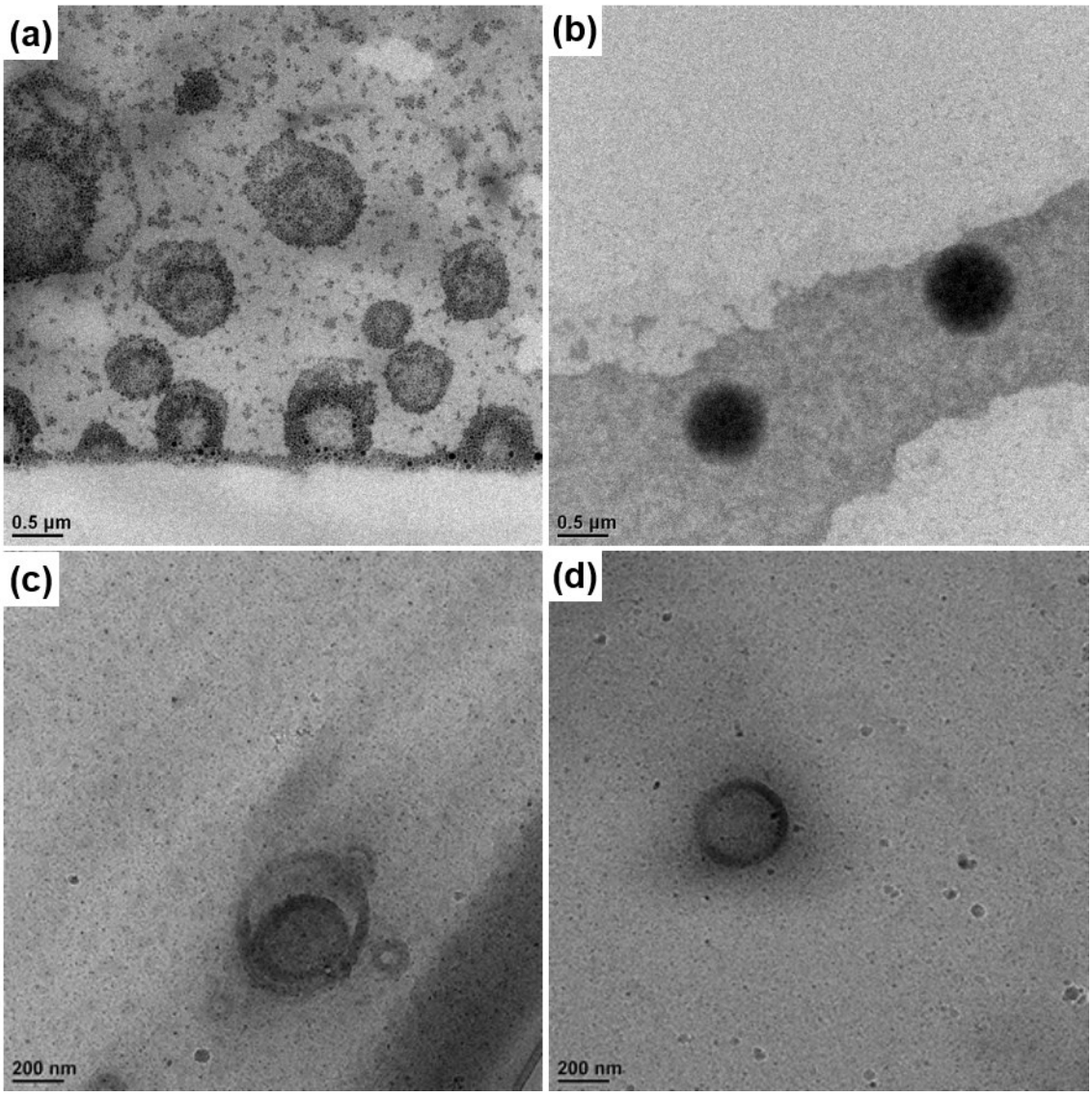

Figure C9. Typical cryo-TEM micrographs obtained from H_2O/*n*-hexadecane/alkylphenol nonionic surfactants stained with uranyl acetate (UA) 1 wt %. Nanoemulsions with (a, b) 2.57 parts per hundred cosurfactant (pph) and (c, d) 4.0 pph cosurfactant. Staining was done with on-the-grid reaction/mixing and the procedure is shown in Ph.D. thesis of Zheng,[1] Dong,[2] and MS thesis of Pustulka.[3] The sample is applied on the TEM grid. Additional small drop of staining solution (1 wt % of UA) is placed on top of the applied sample and allowed to sit for 2–3 minutes before blotted away from the other side of the TEM grid.

1. Zheng, Y. Cryo-electron microscopy of microstructures in self-assembled colloidal systems. Ph.D., University of Minnesota 2000.
2 Dong, J. Cryo-TEM of morphology and kinetics of self-assembled nanostructures, Ph.D., University of Minnesota 2006.
3. Pustulka, K. Polymer stabilized nanosuspensions via flash nanoprecipitation: Particle formulation, structure and freeze drying, MS, University of Minnesota 2006.

V. Cross polarized of microemulsions of H_2O/*n*-hexadecane/alkylphenol nonionic surfactants, 4.0 parts per hundred cosurfactant

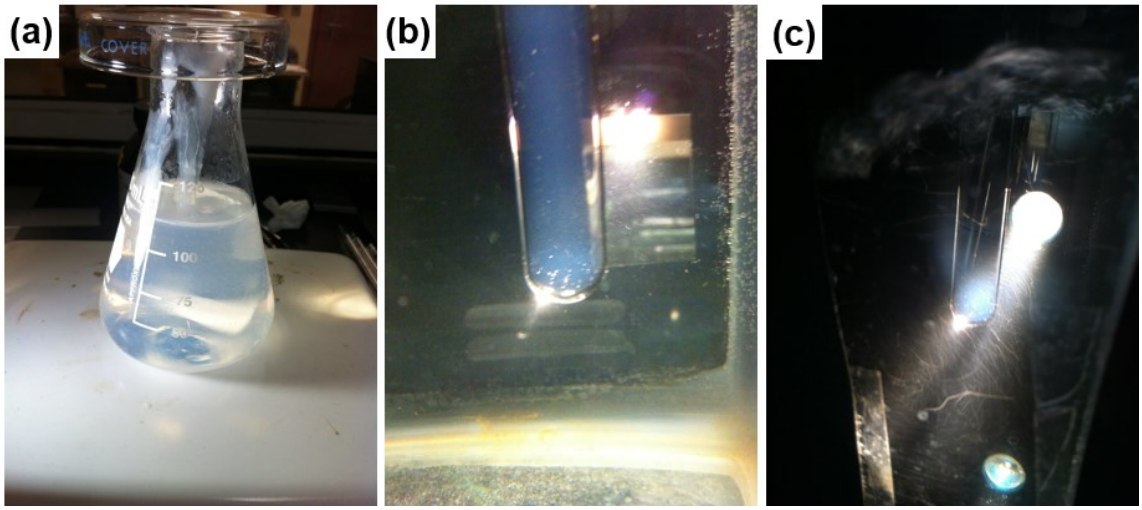

Figure C10. (a) Picture of H_2O/*n*-hexadecane/alkylphenol nonionic surfactants microemulsions with 4.0 parts per hundred cosurfactant. (b, c) are cross polarized pictures of microemulsions at 58 ℃.

Appendix D.

Temperature scans of conductivity and transparency for the emulsions with halogenated alkanes

Conductivity versus temperature plot of H_2O/halogenated oil/alkylphenol nonionic surfactants, 2.2 parts per hundred cosurfactant.

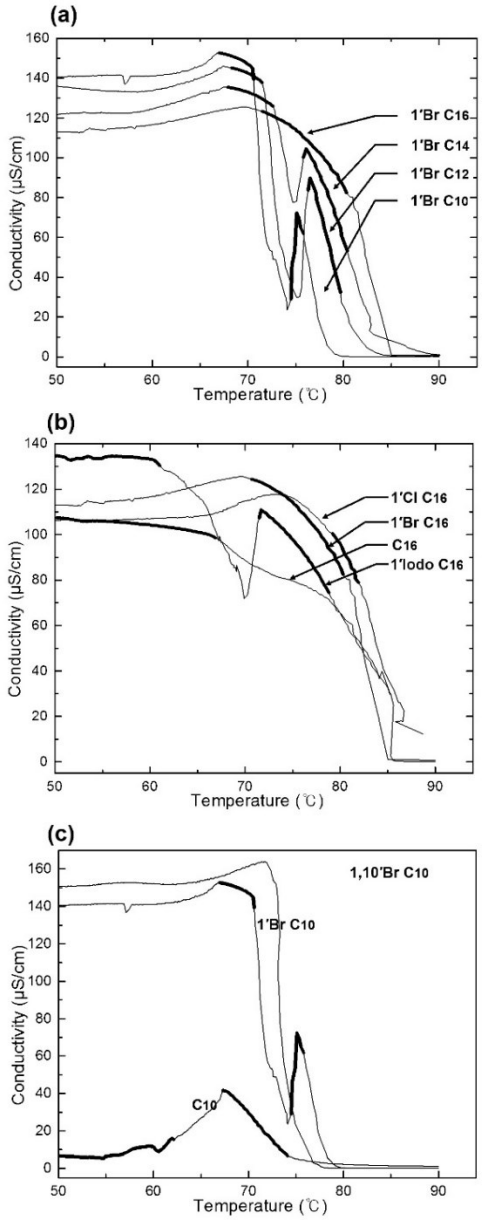

Figure D1. Conductivity versus temperature plots for H_2O/oil/alkylphenol nonionic surfactants with a fixed amount of 2.2 parts per hundred cosurfactant. (a) Brominated alkanes, (b) halogenated hexadecanes, and (c) brominated decanes. Bold segments represent transparent microemulsion regions.